The Atmospheric Dynamics and Habitablity of Temperate Sub-Neptunes

Hamish Innes
Exeter College
University of Oxford

A thesis submitted for the degree of
Doctor of Philosophy

Michaelmas 2023

To my parents, to whom I owe everything.

Abstract

Sub-Neptunes are a subset of exoplanets that lie between the Earth and Neptune in size, have no solar system analogue and yet are one of the most common types of exoplanet in the galaxy. Some sub-Neptunes receive a similar level of stellar flux as Earth, making their atmospheres potentially cool enough to contain liquid water. The aim of this thesis is to simulate the atmospheres of these temperate sub-Neptunes and develop theories describing their atmospheric dynamics and potential habitability.

I use a general circulation model to simulate the atmospheres of a range of dry, temperate sub-Neptunes. I show that their atmospheres are governed by horizontal weak temperature gradients over a broad range of parameter space. Their circulation is dominated by high-latitude jets, but heat is transported from the dayside to the nightside by a residual overturning circulation. I derive a scaling theory to link the strength of this circulation to the instellation.

Next, I calculate the inner edge of the habitable zone for sub-Neptunes with a water surface – "Hycean worlds". Using a 1D radiative-convective model, I show that compositional gradients induced by the condensation of water inhibit convection in a hydrogen-dominated atmosphere. The resulting temperature structures heat the surface and lead to the inner edge of the habitable zone moving outwards compared to traditional calculations.

Lastly, I develop a general circulation model for use in hydrogen-dominated atmospheres with a non-dilute water vapour component. I demonstrate the model's ability to simulate a range of sub-Neptune atmospheres with different deep water contents reaching as high as 70% of the atmosphere by mass. Future work can build on this model to understand how latent heating and compositional gradients impact the observable features and habitability of sub-Neptune exoplanets.

Acknowledgements

I want to start by thanking Ray, without whom I wouldn't have spent the last four years in Oxford nor met many of the people who made them so enjoyable. Thank you for guiding me through my project and giving me the encouragement and freedom to pursue any topic of interest to me. If I can leave Oxford possessing a small fraction of your combined knowledge of climate, fluid dynamics and planetary physics I will consider my time here a success.

Thank you to the Planetary Climate group for being an immense source of intelligence, support and friendship during my studies. Thanks to Maxence for being my lunchtime companion and for indulging my attempts to speak French. Thank you to Shami for your encouragement and guidance through difficult times, and for weekends well spent playing board games at your house. Thanks to Mark, Elsie and Neil for teaching me how to use GCMs, proof-reading my wordy manuscripts and for generally setting a great example of how to be a successful researcher.

To Sally, Namrah, Ed and Richard: it has been a pleasure sharing an office with you. Working on this thesis would have been a much greater toil without your daily humour and companionship. Thank you to everyone in AOPP with whom I spent countless lunches, coffee breaks, happy hours, retreats and Christmas parties.

Thank you to my friends who provided me welcome relief from the (relative) stresses of D.Phil life. In particular, thank you to my housemates Nick, Fiona and Maddy who put up with me in lockdown – our communal meals, TV-bingeing sessions and "parties" helped me get through months of isolation and two bouts of COVID.

Thank you to my family. I feel truly lucky to have two sisters like Mairi and Ailsa, who have always inspired me with their intelligence, determination and kindness. To my parents, thank you for your unwavering support of me, even when I decided to spend four years studying "space weather".

Lastly, thank you to Claire, who has been by my side through the highs and the lows of this D.Phil. You have reminded me that there is so much more to life than a thesis.

Contents

Chapter 1

Introduction

To date, over 5000 exoplanets have been discovered, spanning a wide range of sizes, masses and equilibrium temperatures. Evidence from population studies suggests that most stars in the Milky Way host at least one exoplanet (Cassan et al., 2012). Figure 1.1 shows the current population of exoplanets viewed in radius-orbital period space[1]. The large, highly-irradiated exoplanets in the bottom-right of the diagram are "Hot Jupiters". They were discovered first owing to their large masses and radii, which make them easier to detect via radial velocity or transit measurements. However, subsequent exoplanet surveys have shown that smaller planets with radii $R < 4R_{\oplus}$ are by far the most abundant type of exoplanet in our galaxy. A subset of these small planets are "sub-Neptunes", which are thought to have extended, hydrogen-dominated atmospheres. Chemical equilibrium calculations show that water vapour should be common in their atmospheres. For cool, temperate sub-Neptunes, water can condense, releasing latent heat, forming liquid water clouds and potentially forming liquid water oceans. The potential for a large pool of non-Earth like planets to host liquid water could reshape how we define habitability and the search for life on other planets.

[1] Data from the Nasa Exoplanet Archive, https://exoplanetarchive.ipac.caltech.edu, accessed Monday 30th October, 2023

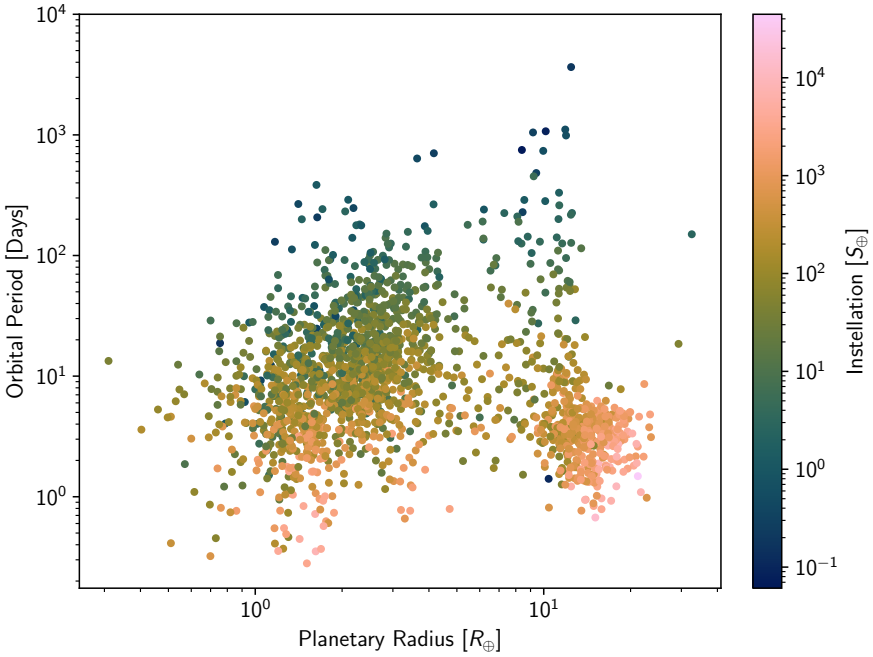

Figure 1.1: The population of discovered exoplanets viewed in radius-orbital period space. Large, strongly irradiated planets in the bottom-right of the diagram are "Hot Jupiters". The most abundant types of planet are smaller, with $R \lesssim 4R_\oplus$. These small planets are subdivided into smaller "super-Earths" ($R < 1.5\text{-}2R_\oplus$) and larger "sub-Neptunes" ($R > 1.5\text{-}2R_\oplus$).

This thesis has three main aims. The first is to understand the atmospheric circulation of temperate sub-Neptunes. The circulation impacts the global temperature structure, mixing of chemical species in the atmosphere, the location of clouds and the habitability of any surface present. The second is to understand how water vapour impacts the habitability of temperate sub-Neptunes, in the process calculating the inner edge of the habitable zone for sub-Neptunes with a water surface. The third is to develop a general circulation model (GCM) that can elucidate the impact of non-dilute water vapour on the atmospheric dynamics of sub-Neptunes. Before expanding on these aims, I will give an overview of the population of sub-Neptunes.

1.1 Super-Earths and Sub-Neptunes

The last decade has seen an explosion in the number of exoplanets discovered with radii between Earth's (1 $R_\oplus$) and Neptune's (3.8 $R_\oplus$). In 2013 an initial analysis of Kepler

objects of interest showed that around 85% of them were below 4 $R_\oplus$, compared to exoplanets discovered outside the Kepler mission, of which 85% were above 4 $R_\oplus$ (Batalha et al., 2013; Batalha, 2014). Subsequent analysis of false-positive rates showed 19.9% of sun-like stars to have at least one sub-Neptune (2 - 4 $R_\oplus$) and 20.3% to have at least one super-Earth (1.25 - 2 $R_\oplus$) with orbital periods of under 85 days (Fressin et al., 2013). This finding is concurrent with other studies which find the occurrence of super-Earth and sub-Neptunes to be between 30 - 50% of all main sequence stars (Mayor et al., 2011; Marcy et al., 2014b; Petigura et al., 2013; Winn and Fabrycky, 2015). Of the 4173 confirmed exoplanets with known radii as of November 2023[2], 32% fall in the "super-Earth" category (1 - 2 $R_\oplus$) and 39% in the "sub-Neptune" classification (2 - 4 $R_\oplus$). Although there is some discussion over the boundary between these two classes (usually defined somewhere between 1.5 - 2 $R_\oplus$), super-Earths are generally defined as rocky planets whose density increases with radius, whereas sub-Neptunes have densities decreasing with radius due to a larger volume of atmosphere (Marcy et al., 2014b; Marcy et al., 2014a; Weiss and Marcy, 2014; Wolfgang et al., 2016). The boundary is marked by the "radius valley" (Fulton et al., 2017), a sparsely populated region between 1.5 - 2.0 $R_\oplus$ (see Figure 1.2). The shape of the valley in radius-instellation space suggests the formation of the two populations is driven by atmospheric mass loss as opposed to the smaller planets forming in a gas-poor region of the proto-planetary disc. The two potential mechanisms driving atmospheric escape are either core-powered mass loss (Gupta and Schlichting, 2019) or photoevaporation (Owen and Wu, 2013). In the former process, the energy for escape is provided by the infrared luminosity generated by the planet's gravitational collapse. In the latter process, the energy for escape is provided by the high energy flux from the host star.

With the relative paucity of atmospheric measurements available for sub-Neptune sized planets, it is very difficult to accurately determine their composition. Many mod-

[2]Data from the Nasa Exoplanet Archive, `https://exoplanetarchive.ipac.caltech.edu`, accessed Thursday 2nd November, 2023

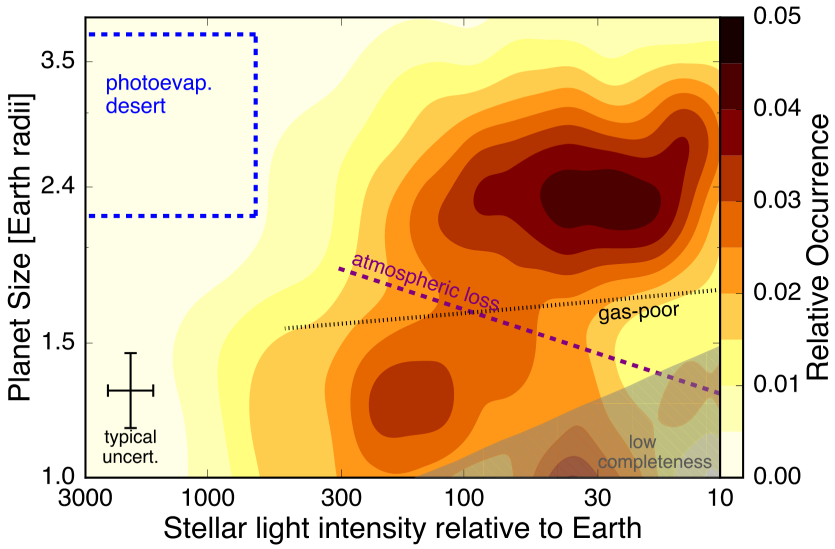

Figure 1.2: The radius valley viewed in radius-instellation space. The data show that the valley moves to higher planetary radii with higher incoming instellation, which suggests that super-Earth's are shaped by atmospheric escape and not by formation in a gas-poor disc. Figure from Fulton et al. (2017).

els explain the inflated radii of sub-Neptunes with the presence of a significant H/He envelope (e.g., Weiss and Marcy, 2014; Marcy et al., 2014b; Lopez et al., 2012; Lopez and Fortney, 2013), but different core models and formation scenarios have degeneracies which can lead to very different compositions fitting the same planetary mass and radius (Miguel and Kaltenegger, 2014; Rogers and Seager, 2010; Adams et al., 2008). These planets likely exhibit a wide range of atmospheric metallicities (Fortney et al., 2013), which makes the ability to obtain transmission spectra very important in breaking degeneracies. The wide range of metallicites possible means that water vapour can be present in non-dilute quantities in the atmosphere (i.e., with mass concentrations of $\gtrsim$ 10%). For temperate sub-Neptunes where non-dilute water vapour content can condense, it is important to understand how the strong compositional gradients and latent heat release induced by this condensation affect their circulation and habitability. In Chapter 6, I present efforts to develop a GCM that can accurately simulate sub-Neptunes with a non-dilute water vapour component.

1.2 Observations of Sub-Neptune Atmospheres

Observations that directly constrain the composition of sub-Neptune atmospheres have typically relied on transmission spectroscopy, a technique whereby one infers the radius of the planet at different wavelengths as it passes in front of its host star. The smaller size and lower equilibrium temperatures of sub-Neptunes makes them less amenable to thermal emission spectroscopy, which is widely used for Hot Jupiters. The majority of early attempts to characterise sub-Neptune atmospheres via transmission spectroscopy were frustrated due to the observed spectrum being "flat", i.e., with no molecular absorption features (e.g. Bean et al., 2011; Kreidberg et al., 2014; Knutson et al., 2014). For example, *Hubble* observations of GJ 1214 b (Harpsøe et al., 2012) showed no features between 1.1 and 1.7 μm. Featureless spectra are generally interpreted as evidence of either a high mean molecular weight atmosphere or the presence of high-altitude clouds obscuring the lower atmosphere.

However, recent observations of GJ 1214 b from the *James Webb Space Telescope* (JWST) showed evidence of strongly reflective hazes owing to the planet's high bond albedo and absorption features on the day and night sides, possibly due to water vapour (Kempton et al., 2023). The observations highlighted how the order of magnitude increase in resolution of *JWST* measurements will be revolutionary in understanding sub-Neptune atmospheric composition.

1.2.1 K2-18 b and Hycean Worlds

The planet K2-18 b (radius 2.71 $R_\oplus$; mass 8.63 ± 1.35 $M_\oplus$ Cloutier et al., 2019)) is a sub-Neptune sized planet discovered in the habitable zone of its M-type host star (Montet et al., 2015). Its Earth-like instellation (1440 ± 80 Wm^{-2}, 1.05 $S_\odot$) and equilibrium temperature (265 ± 5 K) (Benneke et al., 2019b) made it a promising target for atmospheric characterisation (Benneke et al., 2017). In Benneke et al. (2019b), there was a claimed

detection of water vapour in K2-18 b's transmission spectrum using the *Hubble Space Telescope*/WFC3 supplemented with *K2* and *Spitzer* data, which would have made it the first discovery of water in the atmosphere of a habitable zone exoplanet. The abundance of water vapour in its atmosphere was estimated to be between 0.033% and 8.9% in Benneke et al. (2019b) or between 0.02% and 14.80% in Madhusudhan et al. (2020) with the rest of the atmosphere primarily consisting of H_2 gas. Its instellation places it in the "optimistic" habitable zone of its host star since it exceeds the classical runaway greenhouse threshold (Kopparapu, 2013).

The tentative detection of water vapour in the atmosphere of K2-18 b led to intense research on its potential composition and interior structure. In Madhusudhan et al. (2020), three example interior compositions for K2-18 b were discussed, similar to Rogers and Seager (2010):

- A rocky world, with 95% of planetary mass in an iron-rich core and 5% in an outgassed H/He atmosphere. Water would be in the supercritical phase apart from potentially in the upper atmosphere.
- A sub-Neptune with roughly equal masses of rocky core and supercritical and ice phases of H_2O with a low mass H/He envelope.
- A 90-100% by mass water world with a minimal mass H_2 atmosphere.

Subsequent works have built on the latter possibility, suggesting that water-rich sub-Neptunes with surface oceans underlying hydrogen-dominated atmospheres are possible over a broad range of parameter space (Piette and Madhusudhan, 2020; Madhusudhan et al., 2021). These planets have been dubbed "Hycean worlds" (a portmanteau of "hydrogen" and "ocean"). Chemical equilibrium models point to how Hycean worlds may be distinguished from gas giant sub-Neptunes (Yu et al., 2021; Tsai et al., 2021). Ammonia (NH_3) is predicted to be produced thermochemically at high pressures on sub-Neptunes with deep atmospheres. If a shallow surface exists, any ammonia would

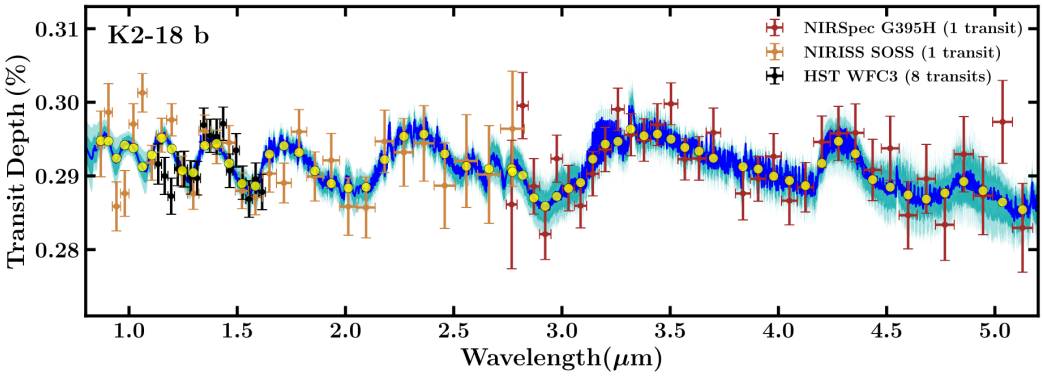

Figure 1.3: Transmission spectrum of K2-18 b obtained with the *NIRISS* and *NIRSpec* instruments of JWST. Orange and Red points represent the JWST data, which covers a much wider range than the *Hubble* data (black points). The plot also shows the median retrieved spectrum (blue line), the 1σ and 2σ contours (medium and light blue) and the median spectrum binned to JWST resolution (yellow dots). Figure taken from Madhusudhan et al. (2023).

be destroyed by photochemistry in the upper atmosphere and not replenished if the surface pressure is low enough. Therefore, the non-detection of ammonia could be indicative of a surface.

K2-18 b was recently observed in transmission with the *NIRISS* and *NIRSpec* instruments on JWST in the 0.9 μm to 5.2 μm range (Madhusudhan et al., 2023). Figure 1.3 shows its transmission spectrum. The peak at 1.4 μm, originally attributed to water vapour (Benneke et al., 2019b), was attributed instead to methane. They speculated that their models were consistent with a low cloud deck and low water vapour content in the upper atmosphere due to cold trapping. There was no detection of ammonia, which led to the claim that K2-18 b could be a Hycean world. Moreover, a tentative detection of the biosignature dimethyl sulphide was also provided as evidence that K2-18 b is habitable, since on Earth it is mainly produced via biogenic processes. In Chapter 5, I will calculate the inner edge of the habitable zone of Hycean worlds with a radiative-convective model, in order to assess the likelihood of observed sub-Neptunes hosting a liquid water ocean. I show that all the currently known sub-Neptunes in the traditional habitable zone, including K2-18 b, would be too hot to sustain liquid water oceans if they host a hydrogen atmosphere greater than 1 bar in pressure.

How common are planets like K2-18 b? Dressing and Charbonneau (2013) estimated from Kepler Objects of Interest, that the occurrence rate of 1.4-4 $R_\oplus$ planets in orbits receiving less than 1 $S_\oplus$ of instellation was around 3%. Given that 75% of the stars within 10 pc are M-dwarfs (Dressing and Charbonneau, 2013), they are far more abundant than planets around sun-like stars. In addition to the abundance of M-dwarf stars, planets around M-dwarfs are much easier to discover by the transit method (Dressing and Charbonneau, 2013). Given the observational advantages of looking for habitable-zone sub-Neptunes around M-dwarfs, obtaining their transit spectra is an explicit aim of JWST (Beichman et al., 2014).

1.3 Structure of Thesis

The discovery of sub-Neptunes in the traditional habitable zone of their host stars has motivated much of the work in this thesis. Despite them being more amenable to atmospheric characterisation than terrestrial-sized planets in the habitable zone, most modelling efforts before this thesis were focused on understanding the atmospheric circulation and habitability of Earth-like planets.

In Chapter 2, "The Atmospheric Dynamics of Exoplanets", I give an overview of previous work on the atmospheric circulation of exoplanets, focusing on how planetary waves shape their flow and how condensing water vapour affects the dynamics of hydrogen-dominated atmospheres.

Chapter 3, "The Dry Dynamics of Temperate Sub-Neptunes", describes the basic circulation structure of temperate sub-Neptunes. It demonstrates that tidally-locked, temperate sub-Neptunes should have very uniform horizontal temperature gradients over a large range of parameter space. The wind structure is dominated not by equatorial jets – as on other tidally-locked exoplanets – but by high-latitude, cyclostrophically balanced jets.

In Chapter 4, "An Introduction to the Runaway Greenhouse Effect", I introduce the runaway greenhouse effect as the mechanism that controls the inner edge of the habitable zone for temperate planets. I provide an overview of efforts to calculate the habitable zone for Earth-like planets, and discuss how the assumptions involved in these calculations may not apply for Hycean worlds.

Chapter 5, "The Runaway Greenhouse Effect on Hycean Worlds", builds on Chapter 4 by attempting to calculate the inner edge of the habitable zone for Hycean worlds, taking into account the effect of compositional gradients and the inhibition of convection on the thermal structure of the atmosphere. I show that the inner edge is much further from the host star than the edge calculated for terrestrial planets, suggesting that most current observational targets would be too hot to host liquid water oceans.

In Chapter 6, "Developing a GCM to Simulate Non-Dilute Water Vapour in Sub-Neptune Atmospheres", I present work towards building a GCM model that can simulate sub-Neptune atmospheres with a non-dilute water vapour component. I show that the presence of condensing non-dilute water causes strong compositional gradients in both the horizontal and vertical directions, which can respectively disrupt jet flows and inhibit convection. Preliminary results show that the strong gradient in radiative heating and cooling near the weather layer can cause a transition from flow dominated by high-latitude jets, to a thermally direct day-to-night flow. I also highlight future improvements to the GCM that could be made, such as the addition of the simplified cloud scheme (to allow for comparison with observations) or a surface ocean parameterisation (to allow for the simulation of Hycean worlds).

Lastly, in Chapter 7 I will summarise the work of my thesis and outline some of the outstanding questions to be tackled in the future.

Chapter 2

The Atmospheric Dynamics of Exoplanets

The aim of this chapter is to provide a review of the atmospheric dynamics of exoplanets and the impact of condensible species on planetary atmospheres.

Models of planetary atmospheres typically attempt to solve a set of non-linear partial differential equations describing the response of a fluid parcel to applied forces and heating. Forces are described with a simplified version of the Navier-Stokes equation (see Section 2.1), and the heating of the system with the first law of thermodynamics. This set of equations is usually intractable to analytic solutions. Two approaches, often complementary, are taken to facilitate our understanding of the system. Firstly, by making approximations valid in specific regimes, the equations of motion can be greatly simplified and solved analytically to provide physical insights to specific circulations. For example, the application of quasi-geostrophic theory in the description of Earth's midlatitude circulation (Charney, 1948) and the use of the shallow water equations to explain superrotation on tidally-locked exoplanets (Showman and Polvani, 2011) are two successful examples of this approach. The second is to use large-scale numerical

simulations, known as General Circulation Models (GCMs) to solve the full set of equations. These models have been applied extensively to explain Earth's weather and climate (Held, 2019), the atmospheres of solar system planets (e.g., Lebonnois et al., 2010; Young et al., 2019; Spiga et al., 2020; Lora et al., 2015) and of exoplanets (e.g., Showman et al., 2015; Pierrehumbert and Hammond, 2019).

As the number and diversity of discovered exoplanets has increased, so too has the demand for an understanding of their atmospheres, particularly since atmospheric dynamics will impact observable features of the atmosphere, such as the day-night contrast (Komacek and Showman, 2016) and the phase curve offset (Parmentier and Crossfield, 2018). Both analytic and numerical methods have been used extensively to probe exoplanet atmospheres, and in this chapter I will provide an overview of the main features their circulation.

This chapter is structured as follows. In the first part, I will give an overview of the dry dynamics of exoplanets. Firstly, in Section 2.1 I will discuss the equations of motion and how they are simplified for GCMs. In Sections 2.3 and 2.4 I will provide an overview of the dynamics of Hot Jupiter and terrestrial exoplanets. Section 2.5 will discuss equatorial superrotation and the planetary wave phenomena that drive it. In Section 2.6 I will explain how the circulation of tidally-locked exoplanets can be better understood by decomposing it into rotational and divergent components. I conclude this part of the chapter in Section 2.7 where I outline how sub-Neptunes fit into the parameter space of exoplanet atmospheres and how my work will provide a baseline understanding of their dynamics.

In the second part of this chapter, I will summarise the effect of condensation on the dynamics on Earth and other planets. I will review how latent heating (Section 2.8.1), clouds (Section 2.8.2) and moist convection (Section 2.8.3) shape circulation. In particular, I focus on non-dilute effects that will be important in the atmosphere of temperate sub-Neptunes: convective inhibition (Section 2.8.3) and horizontal compositional gra-

dients (Section 2.8.4).

2.1 The Primitive Equations

Models of planetary atmospheres (e.g., GCMs) typically attempt to solve the "primitive" equations. To arrive at these equations from the generalised Navier-Stokes equations for a fluid, the following assumptions are made:

1. *The shallow shell approximation.* Here the vertical scale of the system, h, is much smaller than the planetary radius a, such that terms involving planetary radius, r, in the Navier-Stokes equations are replaced with a and terms involving derivatives of r are replace by $\partial/\partial z$. This approximation also allows us to neglect variations in the gravitational acceleration, g, over the domain. In the radial direction (where we would expect deviations from constant g to be greatest), the difference in g between reference radius r_o, $g(r_o)$, and radius $r_o + h$, $g(r_o + h)$, is given by:

$$\frac{g(r_o + h) - g(r_o)}{g(r_o)} = \frac{1}{\left(1 + \frac{h}{r_o}\right)^2} - 1 \tag{2.1}$$

   from which it can be deduced that variations in g can be neglected so long as $h \ll r_o$.

2. *The traditional approximation.* Under this approximation, we neglect the Coriolis force terms in the horizontal momentum equation involving vertical velocity, and metric terms uw/r, vw/r.

These two approximations both rely on the small aspect ratio of motion. Many GCMs also invoke the hydrostatic approximation, such that the dominant momentum balance in the vertical direction is:

$$\frac{\mathrm{d}p}{\mathrm{d}z} = -\rho g, \tag{2.2}$$

where ρ is the density, p is the pressure and g is acceleration due to gravity. This approximation is valid in the limit of $H/L \ll 1$ i.e. vertical length scales H are much smaller than horizontal scales L, or more precisely when $\mathrm{Fr} \cdot z/a \ll 1$, where Fr is the Froude number:

$$\mathrm{Fr} \equiv \frac{U}{NH}, \tag{2.3}$$

where U is a typical horizontal velocity and N is the buoyancy frequency. With these approximations, the equations of motion in pressure coordinates are (Vallis, 2017):

$$\frac{\mathrm{D}\boldsymbol{u}}{\mathrm{D}t} + f\boldsymbol{k} \times \boldsymbol{u} + \nabla_p \Phi = -D_m, \tag{2.4a}$$

$$\frac{\partial \Phi}{\partial p} = -\frac{1}{\rho}, \tag{2.4b}$$

$$\frac{\partial \omega}{\partial p} + \nabla_p \cdot \boldsymbol{u} = 0, \tag{2.4c}$$

$$\frac{\mathrm{D}\theta}{\mathrm{D}t} = \frac{\theta}{c_p T}\dot{Q} - D_\theta, \tag{2.4d}$$

$$p = \rho R T, \tag{2.4e}$$

where $\mathrm{D}/\mathrm{D}t = \partial_t + \omega\partial_p + \boldsymbol{u} \cdot \nabla_p$, with ∇_p the horizontal gradient operator at constant p, ω the pressure velocity $\mathrm{d}p/\mathrm{d}t$, $\boldsymbol{u}$ the horizontal velocity, $\Phi = gz$ the geopotential, θ the potential temperature, $\dot{Q}$ heating sources, c_p the heat capacity at constant pressure, T the temperature and D_m and D_θ describe the dissipation in momentum and potential temperature respectively due to drag or viscosity. Equation (2.4a) is the momentum equation, describing the forces acting on a parcel of gas. Equation (2.4b) is the hydrostatic equation as described above. Equation (2.4c) is the continuity equation, Equation (2.4d) is the first law of thermodynamics and Equation (2.4e) is the ideal gas law which closes the set.

2.2 The Rossby number and Geostrophic Flow

Often it is useful to study the dominant balances in the momentum equation in different dynamical regimes. Defining the Rossby number $\mathrm{Ro} = U/fL$ as the ratio between advective and Coriolis terms in the momentum equation, we can define a regime of geostrophic balance where $\mathrm{Ro} \ll 1$ where:

$$fu = -\left(\frac{\partial \Phi}{\partial y}\right)_p, \quad fv = \left(\frac{\partial \Phi}{\partial x}\right)_p, \tag{2.5}$$

representing flow following contours of constant pressure. Associated with this balance is the thermal wind balance:

$$f\frac{\partial u}{\partial \ln p} = \frac{\partial (RT)}{\partial y}, \quad f\frac{\partial v}{\partial \ln p} = -\frac{\partial (RT)}{\partial x}. \tag{2.6}$$

This balance explains the strong eastward sub-tropical and polar jets on Earth, driven by the equator-to-pole temperature gradient. Perturbations away from geostrophic flow are adjusted over a lengthscale known as the Rossby radius, L_R (see Vallis, 2017). On a global scale, this is given by:

$$L_R = c_0/\Omega \approx \sqrt{RT}/\Omega, \tag{2.7}$$

which gives the length over which the fastest gravity wave, travelling at $c_0 = \sqrt{RT}$, can travel before being restored to geostrophic balance by the Coriolis force (Pierrehumbert and Hammond, 2019). If we compare this length to the radius of the planet, we form the global Weak Temperature Gradient (WTG) parameter $\Lambda = c_0/(\Omega a)$ (Pierrehumbert and Hammond, 2019). If $\Lambda \gg 1$, Coriolis forces are weak globally, and the response to a stationary heating source on the substellar point is to induce upwelling on the day side which overturns onto the night side of the planet. As discussed in Pierrehumbert and Ding (2016), for global weak temperature gradients, we also require the Rossby number $\mathrm{Ro} = U/fL$ to be small compared to Λ, such that to leading order $\nabla_p \Phi \approx 0$ in the momentum equation and fractional horizontal temperature gradients are small.

An *equatorial* Rossby deformation radius can also be defined as the length scale over which equatorial Kelvin waves (see Section 2.5.1) are confined by the beta effect. This is given by:

$$L_{eq} = \sqrt{\frac{c_0}{\beta}}, \tag{2.8}$$

where $\beta \equiv \partial f/\partial y$. If a planet is sufficiently slowly-rotating, the equatorial dynamics occur on a global scale (i.e., $L_{eq} \gg a$ Carone et al., 2015). Note that since $L_{eq}^2/L_R = a$, the two radii are equal when $L_R = L_{eq} = a$, so the WTG regime defined above and the regime where $L_{eq} > a$ are equivalent. Haqq-Misra et al. (2018) classified the circulation regimes of terrestrial exoplanets in three classes. Firstly, the "slow rotator" regime is defined as $L_{eq} > a$, similar to the WTG regime above. The other two classes, "Rhines rotators" and rapid rotators, are dependent on the Rhines scale (Rhines, 1975). This is the length scale over which turbulent motions are organised into jet structures by the β-effect. It is given by:

$$L_{Rh} = \pi\sqrt{\frac{2U_e}{\beta}}, \tag{2.9}$$

where U_e is the characteristic eddy velocity. Haqq-Misra et al. (2018) define the Rhines rotating regime as being where the Rhines lengthscale is less than the planetary radius $L_{Rh} < a$ with the equatorial Rossby radius being greater than the planetary radius $L_{eq} > a$. This regime is characterised by the formation of mid-latitude turbulence driven zonal jets. The rapid rotator regime, defined as $L_{eq} < a$ and $L_{Rh} < a$, is demarcated by a mean zonal circulation which partially spans a hemisphere, and banded cloud formations. These regimes have also been found in other GCM studies of terrestrial planets (e.g. Merlis and Schneider, 2010; Noda et al., 2017; Yang et al., 2014; Kopparapu et al., 2017; Leconte et al., 2013).

It should be noted that L_{Rh} and L_{eq} are not independent. In fact:

$$\frac{L_{Rh}}{L_{eq}} = \sqrt{\frac{U_e}{c_0}} \tag{2.10}$$

In Haqq-Misra et al. (2018), U_e was estimated as the root mean square surface wind speed, which was found to be less than the gravity wave speed, c_o, in all simulations. As such, $L_{Rh} < L_{eq}$ and no regimes were found where both $L_{eq} < a$ and $L_{Rh} > a$. However it was noted that such a regime could conceivably occur on very hot planets (e.g., hot Jupiters) with supersonic wind speeds.

2.3 Hot Jupiter Atmospheres

The atmospheres of hot Jupiters have been extensively studied using GCMs (e.g. Showman and Guillot, 2002; Heng et al., 2011a,b; Showman et al., 2015; Komacek and Showman, 2016; Rauscher and Menou, 2010; Mayne et al., 2017). Although they are much larger and hotter than the sub-Neptunes in the habitable zone, some of the physics and scaling theories developed for their deep atmospheres are more applicable to sub-Neptunes than terrestrial planet theory given the impact the surface has on the dynamics of the latter class.

Most Hot Jupiters are likely to be tidally-locked to their host star due to their short, close-in orbits (Guillot et al., 1996). As such, their dynamics are driven by a strong day-night heating contrast and high equilibrium temperatures of up to 3000 K. GCMs generally agree on the three main qualitative features of their circulation (Showman et al., 2020). Firstly, the strong forcing results in high day-night temperature differences on the order of hundreds of Kelvin. Secondly, the stationary forcing induces a global-scale eddy structures. Thirdly, wide, eastwards equatorial jets with wind speeds on the order of 1 km s^{-1} are ubiquitous across models. Wave dynamics and strong jets can shift the wave patterns eastwards, producing a hot spot offset where the highest temperatures on the planet are not at the substellar point. Figure 2.1 shows how different GCM simulations for different Hot Jupiters all reproduce these features of the circulation, and match phase curve observations from Knutson et al. (2007), which shows a hot spot

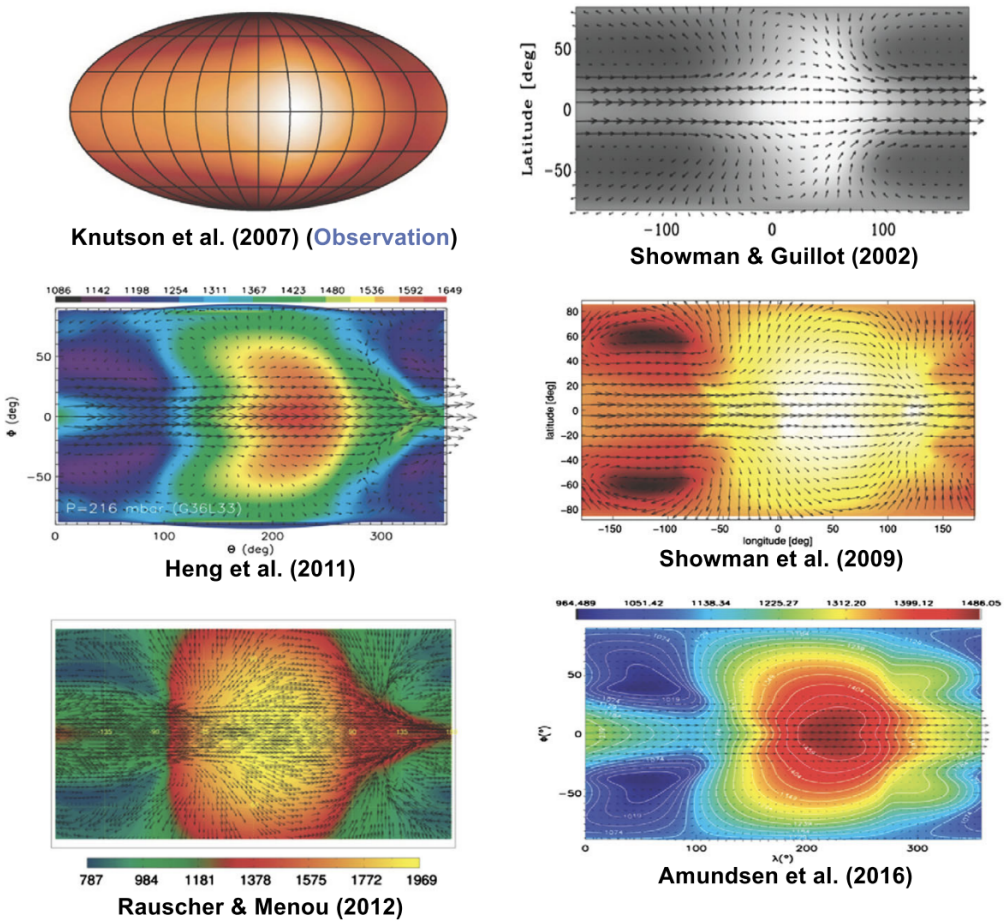

Figure 2.1: GCM simulations of a range of Hot Jupiter atmospheres. The top-left panel shows observations from HD 189733b (Knutson et al., 2007), and the GCM simulations of Showman et al. (2009) model this planet. Heng et al. (2011b), Amundsen et al. (2016), and Showman and Guillot (2002) and Rauscher and Menou (2012) simulations all study HD 209458b. Despite the different model setups, similar circulation regimes are seen in all panels. Figure adapted from Showman et al. (2020).

offset eastwards.

The dynamics of Hot Jupiters can be summarised by the scaling theories of Komacek and Showman (2016) and Zhang and Showman (2017). Following Zhang and Showman (2017), the governing dimensionless parameters are:

- $\Omega\tau_w$ – the product of the planet's rotation rate and wave timescale, where $\tau_w \approx a/\sqrt{gH}$ is the approximate timescale for the fastest gravity wave to travel a planetary radius.

- τ_w/τ_d – the ratio between the wave timescale and the drag timescale (assuming drag is roughly Newtonian i.e. takes the form $\boldsymbol{u}/\tau_d$ in the momentum equation),
- τ_w/τ_r – the ratio between the wave timescale and the radiative timescale. The radiative timescale is approximately:

$$\tau_r = \frac{pc_p}{4g\sigma T^3}, \tag{2.11}$$

  and defines how quickly a layer of atmosphere will relax to radiative equilibrium.
- τ_w/τ_{ad} – the ratio between the wave timescale and the advective timescale $\tau_{ad} \equiv L/U$.

The magnitude of the day-night temperature contrast relative to the magnitude of forcing, $\Delta T/\Delta T_{eq}$, can be written:

$$\frac{\Delta T}{\Delta T_{eq}} \sim 1 - \frac{2}{\alpha + \sqrt{\alpha^2 + 4\gamma^2}}, \tag{2.12a}$$

$$\alpha \equiv 1 + \frac{\left(\Omega + \frac{1}{\tau_d}\right)\tau_w^2}{\tau_r \Delta \ln p}, \tag{2.12b}$$

$$\gamma \equiv \frac{\tau_w^2}{\tau_r \tau_{ad}}, \tag{2.12c}$$

where $\Delta \ln p$ is the thickness of the dynamically active region of the atmosphere in logarithmic pressure space. This metric affects the magnitude of observed thermal phase curves (Koll and Abbot, 2015; Komacek and Showman, 2016; Zhang and Showman, 2017; Hammond and Pierrehumbert, 2017). In general, if the radiative timescale is the shortest timescale, the temperature structure can quickly relax to the radiative equilibrium value, which leads to high day-night temperature contrasts. Similarly a short drag timescale reduces the efficiency of heat transport and results in high ΔT. On the other hand, a short wave timescale reduces the day-night contrast by efficiently smoothing out strong pressure (and therefore temperature) gradients.

There are three broad regimes: drag dominated ($\tau_d\Omega \ll 1$); Coriolis dominated ($\tau_d\Omega \gg 1$) and advection dominated ($\tau_{ad} \ll \Omega^{-1}$, $\tau_{ad} \ll \tau_d$). In the Coriolis force

dominated regime, the above expression simplifies to:

$$\frac{\Delta T}{\Delta T_{eq}} \sim 1 - 1/\left(1 + \frac{\Omega \tau_w^2}{\tau_r \Delta \ln p}\right) \sim 1 - 1/\left(1 + \Lambda^{-1} \frac{\tau_w}{\tau_r \Delta \ln p}\right). \tag{2.13}$$

One can then consider the temperature dependence of the two timescales τ_r and τ_w. From Showman and Guillot (2002), the radiative timescale scales as T^{-3}. The wave timescale, on the other hand, scales roughly with the square root of the atmospheric scale height, $\sim T^{1/2}$. On a hot Jupiter with typical temperatures of the order of 1000 K, the ratio τ_r/τ_w can be very low, with high day-night temperature contrasts (Showman et al., 2015). In this canonical regime, the equatorial standing waves induced by the stationary forcing can pump momentum towards the equator and sustain the jet (see Section 2.5). An equatorial jet is a robust feature of many hot Jupiter models (e.g. Showman et al., 2015; Dobbs-Dixon and Agol, 2013, amongst many others).

For quickly rotating hot Jupiters, the day-night contrast decreases (by Equation 2.13), the dynamics is driven by rotation and by the heating contrast between equator and pole. In this case, baroclinic instabilities in the mid-latitudes drive jets. The canonical and fast-rotating cases are summarised in Figure 2.2.

2.4 Terrestrial Exoplanets

Other than hot Jupiters, terrestrial exoplanets (small, rocky planets with radius $< 2R_\oplus$) are the most widely-studied by GCM simulations (e.g. Yang et al., 2014; Kopparapu et al., 2017; Way et al., 2018; Kaspi and Showman, 2015; Sergeev et al., 2020; Haqq-Misra et al., 2018; Komacek et al., 2019; Hammond and Pierrehumbert, 2017). The dynamics of these planets is distinct from Hot Jupiters for several reasons. Firstly, terrestrial planets are typically modelled with surface pressures of ≈ 1 bar, much less than the typical ≈ 100 bar bottom boundary of Hot Jupiter simulations. Secondly, the stellar heating on terrestrial exoplanets is predominantly absorbed at the surface and re-radiated upwards in the infrared part of the spectrum. This heating from below generates convective in-

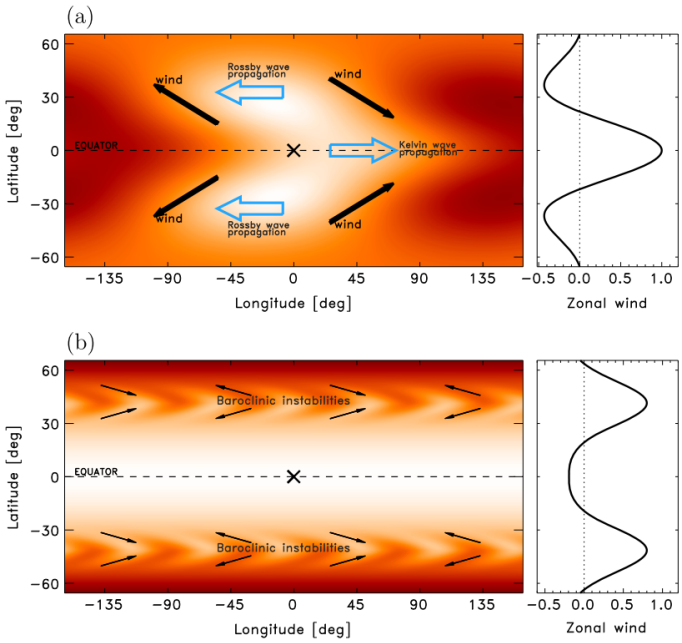

Figure 2.2: Two of the dynamical regimes for tidally-locked hot Jupiters. (a) Strong day-night heating and slower rotation rates cause a Matsuno-Gill pattern which drives an equatorial superrotating jet. (b) For weaker radiative forcing and faster rotation, baroclinic instabilities in the mid-latitudes drive zonal jets with peak winds off-equator. Adapted from Showman et al. (2015)

stability, in contrast to irradiated gas giants which are directly heated by the absorption of stellar radiation. Thirdly, the presence of a surface on terrestrial planets acts as a source of friction to the atmosphere. The dynamics of the resulting turbulent boundary layer is often parametrised in simulations (owing to the small, unresolved lengthscales of motion relative to the model resolution) and can impact the heat and momentum fluxes near the surface. In addition, the frictional boundary layer can (depending on the surface wind direction) act like a source or sink of angular momentum, which can be important for the generation of superrotation (Gierasch, 1975; Rossow and Williams, 1979)

The dynamics of terrestrial exoplanets can be broadly split into two categories based on whether the planet is assumed to be synchronously rotating (more likely for planets on close-in orbits around low mass stars Leconte et al., 2015) or asynchronously rotating, like the Earth.

2.4.1 Asynchronously Rotating Planets

On temperate, asynchronously rotating planets, it is helpful to view the circulation as an extension of Earth-like dynamics to different rotation rates and forcings, especially if the flow is predominantly zonal and diverging from day to night. An important feature of the zonal circulation on Earth and other small, rocky planets in the solar system (e.g., Mars, Venus and Titan) is the Hadley Cell. This zonally-symmetric, large-scale circulation involves air at the equator rising and moving polewards. Conserving angular momentum, an air parcel at latitude φ on a planet of radius a and rotation rate Ω must have zonal wind:

$$u = a\Omega \frac{\sin^2 \varphi}{\cos \varphi}. \tag{2.14}$$

In the model of Held and Hou (1980), the meridional potential temperature is relaxed to a prescribed profile and the equilibrium width of the Hadley cell is estimated to scale with Ω^{-1}. In simulations of non-tidally locked terrestrial GCMs, this dependence on rotation rate is broadly borne out (Kaspi and Showman, 2015; Komacek and Abbot, 2019). The Hadley cell also acts to smooth out meridional temperature gradients within its extent. When rotation rate is increased and the meridional temperature gradients are more pronounced, the sloping of isentropes relative to pressure surfaces leads to baroclinic instabilities and eddy driven zonal jets form with lengthscales comparable to the Rhines scale (Kaspi and Showman, 2015). Figure 2.3 shows the effect of increasing rotation on the Hadley cell width and the emergence of eddy-driven jets, where the breaking of Rossby waves converges zonal momentum towards the source of the disturbance. On the other hand, when planetary rotation rate is decreased significantly from Earth's value, each branch of the Hadley circulation grows to fill its hemisphere. Wave activity generation by baroclinic instabilities decreases, and superrotating jets at the equator are driven by planetary-scale equatorial waves (Mitchell and Vallis, 2010; Laraia and Schneider, 2015). The solar system bodies Venus and Titan fall into this

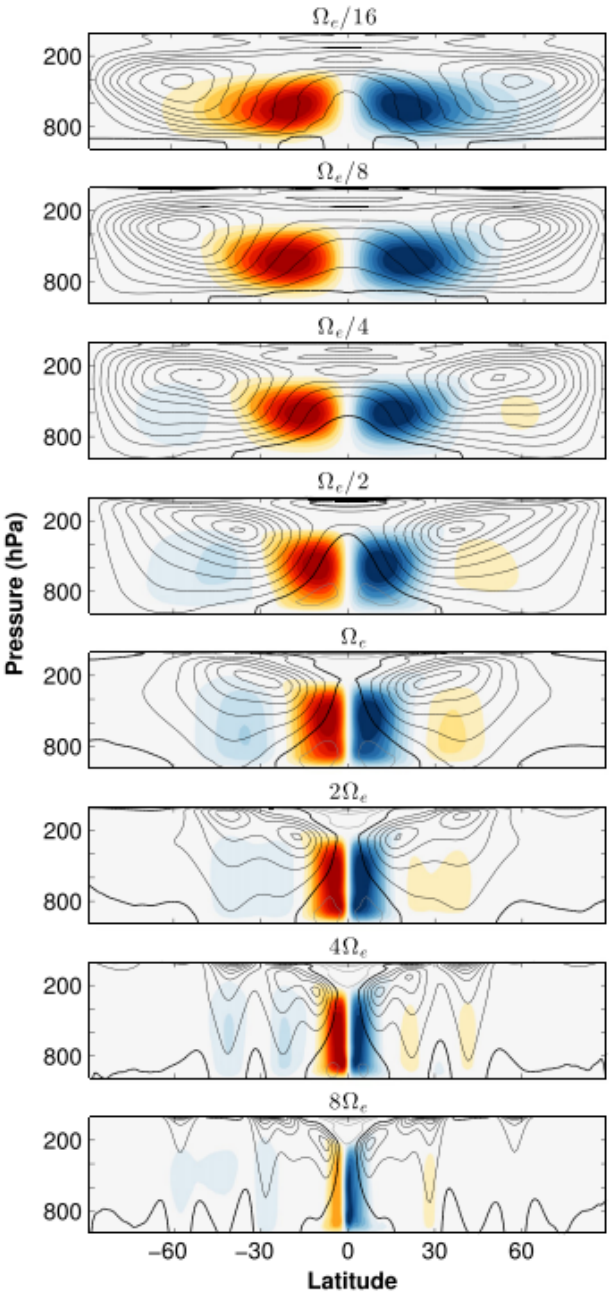

Figure 2.3: The effect of increasing rotation on the flow of terrestrial, non-synchronously rotating exoplanets. The contours represent the zonal wind, whilst the coloured regions represent the mean meridional mass streamfunction. As rotation rate is increased (moving down the panels), the circulation changes from a Hadley cell filling each hemisphere (top panel), to multiple eddy-driven jets. Adapted from Kaspi and Showman (2015)

.

regime.

2.4.2 Synchronously Rotating Planets

For tidally locked exoplanets, the classification of planets as slow rotators, Rhines rotators or fast rotators (as presented in section 2.2) applies. For slow rotation rates, where the Rossby deformation radius is greater than the planetary radius, a thermally direct day-to-night circulation is observed in GCM models (e.g., Edson et al., 2011a; Koll and Abbot, 2016; Noda et al., 2017). As the rotation rate is increased, simulated atmospheres transition towards having a superrotating jet at the equator (Koll and Abbot, 2016), driven by the stationary radiative forcing. For planets where the Rossby deformation radius exceeds the planetary radius but the Rhines length is less than planetary radius, turbulent eddies can produce turbulence driven-jets in the mid-latitudes that break symmetry of the direct overturning circulation found on slow rotators (Haqq-Misra et al., 2018).

The effect of dynamical timescales on the day-night temperature contrasts is different on terrestrial planets compared to Hot Jupiters due to the presence of a surface. Koll and Abbot (2016) models atmospheres of terrestrial planets as a heat engine, with a convective dayside exchanging heat with a subsiding nightside. Work is done by the winds against surface friction. Strong day-night temperature contrasts can be sustained at much lower ratios of τ_w/τ_r than those found for hot Jupiters, largely because warming by subsidence on the nightside has a longer timescale and can exceed the radiative timescale at much lower values of τ_w.

2.5 Planetary Waves and Equatorial Superrotation

A common feature of the dynamics of Hot Jupiter and terrestrial exoplanets is the presence of an eastwards jet on the equator. These jets are "superrotating", i.e. they have more angular momentum than the rotation of the body below. A region of the atmo-

sphere that is locally superrotating can be mathematically defined where:

$$s = \frac{m}{\Omega a^2} - 1 > 0, \tag{2.15}$$

where $m = a\cos\phi(\Omega a\cos\phi + u)$ is the specific angular momentum of the atmosphere (Read, 1986). Rewriting the momentum equation, (2.4a) and taking the zonal average, one finds (Vallis, 2017):

$$\frac{\mathrm{D}\overline{m}}{\mathrm{D}t} = -\frac{1}{a\cos\phi}\frac{\partial}{\partial\phi}\left(\overline{m'v'}\cos\phi\right) - \frac{\partial\overline{m'\omega'}}{\partial p} + X, \tag{2.16}$$

where barred quantities represent zonal averages, dashed quantities zonal eddies (i.e., $A' \equiv A - \overline{A}$) and X viscous forces. In the limit of an inviscid, axially symmetric atmosphere, this reduces to:

$$\frac{\mathrm{D}m}{\mathrm{D}t} = 0, \tag{2.17}$$

and there can be no up-gradient transport of angular momentum (Hide, 1969). In the Held-Hou model where the angular momentum of air parcels in the upper atmosphere is homogenised to stationary equatorial surface parcels with $m = \Omega a^2$, this implies that $s \leq 0$ (i.e. subrotation). It is clear from the right-hand side of Equation 2.16 that up-gradient transfer of angular momentum in inviscid atmospheres ($X = 0$) can only occur if there are non-axisymmetric eddies. In this section I will explain how planetary-scale waves can provide the momentum flux necessary to induce equatorial superrotation.

2.5.1 Equatorial Waves

Slowly-rotating exoplanets (where $\Lambda \gg 1$) can be thought of as exhibiting tropical dynamics globally (Showman et al., 2013) owing to the relative weakness of Coriolis force, which leads to the equatorial Rossby deformation radius approaching or exceeding the planetary radius.

To understand the range of equatorial waves permitted by the equations of motion, we can study shallow water equations. The shallow water equations provide a starting

point to studying the basic effects of rotation on fluid flow. The equations appear in many different geophysical contexts – perhaps the easiest way to visualise them is describing a single layer of fluid of constant density with height h and horizontal velocity $\boldsymbol{u}$. However, the same equations can also be derived for an ideal gas atmosphere, where the height variable corresponds to the mass of atmosphere between two isentropic surfaces (Gill, 1980). As noted by Matsuno (1966), using shallow water equations isn't limited to a single layer, or even discretised multiple layers of fluid but can be generalised to the vertical modes of a stratified atmosphere (see Vallis, 2017).

Kelvin and Rossby waves

The linearised shallow water equations on the β-plane, where $f = \beta y = 2\Omega \cos \phi y/a$ and Ω the rotation rate of the planet, are given by:

$$\frac{\partial \phi}{\partial t} + \left(\frac{\partial u}{\partial x} + \frac{\partial v}{\partial y} \right) = 0, \tag{2.18a}$$

$$\frac{\partial u}{\partial t} - \beta y v + \frac{\partial \phi}{\partial x} = 0, \tag{2.18b}$$

$$\frac{\partial v}{\partial t} + \beta y v + \frac{\partial \phi}{\partial y} = 0, \tag{2.18c}$$

where u, v and ϕ are the non-dimensional zonal wind, meridional wind and geopotential fields respectively. The scalings for time and length $[T] = 1/\sqrt{c\beta}$ and $[L] = \sqrt{c/\beta}$ have been used to non-dimensionalise the fields. We can search for solutions of the form $Y(y) \exp(ikx - i\omega t)$ where k is a zonal wavenumber and ω an angular frequency. As shown by Matsuno (1966), we can manipulate the equations into an eigenvalue problem similar to the quantum harmonic oscillator, with dispersion relation:

$$\omega^2 - k^2 - \frac{k}{\omega} = 2n + 1 \quad (n = 0, 1, 2, \dots), \tag{2.19}$$

and eigenfunctions:

$$\begin{pmatrix} v \\ u \\ \phi \end{pmatrix} = \begin{pmatrix} i(-\omega_{nl}^2 - k_x^2)\psi_n \\ \frac{1}{2}(-\omega_{nl} - k_x)\psi_{n+1} + n(-\omega_{nl} + k_x)\psi_{n-1} \\ \frac{1}{2}(-\omega_{nl} - k_x)\psi_{n+1} - n(-\omega_{nl} + k_x)\psi_{n-1} \end{pmatrix}, \tag{2.20}$$

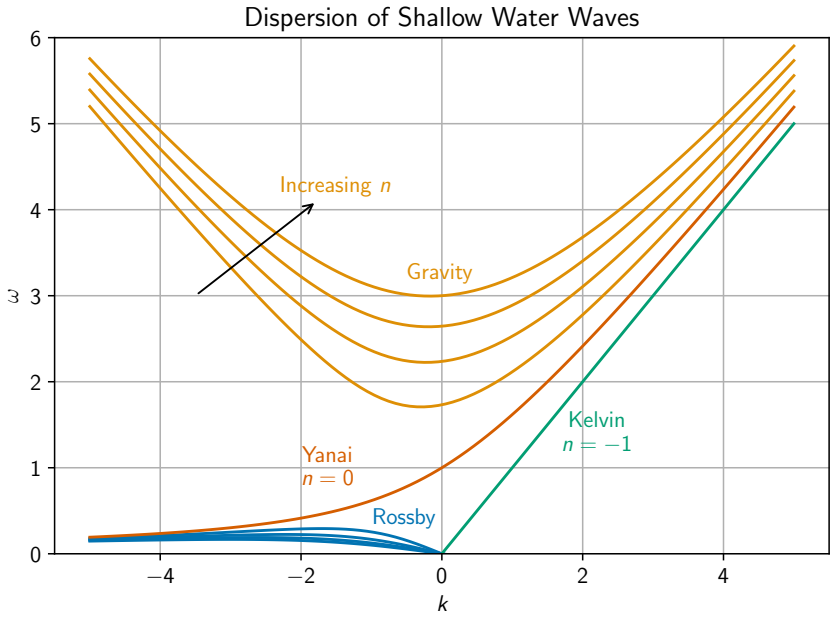

Figure 2.4: The dispersion of four types of waves found from solving the linear shallow water equations on the equatorial beta plane.

where $\psi_n = e^{-\frac{1}{2}y^2} H_n(y)$ with $H_n(y)$ being the n^{th} Hermite polynomial (see Vallis, 2017) and l denoting the different roots of Equation 2.19. The three roots of Equation 2.19 correspond to different types of planetary waves. Some special cases of n require more thought. For $n = 0$, Equation 2.19 permits a westwards travelling gravity wave, which is unphysical if we wish solutions to vanish as $|y| \to \infty$. The remaining curve for $\omega > 0$ is known as a "Yanai" wave, which looks like a gravity wave for $k > 0$ but a Rossby wave for $k < 0$. In addition, Equation 2.19 assumes that there is a non-zero meridional velocity. However, the equations permit a solution with vanishing meridional winds ($v = 0$), which corresponds to a solutions with $\omega = k$ and $(\phi, u) \propto \exp(-y^2/2)$. These are Kelvin waves, in geostrophic balance and confined by the change in sign of the Coriolis force between hemispheres. Figure 2.4 illustrates the dispersion of these modes. Figure 2.5 shows the geopotential perturbation profile for the $n = 0$ and $n = 1$ modes. From 2.20 we can see that the ϕ and u profiles will be even across $y = 0$ for odd n, odd across $y = 0$ for even n and vice-versa for the v field (see Figure 2.5).

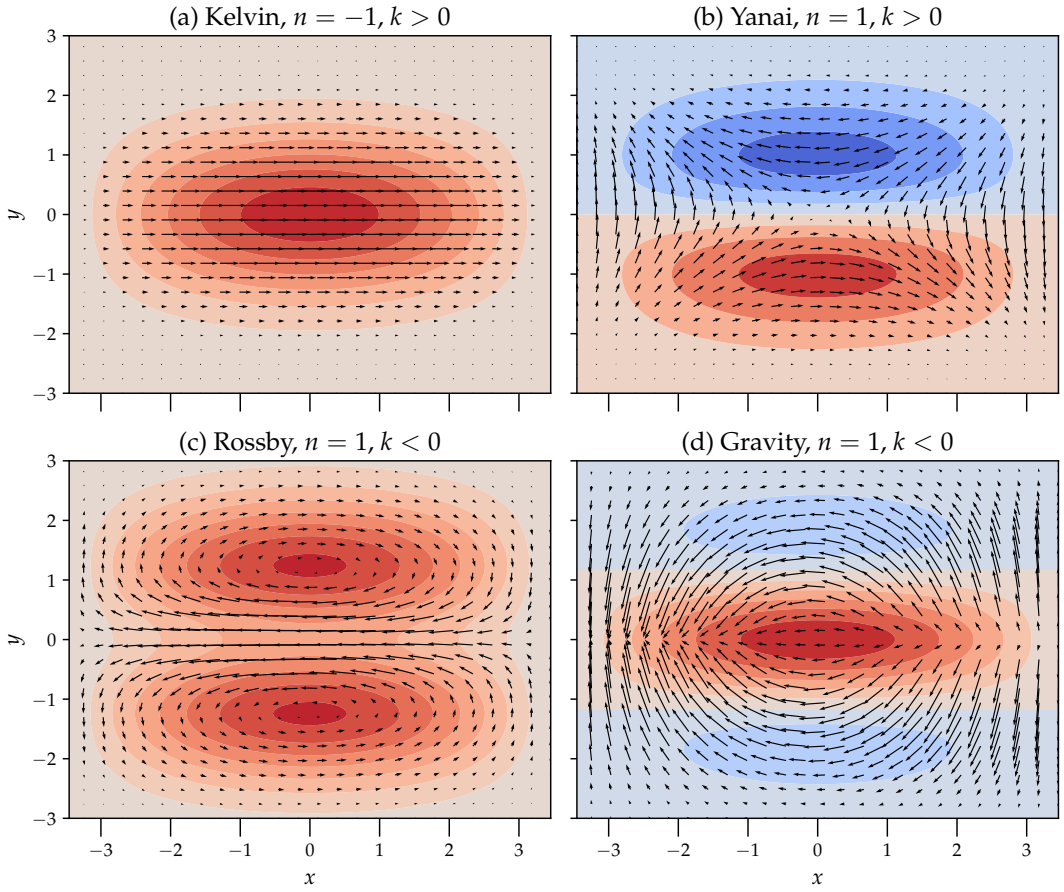

Figure 2.5: Geopotential fields for the $n = 0$ and $n = 1$ modes of the shallow water equations on a β-plane. Arrows indicate the wind direction. Red and blue regions represent positive and negative geopotential perturbations respectively. The values of k chosen were ± 0.5, and half a wavelength in the x direction is shown.

Forced stationary waves

On a tidally-locked exoplanet, the forcing of the shallow water equations can be represented as a stationary mass source in the upper layer of the model. As shown by Matsuno (1966) and Gill (1980), we can use the eigenfunctions of the free solution as an orthogonal basis to solve for the forced problem. If we impose equal Newtonian damping on all three variables, i.e. $\partial_t \to \partial_t + \alpha$, and impose a forcing $Q = Q_0 e^{-y^2/2} e^{ikx}$ where Q_0 is a constant and k a zonal wavenumber, we can find an analytical solution in terms of the Kelvin mode and the $n = 1$ Rossby and gravity wave modes (see Figure 2.6). The response is dominated by the lower frequency Kelvin and Rossby modes because they

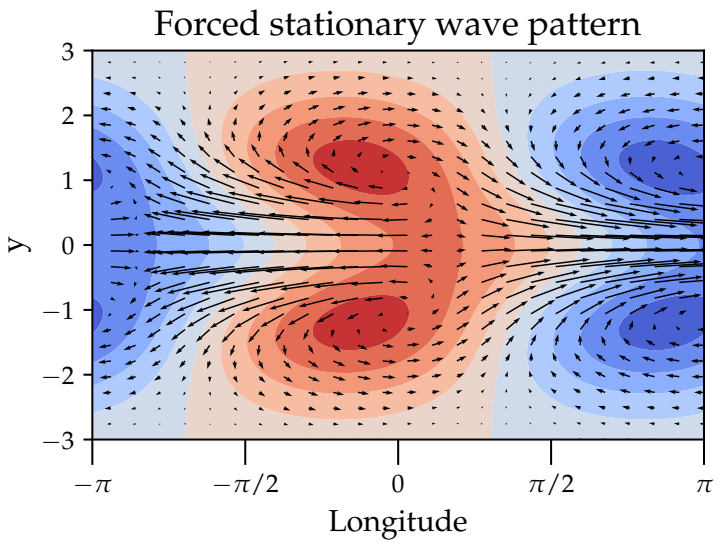

Figure 2.6: The stationary wave pattern formed as a result of a forcing proportional to $e^{-y^2/2}\cos(kx)$ with damping coefficient $\alpha = 0.2$ and $k = 0.5$. Red and blue regions are regions of positive and negative geopotential perturbation respectively. The arrows indicate the direction of flow.

are closer to being in resonance with the 0-frequency forcing function. The positive-perturbation Rossby modes are phase-shifted westwards whilst the Kelvin wave pattern is phase-shifted eastwards. The condition of equal radiative and frictional drag can also be relaxed and still yield analytical results (albeit with more algebraic complexity, see Showman and Polvani (2011)).

The chevron pattern in Figure 2.6 is similar to the temperature structure seen in GCM simulations of Hot Jupiters and terrestrial exoplanets. The stationary eddy forcing of the mean flow at the equator has a term proportional to:

$$-\frac{\partial \overline{u'v'}}{\partial y}, \tag{2.21}$$

and the chevron pattern in Figure 2.6 has $\overline{u'v'} < 0$ in the northern hemisphere and $\overline{u'v'} > 0$ in the southern hemisphere, driving momentum towards the equator. In the models of Showman and Polvani (2011) a forcing term that represents mass with $u = 0$ being transferred to the active upper layer of the model when $Q > 0$ is also added to the model. Since $u < 0$ in the regions of upwelling in Figure 2.6, this acts to increase the

momentum at the equator and reinforce the positive acceleration there.

Expanding on this work, Tsai et al. (2014) and Hammond and Pierrehumbert (2018) looked at the effect of adding a uniform and sheared zonal flow respectively on the wave structure. Both agree that the shift of a planet's hot spot eastwards of the substellar point is due to Doppler shift of the Rossby and Kelvin waves by the mean flow. Moreover, the presence of a mean zonal flow decreases the zonal eastwards acceleration at the equator present in the model of Showman and Polvani (2010). As the zonal flow shifts the phase of the waves towards $\pi/2$, the waves become more in phase, reducing the acceleration caused by zonal momentum convergence and providing a mechanism for the equatorial jet to equilibriate.

2.5.2 Other routes to superrotation

Superrotation is also present in the atmospheres of the slowly-rotating planets and moons of our solar-system. Venus has westward winds at the equator (superrotating with respect to its retrograde rotation) on the order of 100 m s^{-1} (Widemann et al., 2008), and measurements of Titan's winds using ground-based spectroscopy and the *Cassini* mission show a peak equatorial jet speed of 200 m s^{-1} (Kostiuk et al., 2001; Achterberg et al., 2008). The atmospheres of Venus and Titan are not forced with the strong stationary radiative forcing of tidally-locked exoplanets and are slowly rotating. As such, the mechanism for generating superrotation is not the stationary wave eddy-forcing of the equatorially-trapped Matsuno-Gill pattern.

On Venus, two main mechanisms are proposed for the generation of superrotation. The first is the role of diurnal and semi-diurnal thermal tides, which act to transport momentum vertically into the cloud layer which is strongly heated by shortwave absorption (Newman and Leovy, 1992; Takagi and Matsuda, 2007). The second is the transport of momentum by horizontal transient eddies. The global-scale Hadley circulation accelerates high-latitude jets, which can become unstable to shearing instabilities

(Iga and Matsuda, 2005; Wang and Mitchell, 2014). The resulting instability can produce the necessary equatorwards flux in zonal momentum to accelerate superrotating jets in idealised models of Venus's atmosphere (Mitchell and Vallis, 2010). In the mechanism described in Wang and Mitchell (2014), the slow rotation rate of the planet and associated suppression of mid-latitude baroclinicity (Zurita-Gotor et al., 2022) allows for an equatorial Kelvin wave to overlap with Rossby waves at mid-latitudes. The meridional shear in zonal winds allows Rossby waves travelling westwards relative to the mean flow to phase lock with eastwards travelling Kelvin waves. In contrast to thermal tides which are widely accepted to produce equatorial superrotation on Venus (Lebonnois et al., 2010; Mendonça and Read, 2016; Horinouchi et al., 2020), the role horizontal shear instabilities is less clear, with Horinouchi et al. (2020) finding that they acted to decelerate zonal flow at the equator. Recent models of Titan's atmosphere suggest a complex mixture Rossby, Kelvin and gravity waves all have a role in accelerating equatorial jets (Lewis et al., 2023).

In Chapter 3 I will show that the presence of a Rossby-Kelvin-like instability similar to the one found in (Wang and Mitchell, 2014) can drive superrotation in the atmosphere of sub-Neptune exoplanets.

2.6 The Helmholtz Decomposition of Tidally-Locked Circulation

Understanding the circulation of tidally-locked exoplanets using metrics derived from studies of Earth's circulation can often obscure the underlying dynamics. For example, a widely used diagnostic is the meridional mass streamfunction, Ψ, defined as:

$$\Psi = \frac{2\pi a \cos\phi}{g} \int_0^p \overline{v}\, \mathrm{d}p\,, \tag{2.22}$$

where $\overline{v}$ is the zonally-averaged meridional wind field. For planets with approximately zonally symmetric circulations (e.g., Earth, Venus), Ψ gives a good picture of the overturning circulations such as the Hadley cell. However, on tidally-locked exoplanets, we expect the predominant thermally-direct circulation to be directed from day to night, which interferes with the zonal symmetry that makes Ψ attractive. Often the circulation is described as a Hadley cell on the dayside, but an anti-Hadley cell on the nightside (Heng et al., 2011b; Charnay et al., 2015a; Haqq-Misra et al., 2018).

Hammond and Lewis (2021) offered a simplification of this view. Wind fields $(\boldsymbol{u}, \boldsymbol{v})$ of GCM simulations of tidally-locked exoplanets were decomposed using the Helmholtz decomposition into the sum of a divergence-free (u_r, v_r) and curl-free components (u_d, v_d). The divergent component was found to capture the thermally-direct day-night circulation, whereas the rotational component contains the equatorial jet and wave-like structures (see Figure 2.7). Given the symmetry of the overturning circulation, it is clearer to define a streamfunction in the tidally-locked coordinate system (Koll and Abbot, 2015). In tidally-locked coordinates, the line of zero degrees latitude is the terminator, and the latitude coordinate runs from 90° at the substellar point to −90° at the antistellar point. In this coordinate system, the meridional velocity v_{TL} is directed the from nightside to the dayside. The tidally-locked streamfunction is then defined as:

$$\Psi_{TL} = \frac{2\pi a \cos\phi}{g} \int_0^p v_{d,TL} \, \mathrm{d}p \,, \tag{2.23}$$

where $v_{d,TL}$ is the divergent component of the meridional velocity in tidally-locked coordinates. Figure 2.8 shows Ψ and Ψ_{TL} calculated from GCM simulations of a tidally-locked terrestrial planet. The maximum value of Ψ_{TL} is an order of magnitude larger than the value of Ψ, showing that the predominant overturning circulation is the day-night circulation. The presence of a strong day-night divergent circulation is necessitated by the vertically-averaged equation for the transport of dry static energy:

$$\langle s \nabla \cdot \boldsymbol{u_{TL}} + \boldsymbol{u_{TL}} \cdot \nabla s \rangle = R, \tag{2.24}$$

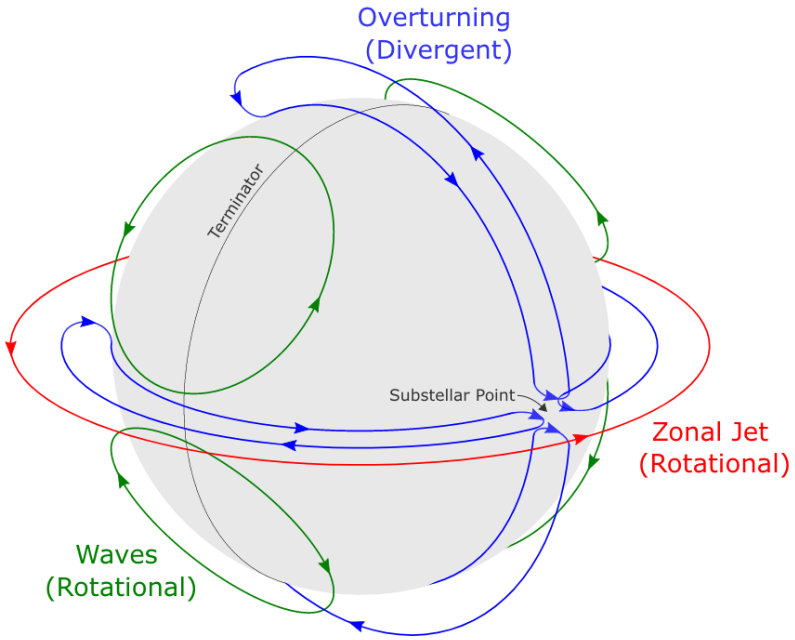

Figure 2.7: The rotational and divergent components of the circulation of a tidally-locked exoplanet. The overturning circulation (blue) is described by the divergent component, whereas the eddy and jet structures (green and red respectively) are captured in the rotational component. From (Hammond and Lewis, 2021).

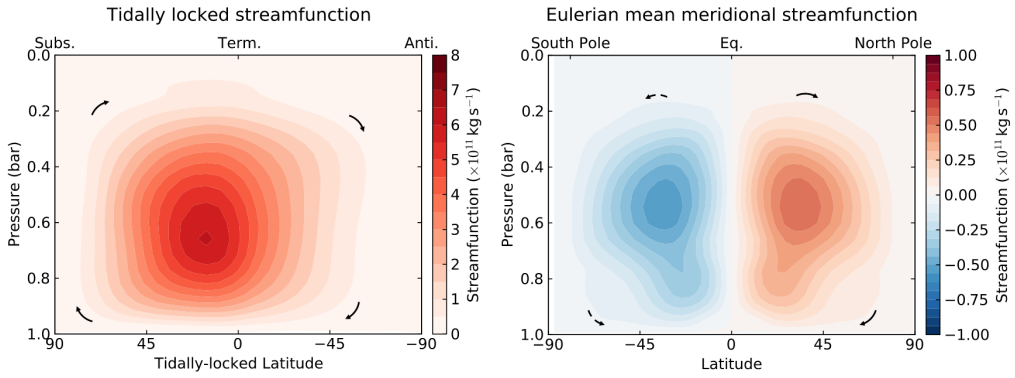

Figure 2.8: The mean meridional mass streamfunction in conventional latitude-longitude coordinates (right), and tidally-locked coordinates (left) for a tidally-locked terrestrial planet. The strength of the circulation is an order of magnitude larger in the tidally-locked coordinates. From (Hammond and Lewis, 2021)

where s is the dry static energy, R is the net radiative heating and $\langle \cdot \rangle$ represents vertical averaging. For atmospheres with weak temperature gradients the first term in Equation 2.24 dominates, so the divergent circulation must balance the radiative heating of the circulation.

In Chapter 3 I will use Equation 2.24 to predict how the strength of the overturning circulation on sub-Neptunes scales with instellation in GCM simulations.

2.7 Dry Dynamics on Temperate Sub-Neptunes

Although there have been many GCM simulations of hot Jupiters and terrestrial exoplanets there have been comparatively fewer studies of sub-Neptune atmospheres, with most focused on GJ 1214 b. The works of Menou (2012), Zhang and Showman (2017) and Drummond et al. (2018) investigated the effect of varying metallicity on the atmosphere of GJ 1214 b, and generally agreed that increased metallicity decreases equatorial jet width and increases the day-night temperature contrast. The effect of clouds on the dynamics and spectra of GJ 1214 b has also been probed (Charnay et al., 2015a,b). The atmosphere of GJ 1214 b has also been used to test the differences between standard primitive equation GCM models and models which integrate the equations of motion without the traditional, hydrostatic, and shallow approximations (Mayne et al., 2019; Christie et al., 2022). For hot sub-Neptunes it was found that including these non-primitive terms could change the structure of the deep atmosphere and also affect the location of a planet's hot spot. The deep atmosphere on sub-Neptunes also affects the equilibration times of GCMs (Wang and Wordsworth, 2020), with equilibration times of 10^4 to 10^5 Earth days often required to reach a steady state.

Previous to this thesis, only one published work has studied the atmosphere of K2-18b with a GCM (Charnay et al., 2021). The circulation was found to be dominated by an overturning day-night circulation, which controlled the location of clouds. The

cooling required to induce condensation and cloud cover occurred either at the terminators (from radiative cooling) or at the substellar point (from adiabatic cooling on ascent). Which mechanism dominated depended strongly on the size and density of cloud condensation nuclei, as well as the assumed metallicity of the atmosphere.

Although few sub-Neptunes with hydrogen-dominated atmospheres on the threshold of H_2O condensation have been discovered and characterised, they may prove to be common given the abundance of sub-Neptunes and their predicted compositions (Kite et al., 2020). Water clouds in temperate sub-Neptunes have been proposed as an aerial biosphere (Seager et al., 2021), and their structure, location and lifetime are affected by the underlying 3D dynamics.

It is likely that the circulation of temperate sub-Neptunes is distinct from the well-studied Hot Jupiters and terrestrial exoplanets. The dynamics of terrestrial exoplanets is driven by shortwave heating of the surface, with energy communicated upward by convection and infrared radiation. In contrast, the energy in sub-Neptunes (excluding Hycean worlds) is deposited by shortwave absorption in the atmosphere, which can stabilise temperature-pressure profiles to convective instability. Sub-Neptunes also lack a distinct surface to act as a source of drag on the circulation. In addition, hydrogen dominated atmospheres typically have a much higher heat capacity per unit mass, which increases the radiative timescale in comparison to high mean molecular weight terrestrial planets. In comparison to Hot Jupiters, a much smaller planetary radius, a, increases the weak temperature gradient parameter, $\Lambda = \sqrt{RT}/\Omega a$, making the elimination of strong temperature gradients by planetary waves more efficient. Moreover, increasing Λ reduces the impact of standing equatorial waves in the atmosphere, which could reduce the strength of any equatorial jet (e.g., Carone et al., 2015). For both Hot Jupiters and sub-Neptunes, the vertical scale of the waves (and therefore the wave speed) is set by the penetration depth of shortwave heating, and we should expect the scalings of Equation 2.12a to be valid, albeit with different values for the non-dimensional param-

eters.

In Chapter 3 I will use a simplified dry GCM in order to characterise the circulation of a range of temperate sub-Neptunes. In particular, I will aim to answer the following questions:

1. What characterises the general circulation of temperate sub-Neptunes?
2. Is there superrotation on sub-Neptunes, and if so what mechansisms generate and sustain the superrotating circulation?
3. Do all temperate sub-Neptunes lie in the same circulation regime?
4. Can we use theories of geophysical fluid dynamics to explain how aspects of the circulation vary with input parameters such as rotation rate and stellar instellation?

2.8 Condensation and Moist Effects

Condensing water vapour has an important impact on the dynamics of the Earth and gas giant exoplanets. As explained in Chapter 1, we expect temperate sub-Neptunes with high metallicity atmospheres to be water-rich and influenced by the release of latent heat when it condenses. In this section, I will give a broad overview on the effect of water vapour on global circulation.

2.8.1 Latent heat release

Firstly, the latent heating released by condensational processes is important in the global energy budget of cooler planets. We can define the moist static energy (MSE) as:

$$h = c_p T + gz + Lq, \tag{2.25}$$

where $c_p T$ represents sensible heating, gz the gravitational potential energy and Lq the contribution from moisture (L is the latent heat of the phase change and q the specific humidity of the condensible in the vapour phase). The MSE is conserved during (in this form, strictly dilute) moist adiabatic processes (Vallis, 2017; Pierrehumbert, 2010) and is often used to track the global energy budget with the inclusion of moisture. To determine whether latent heating will have a significant effect on the energy budget, one can look at the inverse Bowen ratio (Bowen, 1926):

$$\frac{Lq}{c_p T}, \tag{2.26}$$

i.e. the ratio between the latent and sensible heating. For example, in the Earth's tropics, we have a typical value of q being 0.01, which gives $Lq/(c_p T) \approx 0.1$. This is a non-negligible proportion of the total energy. In Frierson et al. (2006) and Frierson et al. (2007), a simplified GCM of an aqua-planet explored the effects of latent heating on energy transports in the atmosphere. Water vapour was included as a component of the atmosphere that did not interact with the radiation scheme. They found that in the moist cases the strength of the Hadley cell decreased and jets moved polewards. The weakening of the Hadley circulation with increasing moisture was also found in Kaspi and Showman (2015). They posited that on warmer planets with a larger moisture content, eddy meridional latent heat fluxes can enhance polewards energy transport, therefore requiring less mass transport in the Hadley circulation for equivalent energy transport to balance the energy budget.

On tidally-locked terrestrial exoplanets, the latent heat flux is mainly directed from the day-side to the night-side of the planet and can act to lower day-night temperature contrasts (Edson et al., 2011b). However, the consensus on the magnitude of this effect varies. In Merlis and Schneider (2010), an increased latent heat flux towards the night-side was associated with a compensating drop in the dry heat flux. Sergeev et al. (2020) however, in their simulations of Trappist-1e and Proxima b, found that the latent heat fluxes on the eastern terminator were on the order of 1% of the dry static energy fluxes.

2.8.2 Clouds and Radiative Effects

Moving away from latent heating effects, water vapour is a strong greenhouse gas due to its infrared opacity. In studies of terrestrial GCMs that include water vapour as a radiatively active component, increased water vapour is associated with increased surface temperatures. The water vapour feedback has been extensively studied in 1D models, with particular focus being put on the "runaway greenhouse" effect (Komabayasi, 1967; Ingersoll, 1969). Above a critical instellation (the Komabayasi-Ingersoll limit), surface temperature exhibits a sharp increase as the increased opacity from water vapour places a limit on the outgoing longwave radiation (and therefore the planet's ability to cool). This instellation limit is the canonical way to define the inner edge of a star's habitable zone (Kopparapu, 2013)

In 3D GCM studies of the inner edge of the habitable zone, cloud feedbacks play a crucial role. Firstly, cloud droplets scatter shortwave radiation, increasing the albedo of cloudy regions. Secondly, clouds are very opaque to longwave radiation. Infrared radiation emitted by a planet's surface with temperature T_s will be absorbed by the cloud and re-emitted with a (approximate) black body spectrum with characteristic temperature $T < T_s$. This reduces the OLR which in turn warms the atmosphere. Higher clouds emit at a lower temperature and therefore tend to have a net warming effect, compared to lower clouds which emit with a temperature more comparable to the surface temperature and can be net cooling. This is a simplistic overview of the processes at play – a full treatment requires study of the different types of cloud (e.g. cumulus, stratus etc.) and the convective processes which lead to their formation (Gettelman and Sherwood, 2016).

For terrestrial planets orbiting M-dwarf stars, the link between cloud structures and rotation rate is particularly important (Yang et al., 2013, 2014). Planets in the slow-rotating regime tend to have regions of vigorous convective upwelling on their day sides,

increasing the albedo and cooling the planet. Yang et al. (2013) found this almost doubled the runaway greenhouse instellation. Moreover, Haqq-Misra et al. (2018) and Komacek and Abbot (2019) found that fast-rotating planets with Rhines and Rossby length scales less than the planetary radius significantly reduced the day-side cloud cover as clouds were advected eastward from the substellar point and broken up due to eddy-mean flow interactions, leading to an increased surface temperature.

2.8.3 Moist Convection

Moist convection is ubiquitous in the atmospheres in our solar system with condensibles. Broadly speaking, it is driven by buoyant, moist parcels of air rising, generating turbulent mixing and releasing latent heat. On Earth, moist convection sets the lapse rate in the tropics and provides a large source of energy to the Hadley cell (Emanuel and Hide, 1995; Pierrehumbert, 2002). Convection is also responsible for many of the storms and clouds visible in the atmospheres of the solar system gas giants (Palotai et al., 2023).

Instability of an atmosphere to convection can be understood using a simple parcel method. If an air parcel's density when lifted upwards adiabatically by a pressure $-\mathrm{d}p$ from pressure p is less than the density of the surrounding air, then it will be unstable to convective mixing. The criterion for convection can be written:

$$\rho_{\mathrm{ad}}(p - \mathrm{d}p) < \rho_{\mathrm{am}}(p - \mathrm{d}p), \tag{2.27}$$

where "am" represents the ambient density and "ad" the density of the lifted parcel. Taking the logarithm of both sides and using the ideal gas law $p = \rho R_* T/\mu$ (where μ is the mean molecular weight of the gas and R_* is the universal gas constant), we get:

$$\nabla_{\mathrm{ad}} - \nabla_{\mu,\mathrm{ad}} < \nabla_{\mathrm{am}} - \nabla_{\mu,\mathrm{am}}, \tag{2.28}$$

where $\nabla_x \equiv \mathrm{d}\ln T_i/\mathrm{d}\ln p$ and $\nabla_{\mu,i} \equiv \mathrm{d}\ln \mu_i/\mathrm{d}\ln p$. In the absence of mean molecular weight gradients, Equation 2.28 reduces to the standard moist convective instability

criterion, where for instability the lifted parcel's temperature should exceed the ambient temperature. In the absence of condensation but in an environment with compositional gradients, setting $\nabla_{\mu,\mathrm{ad}} = 0$ gives the Ledoux criterion:

$$\nabla_{\mathrm{am}} - \nabla_{\mathrm{ad}} - \nabla_{\mu,\mathrm{am}} > 0. \tag{2.29}$$

Convection induced by compositional gradients is the dominant mode of convection in the Earth's core (Fearn and Loper, 1981).

On Earth, dry convection convection is usually confined to the boundary layer of the atmosphere as the free troposphere is stable relative to the dry adiabat. However, moist parcels that reach their lifted condensation level (LCL) will condense and release latent heat. The temperature profile, ∇_{ad}, of a lifted, saturated parcel will be the moist adiabat (Pierrehumbert, 2010; Ding and Pierrehumbert, 2016):

$$\nabla_{\mathrm{ad,moist}} = \frac{\overline{R}}{\overline{c}_p} \frac{1 - q_{\mathrm{sat}} + \frac{L q_{\mathrm{sat}}}{\overline{R} T}\left(1 - \varpi q_{\mathrm{sat}}\right)}{1 - q_{\mathrm{sat}} + \beta \frac{L q_{\mathrm{sat}}}{\overline{c}_p T}\left(1 - \varpi q_{\mathrm{sat}}\right)}, \tag{2.30}$$

where $\varpi \equiv 1 - \mu_d/\mu_v$ (where μ_d and μ_v are the mean molecular weights of the dry and vapour components respectively), q_{sat} is the saturation vapour concentration of the air, $\beta \equiv \mathrm{d}\ln p_{\mathrm{sat}}/\mathrm{d}\ln T$ is the gradient of the vapour-liquid phase curve, L is the latent heat of vapourisation (or sublimation if T is below the triple point of water) and $\overline{R}$ and $\overline{c}_p$ are the mass-weighted gas constants and specific heat capacities of the lifted air. Equation 2.30 clearly reduces to the dry lapse rate $R_d/c_{p,d}$ as $q_{\mathrm{sat}} \to 0$ and the pure steam lapse rate $1/\beta$ as $q \to 1$. The effect of latent heating acts to reduce the adiabatic lapse rate, destabilising the atmosphere. Temperature profiles in the tropics are typically conditionally stable, i.e. they are stable to dry convection, but unstable to moist convection.

Convective Inhibition

In non-dilute atmospheres with a condensing component, the mean molecular weight gradient terms $\nabla_{\mu,\mathrm{ad}}$ and $\nabla_{\mu,\mathrm{am}}$ become important in determining the static stability.

Unlike for dry convection, these quantities are now linked to the temperature profiles ∇_x via the Clausius-Clapeyron relation:

$$\nabla_{\mu,x} = q\varpi(\beta\nabla_x - 1). \tag{2.31}$$

Combining Equation 2.31 with 2.28 yields the following criterion for convection:

$$(\nabla_{\rm am} - \nabla_{\rm ad})(1 - \varpi\beta q) > 0. \tag{2.32}$$

When the mean molecular weight of the condensible component is lighter than the background gas, $\varpi < 0$, and Equation 2.32 is equivalent to the Schwarzschild criterion $\nabla_{\rm am} > \nabla_{\rm ad}$. However, if $\varpi > 0$, i.e., the mean molecular weight of the condensible component exceeds that of the background gas, convection will only occur for superadiabatic temperature gradients when $q < q_c \equiv 1/(\beta\varpi) \approx R_v T/(\varpi L)$, i.e., when the condensible concentration is below a critical threshold. If $q > q_c$ a strong compositional gradient is induced in superadiabatic temperature structures, since high pressure regions are enriched with heavier condensible substances and low pressures are depleted. In the absence of convection in these regions, the lapse rate is predicted to be controlled by the most efficient energy transport mechanism, usually radiative transfer (Guillot, 1995; Leconte et al., 2017). The inhibition of convection in the gas giant atmospheres of our solar system was first predicted by Guillot (1995), who found that temperature structures on Uranus and Neptune detected by *Voyager 2* are consistent with superadiabatic radiative temperature gradients at the 1 – 2 bar level. Li and Ingersoll (2015) predicted the presence of inhibited layers in Saturn's atmosphere. In their model, the inhibition of convection allows for convectively available potential energy (CAPE) to build up in the lower atmosphere and be released in episodic storm events (Sanchez-Lavega, 1994) when radiative cooling of the upper atmosphere breaks the compositional stabilisation. Condensing regions where $q > q_c$ were also shown to be stable to double-diffusive instability in Leconte et al. (2017). They predict that the interior temperature of the gas giants would be higher than expected due to the formation of deep, convectively-inhibited ra-

diative layers with large superadiabatic lapse rates. The change in temperature structure predicted could impact the retrieval of elemental abundances in the interior of these planets. In Chapter 6 I will investigate whether convection can be sustained in a 3D model of sub-Neptunes with condensing water vapour concentrations above the critical q_c threshold.

2.8.4 Horizontal Compositional Gradients

The horizontal distribution of moisture can also impact the vertical shearing of winds. To see this we can consider the balance of forces on fluid parcel in the meridional direction can be written (neglecting advective terms):

$$\frac{u^2 \tan\phi}{a} + fu = -\frac{1}{a}\frac{\partial \Phi}{\partial \phi}. \tag{2.33}$$

Taking the derivative of this equation with respect to $\ln p$, and using the hydrostatic equation (Equation 2.4b), we get:

$$\frac{\partial}{\partial \ln p}(u^2 \tan\phi + afu) = R_d \frac{\partial T_v}{\partial \phi}, \tag{2.34}$$

where $T_v \equiv T(1 - \varpi q)$ is the virtual temperature, which takes into account the variation in density due to composition. If the horizontal distribution of condensible species in a weather layer is set by the Clausius-Clapeyron relation, then we would expect regions with colder thermodynamic temperature T to be depleted in q, and vice versa. On Earth, where the condensible species is lighter than background air and $\varpi < 0$, this means that meridional gradients in virtual temperature are always of the same sign to gradients of thermodynamic temperature. This leads to the temperature contrast between equator and pole resulting in an increase in zonal winds with height via Equation 2.34. However, in hydrogen-dominated atmospheres where the condensing component of the atmosphere is heavier than the background, $\varpi > 0$, and the virtual temperature gradient can be opposite in sign to the thermodynamic temperature gradient

if q is large enough. To quantify this effect, we can use the definition of T_v to write

$$\frac{\partial \ln T_v}{\partial \phi} = \frac{\partial \ln T}{\partial \phi}\left(1 + \frac{\partial}{\partial \ln T}\ln(1 - \varpi q)\right). \tag{2.35}$$

Since we are working in pressure coordinates, all derivatives are taken held at constant pressure. If we assume that q is held at saturation, then using the Clausius-Clapeyron relation we can write:

$$\frac{\partial \ln q}{\partial \ln T} = \beta(1 - \varpi q), \tag{2.36}$$

and Equation 2.35 reduces to:

$$\frac{\partial \ln T_v}{\partial \phi} = (1 - \varpi\beta q)\frac{\partial \ln T}{\partial \phi}. \tag{2.37}$$

In Equation 2.37 we have proven that above the same critical water concentration that inhibits convection, $q_c \equiv 1/(\varpi\beta)$, we should expect the gradient in virtual temperature to be opposite to the gradient in thermodynamic temperature. This "humidity wind" that reverses vertical wind shears has been invoked to explain the orientation of convective plumes on Uranus (Zi-Ping Sun et al., 1991) and to reconcile observations of Neptune's winds with theory (Tollefson et al., 2018). In Chapter 6 I will show that the reversal in wind shear due to compositional gradients can limit the vertical extent of jets on sub-Neptune exoplanets.

2.9 Moist Dynamics on Temperate Sub-Neptunes

The effect of condensing water vapour in a temperate sub-Neptune atmosphere has only been studied once, in Charnay et al. (2021). As discussed in Section 2.7, they found the global distribution of clouds to depend strongly on cloud microphysical properties. However the extent of condensation was limited due to a small proportion of the upper atmosphere due to warm temperatures. For cooler sub-Neptunes, we would expect the effects of latent heating and moist processes to become more pronounced since condensation will occur in the dynamically active region of the atmosphere.

Theoretical studies predict that sub-Neptunes could have a range of compositions ranging from hydrogen-dominated to volatile-dominated water worlds (Kite et al., 2020; Kite and Barnett, 2020; Madhusudhan et al., 2020). Enhancements of water vapour over metallicities of 10x and above can make water vapour non-dilute in the atmosphere, with 100x solar metallicity chemical equilibrium models giving typical water concentrations of 0.35 (Charnay et al., 2021; Tsai et al., 2021). The effect of non-dilute dynamics on the circulation of terrestrial exoplanets has been studied in Pierrehumbert and Ding (2016). They found that as terrestrial atmospheres become water-dominated, the dynamics become barotropic, and the relative humidity tends towards 100%. However, the atmospheres studied in this work were nitrogen-dominated. As highlighted in Sections 2.8.3 and 2.8.4, the presence of condensing water in a hydrogen-dominated atmosphere is expected to shut off convection and alter the vertical structure of jets.

In Chapter 6 I present the development of a GCM capable of simulating non-dilute moisture in the atmosphere of a sub-Neptune exoplanet. Along with necessary adjustments to the dynamical core, I also include a simplified hydrological cycle. The convective adjustment scheme used will account for compositional gradients and convective inhibition. In future, I hope the model can be used to answer questions such as:

1. How does the release of latent heat and moisture gradients affect the large-scale dynamics of temperate sub-Neptunes?

2. Does latent heat release alter the strength of the overturning circulations responsible for energy transport?

3. Is convection robustly inhibited in atmospheres where $q > q_c$ in the condensing region and how does this affect the distribution of water vapour in the atmosphere?

4. How are the condensing regions of the atmosphere spatially distributed and can this impact potential observations of sub-Neptunes?

The results from Chapter 5 also show that the inhibition of convection will have a profound impact on the temperature structure of Hycean worlds, i.e. sub-Neptunes with a liquid water ocean. However, given the uncertainty of modelling the planetary boundary layer of a Hycean world that has steep, super-adiabatic temperature gradients (from convective inhibition), I choose to only model sub-Neptunes without a surface.

Chapter 3

The Dry Dynamics of Temperate Sub-Neptunes

The results of this chapter were published in Innes and Pierrehumbert (2022).

More than half of all sun-like stars host a planet with a radius between that of Earth and Neptune (Fressin et al., 2013). As discussed in Chapter 1, a large proportion of these planets are "sub-Neptunes" with extended, hydrogen-dominated atmospheres. Particular interest has been focused on temperate sub-Neptunes, in particular because they could host liquid water either at the surface (Hycean worlds, Madhusudhan et al. (2020)) or in cloud droplets aloft, which could act an aerial biosphere (Seager et al., 2021). These planets are slowly-rotating (if tidally-locked) and have very long radiative timescales, which should place them in a different parameter space to Hot Jupiters and terrestrial exoplanets.

In this chapter I will simulate a range of dry temperate sub-Neptunes to try and understand their basic underlying circulation. In Sections 3.1.1 and 3.1.2 I will introduce the ExoFMS GCM that will be used for the suite of simulations and set out the

region of parameter space to be explored. Section 3.2 outlines the main findings of this chapter. I will show that the circulation of temperate sub-Neptunes is dominated by high-latitude jets and global weak temperature gradients. The main divergent circulation is a day-to-night flow, but a residual equator-to-pole overturning circulation provides the angular momentum to sustain the high-latitude jets. I derive a scaling relation to link the strength of the overturning circulation to the instellation received by a planet. In the upper atmosphere, a superrotating jet formed by wave instabilities is found. In Section 3.3, I compare my simulations to the only other simulation of a temperate sub-Neptune. I find that my results differ qualitatively from these results and offer possible explanations for these differences. I also demonstrate why we should expect most temperate sub-Neptunes to fall in a similar parameter regime to those in my simulations. Finally, I recommend future work to determine the disparities between different dynamical cores when modelling sub-Neptunes.

3.1 Model

3.1.1 ExoFMS

The GCM used for this study is ExoFMS, which is based on GFDL's Flexible Modelling System (Lin and Rood, 1997; Lin, 2004) which uses a finite volume dynamical core on a cubed-sphere grid with physics modules adapted for exoplanetary study. ExoFMS has been used previously to study the atmospheres of terrestrial exoplanets (Pierrehumbert and Ding, 2016; Hammond and Pierrehumbert, 2017, 2018; Pierrehumbert and Hammond, 2019) and gas giants (Lee et al., 2020).

The dynamical core solves the primitive equations with a σ-p vertical coordinate that follows contours of constant geopotential on the bottom boundary and transitions into a pure pressure coordinate in the upper atmosphere. The form of the equations is the same as Equations 2.4. The diabatic heating rate $\dot{Q}$ is largely determined by the

radiative transfer scheme. We use a double-grey scheme, where the radiation is split into two bands: shortwave (SW) and longwave (LW). The incoming stellar radiation is assumed to be only in the SW band and we assume the atmosphere only emits in the LW part of the spectrum. The LW and SW opacities ($\kappa_{\rm LW}$ and $\kappa_{\rm SW}$ respectively) define optical depths ($\tau_{\rm LW}, \tau_{SW}$) via the relation:

$$\tau_i = \frac{2\kappa_i}{g}\frac{p}{p_{\rm o}} \quad i \in ({\rm SW}, {\rm LW}) \tag{3.1}$$

using the hemi-isotropic closure to approximate the angular dependence of τ (Pierrehumbert, 2010). Here we have neglected any pressure dependence of the two opacities, which is likely to be a false assumption at higher pressures where collisional-induced absorption of H_2 becomes dominant (and scales as $\rho^2 \sim p^2$ for an isothermal atmosphere). We justify this simplification in section 3.1.2. The downwards SW flux, S_- and the upwards and downwards LW fluxes, (F_+, F_-), are then calculated via:

$$S_- = S_{\rm o} e^{-\tau_{\rm SW}} \tag{3.2}$$

$$F_- = \int_{\rm o}^{\tau} \sigma T^4(\tau') e^{-(\tau-\tau')}\,{\rm d}\tau' \tag{3.3}$$

$$F_+ = F_{\rm int} e^{-(\tau_{\rm o}-\tau)} + \int_{\tau}^{\tau_{\rm o}} \sigma T^4(\tau') e^{-(\tau'-\tau)}\,{\rm d}\tau' \tag{3.4}$$

where $S_{\rm o}$ is the instellation, $F_{\rm int}$ is the longwave flux radiating upwards from the interior of the planet, $\tau_{\rm o}$ is the LW optical depth at $p = p_{\rm o}$ and σ is the Stefan-Boltzmann constant. We note that the incoming SW radiation does have a zenith angle dependence, however we are neglecting this dependence on the grounds that the direct beam is largely converted to diffuse radiation by scattering in the optically thick section of the atmosphere (this assumption breaks down in the upper atmosphere where the direct beam is not yet scattered). The radiative heating rate is calculated from these fluxes as:

$$\dot{Q}_{\rm rad} = g\frac{\rm d}{{\rm d}p}(F_+ - F_- - S_-). \tag{3.5}$$

Enthalpy-conserving dry convective adjustment is performed if the vertical temperature gradient $\partial_p T$ exceeds that of the dry adiabatic R/c_p.

The model was run with mean molecular weight, μ, which sets the value of the gas constant R through $R = R_*/\mu$, where R_* is the universal gas constant, 8.314 J K^{-1}mol^{-1}. The heat capacity at constant pressure, c_p, was set by assuming the atmosphere behaved as an ideal diatomic gas with $R/c_p = 2/7$.

3.1.2 Experiment Setup

We use the temperate sub-Neptune K2-18 b as our control experiment. K2-18 b is the first sub-Neptune with Earth-like instellation to have its atmosphere characterised by transmission spectroscopy. Its radius (2.61 $R_\oplus$ (Cloutier et al., 2019)) and mass ($(8.63 \pm 1.35) M_\oplus$ (Cloutier et al., 2019)) place it close to the peak of the sub-Neptune population density distributions (Owen and Wu, 2017) making it an ideal candidate for generalised GCM experiments. The claimed discovery of water vapour in its atmosphere (Benneke et al., 2019a) also makes it an interesting test case for the effects of a condensible substance that is heavier than the surrounding bulk atmosphere.

Table 3.1 describes the parameters for the control run. The two-stream opacity values and mean molecular weight value μ are taken from a study of the atmosphere of GJ-1214b (Menou, 2012), and were found to provide a reasonable fit to the temperature-pressure profile from Scheucher et al. (2020) where real-gas radiative transfer calculations under chemical equilibrium conditions were carried out (see Figure 3.1). The largest discrepancy comes in the deep atmosphere (below 1 bar), where the grey gas solution significantly underestimates the temperature. This is likely due to two main factors. Firstly, as previously mentioned, collisional-induced absorption can increase the LW opacity at the bottom of the atmosphere greatly. However, including an additional opacity proportional to p only increases the high-pressure temperature either if there is a significant internal flux, or if shortwave heating penetrates to the high-pressure region. Estimates of the internal temperature of K2-18 b (calculated using estimates of the residual heat of formation) correspond to internal fluxes of around 1 to 4 Wm^{-2} (Blain

Table 3.1: Control experiment parameters

Parameter	Value	Comment
Planetary parameters		
a ($R_\oplus$)	2.61	Benneke et al. (2019a)
Rotation period (Earth days)	32.9396	Cloutier et al. (2017)
S_0 (W m^{-2})	1368	Benneke et al. (2019a)
g (m s^{-2})	12.43	Benneke et al. (2019a)
Atmospheric parameters		
μ (g mol^{-1})	2.2	Menou (2012), solar metallicity
R (J kg^{-1}K^{-1})	3779	Menou (2012), solar metallicity
R/c_p	2/7	Ideal diatomic gas
c_p (J kg^{-1}K^{-1})	$R \times \frac{1}{R/c_p}$	—
κ_{LW} (cm^2 g^{-1})	2×10^{-2}	Menou (2012), solar metallicity
κ_{SW} (cm^2 g^{-1})	8×10^{-4}	Menou (2012), solar metallicity
T_{int} (K)	70	Consistent with Blain et al. (2021) and Piette and Madhusudhan (2020)
Numerical parameters		
Horizontal grid resolution	C48	Each side of cubed sphere has 48×48 resolution (Putman and Lin, 2007)
Vertical grid resolution	50	—
Bottom boundary reference pressure (Pa)	10^6	—
Top boundary pressure (Pa)	10	—
Experiment run time (Earth days)	20000	—
Substellar longitude	0°	—

et al., 2021) which is not enough to increase the lower-layer temperatures significantly.

We investigated the effect of adding a term proportional to p in both LW and SW opacities such that the optical depths were of the form:

$$\tau = \tau_0 \left(f \left(\frac{p}{p_0} \right)^2 + (1 - f) \frac{p}{p_0} \right) \tag{3.6}$$

where f is a constant between 0 and 1. The opacity of a real-gas atmosphere will not be constant with pressure for a number of reasons. Firstly, there may be chemical heterogeneity in the atmosphere which causes the chemical composition (and therefore opacities) to vary in height in the atmosphere. Secondly, the pressure-broadening of lines becomes stronger at higher pressures. Thirdly, for molecules with significant collision-

induced absorption spectra (e.g., hydrogen) the optical depth increases as the square of the density of molecules (since the absorption is induced by pairwise interactions). This leads to τ increasing non-linearly with pressure. When $f = 0.8$ for the LW band (note we cannot set $f = 1$ for the LW band since this causes diverging temperatures at $p = 0$), we do not see a significant change in the temperature profiles (see purple curve in Figure 3.1) and the curve is a worse fit to the Scheucher et al. (2020) profile. When $f = 1$ for the SW band, we find the temperature is much hotter at the bottom of the atmosphere, better matching the Scheucher et al. (2020) profile at the bottom boundary. In Appendix A, we show the result of running one of our 6 day period experiments with this altered SW opacity. This experiment produces qualitatively similar results to our constant-κ approach, though we note the magnitude of the zonal winds when using pressure-dependent opacities differs notably. We found that including a second SW band with a lower optical depth (≈ 1) was much more effective at heating the lower atmosphere. An experiment run with this modification did not affect the dynamics in an appreciable way.

We study the effect of varying rotation rate by running the experiment with a faster rotation rate of $P = 6$ days. K2-18 b is a slow-rotator and lies within the "weak temperature gradient" regime of parameter space (Pierrehumbert and Hammond, 2019). Therefore while we expect decreasing the rotation rate not to change the dynamical regime of the atmosphere, increasing the rotation rate could produce interesting changes to the dynamics. We choose $P = 6$ days since this is the rotation rate of TRAPPIST-1e, a planet with a temperate equilibrium temperature of 251 K orbiting an ultra-cool M-star with effective temperature 2550 K (Gillon et al., 2016). Most observed M-dwarfs have an effective temperature greater than this value (Casagrande et al., 2008; Rajpurohit et al., 2013), so we would expect temperate exoplanets around the majority of M-dwarfs to have longer rotation periods than TRAPPIST-1e, making it approximately an upper limit on rotation rate.

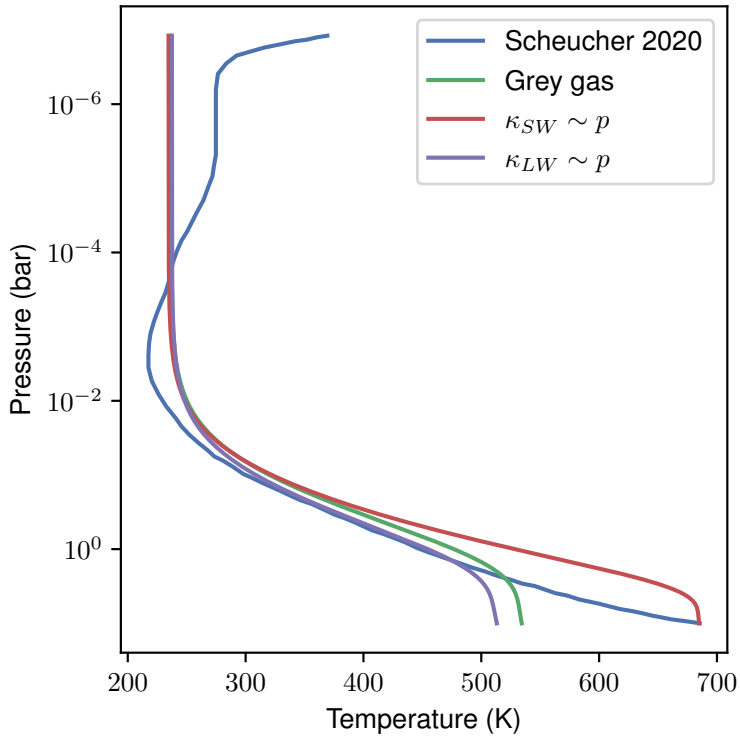

Figure 3.1: Comparison of the radiative equilibrium profile calculated using a simple grey gas scheme with a correlated-k chemical equilibrium model from Scheucher et al. (2020). We also include profiles calculated with pressure dependent opacities in the LW (purplecurve)and SW (red curve) bands.

Table 3.2: Experiment setup

Experiment name	Difference to control
PKc	Control experiment (see Table 3.1)
PKh	$S = \frac{1}{2}S_0$
PKd	$S = 2S_0$
P6c	P = 6 days
P6h	P = 6 days, $S = \frac{1}{2}S_0$
P6d	P = 6 days, $S = 2S_0$

We also investigate changing the value of the instellation, running the simulation with $S \in \{\frac{1}{2}S_0, S_0, 2S_0\}$ where S_0 is K2-18 b's instellation.

Table 3.2 summarises all the experiments.

3.2 Results

3.2.1 Convergence

Firstly, we investigate the convergence of the model runs. Figure 3.2 shows the total kinetic energy of each model run as a function of day, defined as:

$$E_k = \int_A \int_0^{p_s} \frac{\mathrm{d}p}{2g}(u^2 + v^2)\,\mathrm{d}A\,, \tag{3.7}$$

where $\int \cdot \mathrm{d}A$ is an integral over horizontal area. The kinetic energy of the model runs takes an extremely long time to reach a steady-state, on the order of > 15000 Earth days (note unless otherwise specified, a "day" is an *Earth* day, i.e., 86400 seconds). On the other hand, the maximum and minimum zonal wind of the model reach a steady state on day ≈ 10000 for the 33 day period runs, and < 5000 days for the 6 day period runs. Whilst the kinetic energy is dominated by the denser lower atmosphere, the jet speeds are maximal in the upper atmosphere which takes a shorter period of time to reach its steady state. The globally-integrated outgoing longwave radiation (OLR) of the model reaches equilibrium with the incoming stellar radiation after ≈ 1000 days. In Wang and Wordsworth (2020) the convergence of the lower atmosphere took on the order of 10^5 days, after which the kinetic energy of the atmosphere reached a steady-state value. Our timescale appears to be shorter, which could be attributed to two things: firstly, our model has a lower bottom boundary pressure of 10 bar so the radiative timescale will be shorter at the bottom of our model; secondly, we initialised the simulations with the vertical temperature profile equal to the analytic radiative equilibrium temperature of a 1D grey gas model. As shown in section 3.2.2, since there are extremely weak horizontal temperature gradients throughout the atmosphere, 3D vertical temperature profiles match the analytic profile well. This would reduce the length of time the lower atmosphere has to adjust to radiative equilibrium (compared to initialising on an isothermal profile, as done in Wang and Wordsworth (2020) and previous studies of GJ 1214 b).

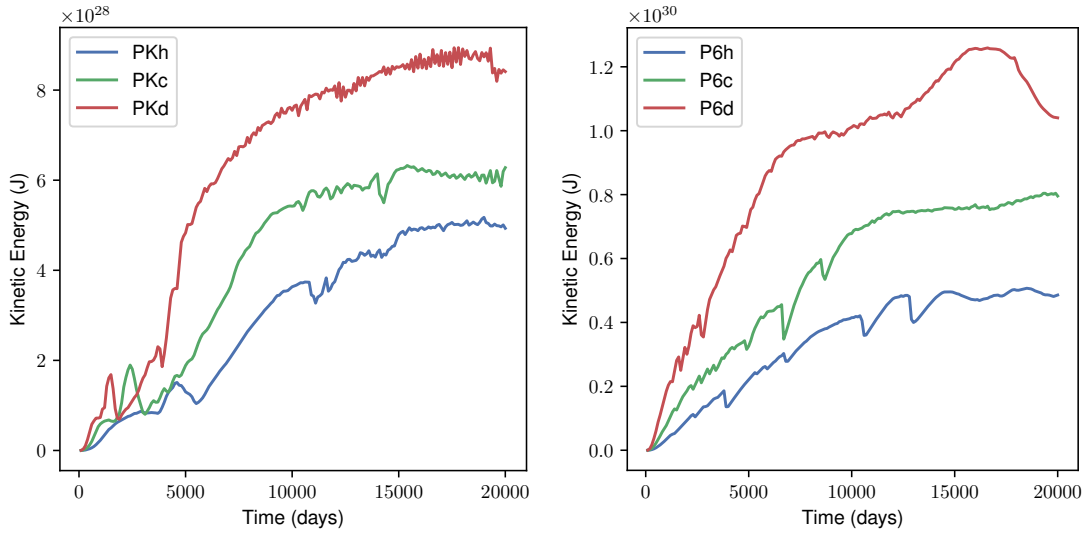

(a) **(b)**

Figure 3.2: The kinetic energy of the runs as a function of model time. (a) The 33 day period runs, with lines indicating different levels of instellation. (b) Equivalent to (a) but with 6 day period runs.

3.2.2 Temperature Structure

Figure 3.3 shows the horizontal temperature structure of the six runs at 100 mbar. The slower rotating experiments (with P = 33 days) show extremely horizontally uniform temperature profiles, with the temperature varying on the order of 1 K apart from near the poles, where there is a more significant drop in temperature in cold, vortex-like structures. In contrast, the faster rotating experiment shows a much larger temperature drop between equator and pole. The faster-rotating experiments support stronger cyclostrophic jets than the 33 day experiment (see sections 3.2.3 and 3.2.4) which in turn require larger meridional temperature gradients to sustain them by gradient wind balance. The slower-rotating experiments are also less uniform zonally, especially near the poles where meridional and zonal winds are of the same magnitude in some regions. In the 6-day period experiments, however, the wind field is extremely zonally uniform at all latitudes. The vertical temperature profiles in all runs closely fit the analytic 1D temperature profile assuming perfect heat redistribution, apart from near the poles. Fig-

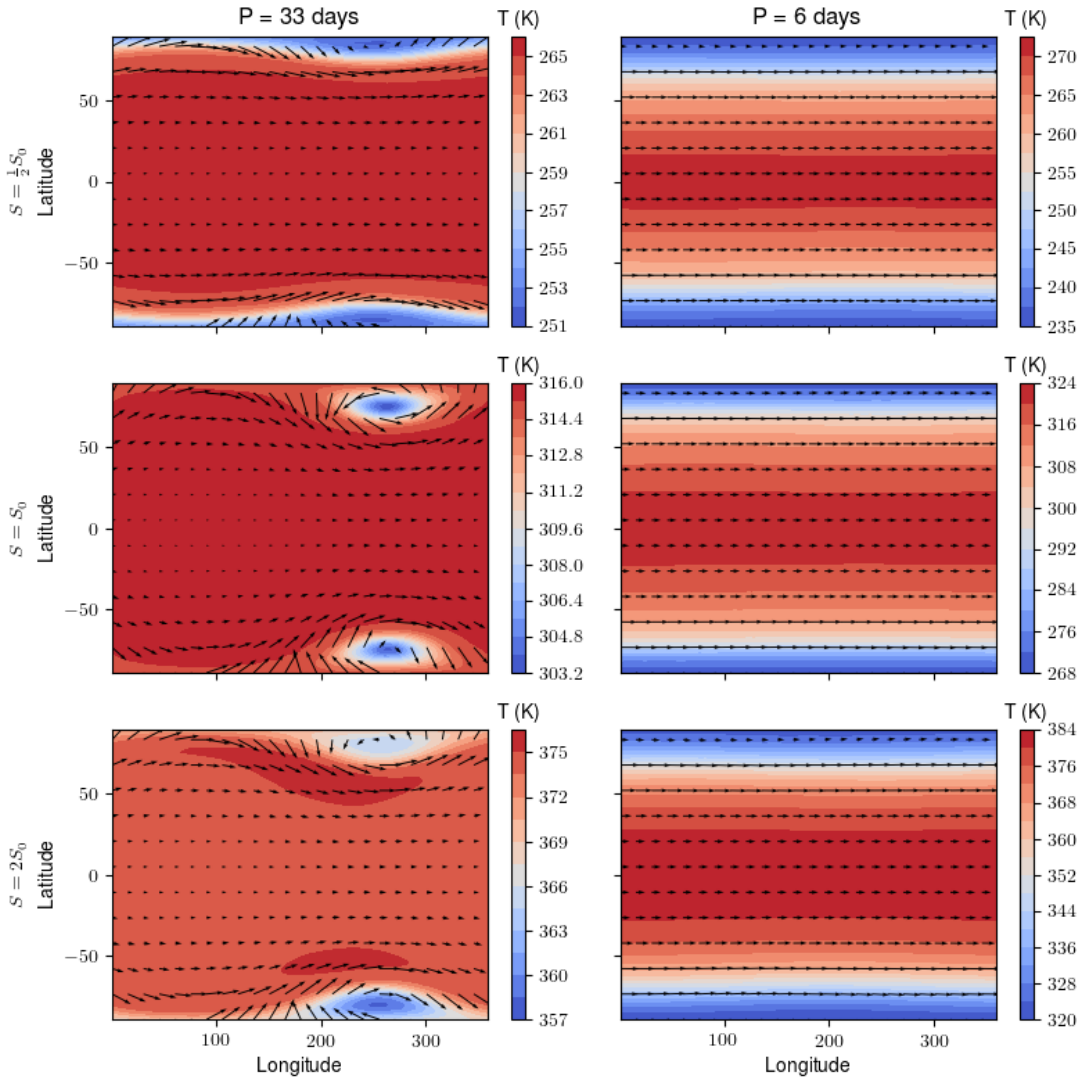

Figure 3.3: The 100 mbar level temperature profiles for the experiments. For the 33 day period experiments, the temperature varies on the order of 1 K throughout most of the horizontal plane apart from at a cold spot near (but offset from) the poles. For the 6 day period experiments, there is a much larger temperature drop from equator to pole. Note the substellar point is at 0° longitude.

ure 3.4 shows vertical temperature profiles at different latitudes and longitudes and in comparison to the 1D analytic solution for the control experiment. On the equator, in the zonal direction there is very little temperature variation. Moving polewards from the substellar point, however, there are significant variations in temperature away from radiative equilibrium. The weak temperature gradients in the tropics and mid-latitudes can be explained from a simple scaling argument, following Pierrehumbert and Ding

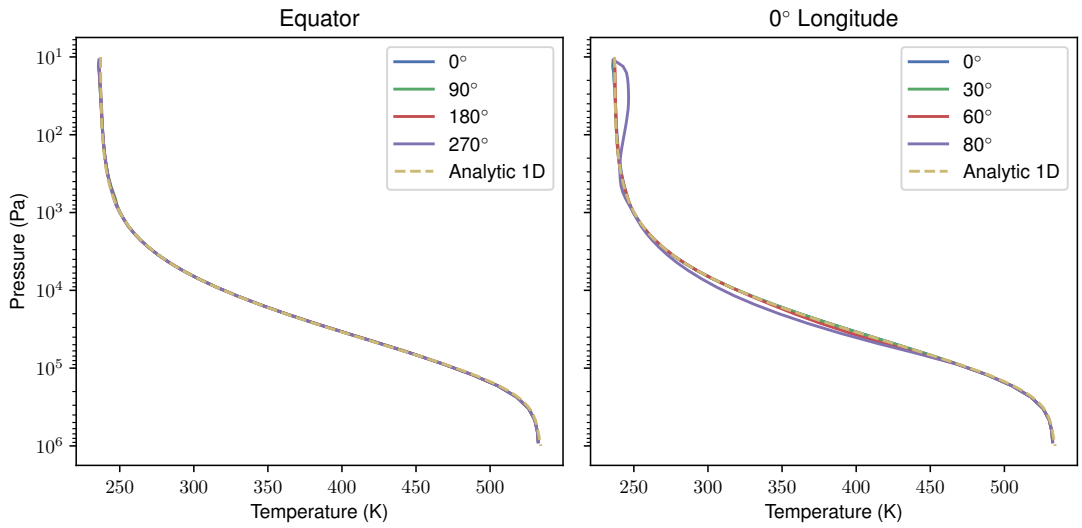

Figure 3.4: Horizontal temperature profiles for the control experiment. Left: On equator, the temperature profiles are very uniform and conforming to the analytic 1D solution. Right: In the latitudinal direction, there are deviations from uniform temperature gradients, but only near the poles.

(2016). The momentum equation, written in non-dimensionalised form is:

$$\mathrm{Ro}^2(\boldsymbol{u}\cdot\nabla u - uv\tan\phi) - \mathrm{Ro}\cdot f v = -\Lambda^2\partial_x\Phi, \tag{3.8}$$

where Ro is the Rossby number, $U/(\Omega a)$, and Λ is the weak temperature gradient (WTG) parameter $c_o/(\Lambda a)$ (Pierrehumbert and Ding, 2016; Pierrehumbert and Hammond, 2019), which is the ratio of the Rossby deformation radius to the planetary radius (c_o is a characteristic wave speed). If we approximate the atmosphere as isothermal with characteristic temperature T, this wave speed $\sim\sqrt{RT}$. For weak horizontal temperature gradients, we require $\Lambda \gg 1$ and $\mathrm{Ro} \gg 1$ such that $\partial_x\Phi \sim \partial_x T \approx 0$. Using estimates from our experiments, the 33 day period simulations have $\mathrm{Ro} \approx 10$, $\Lambda \approx 30$, whilst the 6 day period simulations have $\mathrm{Ro} \approx 3$, $\Lambda \approx 10$, confirming that both cases are firmly within the WTG regime, with the slower-rotating experiments expected to be more strongly uniform in temperature. In contrast, temperate terrestrial simulations (such as Pierrehumbert and Hammond (2019)) often have high μ atmospheres, making $\Lambda < 1$ and exciting a strong wave response. GJ 1214 b, being much hotter and faster rotating, has $\Lambda \approx 1$, being greater than or less than 1 depending on the assumed metallicity of its at-

mosphere (see section 3.3.1). This result can also be interpreted using the theory from Zhang and Showman (2017) in the low-drag limit, where the day-night temperature contrast compared to the equilibrium contrast is given by:

$$\frac{\Delta T}{\Delta T_{\mathrm{eq}}} \sim 1 - \frac{2}{\alpha + \sqrt{\alpha^2 + 4\gamma^2}}, \tag{3.9a}$$

$$\alpha = 1 + \frac{\Omega \tau_{\mathrm{w}}^2}{\tau_{\mathrm{r}} \Delta \ln p}, \tag{3.9b}$$

$$\gamma = \frac{\tau_{\mathrm{w}}^2}{\tau_{\mathrm{r}} \tau_{\mathrm{a,eq}} \Delta \ln p}, \tag{3.9c}$$

where τ_{r}, τ_{w} and $\tau_{\mathrm{a,eq}}$ are the radiative, wave and cyclostrophic advective timescales respectively (Zhang and Showman, 2017). If we write the wave timescale as $a/\sqrt{RT} = 1/(\Omega\Lambda)$ and the advective timescale as:

$$\tau_{\mathrm{a,eq}} = \frac{a}{U_{\mathrm{eq}}}, \tag{3.10}$$

$$= \frac{a}{\sqrt{R \Delta T_{\mathrm{eq}} \ln p}}, \tag{3.11}$$

$$= \frac{1}{\kappa \Lambda \Omega \sqrt{\ln p}}, \tag{3.12}$$

where $\kappa^2 \ll 1$ is the ratio between the equilibrium day-night temperature difference and the characteristic temperature of the atmosphere, then:

$$\alpha = 1 + \frac{1}{\tau_{\mathrm{r}} \Omega \Lambda^2 \Delta \ln p}, \tag{3.13}$$

$$\gamma = \frac{\kappa \sqrt{\ln p}}{\Lambda \tau_{\mathrm{r}} \Omega}. \tag{3.14}$$

The radiative timescale at the $\tau = 1$ level can be estimated as:

$$\tau_{\mathrm{r}} = \frac{c_p p(\tau = 1)}{4\sigma T^3 g} = \frac{c_p p_s}{4\sigma T^3 g \tau_{\mathrm{LW}}} \approx 8 \text{ days}, \tag{3.15}$$

which means $(\tau_{\mathrm{r}}\Omega)^{-1} = 1$ for the $P = 33$ day experiment and 0.1 for the $P = 6$ day experiments. Therefore in all our experiments we can predict $\alpha \approx 1$ and $\gamma \ll 1$, which corresponds to $\Delta T/\Delta T_{\mathrm{eq}} \ll 1$ (i.e., low day-night temperature contrasts).

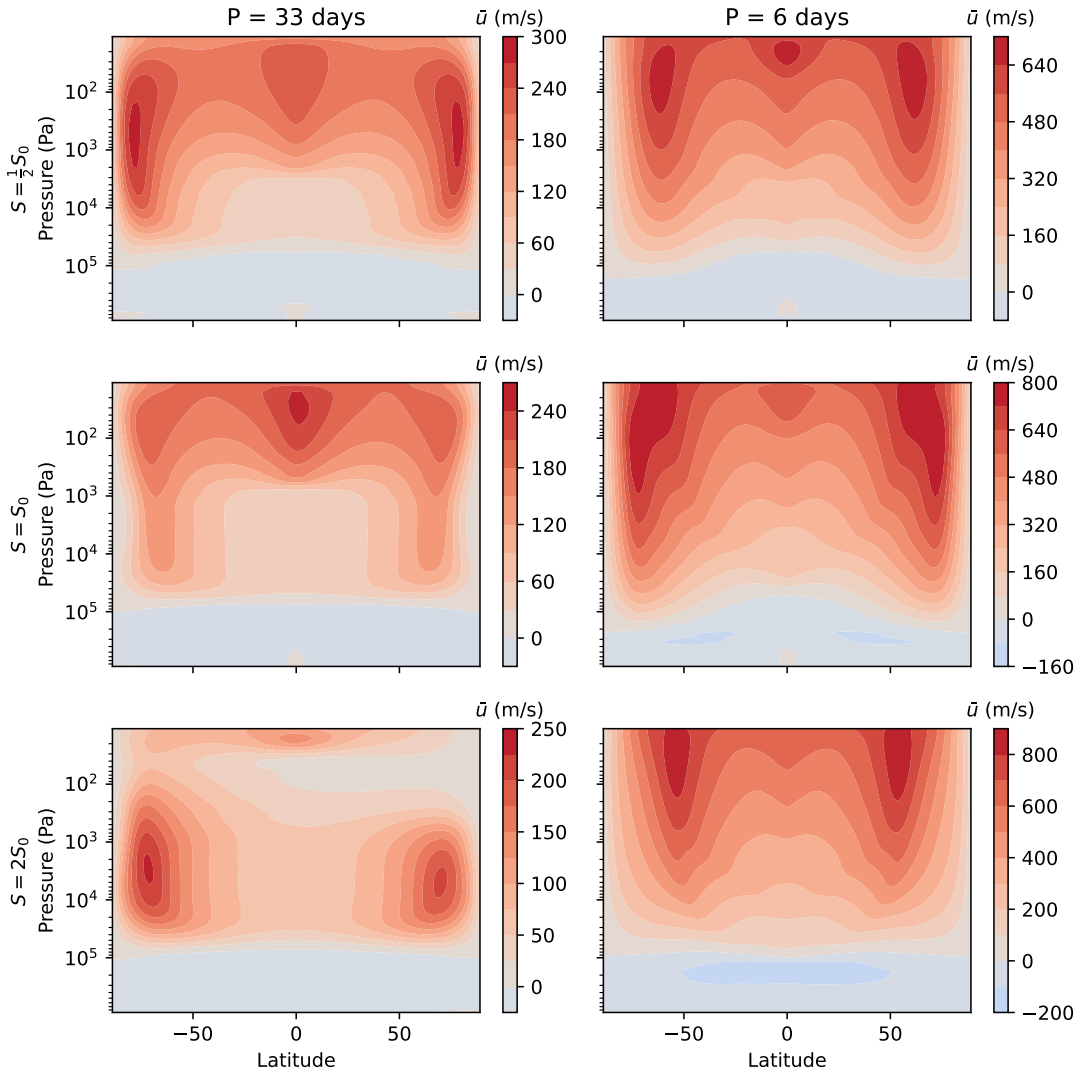

Figure 3.5: The zonal mean zonal wind for each of the six experiments. All circulations exhibit high latitude cyclostrophic jets. All experiments show equatorial super rotation, in some cases forming a third maximum on-equator.

3.2.3 Zonal Circulation

Next, we look at the zonal circulation. The temperature and wind profiles in our model runs were largely zonally symmetric, meaning the zonally averaged circulation is a good way of reducing the dimensions of the output data. Figure 3.5 shows the zonal mean zonal wind of each dry run. The common feature of all the circulations is the presence of two high-latitude cyclostrophic jets in steady-state balance. Figure 3.6 shows the

Table 3.3: Maximum meridional velocity in the time-averaged flow

Experiment name	Maximum v (m/s)
PKh	193
PKf	265
PKd	383
P6h	7
P6f	13
P6d	29

non-negligible terms in the zonally averaged meridional momentum equation:

$$\frac{1}{a}\left[v\partial_\phi v\right] + \frac{\left[u^2\right]\tan\phi}{a} + \left[fu\right] = -\frac{1}{a}\left[\partial_\phi \Phi\right], \tag{3.16}$$

where $[\cdot]$ represents zonally averaged terms. The experiments with the shorter period orbit are very close to gradient wind balance, with the pressure gradient induced by the temperature contrast between the equatorial regions and the polar regions balanced by the Coriolis forces and cyclostrophic terms in the momentum equation. In contrast, in the slower-rotating experiments, non-linear advective terms become important near the poles, where the meridional wind reaches its maximum magnitude value. Non-primitive terms in the momentum equation were found to be negligible throughout. Table 3.3 shows the maximum value of the time-averaged meridional velocity in each of the experiments, from which it is clear that the meridional velocity is an order of magnitude stronger in the slower-rotating experiment.

We do not currently have a theory for predicting the strength of this zonal circulation. The gradient wind balance shown in 3.6 is a diagnostic balance which does not illuminate how the atmosphere arrives in its final state. In other GCM studies of tidally-locked exoplanets (Komacek and Showman, 2016; Zhang and Showman, 2017), the RMS wind is linked to the advective, wave and radiative timescales. However, in these studies the wind speed also depends on an equilibrium temperature profile which is prescribed in the model. In our grey gas model, this equilibrium temperature profile is not known a priori which makes it difficult to produce similar scaling relations. We note that at

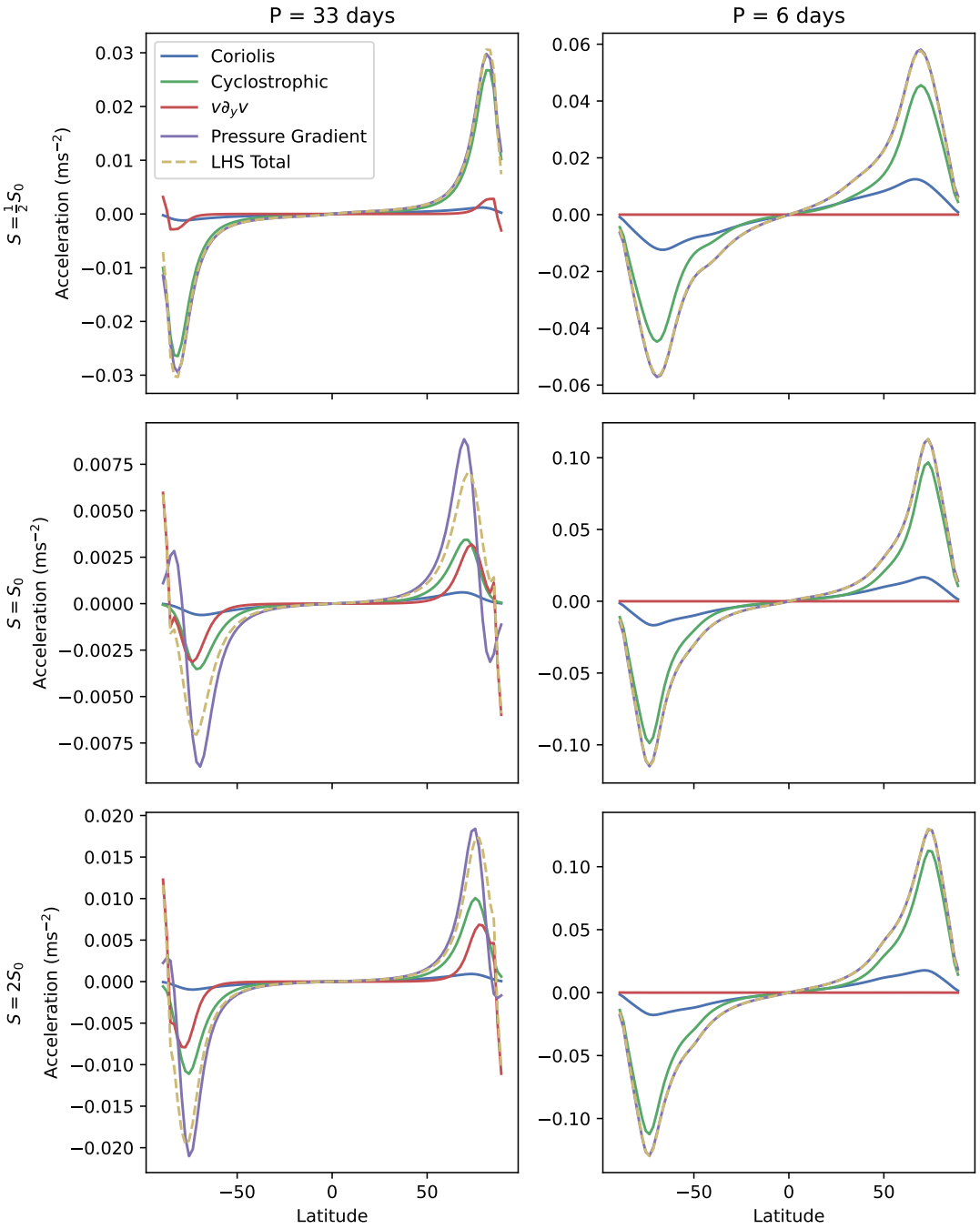

Figure 3.6: Meridional momentum balance for each of the dry simulations at the 10 mbar level. For the six-day period experiments (right-hand side), classical gradient-wind balance sustains the jets, whereas in the 33 day period experiments the non-linear advection term is also significant to the balance.

each rotation rate, the zonal jet strength is approximately the same at each instellation, but that it increases greatly with increasing rotation rate. An angular momentum con-

serving wind moving from the equator with $u = 0$ would have speed:

$$u_{\mathrm{AM}} = a\Omega \frac{\sin^2 \phi}{\cos \phi} \tag{3.17}$$

at latitude ϕ. For jets at $\phi = 75°$, this gives $u_{\mathrm{AM}} = 130$ m/s for the 33 day period case and $u_{\mathrm{AM}} = 730$ m/s for the 6 day period case, which is the correct order of magnitude for the results shown in Figure 3.5. However, we note that there is no requirement for the zonal wind speed to be 0 at the equator (as in a classical Hadley circulation) since there is no friction at the bottom of the model. We investigate the overturning circulation in the next section.

3.2.4 Overturning Circulation

To investigate the origin of the high-latitude zonal jets, we look at the mean meridional overturning circulation. In the conventional (λ, ϕ) coordinate system, the mass streamfunction is given by:

$$\psi_m(\phi, p) = \frac{2\pi a \cos \phi}{g} \int_0^p [v](\phi, p')\, \mathrm{d}p' , \tag{3.18}$$

which represents the meridional mass flux between the top of the atmosphere ($p = 0$) and a pressure level p. Figure 3.7 shows this mass streamfunction for the six experiments. The zonal-mean circulation follows contours of constant ψ_m, so positive (red) regions indicate clockwise circulation around contours, and (blue) regions anticlockwise circulation. In all six cases we see a net overturning circulation from equator to pole in both hemispheres. In the theory of non-synchronously rotating planets, having $\mathrm{Ro} \gg 1$ leads to a global Hadley-like circulation (e.g. Venus and Titan), which transports energy from the tropics to the poles to balance the gradient in stellar heating (Held and Hou, 1980; Vallis, 2017; Kaspi and Showman, 2015). This Hadley circulation also transports angular momentum from the equator polewards and spins up sub-tropical jets on Earth. Our experiments differ from the classical Held-Hou model in two main

ways: firstly, we do not have a drag layer at the bottom of the atmosphere which can inject angular momentum into the atmospheric flow by imposing a torque on westwards moving surface-flow. Secondly, the forcing in our model is non-axisymmetric and centred on the substellar point, meaning the main heating contrast is between substellar and antistellar points in contrast to between equator and pole in the original Held-Hou model.

Since there is no surface to inject angular momentum into our atmosphere, the positive angular momentum associated with jets in the upper atmosphere is balanced by a retrograde circulation in the lower atmosphere. Spinning up from rest, the radiative heating at the equator causes rising motion. Air moving polewards higher up in the atmosphere rotates in the prograde direction, conserving angular momentum, whereas the return flow will have retrograde motion in the absence of friction. How these two circulations interact is unclear and requires more study. As mentioned above, since u is not fixed at 0 at the equator, it is difficult to use this as a theory to predict the jet speed away from the equator. However, the qualitative picture of air from the equator moving polewards and accelerating the jets provides a rough order-of-magnitude estimate of the jet wind speeds.

Figure 3.8 shows the mass streamfunction of the control experiment during spin-up (averaged between 4000 and 5000 days). The overturning circulation that would spin up angular momentum conserving jets is clear on the left-hand panel. The picture in the upper atmosphere is similar except the magnitude of the streamfunction is lower, since similar meridional velocities in the upper atmosphere transport less mass.

In previous studies of tidally-locked planets, the zonal circulation has sometimes been split into a dayside Hadley circulation and a nightside anti-Hadley circulation (e.g. Charnay et al., 2015b) – however, this can obscure a more direct circulation between dayside and nightside (Hammond and Lewis, 2021). We therefore follow Hammond and Lewis (2021) in calculating the mass streamfunction in tidally-locked coordinates

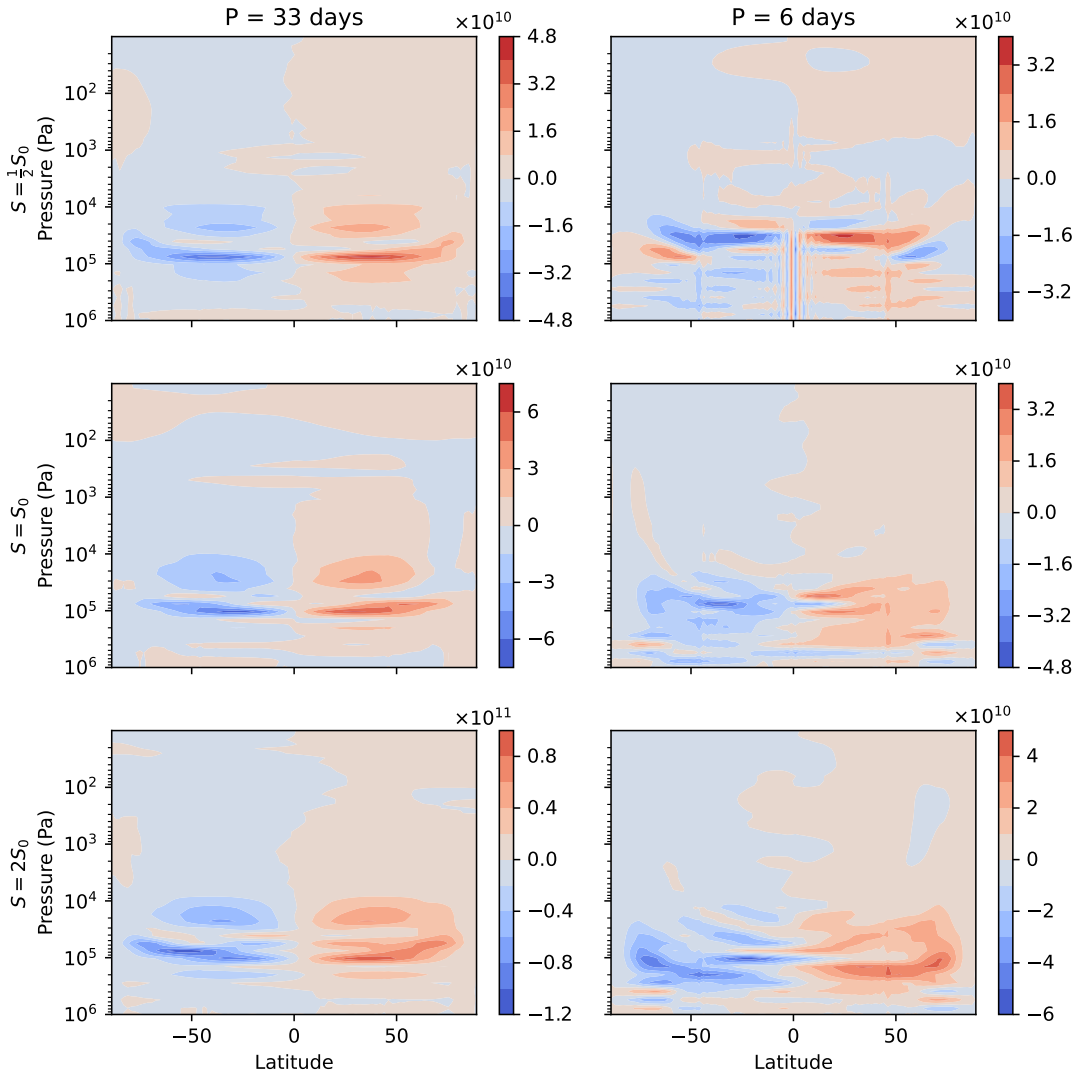

Figure 3.7: The meridional mass streamfunction for the six experiments (contours in units of kg/s). All the experiments show some form of net overturning from the equator to pole.

(Koll and Abbot, 2015). The tidally-locked latitude, ϕ_{TL}, is 0 degrees at the North and South poles, 90 degrees at the substellar point and -90 degrees at the antistellar point. The tidally locked longitude, λ_{TL}, is 0 on the semi-circle passing through the substellar point, North Pole and antistellar point and increases towards the Eastern terminator. In this coordinate system, one can define a streamfunction:

$$\psi_{TL} = \frac{2\pi a \cos\phi_{TL}}{g} \int_0^p [v_{TL}]_{TL}(\phi_{TL}, p')\, \mathrm{d}p\,, \tag{3.19}$$

where $[\cdot]_{TL}$ represents an average over λ_{TL}, and v_{TL} is the component of the wind in the

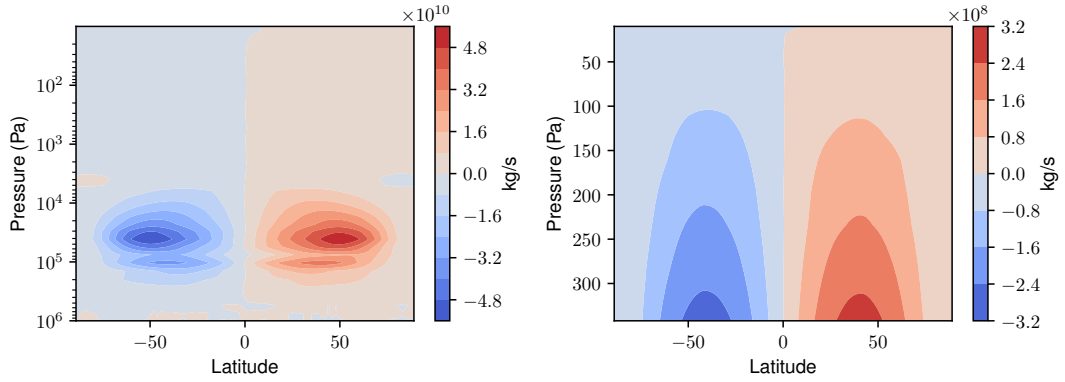

Figure 3.8: The mass streamfunction of the control experiment averaged between 4000 and 5000 days during spin-up. Left: A view of the the whole atmosphere with it's clear overturning circulation from equator to pole. Right: The upper atmosphere's streamfunction has similar structure (though is obscured on the left due to the magnitude), highlighting that the upper atmosphere is spun up via a similar mechanism.

direction of increasing ϕ_{TL} (and not just the conventional meridional wind in a different coordinate system). Figure 3.9 shows the streamfunction in this coordinate system. In all experiments, a direct day-night circulation is driven by radiative heating. In the six-day period experiments, there is also a small area of counter-circulation near the poles, where the jet region near the pole is associated with a downwelling region on the the dayside and upwelling on the nightside. One can also see, in all six cases, that the flow is partially splits into two sub-circulations, with a stronger one on the dayside and a weaker one on the nightside. Thinking in terms of the conventional mass streamfunction, this would explain why we see a circulation from equator to pole – because the "anti-Hadley" circulation on the nightside is weaker than the conventional Hadley-like circulation on the dayside (due to weaker radiative forcing on the nightside).

We note that this circulation is on average an order of magnitude larger than the overturning circulation in latitude-longitude coordinates, confirming that this is the dominant overturning circulation.

To better distinguish the overturning circulation from the zonal jet structure, we can decompose the horizontal winds into their divergent and rotational components

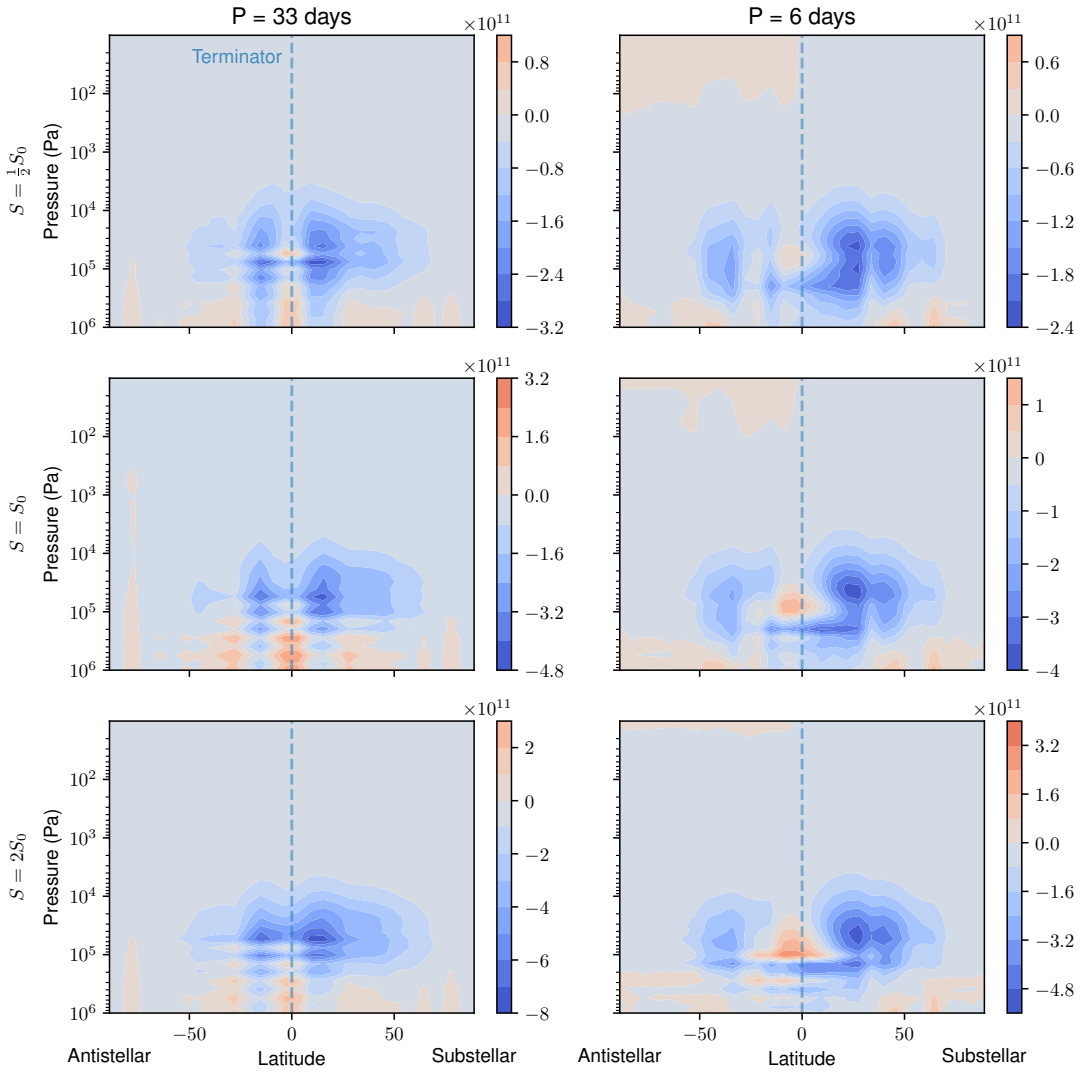

Figure 3.9: The tidally-locked mass streamfunction, ψ_{TL} (units kg/s). This shows more clearly the stronger overturning circulation between dayside and nightside (c.f. Figure 3.7)

(Hammond and Lewis, 2021):

$$\boldsymbol{u} = \boldsymbol{u}_{\mathrm{div}} + \boldsymbol{u}_{\mathrm{rot}}, \tag{3.20a}$$

$$\boldsymbol{u}_{\mathrm{rot}} = \boldsymbol{k} \times \nabla\psi, \tag{3.20b}$$

$$\boldsymbol{u}_{\mathrm{div}} = -\nabla\chi, \tag{3.20c}$$

where ψ is a streamfunction and χ is a velocity potential which can be calculated from the vorticity and divergence of the velocity respectively. Importantly, the meridional rotational velocity is given by $v_{\mathrm{rot}} = \partial_x\psi$, which vanishes when averaged in the longi-

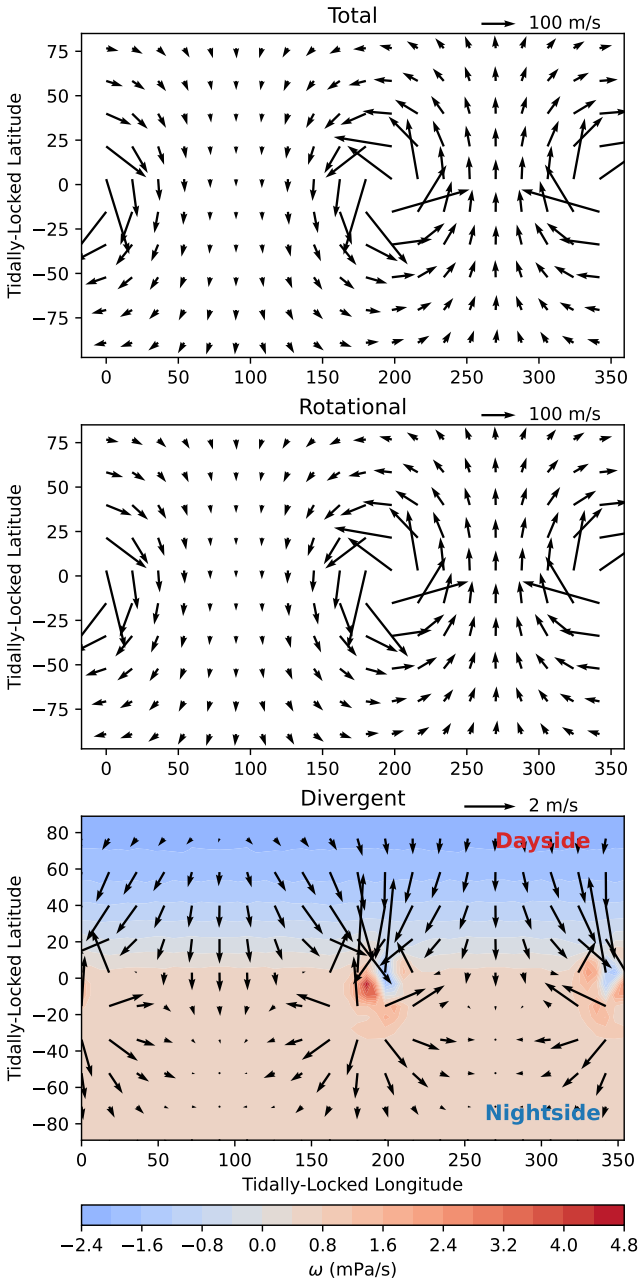

Figure 3.10: Total, rotational and divergent components of the wind field of the control experiment at 100 mbar. The rotational component of the wind dominates the circulation, but the small divergent component is responsible for the mass transport between dayside and nightside. The bottom plot also shows the pressure velocity, ω, which illustrates the upwelling on the dayside and downwelling on the nightside of the planet.

tudinal direction. Therefore, the mass streamfunction depends only on the divergent component of the velocity field. This is true in both conventional latitude-longitude and tidally-locked coordinate systems. Figure 3.10 shows the total, rotational and divergent

winds for the control experiment at 100 mbar, along with the pressure velocity. We find that the velocity is dominated by the rotational component with magnitude on the order of 100 m/s. However, the divergent component responsible for the overturning circulation, shown in the bottom of Figure 3.10, is predominantly directed from dayside to nightside.

We can estimate the dependence of the tidally-locked streamfunction on instellation using the steady-state equation for the transport of dry static energy, $s \equiv c_p T + \Phi$:

$$\nabla \cdot (s\boldsymbol{u}_{\mathrm{TL}}) = \dot{Q}, \tag{3.21}$$

where $\dot{Q}$ is the heating rate per unit mass. Taking the average over the tidally-locked longitude and integrating over $\mathrm{d}p/g$, we find:

$$\int_0^p \frac{\mathrm{d}p}{g} \frac{1}{a\cos\phi} \partial_\phi [v_{\mathrm{TL}} s \cos\phi] = [S - F], \tag{3.22}$$

where S is the pressure-integrated solar heating and F is the pressure-integrated outgoing flux. We now approximate this equation to find a scaling balance of terms by making a series of approximations. Firstly, we assume that the dry static energy and v_{TL} are uncorrelated in the zonal and vertical directions. We also assume that if the temperature gradients are weak enough, then $\Delta s/s \ll \Delta v/v$ such that:

$$\int_0^p \frac{\mathrm{d}p}{g} \frac{1}{a\cos\phi} \partial_\phi [v_{\mathrm{TL}} s \cos_\phi] \approx \langle [s] \rangle \int_0^p \frac{\mathrm{d}p}{g} \frac{1}{a\cos\phi} \partial_\phi ([v_{\mathrm{TL}}] \cos\phi), \tag{3.23}$$

where $\langle \cdot \rangle$ represents a column average. Note that the integral term in 3.23 is proportional to ω which is in term proportional to $\partial_\phi \psi_{\mathrm{TL}}$. To approximate $[S - F]$, we note that when $p \to p_s$, S becomes the incoming stellar radiation and F the OLR, which vary over the scale S_0 in the ϕ_{TL} direction. We approximate that this scaling holds at the level of the maximum streamfuncton too. Thus we get the scaling:

$$\psi_{\mathrm{TL}} \sim \frac{a^2 S_0}{\langle [s] \rangle}. \tag{3.24}$$

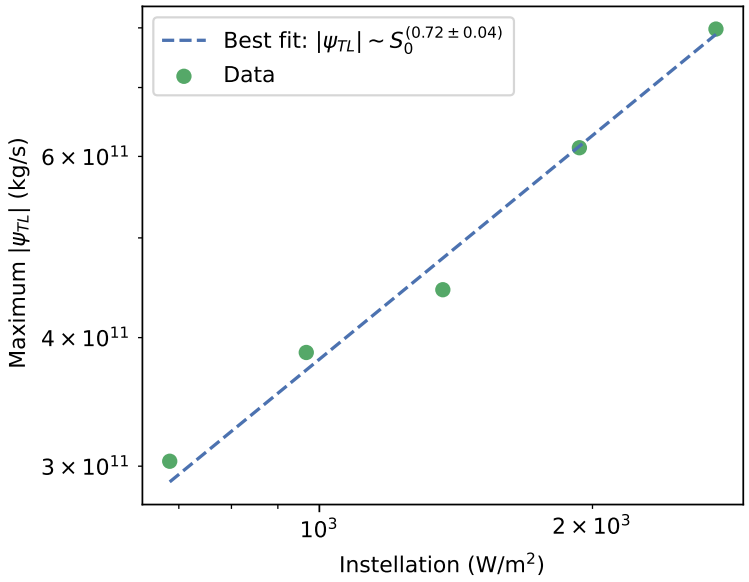

Figure 3.11: The maximum absolute value of the tidally-locked streamfunction as a function of instellation. The best fit power law to the data shows $\psi_{\mathrm{TL}} \sim S_{\mathrm{o}}^{0.72 \pm 0.04}$, which is in agreement with the theoretical exponent, 0.75.

The dry static energy, $s = c_p T + \Phi$, scales as $\max(c_p T, \Phi) \sim T \sim S_{\mathrm{o}}^{1/4}$ if we assume $\Phi \approx RT$ i.e. the region integrated over is roughly one scale height. This gives the final scaling $\psi_{\mathrm{TL}} \sim S_{\mathrm{o}}^{3/4}$. Note that there is no dependence on the rotation rate in this expression.

Figure 3.11 shows the maximum absolute value of the tidally-locked streamfunction from five experiments at different instellations. The best-fit power law relation has exponent 0.72 ± 0.04, which is in agreement with the theoretical prediction of $\frac{3}{4}$.

3.2.5 Equatorial Superrotation

In each of the experiments shown in Figure 3.5, there is equatorial superrotation. Figure 3.12 quantifies this in terms of the zonal mean local superrotation index, $\bar{s}$ (Read, 1986), where $\bar{s} > 0$ represents a region that is locally superrotating (i.e. has greater angular momentum than the bulk rotation of the planet at the equator). There are two main types of mechanism thought to drive superrotation in planetary atmospheres (Wang and Mitchell, 2014). The first is through generating eddies from non-axisymmetric forcing, e.g. via tidally-locked solar heating (Showman and Polvani, 2011; Tsai et al., 2014;

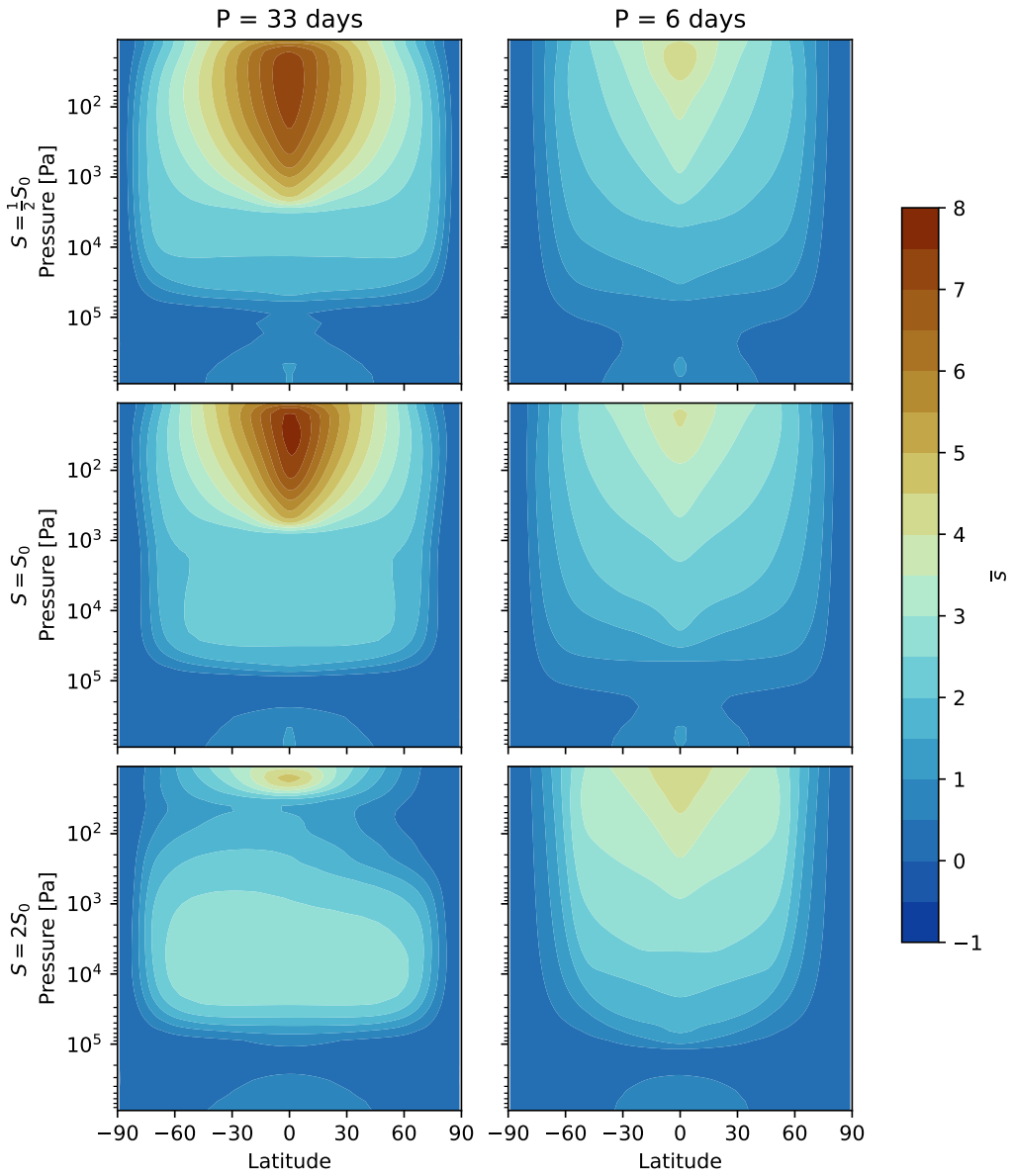

Figure 3.12: The zonally-averaged local superrotation index, $\bar{s}$ (defined in Equation 2.15), for each of the experiments. Positive values indicate local superrotation.

Hammond and Pierrehumbert, 2018), from convective heating (e.g. Lian and Showman, 2010; Liu and Schneider, 2011) or from tidal heating (Lebonnois et al., 2010; Horinouchi et al., 2020). The second is from shear instabilities in atmospheres with axisymmetric forcing (e.g. Iga and Matsuda, 2005), which is observed in idealized simulations of slow-rotating planets (Mitchell and Vallis, 2010) and proposed as a potential mechanism driving superrotation in Titan's atmosphere (Wang and Mitchell, 2014).

In our simulations, there are two distinct types of superrotation. During spin-up, there is superrotation at the equator at the pressure levels of radiative heating, which is likely due to the stationary wave response to the radiative forcing (see regions where $\bar{s} > 0$ at $\approx 10^4$ Pa in Figure 3.12). Since we are strongly in the weak temperature gradient regime (with a low mean molecular weight atmosphere and slow rotation rate), the Rossby radius of deformation is large, and there is only a weak excitation of equatorial Rossby and Kelvin waves required to drive superrotating jets, which are often seen in simulations of tidally-locked terrestrial exoplanets (e.g. Pierrehumbert and Hammond, 2019). This is most likely the reason we don't see an on-equator maximum of zonal wind in the lower atmosphere (at around $10^4 - 10^5$ Pa). In the stratosphere, however, we see a sudden transition to superrotation caused by an instability. All experiments show a maximum in $\bar{s}$ near the upper boundary of the model, which is particularly strong in the $S = \{\frac{1}{2}S_0, S_0\}$, $P = 33$ day experiments. Figure 3.13 shows the development of superrotation in the upper atmosphere over a period of ≈ 40 days, where momentum is transported from the high latitude jet towards the equator. We performed additional experiments to test whether the location of the upper boundary or the damping in the sponge layers affected the presence of the instability. The model top of a GCM provides a challenge, since often non-physical boundary conditions have to be specified to ease solving the governing equations numerically. In ExoFMS, there is an $\omega = 0$ boundary condition that keeps the model top fixed at a constant pressure. This can lead to the spurious reflection of waves from the model top which are removed by introducing some form of damping to the top model layers (known as a sponge layer). There are several forms of sponge layer (Jablonowski and Williamson, 2011) – our model gradually increases the divergence damping coefficient towards the model top as:

$$d_2 = d_{2,0}\left[1 - 3\tanh\left(\frac{1}{10}\log\left(\frac{p}{p_0}\right)\right)\right], \tag{3.25}$$

where $d_{2,0}$ is a constant coefficient, set to 0.02 in our simulations – large enough to

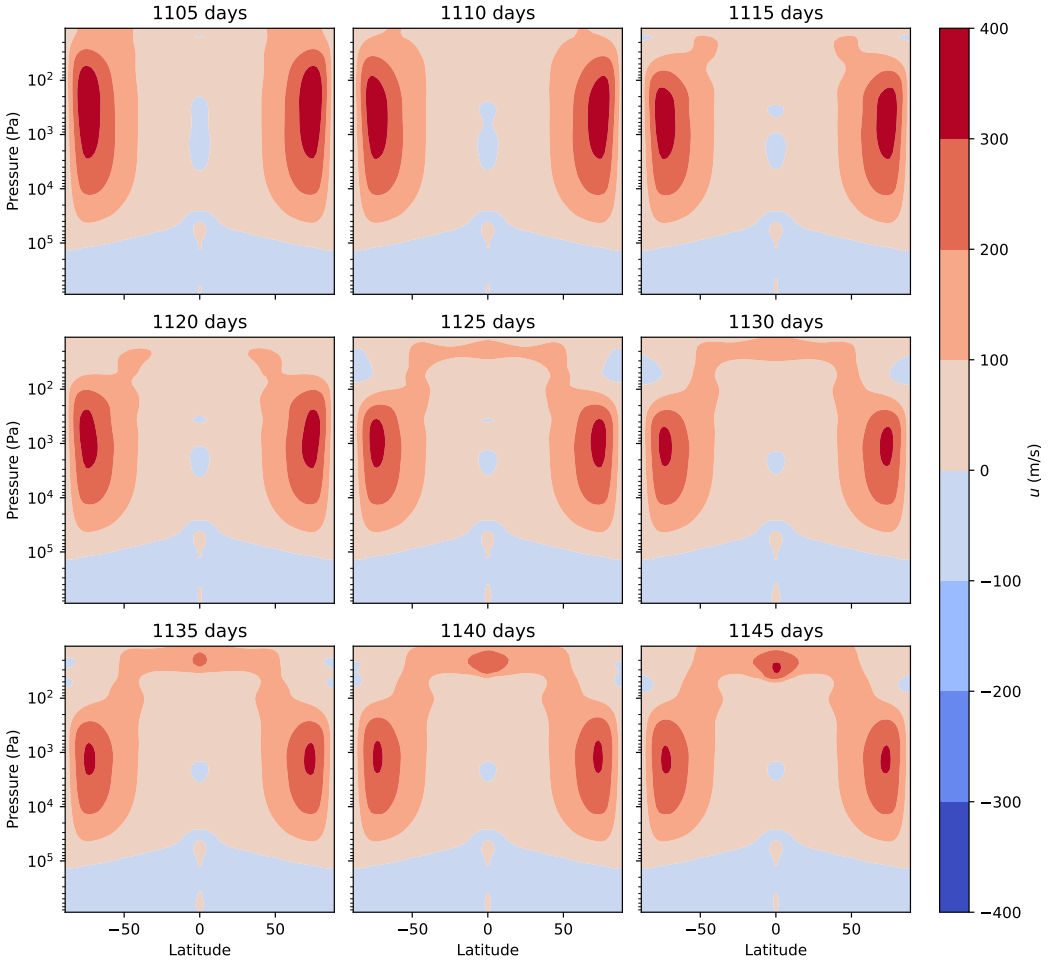

Figure 3.13: The zonal-mean zonal wind of the P6h run during the development of the transient instability causing superrotation. On the timescale of tens of days, momentum in the upper atmosphere is transferred from the poles to the equator.

maintain model stability but small enough not to affect the angular momentum budget of the atmosphere (Lee et al., 2021). In the top two layers, the value of $d_{2,0}$ is doubled, then quadrupled respectively to provide a stronger sponge layer damping.

To test the robustness of the superrotation, firstly we reduced the model-top pressure by a factor of 100, from 10 Pa to 0.1 Pa. We found that the instability still occurred, but at a lower pressure of around 2 Pa (c.f. 40 Pa in the 10 Pa model top simulations). In the 33 day period experiments, we noted that the onset of superrotation occurred at a much later time, usually around 10000-13000 days, around the time when the high-latitude zonal jets have extended to the top of the atmosphere. This, along with our

experiment changing the model top pressure, suggests that model-top effects could be playing a role in triggering the instability.

Secondly, we removed the pressure dependence of $d_{2,0}$ and set it to its minimal value. This had little effect on the outcome of the simulations, with the instability occurring at a similar pressure level and time as the control. This proves that the instability is not an artefact of the increase of divergence damping near the sponge layer.

Lastly, we increased the depth and strength of the sponge layer, such that the top five layers were sponge layers, and increased the damping divergence coefficient to 0.05. In this experiment, the instability still occurred, but the magnitude of the resulting equatorial zonal wind was reduced by around a factor of two.

Note that divergence damping is only one choice of sponge-layer mechanism. Another common choice is the presence of Rayleigh friction in the top layers. However, we did not use this because it is known to actively violate angular momentum conservation and have implications for the upper atmosphere (Shaw and Shepherd, 2007; Jablonowski and Williamson, 2011). We proceed with our analysis, noting that this feature of the circulation seems to be robust to changes in damping but not ruling out that the model top could affect the circulation.

If we look at the zonal-eddy height field, h^* as function of time at the 40 Pa level (Figure 3.14), we can see that there is a eastward travelling disturbance which couples the equatorial region to the vortices near the pole. We note that the pattern of disturbance looks similar to the eddy height fields seen in Mitchell and Vallis (2010) (Figure 14) and the pressure perturbation fields in Wang and Mitchell (2014) (Figures 1 and 2), suggesting that a Rossby-Kelvin (RK) instability may be responsible for the acceleration of the superrotation. The RK instability is caused by a coupling of equatorial Kelvin waves and high-latitude Rossby waves, and occurs in the regime where the Froude number of the flow (the ratio between the frequency of the Rossby and Kelvin waves) is between 1-3

(Wang and Mitchell, 2014). The Froude number is given by:

$$\mathrm{Fr} = \frac{U_o / \cos(\phi_{\max})}{U_{\mathrm{eq}} + NH/m}, \tag{3.26}$$

where U_o is the high-latitude jet speed at latitude $\phi_{\max}$, U_{eq} is the equatorial wind speed, N is the buoyancy frequency, H the scale-height of the disturbance and m the vertical wavenumber (i.e. $m = 1$ represents the gravest baroclinic mode of disturbance). Since the disturbance occurs in the stratosphere of our model where the grey-gas equilibrium temperature is constant, we can approximate $NH \approx \sqrt{RT_s}$ where T_s is the skin temperature of the atmosphere. Neglecting the equatorial wind speed during instability, we can approximate Fr using $U_o \approx 400\,\mathrm{ms}^{-1}$, $\phi_{\max} \approx 75°$ and $T_s \approx 230\,\mathrm{K}$ which gives a Froude number of ≈ 1.6, placing the atmosphere in the correct parameter regime for the RK instability to take place.

Figure 3.15 shows the Hovmöller diagram of the zonal-eddy height field. There is a clear Eastwards travelling wave pattern in the horizontal equatorial structure with constant phase velocity. In the high-latitude regions, this structure remains but with an added beating in the pattern. Performing a Fourier transform in both time and space, we can extract the phase speed of the eastward travelling component, and find it to be around $330\,\mathrm{ms}^{-1}$ at the equator, comparable to the speed of the high-latitude jets and to a characteristic Kelvin wave timescale, which is on the order of hundreds of ms^{-1}. Performing this Fourier transform on the high-latitude data also confirms that the beating pattern in the high-latitude data is at 0 frequency, and represents the zonal wavenumber 1 time-mean background in the height field. The vertical structure of the wave-pattern is more complicated, but somewhat resembles a standing wave structure near the equator, suggesting the instability could be barotropic in nature.

Lastly, we can show that this wave structure directly leads to the acceleration of zonal wind at the momentum. If we decompose the zonal-mean zonal wind equation

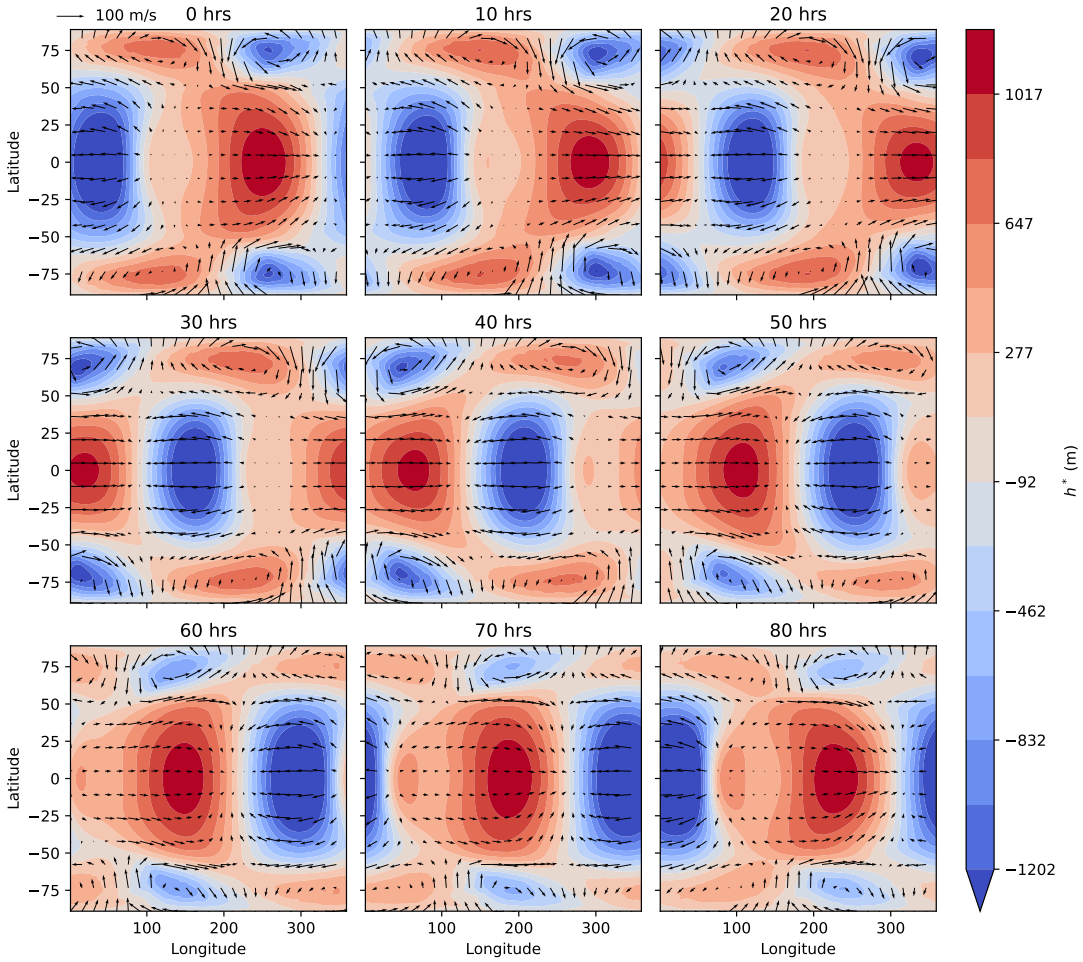

Figure 3.14: The zonal-eddy height field, h^*, at the 40 Pa level across an 80 hour period of time during which the instability is forming. The arrows represent the zonal-eddy wind field. There is an eastward travelling wave-like disturbance with zonal wavenumber 1.

into mean, zonal-eddy and time-eddy components, we get:

$$\frac{\partial[\bar{u}]}{\partial t} = -\frac{1}{a\cos^2\phi}\partial_\phi\Big\{\Big(\underbrace{[\bar{u}][\bar{v}]}_{\substack{\text{mean}\\\text{flow}}} + \underbrace{[\bar{u}^*\bar{v}^*]}_{\substack{\text{stationary}\\\text{eddies}}} + \underbrace{[\overline{u'v'}]}_{\substack{\text{transient}\\\text{eddies}}}\Big)\cos^2\phi\Big\} \tag{3.27}$$

$$+ \omega \text{ terms, Coriolis terms etc.,}$$

where overlined and bracketed terms represent time and zonal means respectively, and starred and dashed terms represent deviations from time and zonal means respectively. This equation represents the meridional flux of momentum due to the mean flow, stationary eddies and transient eddies on the mean jet speed. Figure 3.16 shows the three horizontal terms in equation 3.27 as a function of latitude (vertical terms are negligible

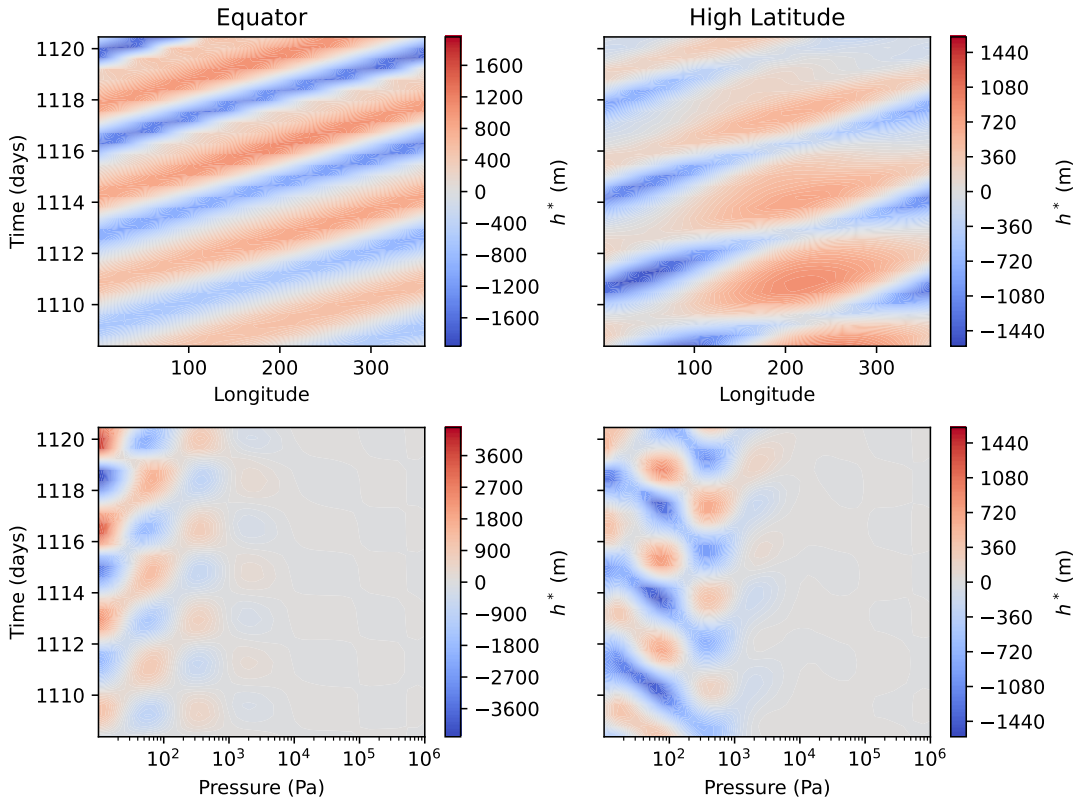

Figure 3.15: Hovmöller diagrams of the zonal-eddy height field, h^*, averaged over the equatorial region (left column) and high-latitude regions (i.e. 50-80 degrees, right column). Top row: There is a clear zonal wavenumber 1 wave in the height field propagating eastwards. This structure is also clear at high latitudes, however there is also some beating in the response. Bottom row: The vertical structure of the waves at the equator suggests standing waves, however the vertical structure at high-latitudes is more complicated.

in comparison). One can see that the mean flow acts to transport momentum away from the equator (positive gradient), whereas both the stationary and transient eddies pump momentum towards the equator, with the eddy accelerations dominating helping to accelerate the equatorial jet at this level.

3.2.6 Transformed Eulerian Mean Circulation

Understanding the zonal mean circulation of the Earth's mid-latitudes can be clarified by using the Transformed Eulerian Mean (TEM) view of the circulation (Andrews and McIntyre, 1976). Consider the thermodynamic equation decomposed into mean and

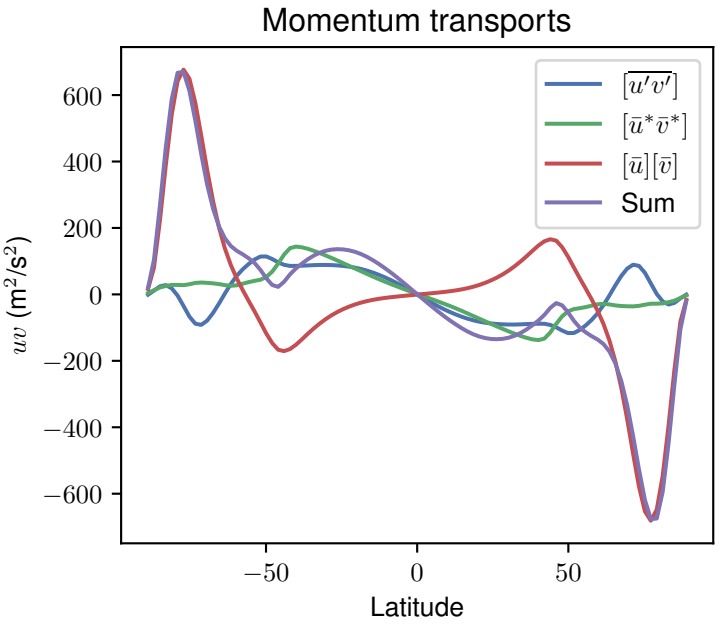

Figure 3.16: Terms in equation 3.27 at the 40 Pa level. A negative gradient at the equator represents a convergence of eastwards momentum, causing an acceleration of the mean flow.

eddy components:

$$\frac{\partial[\theta]}{\partial t} + \frac{[v]}{a}\frac{\partial[\theta]}{\partial \phi} + [\omega]\frac{\partial[\theta]}{\partial p} = -\frac{1}{a\cos\phi}\frac{\partial[\theta^* v^* \cos\phi]}{\partial \phi} - \frac{\partial[\theta^*\omega^*]}{\partial p} + [S] \tag{3.28}$$

where $[S]$ represents the zonal-mean diabatic source terms. In the Earth's mid-latitudes, where the quasi-geostrophic approximation holds, the dominant balance in the time mean circulation is between $[\omega]\,\partial[\theta]/\partial p$ (adiabatic cooling) and $-\,\partial[\theta^* v^* \cos\phi]/\partial\phi$ (horizontal eddy heat fluxes). This can obscure the effect of diabatic heating, S, which is often a small residual term even though it drives the circulation and the eddies. To solve this problem, one can define a non-divergent residual mean circulation, consisting of a residual meridional velocity (v_{res}), pressure velocity (ω_{res}) and streamfunction (ψ_{res}):

$$v_{\text{res}} \equiv [v] - \frac{\partial}{\partial p}\left(\frac{[\theta^* v^*]}{\partial[\theta]/\partial p}\right) \tag{3.29}$$

$$\omega_{\text{res}} \equiv [\omega] + \frac{1}{a\cos\phi}\frac{\partial}{\partial y}\left(\frac{[\theta^* v^*]\cos\phi}{\partial[\theta]/\partial p}\right) \tag{3.30}$$

$$\psi_{\text{res}} = \frac{2\pi a\cos\phi}{g}\int_0^p v_{\text{res}}\mathrm{d}p \tag{3.31}$$

$$\frac{1}{a\cos\phi}\frac{\partial(v_{\text{res}}\cos\phi)}{\partial\phi} + \frac{\partial\omega_{\text{res}}}{\partial p} = 0 \tag{3.32}$$

This residual more directly represents the effects of the diabatic heating, $[S]$, on the zonal circulation. In the quasi-geostrophic limit, rewriting the equations in terms of the residual variables removes explicit eddy terms from the thermodynamic equation. All the eddy terms end up as forcing terms in the zonal momentum equation and can be represented as the divergence of the Eliassen-Palm (EP) flux (Vallis, 2017). In pressure coordinates, the momentum equation can be written as:

$$\frac{\partial[u]}{\partial t} + \frac{v_{\text{res}}}{a}\frac{\partial[u]}{\partial\phi} + \omega_{\text{res}}\frac{\partial[u]}{\partial p} - \frac{[u]v_{\text{res}}\tan\phi}{a} = \frac{1}{a\cos\phi}\nabla\cdot\boldsymbol{F} + \text{Dissipation} \tag{3.33}$$

where $\boldsymbol{F}$ is the EP flux, given by:

$$F_\phi = a\cos\phi\left(\chi\frac{\partial[u]}{\partial p} - [u^* v^*]\right) \tag{3.34}$$

$$F_p = a\cos\phi\left(\left\{f - \frac{[u]\cos\phi}{a\cos\phi}\right\}\chi - [\omega^* u^*]\right) \tag{3.35}$$

$$\chi \equiv \frac{[\theta^* v^*]}{\partial[\theta]/\partial p} \tag{3.36}$$

Firstly, we can use the TEM formalism to look at the residual streamfunction, to see if there is significant compensation between eddy heat fluxes and the mean flow. Figure 3.17 shows the conventional and residual streamfunctions. One can see that the residual streamfunction differs little from the Eulerian streamfunction except at around 0.1 to 1 bar near the poles, where the eddy heat fluxes are strongest. The order of magnitudes of the horizontal eddy heat fluxes, adiabatic cooling and the diabatic heating were inspected. It was found that the diabatic heating was never negligible compared

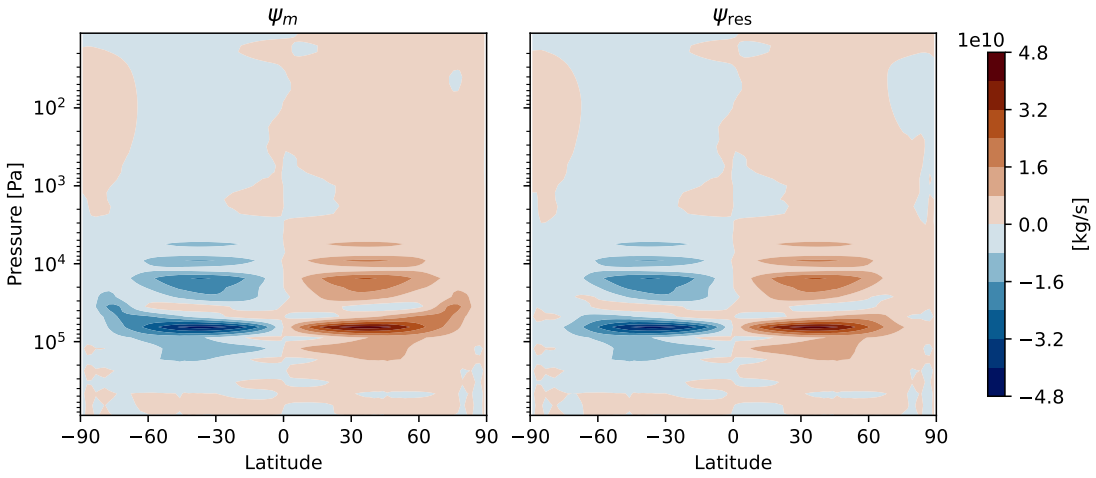

Figure 3.17: Left: The conventional meridional mass streamfunction. Right: The Transformed Eulerian Mean residual mass streamfunction. Both streamfunctions were calculated from the PKc experiment data.

to the eddy or adiabatic cooling, with the eddy heat fluxes being negligible everywhere other than at latitudes polewards of 70°, and stronger at low pressures (below 10^3 Pa). For these reasons the overturning circulation (which is strongest at around 1 bar) does not change significantly in the TEM picture. We can also inspect the EP flux during the acceleration of the low pressure equatorial jet discussed in the previous section. Figure 3.18 shows the EP flux (quivers) and its divergence (contours) for the P6h experiment during the spin up of the low pressure jet. One can clearly see divergence in the EP flux, centred on the equator near 30 Pa. This divergence is associated with an acceleration of the mean flow due to eddies. The TEM form of the primitive equations gives a cleaner view of the acceleration driven by eddies than the standard Eulerian framework pictured in Figure 3.16. This is because in the quasi-geostrophic limit if waves are linear, steady-state and conservative, it can be shown $\nabla \cdot \boldsymbol{F} = 0$ and there can be no acceleration of the mean flow. In this case, the eddy momentum flux $[u^* v^*]$ can induce a compensating mean overturning flow (as seen in Figure 3.16 where the mean and eddy fluxes are often of similar magnitude and opposite sign). In the TEM picture, however, the EP flux directly represents the accelerating effect of eddies on the zonal winds.

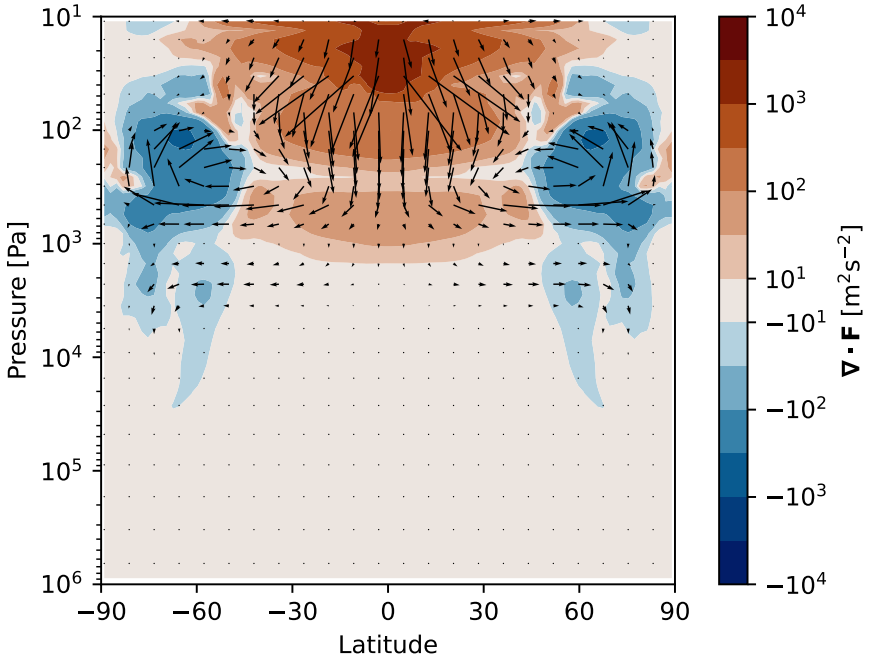

Figure 3.18: The Eliassen-Palm flux and its divergence, time-averaged between 1125 and 1145 days, in the P6h experiment studied previously in Figures 3.13 to 3.16. Quivers show the EP flux, and the contours the divergence. The ϕ and p components of the flux have been scaled by $(\pi a)^{-1}$ and $(p \log(p_t/p_b))^{-1}$ respectively, where p_t = 10 Pa and $p_b = 10^6$ Pa, following Jucker (2021).

3.3 Discussion

3.3.1 Comparison to other studies

We now compare our findings to other similar studies. The only other GCM study of K2-18 b (Charnay et al., 2021) (from now on referred to as C21), found a weak equatorial jet (speed around 50 m/s) at the 0.1-1 bar level and no high-latitude prograde jets for their solar metallicity runs (which are most comparable to the PKc experiment). The atmosphere was dominated by the overturning circulation from day to night. This is in marked contrast to our simulations, where the strongest jets were high-latitude and the overturning day-night circulation, although being the dominant overturning circulation, was small in comparison to the rotational circulation. We find that the magnitude of equatorial jet speed at the level of heating (around 0.1 to 1 bar) in our PKc run (≈

40 m/s) to be similar to the ≈ 50 m/s strength equatorial jet in C21. A significant difference in the model of C21 is their inclusion of real-gas radiation, in comparison to our grey-gas scheme. This leads to a cooler troposphere in their model, along with larger vertical temperature gradients. One way this could influence the dynamics is in the setting of the equatorial Rossby radius, which in dimensionless form (normalised by planetary radius) is:

$$\mathcal{L} = \sqrt{\frac{NH}{2\Omega a}}, \tag{3.37}$$

where $N \equiv \sqrt{g/T(g/c_p + \mathrm{d}T/\mathrm{d}z)}$ is the buoyancy frequency and H the atmospheric scale height. We find that between 0.1-1 bars, C21 has vertical temperature gradients closer to adiabatic, leading to our value of N being approximately 3 times larger than theirs, with relatively good agreement higher in the atmosphere. With a smaller L_R, Rossby waves are trapped closer to the equatorial region and we would expect a stronger stationary wave response, and perhaps a stronger jet. However, given the qualitative similarity between past studies using grey-gas and real-gas radiation (e.g. Lee et al., 2021; Komacek and Abbot, 2019; Kaspi and Showman, 2015), it would be surprising if the different radiation schemes accounted for all of the difference between the models. Other factors that could explain the disparity in wind structure include the type and strength of numerical damping schemes used and the type of dynamical core. ExoFMS uses a cubed-sphere grid, whereas the LMD generic GCM used in C21 uses a latitude-longitude, which could produce variation between the models in the polar region where the latitude-longitude grid contains a singularity. The presence of high-latitude jets should be a robust result of transporting angular momentum from equator to poles, and our model should in theory produce less distortion at the poles due to the lack of coordinate singularity.

On a qualitative level, our results look most similar to previous studies of sub-Neptune GJ 1214 b with solar metallicity, such as those found in Kataria et al. (2014) and Drummond et al. (2018), who find high-latitude jets and also superrotation near

the top of the atmosphere. Our results also look qualitatively similar to those in Wang and Wordsworth (2020) at earlier model times (around 1000-2000 days), in which two distinct high-latitude jets form. However, in Wang and Wordsworth (2020) the jets collapse into one wide equatorial jet as the kinetic energy converges to equilibrium, which is not seen in our model. We note that although GJ 1214 b is similar in radius to K2-18 b, it has a rotation period of 1.58 days (Berta et al., 2011) so we would expect much more pronounced equatorial dynamics and a stronger stationary wave acceleration of the equatorial jet. The greater instellation (23 600 Wm^{-2} Wang and Wordsworth, 2020) has a much smaller effect on the WTG parameter (which goes as $T^{1/2} \sim S_0^{1/8}$) but will affect the dynamics via the radiative timescale, which will be much shorter and therefore pronounce day-night temperature contrasts (Zhang and Showman, 2017). Estimating the WTG parameter,$\Lambda = c_0/(\Omega a) \approx \sqrt{RT}/(\Omega a)$ (the last assumption being valid if we assume the dynamics occurs on a height scale smaller than the atmospheric scale height) for GJ 1214 b using values found in Wang and Wordsworth (2020), we find $\Lambda = 1.8$ for solar metallicity. Thus under the assumption of a low mean molecular weight atmosphere, we might expect GJ 1214 b to be in a qualitatively similar dynamical regime to K2-18 b.

3.3.2 Scaling Λ for general sub-Neptunes

We now consider how the WTG parameter depends on stellar and planetary parameters, to see if we can expect most temperate sub-Neptunes to have $\Lambda \gg 1$. If we use the equilibrium temperature $T_{eq} \sim (S_0/\sigma)^{1/4}$ in estimating Λ, we note:

$$S_0 = \frac{F}{4\pi d^2}, \tag{3.38}$$

where F is the stellar luminosity and d is the planet's orbital distance. Using Kepler's third law (note for a tidally-locked planet the orbital frequency is equal to the planet's

rotation frequency):

$$d^2 = \left(\frac{GM_s}{\Omega^2}\right)^{\frac{2}{3}}, \tag{3.39}$$

where M_s is the stellar mass, we find:

$$S_0 = \frac{F}{4\pi G^{\frac{2}{3}}} M_s^{-\frac{2}{3}} \Omega^{\frac{4}{3}}. \tag{3.40}$$

If we assume $\Lambda = \sqrt{RT}/(\Omega a)$ this leads to an approximate scaling:

$$\Lambda \sim R^{\frac{1}{2}} F^{\frac{1}{8}} M_s^{-\frac{1}{12}} \Omega^{-\frac{5}{6}} a^{-1}. \tag{3.41}$$

We note that for M-type stars, F varies from around $3 \times 10^{-4} L_\odot$ to 0.069 $L_\odot$ (making $(F_{\max}/F_{\min})^{1/8} \approx 2$), and M_s varies from 0.08 to 0.57 $M_\odot$ (making $(M_{s,\max}/M_{s,\min})^{1/12} \approx 1.2$) (Pecaut and Mamajek, 2013). If we restrict our focus to sub-Neptunes, a varies from around 2 to 4 $R_\oplus$, i.e. by a factor of two. Therefore, we expect that Λ varies mostly due to the global rotation rate Ω, and the composition ($R \propto \mu^{-1}$), since $M_s^{-1/12}$ and $F^{1/8}$ do not vary significantly across the range of M-dwarf stars and a^{-1} does not vary significantly for sub-Neptunes.

Figure 3.19(a) shows Λ for all discovered sub-Neptune exoplanets with orbital period less than 100 days, assuming tidal-locking[1]. We plot Λ for low-metallicity ($\mu = 2.2$) and high-metallicity ($\mu = 10$) atmospheres, and find that in both cases $\Lambda \gg 1$ for the majority of sub-Neptunes. The best fit power law to the data also shows $\Lambda \sim P^{0.83 \pm 0.01}$, which is in agreement with equation 3.41, and confirms the analysis that other parameters such as stellar mass and flux do not vary greatly over the range of sub-Neptune exoplanets.

We stress that having $\Lambda > 1$ does not imply that all the planets in Figure 3.19(a) will exhibit weak horizontal temperature gradients. As discussed in Komacek and Showman (2016), Zhang and Showman (2017) and section 3.2.2, temperature gradients also depend on the radiative timescale. Since $\tau_r \propto T^{-3} p(\tau = 1)$, planets with high equilibrium

[1]Data from the Nasa Exoplanet Archive, `https://exoplanetarchive.ipac.caltech.edu`, accessed Friday 10th September, 2021

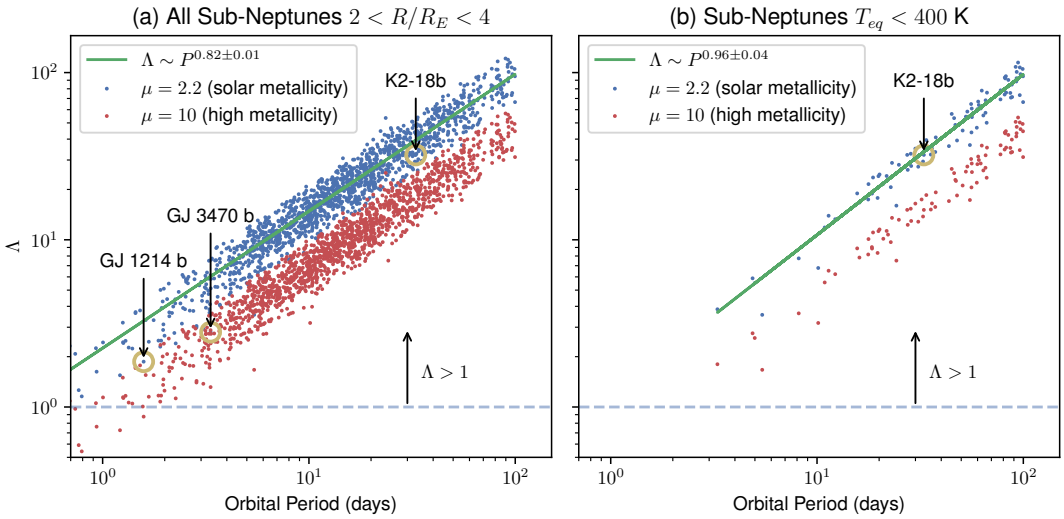

Figure 3.19: The weak temperature gradient parameter for observed sub-Neptunes with orbital period < 100 days, assuming tidal-locking. The blue data series assumes a mean-molecular weight of 2.2 (c.f. this study), whereas the red series has $\mu = 10$ to represent a higher metallicity atmosphere. (a) For all sub-Neptunes, we have $\Lambda > 1$ in the majority of cases, and that the scaling $\Lambda \sim P^{0.83} \approx P^{5/6}$ is in agreement with equation 3.41, confirming that parameters a, $M_s^{1/12}$ and $F^{1/8}$ do not vary greatly over the range of sub-Neptunes. We also highlight the value of Λ for three example sub-Neptunes (assuming $\mu = 2.2$). (b) Same as (a), but filtered for $T_{eq} < 400$ K. Here $\Lambda > 1$ for all cases, but the scaling for Λ is less accurate suggesting other parameters require scaling for.

temperatures can have very short radiative timescales and will therefore exhibit strong day-night temperature contrasts. In addition, high-metallicity atmospheres where the level of radiative cooling, $p(\tau = 1)$, is high in the atmosphere due to increased long-wave opacity, will also have short radiative timescales. In Figure 3.19(b), we plot sub-Neptunes for which the equilibrium temperature, T_{eq}, is less than 400 K. Here $\Lambda > 1$ always, and since T is lower we can be more confident these sub-Neptune atmospheres will have long radiative timescales similar to those in this study and exhibit similar dynamics to our simulated atmospheres. In addition, this analysis holds only if we can assume tidal-locking. For planets with rotation rates on the order of $\approx$ 100 days, the tidal-locking time will likely exceed the system lifetime (Barnes, 2017). If a sub-Neptune is not tidally-locked, its rotation rate, Ω, would be unconstrained and could be much greater than the rate implied by a 1:1 spin-orbit resonance.

3.3.3 1D vs 3D Modelling

The weak horizontal temperature gradients exhibited by the model is an important result, since it validates the use of 1D models in the study of sub-Neptune atmospheres (e.g. Madhusudhan et al., 2020; Blain et al., 2021), which are likely to be accurate so long as they don't require horizontal or vertical wind structures to be accurate (since these quantities are *not* horizontally uniform).

However, understanding the 3D structure of these atmospheres is important for some contexts. For example, estimates of the "K_{zz}" parameter in 1D chemistry models often rely on having information on the characteristic vertical velocities in an atmosphere (Zhang and Showman, 2018). Since the vertical velocities in a GCM are controlled by the divergent circulation, scalings like equation 3.24 which link the divergent circulation to planetary parameters could be useful in estimating such quantities. Moreover, transport processes important in moving around chemical tracers and cloud particles are inherently 3D processes and so may not be amenable to simple 1D modelling.

3.3.4 Model Limitations and Future Work

The grey gas radiation used in our model is a crude approximation of the full radiative transfer calculation. As discussed in the introduction, we underestimate the temperature of the deep atmosphere by around 100 K compared to real-gas 1D simulations. Moreover, grey gas atmospheres have a tendency to be sub-adiabatic throughout the atmosphere, underestimating the value of the vertical temperature lapse-rate. This is the same effect that led to our overestimation of N compared to (Charnay et al., 2021), though we note that in C21 the temperature profile is close to adiabatic in a very limited section of the atmosphere. However, the grey-gas scheme produces qualitatively similar temperature profiles to the real-gas models and should be valid for looking at global-scale circulations. Moreover, the grey-gas scheme is much less prohibitive in terms of

its computational speed compared to using real-gas radiation, and allows us to run several comparative models of sub-Neptune atmospheres out to tens of thousands of Earth days.

In this study we have examined the dry dynamics of the atmosphere to highlight the basic dynamical behaviour. The tentative detection of water vapour in the atmosphere of K2-18 b (Benneke et al., 2019a) and subsequent modelling (Blain et al., 2021; Charnay et al., 2021) have shown that there are circumstances under which water can condense in the atmospheres of sub-Neptunes. In Chapter 6 we extend this work to include the effects of moisture.

We would also encourage an inter-comparison similar to the TRAPPIST Habitable Atmosphere Intercomparison (THAI) project (Fauchez et al., 2021) to look at the differences between GCMs when modelling a fiducial sub-Neptune exoplanet. The difference between seemingly similarly set-up GCM experiments (e.g. between ours and Charnay et al. (2021)) suggests that further collaboration is required to illuminate the differences caused by different dynamical cores, physical parametrisations and damping schemes. A good starting point would be an intercomparison between grey models to highlight dynamics – efforts to this effect are currently underway (Christie et al., 2022)

Lastly, more work could be done on the instability found in the upper atmosphere to fully diagnose its origin and effect on the atmosphere, perhaps in the form of simplified models.

3.4 Conclusions

In this chapter I have presented a suite of GCM simulations aimed at modelling temperate sub-Neptune planets, using K2-18 b as the control experiment. Overall these atmospheres exhibit weak horizontal temperature gradients. I found that these atmospheres are dominated by high-latitude cyclostrophic jets, with weak equatorial superrotation

in the lower atmosphere and strong, instability-driven equatorial jets in the upper atmosphere. I confirmed the result of Wang and Wordsworth (2020), finding that the model runs have convergence times on the order of tens of thousands of days, increasing with slower rotation rate and lower instellation. I found that the high-latitude jets are cyclostrophically balanced in the fast-rotating experiment, with non-linear advective terms providing a significant proportion of the balance in the slower-rotating, hotter experiments. Using the framework of Hammond and Lewis (2021), I decomposed the circulation into divergent and rotational components in tidally-locked coordinates, and found that although the dominant flow was rotational, the overturning circulation was dominated by a day-night circulation responsible for redistributing the energy deposited by instellation from dayside to nightside. I provided a scaling argument for how the strength of this circulation varies with instellation, finding that the tidally-locked streamfunction should scale as $S_o^{3/4}$.

In all experiments, equatorial superrotation was observed in the upper stratosphere of the model, driven by an instability similar in structure to the one modelled in Wang and Mitchell (2014) to explain superrotation in slow, non-synchronously rotating planets such as Venus and Titan. I showed that this instability occurred in the correct parameter regime as in Wang and Mitchell (2014), and that it provided eddy-momentum fluxes which could transport zonal momentum from the high-latitude jets towards the equator.

Finally, I compared my results to the literature, finding the results differ qualitatively to Charnay et al. (2021), who model K2-18 b using the LMD Generic GCM. I offered some reasons why the model could produce different findings, but ultimately recommend some form of intercomparison between GCM models to illuminate the effects of different physical parametrisations and dynamical cores on the atmospheres of sub-Neptunes.

Chapter 4

An Introduction to the Runaway Greenhouse Effect

The runaway greenhouse effect is a positive warming feedback that causes planetary atmospheres absorbing too much stellar radiation to heat up significantly. In this section of the thesis, I will introduce the runaway greenhouse effect, explain its relevance to planetary habitability and outline how I will study it in relation to hydrogen-dominated sub-Neptunes (or "Hycean worlds").

In Section 4.1 I will provide a short introduction to the runaway greenhouse effect and how it controls the inner edge of the habitable zone. In Sections 4.2 and 4.3 I will summarise early attempts to understand the runaway greenhouse effect with simple 1D models of planetary atmospheres. In Section 4.4 I will outline an analytic method of calculating the maximum cooling of a greenhouse climate, which will prove useful in Chapter 5. Lastly, in Section 4.5 I will explain why conventional models of the runaway greenhouse effect may not apply to Hycean worlds, motivating the calculations of the inner edge of the sub-Neptune habitable zone in Chapter 5.

4.1 Background

The runaway greenhouse effect refers to the positive feedback loop whereby the increasing water vapour content of a planet's atmosphere increases its warming, which in turn enhances the water vapour content of the atmosphere. The effect was first studied in relation to Venus's atmosphere. Observations show that Venus has an enhanced abundance of Deuterium (Donahue et al., 1982), which has been interpreted as evidence of a past water-rich atmosphere (McElroy et al., 1982). The runaway greenhouse effect provides a mechanism by which a water-rich Venus could have lost an Earth-like initial water inventory. If the average instellation absorbed by a planet exceeds the maximum radiation a planet can emit to space, the atmosphere warms and the stratospheric water vapour abundance increases. For Earth-like planets with a surface temperature exceeding 320 K, the stratospheric water vapour becomes a major component of the atmosphere (with a mixing ratio > 0.001) (Kasting, 1988). The rate of photodissociation of water by EUV and XUV photons increases, and hydrodynamic escape of the resulting hydrogen becomes non-negligible, resulting in the loss of the planet's water inventory over geological timescales.

In simplified models of the runaway greenhouse, the inability of the planet to cool remains fixed as the planet heats, and the atmosphere can never regain equilibrium. In reality, there are mechanisms which allow the planet to increase its OLR and exit the runaway state. Firstly, as the planet heats, the peak of its thermal emission moves to shorter wavelengths (by Wien's displacement law). In a non-grey model, the absorption cross-section of water vapour decreases with decreasing wavelength, allowing the planet to increase its OLR (especially in the "window" regions of water's spectrum where the absorption coefficient is lowest). Secondly, for a planet with a fixed water inventory, the lower atmosphere can end up under-saturated as the planet heats and remains on a dry adiabat. At high enough temperatures, the OLR becomes dominated by emission from

the dry regions of the atmosphere, bypassing the water-vapour feedback and increasing the planet's OLR (Boukrouche et al., 2021). These mechanisms become important at temperatures above 1400 K and are therefore crucial in understanding the evolution of hot, rocky planets with magma oceans (Lichtenberg et al., 2021)

The runaway greenhouse effect is proposed as the main limiting factor setting the inner-edge of an Earth-like planet's habitable zone (Kasting et al., 1993; Kopparapu, 2013). Calculating the limiting OLR of the planet's atmosphere is therefore crucial in the search for extraterrestrial life and target selection for the next generation of space telescopes set to hunt for Earth-sized planets, e.g., *PLATO* and *HabEx* (Rauer et al., 2014; Gaudi et al., 2018). Cloud-free 1D models suggest the inner edge of the habitable zone for a sun-like star could be as high as 0.99 AU (Kopparapu, 2013). However, the strict upper limit on OLR imposed by 1D models is relaxed when hot, Earth-like climates are simulated using general circulation models (e.g., Leconte et al., 2013; Wolf and Toon, 2014), predominantly due to the presence of undersaturated regions in the atmosphere which can more efficiently cool to space. Water clouds dramatically impact the inner edge of the habitable zone. In Yang et al. (2013) and Yang et al. (2014), the presence of clouds on the dayside of slowly-rotating, tidally-locked terrestrial exoplanets can cool atmospheres by providing a high shortwave albedo. However, in simulations of Venus's early atmosphere, the formation of nightside clouds in a pure steam atmosphere can cause warming and prevent formation of a liquid surface ocean at instellations lower than the classical runaway limit (Turbet et al., 2021), suggesting the presence of climate bistability (Turbet et al., 2023).

As discussed in Section 1.2.1, "Hycean Worlds" (Madhusudhan et al., 2021) are a proposed subset of water-rich sub-Neptunes with hydrogen-dominated atmospheres. To understand if Hycean worlds are habitable, it is necessary to calculate their runaway greenhouse instellations. Previous studies of the temperature-pressure profiles of Hycean worlds (Piette and Madhusudhan, 2020; Madhusudhan et al., 2021) suggest that

temperate surface temperatures can be achieved for Earth-like instellations. However, several elements of these models could lead to lower-than-expected surface temperatures. Firstly, the majority assume a fixed water vapour concentration in the atmosphere, leaving much of the atmosphere under-saturated and therefore more optically thin to water vapour compared to a fully-saturated atmosphere. Secondly, they neglect the impact of water vapour on the convective lapse rate, a crucial element of the runaway greenhouse effect (see Section 4.3). Thirdly, the water vapour continuum opacity is not included, which can provide a significant source of infra-red opacity when the atmospheric water vapour content is non-dilute. Finally, the models don't include the effect of compositional gradients on the static stability of the atmosphere, which can profoundly impact the temperature structure of the atmosphere. In Chapter 5, I will use a radiative-convective model that accounts for all of these processes and aims to calculate the inner edge of the habitable zone for sub-Neptunes.

Before this, however, I will briefly review the early theories of the runaway greenhouse effect which elucidate in clear terms the underlying physics involved.

4.2 Radiative Equilibrium Limit

Early studies of the runaway greenhouse atmosphere attempted to determine the maximum cooling of a stratosphere in radiative equilibrium (Ingersoll, 1969; Komabayasi, 1967). Consider a planet with an optically grey atmosphere. In the limit where solar absorption occurs at the surface of a planet, we can solve for the outgoing longwave radiation (OLR) as (Pierrehumbert, 2010):

$$2\sigma T^4 = \mathrm{OLR}(\tau + 1), \tag{4.1}$$

where τ is the longwave optical depth and T is the temperature. If the optical depth of the atmosphere is dominated by the water vapour component, which itself is constant in the stratosphere and at saturation, then we can write (at the tropopause with

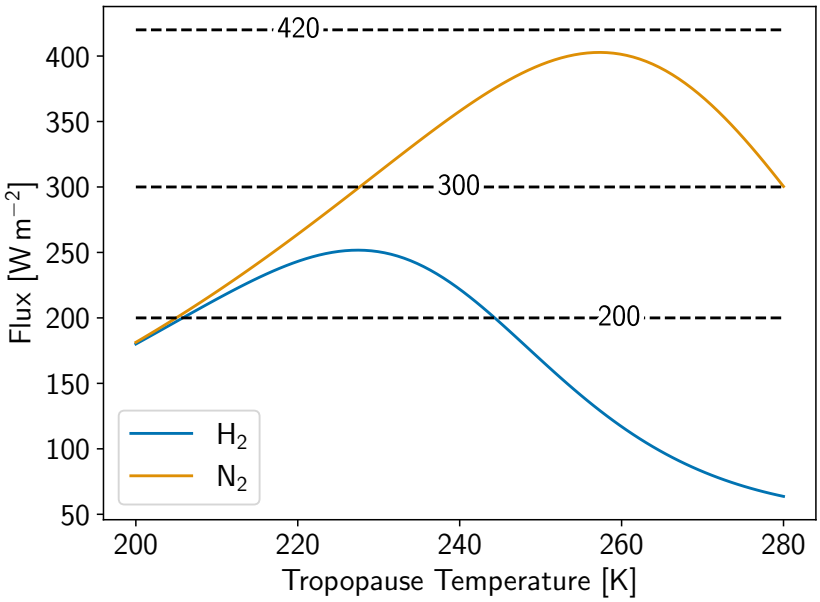

Figure 4.1: Solutions to Equation 4.1. Blue and orange lines represent $2\sigma T_{tp}^4/(\tau_{tp}+1)$ for a H_2 and N_2 background gas respectively. Stable equilibrium solutions for a given OLR (black dashed lines) exist at intersections where the coloured lines have positive gradients. For each curve, there is a maximum OLR that can be attained.

temperature T_{tp} and optical depth τ_{tp}):

$$\tau_{tp} = \frac{\varepsilon \kappa_w}{2g} q_{\text{sat}}(p_{tp}, T_{tp}) p_{tp}, \tag{4.2}$$

where κ_w is a characteristic grey opacity of the water vapour, q_{sat} is the saturation vapour concentration and ε is the ratio in mean molecular weight (MMW) between the condensible component of the atmosphere and the background gas. We can graphically plot solutions to Equation 4.1 for different values of the OLR, which in global equilibrium should be equal to $1/4(1-\alpha)S$ where α is the Bond albedo of the atmosphere and S is the incoming stellar radiation. For different background gases (i.e., varying ε), the maximum OLR that can be sustained varies from ≈ 250 W m^{-2} for a H_2 background to $\approx$ 400 W m^{-2} for an N_2 background (assuming $p_{tp} = 0.1$ bar). For average absorbed instellations above this value, the atmosphere cannot cool sufficiently to maintain radiation balance and will heat up until another mechanism allows the atmosphere to cool.

Qualitatively, if we were to steadily increase the incoming stellar radiation from a

low value, the atmosphere would initially respond by increasing the temperature of the tropopause in order to radiate more energy to space. However, past the turning point in Figure 4.1, the increased water vapour mixing ratio of the tropopause causes the stratosphere to become optically thick, and the radiation emitted at the top of the atmosphere would decrease, despite T_{tp} increasing.

4.3 The Effect of a Troposphere

The above analysis does not account for the effect of a convective troposphere, which changes the thermal structure of the lower atmosphere dramatically. If the pressure level at which the longwave optical depth is unity lies within the convective troposphere, then the OLR limit calculated from radiative equilibrium no longer applies. In this case, for simplicity we model the atmosphere as a moist adiabat integrated from a surface temperature T_s. At low surface temperatures, emission comes predominantly from the surface and does not exceed σT_s^4. As the surface temperature increases, a higher proportion of the atmosphere becomes water vapour. As water becomes the predominant component of the atmosphere, the temperature-pressure profile tends towards the pure steam adiabat, and the increased water vapour content of the atmosphere makes it optically thick to thermal radiation. At high surface temperatures, the temperature at which $\tau = 1$ becomes decoupled from the surface temperature and fixed, leading to a maximum OLR known as the Simpson-Nakajima limit (Simpson, 1929; Nakajima et al., 1992). This is illustrated in Figure 4.2. Figure 4.3 shows the OLR for a pure steam atmosphere, a N_2-H_2O atmosphere and a H_2-H_2O atmosphere as a function of surface temperature. The cases with dry components all converge to the Simpson-Nakajima limit of approximately 280 W m^{-2} at high surface temperatures. However, for background gases of different mean molecular weights, the OLR at intermediate surface temperatures can undershoot (e.g., H_2) or overshoot (e.g., N_2) this limit. A detailed explanation

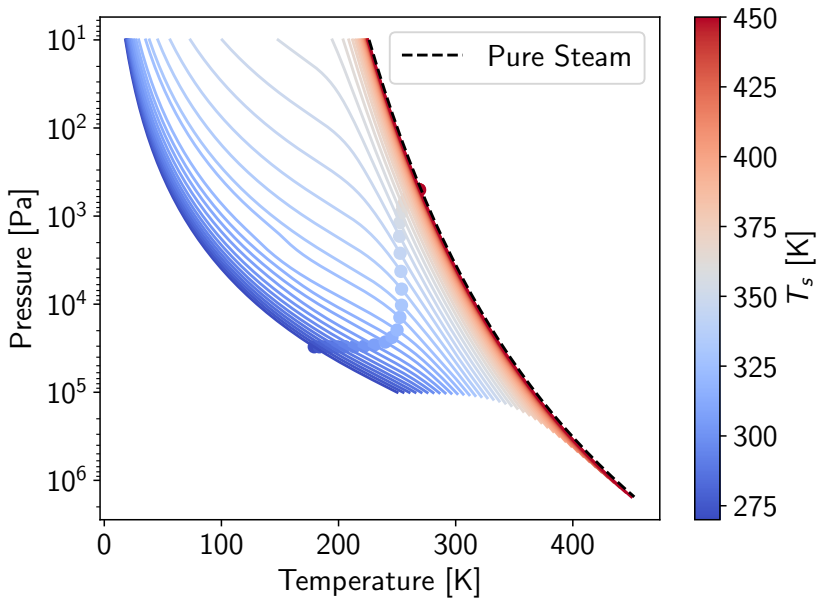

Figure 4.2: Temperature-pressure profiles for a H_2-H_2O atmosphere at different surface temperatures. The dots represent the point at which $\tau = 1$. As surface temperature increases, the profiles all converge to the pure steam adiabat, and the temperature at $\tau = 1$ becomes fixed

of this effect is found in Koll and Cronin (2019), though qualitatively for a given temperature and total pressure in the atmosphere, the H_2-H_2O atmosphere will contain a higher proportion of water vapour by mass than the N_2-H_2O mixture, enhancing the opacity due to water vapour and its greenhouse effect.

4.4 A Simple Grey Model of the Runaway Greenhouse

To help us understand the origins of a fixed OLR limit, a simple model can be constructed. Consider a pure-steam atmosphere that has grey longwave opacity τ. In the optically thick limit, the OLR can be approximated as:

$$\mathrm{OLR} = \int_0^\infty \sigma T^4 e^{-\tau} \, \mathrm{d}\tau \, . \tag{4.3}$$

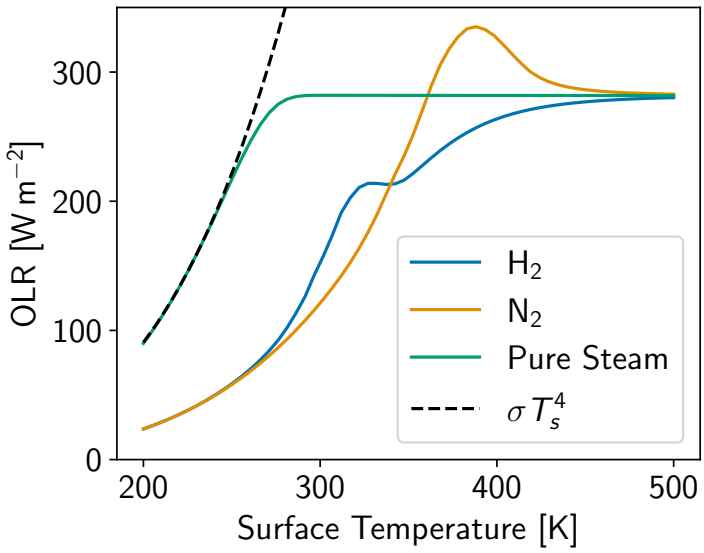

Figure 4.3: OLR as a function of surface temperature for moist adiabatic atmospheres. Blue and orange curves represent atmospheres with a dry background pressure of 1 bar, and the green curve represents a pure steam atmosphere lying on the liquid-vapour phase equilibrium boundary.

For the single component steam atmosphere lying on the liquid-vapour phase boundary, the optical depth is given by:

$$\tau(T) = \frac{\kappa_w p_{\mathrm{sat}}(T)}{\bar{\theta} g}, \tag{4.4}$$

where $\bar{\theta}$ is a constant between 0 and 1 that represents the effect of averaging over a hemisphere in the two-stream approximation. To make progress with an analytic solution, we use a simplified polynomial version of the saturation vapour pressure of water (Koll and Cronin, 2019):

$$p_{\mathrm{sat}}(T) = p_0 \left(\frac{T}{T_0} \right)^{\beta_0}, \tag{4.5}$$

where $\beta_0 \equiv L/(R_v T_0)$ and (p_0, T_0) is a reference point on the equilibrium liquid-vapour phase curve. We choose the reference pressure to be close to the point at which $\tau = 1$ for a pure steam atmosphere (with $\kappa_w = 0.01$ m^2 kg^{-1}), which is close to the triple point of water (i.e., $T_0 = 273$ K, $p_0 = 612$ Pa).

Using Equation 4.5 in Equation 4.4 and eliminating T in favour of τ in Equation 4.1, we find:

$$\mathrm{OLR} = \sigma T_o^4 \Gamma(1 + 4/\beta_o), \tag{4.6}$$

where Γ is the standard gamma function. This simple model for the Simpson-Nakajima limit gives a limiting OLR of 290 W m^{-2}, very close to the real-gas radiation value of approximately 280 W m^{-2}. Although it may seem like the result is independent of the water vapour opacity chosen, in reality it is implicitly included in our choice of (p_o, T_o). We will build on this simple model to explain results later in this thesis (Chapter 5, Sections 5.3.4 and C).

4.5 The Impact of an H_2-He Background and Convective Inhibition

As interest around hydrogen-dominated habitable worlds has grown, it is important to assess the impact of hydrogen as a background gas as opposed to nitrogen or other high MMW gases. Hydrogen gas's main source of opacity is its collision-induced absorption (CIA) spectrum. Since the strength of absorption scales as the density of the atmosphere squared, CIA becomes an important factor in H_2 atmospheres of around 1 bar or thicker, with 40 bars of pure H_2 allowing habitable surface temperatures out to 1.5 AU for an M star and 10 AU for a G star (Pierrehumbert and Gaidos, 2011). Accounting for absorption and water vapour feedbacks is necessary to further constrain the inner edge of the habitable zone. Koll and Cronin (2019) calculated the inner edge of the habitable zone for hydrogen-dominated atmospheres assuming a moist adiabatic temperature structure, and found, as in Figure 4.3, that the OLR doesn't overshoot the pure steam limit in comparison with high MMW background gas atmospheres.

Chapter 5 aims to build on Koll and Cronin (2019) by introducing the effect of MMW-induced convective inhibition on the temperature profiles of hydrogen-dominated planets. For atmospheres with a condensing component heavier than the background

gas, decreasing temperatures with altitude leads to a sharp decrease in MMW between the lower atmosphere and the upper atmosphere. If the concentration of the condensible is high enough, compositional gradients stabilise the atmosphere to convection (Guillot, 1995; Li and Ingersoll, 2015; Leconte et al., 2017) and double-diffusive instabilities (Leconte et al., 2017) even if the lapse rate is super-adiabatic. See section 2.8.3 for a more detailed introduction to convective inhibition. The atmospheric structure of runaway atmospheres is often assumed to be on a moist adiabat integrated upwards from the surface. However, if the surface temperature is high enough, high moisture contents will inhibit convection and lead to radiative layers in the lower atmosphere. I will discuss this effect in further detail in Section 5.1. I aim to calculate new limiting instellations for sub-Neptunes hosting a liquid water ocean with a hydrogen-dominated atmosphere.

4.5.1 Super-Runaway States

Even a liquid water ocean can be too hot to be habitable for life as we know it, but from the standpoint of planetary structure a second important transition occurs when the surface temperature of the water layer reaches the critical point. At this point, the liquid-gas phase transition of water disappears. More importantly for our purposes, H_2 is completely miscible with supercritical water (Soubiran and Militzer, 2015), so that gaseous solubility is no longer limited by Henry's Law (miscibility is expected for helium and other gases as well.) In consequence, a hydrogen envelope could not remain distinct from the supercritical water interior, but instead would mix into it and be diluted into the supercritical ocean. It is an interesting theoretical question how long it would take for such mixing to occur if the planet started out with a distinct hydrogen envelope, but the more plausible scenario for a planet with an initial H_2-H_2O composition is that the system would start out with a supercritical H_2-H_2O mixture. The H_2 would never phase-separate into a distinct layer if the equilibrium radiation balance maintains supercritical

conditions with respect to water. For this reason, we put particular emphasis on defining planetary parameters for which the ocean surface temperature approaches the critical point of water. The chief goal of the following chapter is to identify conditions in which a subcritical liquid water ocean can coexist with a hydrogen-rich atmosphere. Some speculations on the state a sub-Neptune settles into when those conditions are not met are offered.

Chapter 5

The Runaway Greenhouse Effect on Hycean Worlds

The results in this chapter were published in Innes et al., 2023.

Chapter 4 described how the inner edge of the habitable zone is typically calculated for terrestrial planets and highlighted the potential impact of hydrogen as the dominant background gas. In this Chapter, I present calculations of the runaway limit for Hycean worlds, firstly by considering the greenhouse effect of a dry H_2-He, and then considering the effects of water vapour in the atmosphere.

The chapter is structured as followed. In Section 5.1 I will discuss the H_2-He inventory required to produce a strong enough greenhouse effect to drive surface temperatures to the critical point of water. This will give an upper-bound on the instellation a planet can receive from its host star before entering a runaway state. In Section 5.2 I will extend the model to deal with atmospheres with a water vapour component. I will then discuss our results in the context of the literature in Section 5.3.

5.1 Hydrogen-Helium Atmosphere Above a Water Ocean

5.1.1 Model

To find an upper bound on the hydrogen inventory of a planet that maintains a liquid water surface, a hydrogen-helium atmosphere above a water ocean is modelled. The temperature structure of the atmosphere is assumed to be the dry adiabat for a hydrogen-helium mixture with solar abundances (Asplund et al., 2009), giving a He mass fraction of 0.25188 and a H_2 fraction of 0.74812. The contribution of water vapour to the atmosphere is neglected (similar to the calculation in Pierrehumbert and Gaidos (2011)). This is an unphysical assumption given warm temperatures will naturally lead to the water evaporating from the surface ocean and mixing with the hydrogen-helium gas. However, it serves as an easily calculated upper limit on the hydrogen-helium content of a planet with temperate instellation since water vapour is expected to act as a greenhouse gas, reducing the ability of the planet to cool. The choice of a purely adiabatic atmosphere is justified from test runs using a full radiative-convective iteration (see Section 5.2). The tropopause (at $\approx$ 0.05 bars) was typically at lower pressures than the infra-red photosphere (at $>$ 0.1 bar).

Radiative fluxes were calculated in the longwave (LW) and shortwave (SW) regions of the spectrum using the SOCRATES radiative transfer code (Edwards and Slingo, 1996), the details of which can be found in Appendix B. In the SW calculation, we specify a surface albedo of 0.12. This represents Earth's globally-averaged value which exceeds that of liquid water (0.06) due to the presence of land. A value of 0.12 was chosen so that the results are comparable those in the literature (Goldblatt et al., 2013; Koll and Cronin, 2019). The exact value will not drastically affect the runaway limit, since at this point most of the shortwave radiation is absorbed above the surface.

To calculate the maximum hydrogen inventory possible before an ocean is driven supercritical, fluxes were calculated for an atmosphere on a dry adiabat with surface temperature equal to the critical temperature of water, 647 K. The surface pressure (p_s) was varied logarithmically between 0.5 bar and the critical pressure of water, 220 bar. The SW fluxes were calculated using a solar instellation value of 1361 W m^{-2}, however it was noted that since the temperature structure of the atmosphere is fixed, the results can simply be multiplied by a constant factor to retrieve the SW fluxes for any arbitrary instellation. The surface gravity was kept constant at the Earth value, 9.81 m s^{-2}. As noted in Pierrehumbert and Gaidos (2011), the OLR depends on the surface gravity in the combination of p_s^2/g, so changing g can be accounted for simply by rescaling p_s. Increasing the surface gravity from its terrestrial value would be equivalent to lowering the surface pressure, i.e. increasing the OLR (assuming the change in Rayleigh scattering, which scales as p_s/g, does not cause the planetary albedo to change significantly). Therefore, for the same level of instellation, a planet with a higher surface gravity can host a higher pressure atmosphere before going supercritical. Nevertheless, the surface gravity of temperate sub-Neptunes is expected to be of a similar order of magnitude to the Earth. Of the 212 planets between 1.0 and 4.0 $R_\oplus$ with well-defined mass, radii and stellar parameters, the mean surface gravity is 15.9(6) m s^{-2} (maximum 66.4 m s^{-2}, minimum 1.90 m s^{-2}, data via the NASA Exoplanet Archive[1]). Although a lower Earth-like value is employed, similar qualitative results are expected for a slightly higher surface gravity. The use of the Earth-like value also permits comparison of the results with the literature, the majority of which employs an Earth-like surface gravity. We consider atmospheres irradiated by a G star and an M star (details of their spectra can be found in Appendix C).

[1] Accessed on 2023-06-13 at 18:17, returning 212 rows.

5.1.2 Results

Only moderate pressures of hydrogen and helium are required to force surface temperatures to supercritical values. Figure 5.1 shows the OLR and SW absorption of these atmospheres as a function of surface pressure. The intersection points between the OLR curve (green) and the SW absorption curves (blue and orange depending on stellar type) signify atmospheric configurations in global equilibrium. For a pure H_2-He atmosphere with solar instellation, S_0, approximately 10 bars of atmosphere will cause a large enough greenhouse effect due to CIA to drive the surface ocean supercritical. The SW absorption in the G-star experiments was reduced relative to the M-star thanks to the enhanced Rayleigh scattering cross sections at low wavelengths. However, the change in stellar type causes minimal differences in the qualitative behaviour of our model. Naturally, lower instellation values require larger atmospheric masses to warm the surface to the critical temperature, and atmospheres irradiated with less than 1% of solar radiation would require a surface pressure greater than the critical pressure of water to reach the critical temperature.

5.2 Adding Water Vapour to the Atmosphere

5.2.1 Model Setup

Thermodynamics

Water is added to each layer at its saturation pressure value (i.e. the relative humidity is assumed to be 100%). Analytic expressions for the saturation vapour pressure given by Wagner and Pruß (2002) are used, generating a lookup table of values for each temperature for faster on-the-fly calculation.

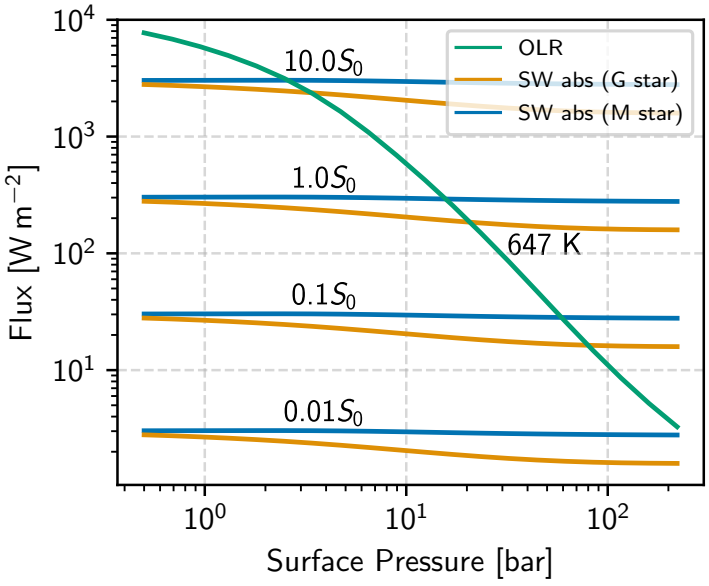

Figure 5.1: Outgoing longwave radiation (OLR) and shortwave (SW) absorption as a function of surface pressure. The green curve represents the OLR of an H_2-He atmosphere on a dry adiabat with surface temperature equal to the critical temperature of water. The blue and orange curves show the SW absorption at different instellations relative to solar (S_0) for an M star and G star respectively.

Radiative Procedures

As in Section 5.1, radiative fluxes are calculated with the SOCRATES radiative transfer code. Unlike in Section 5.1 where an inverse modelling approach was taken, the model is now timestepped by iterating the temperature according to:

$$\frac{\partial T}{\partial t} = A(p)\frac{\partial F_{\text{net}}}{\partial p}, \tag{5.1}$$

where T is the temperature, F_{net} is the net flux two-stream flux calculated at the edge of each model layer (defined such that F_{net} is positive if the net flux is upwards, in the $-p$ direction). The coefficient $A(p)$ varies in each model layer in order to approach radiative equilibrium (where $\partial_p F_{\text{net}} = 0$) as fast as possible. The method described in Malik et al. (2017), where $A(p)$ is decreased if temperature oscillations are detected in that temperature layer and increased on each iteration otherwise. For our purposes we only need to compute the correct equilibrium profile, and do not need to compute the

actual time series as the system adjusts to equilibrium.

Using this approach, the independent variable is the instellation, S, as opposed to the surface temperature, T_s, which is permitted to vary until the atmosphere reaches local and global radiative equilibrium.

Convective Adjustment

After each iteration, the temperature-pressure profile is checked for instability to convection. We use the instability criterion modified for use in atmospheres where water vapour is at saturation with a lower mean molecular weight background gas (Leconte et al., 2017):

$$(\nabla_{\mathrm{am}} - \nabla_{\mathrm{ad}})(1 - \beta q \varpi) > 0, \tag{5.2a}$$

$$\text{with} \quad \nabla_x \equiv \frac{\mathrm{d} \ln T_x}{\mathrm{d} \ln p}, \tag{5.2b}$$

$$\beta \equiv \frac{\mathrm{d} \ln p_{\mathrm{sat}}}{\mathrm{d} \ln T}, \tag{5.2c}$$

$$\varpi \equiv (1 - \mu_d / \mu_v). \tag{5.2d}$$

The “am" and “ad" suffixes denote “ambient" and “adiabatic" respectively, p_{sat} is the saturation vapour pressure, T is the temperature and μ_d and μ_v are the MMWs of the dry and condensing vapour gases respectively. The first term in Equation 5.2a is the Schwarzschild criterion (Schwarzschild, 1906) for convective instability when the ambient lapse rate is greater than the moist adiabatic lapse rate. The second term represents the effect of mean molecular weight gradients in an environment where water vapour is held at its saturation vapour pressure value. When the water vapour concentration, q, exceeds a critical value, $q_c \equiv 1/\beta\varpi$, the parcel is no longer unstable to convection despite any super-adiabatic lapse rates. The value of the moist adiabatic lapse rate, ∇_{ad} is calculated using the expression in Ding and Pierrehumbert (2016), which accounts for water vapour being a non-negligible component of the atmosphere but neglects the effects of retained condensates. We replace occurences of $L/R_v T$ (where L is the latent heat of

vaporization above the triple point and the latent heat of sublimation below and R_v is the gas constant of water in J kg^{-1}) in the lapse rate formula with the more appropriate β factor obtained directly from a lookup table. Any other factors of L are calculated using a lookup table using fits from Wagner and Pruß (2002). This accounts for vanishing L as T approaches the critical temperature of water (647 K). However, we note that at temperatures approaching the critical point of water, the non-ideal equation of state of water vapour will become important but is neglected in this current work for simplicity. Convective adjustment is performed pairwise on layers working upwards from the bottom of the atmosphere. If Equation 5.2a is satisfied, we adjust the temperature of both layers to the moist adiabat. This procedure is repeated until convergence is reached.

Note that when $q > q_c$, a saturated layer with lapse rate ∇_{am} *less than* the adiabatic lapse rate – even an isothermal layer – is unstable, and in our scheme is convectively adjusted to the saturated adiabat; radiative cooling may then cause further steepening of the lapse rate.

The implementation of Equation 5.2a leads to two radiative zones forming in the atmosphere when temperatures near the surface are high enough – a traditional stratosphere in the upper atmosphere with low lapse rates and a convectively-inhibited radiative zone below the first convective region. Since the atmosphere is optically thick in this region, the radiative lapse rate is usually high and requires higher vertical resolution. We ran the model with 200 layers, with the bottom 100 layers dedicated to resolving this radiative region of the atmosphere. In the traditional stratosphere we implement a cold trap for moisture, setting the moisture concentration to its minimum value at pressures lower than the moisture minimum (as in Ingersoll, 1969; Goldblatt et al., 2013; Ding and Pierrehumbert, 2016). This prevents the moisture concentration increasing as the saturation vapour pressure of water increases in the upper atmosphere (though we note that oxidation of methane can produce an increase in water vapour mixing ratio in the Earth's stratosphere Frank et al., 2018).

Surface Physics

At the surface we implement a rudimentary heat transfer scheme which transfers sensible heat from the surface to the lowest model layer. This prevents the surface temperature becoming unphysically hotter than the lowest model layer and is a simple attempt to represent some of the heat exchange processes in the turbulent boundary layer. The surface energy equation is:

$$\rho_s c_s h \frac{\mathrm{d}T_s}{\mathrm{d}t} = -F_{\mathrm{net}}(p_s) + c_p \rho_{\mathrm{air}} C_D U (T(p_s) - T_s), \tag{5.3}$$

where values for the surface density (ρ_s) and heat capacity (c_s) are taken to be those of liquid water and h (the bucket depth) is taken as 1 m. The drag coefficient C_D and the characteristic drag velocity U are taken to be 0.001 and 10 m s^{-1} respectively, from Pierrehumbert (2010). The effect of varying these parameters had a negligible effect on the overall temperature structure of the atmosphere and the final conclusions of this work.

In traditional calculations of the runaway greenhouse limit using an inverse modelling approach (e.g. Kasting et al., 1993), the surface pressure p_s is taken to be the sum of a constant dry component, p_o, and the saturation vapour pressure at the specified surface temperature T_s. Surface pressure can increase with temperature, allowing an increase in total atmospheric mass as more water vapor is added to the atmosphere. However, holding p_o fixed as temperature increases leads to an implied change in the dry mass of the atmosphere as temperature changes, because the mean molecular weight of the atmosphere varies and the concentration of the dry mass is not uniform over the profile. For inverse climate modeling, it is straightforward to allow p_s to vary with temperature, but with radiative-convective calculations that compute equilibria using time-stepping or related iterations, the re-gridding needed to allow p_s to vary becomes unwieldy and can lead to numerical issues. For that reason, we make the additional simplification of holding p_s itself fixed, until conditions make such an assumption phys-

ically inconsistent. The expedience of holding p_s fixed was also used in the calculations of Figure 9 in Piette and Madhusudhan (2020), which were carried out with a water-saturated atmosphere. In such calculations, there is an additional reduction in implied dry mass as temperature increases, as p_o needs to be reduced in order to compensate for the increase with temperature of surface water vapor partial pressure. As long as this change isn't drastic, it is of little consequences for our purpose, as we are not attempting to track the actual time evolution of an atmosphere. It only means that the dry air mass in the equilibrium state is somewhat different from what was specified for the initial condition of the calculation. The magnitude of the difference will be quantified in Section 5.3.3.

When the surface saturation vapor pressure approaches the specified p_s, $p_o \to 0$ and it is no longer possible to keep surface pressure fixed as surface temperature is further increased. To deal with this case, we introduce a pure-steam layer for $p > p_s$, extending to a greater surface pressure p_s'; we then time-step the radiative-convective model only for $p < p_s$, computing the radiation from the pure steam layer assuming it to lie on the pure-steam (i.e dewpoint) moist adiabat, as discussed in Pierrehumbert and Ding (2016). Since water vapour is heavy and non-buoyant in a hydrogen-dominated background atmosphere, it will remain at the bottom of the atmosphere.

A radiative layer in the lower levels of the atmosphere tends to dry out the upper atmosphere (due to its steep lapse rates), leading to a layered structure with pure water vapor at the bottom, nearly pure hydrogen-helium at the top, and a sharp transition layer between the two. All of the mass of hydrogen and helium resides in the upper layer, and the opacity of this layer (which in turn depends on the dry hydrogen-helium mass) strongly affects the conditions for the surface temperature to enter a runaway state.

In cases which require a pure steam layer at the bottom, we set the bottom of the atmosphere to a fixed surface temperature (which fixes the surface pressure as the sat-

uration vapour pressure at this temperature). The approach in this case is to determine the instellation which is compatible with the specified surface temperature, requiring multiple runs of the time-stepped model. Unlike the usual inverse climate modeling approach, the required instellation cannot be determined by just computing the OLR corresponding to a given $T(p)$ profile, since the profile is affected by the instellation through stellar absorption within the atmosphere. Instead, we need to guess an instellation, time-step the model (subject to a lower boundary condition provided by the steam layer) until $T(p)$ reaches equilibrium, and then check the top of atmosphere balance. The instellation is then adjusted until top of atmosphere balance is achieved. When the surface temperature is too high, the OLR becomes decoupled from surface temperature owing to the optically thick steam layer, and so equilibrium cannot be reached when instellation exceeds a threshold value, which defines the runaway condition. For instellation above the runaway threshold, the temperature increases until some process intervenes to allow OLR to increase again, as discussed in Boukrouche et al. (2021) and Pierrehumbert (2023). In this paper, we do not compute the super-runaway equilibrated state, but for a water-rich sub-Neptune with a deep water layer the deep temperature will be above the critical point of water.

5.2.2 Experimental Procedure

To model the effect of different dry mass paths (i.e., dry mass per unit area of atmosphere), we run the model with two surface pressures – 1 bar and 10 bar. As described above, this surface pressure is held constant until $q(T_s, p_s) = 1$ is reached at the bottom of the atmosphere, after which the surface temperature and pressure are increased on the pure steam adiabat. Since steep radiative lapse rates keep the atmosphere relatively dry at all pressures except very close to the surface, this acts to keep the dry mass path of the atmosphere relatively constant at $\approx 10^4\,\mathrm{kg\,m^{-2}}$ for the 1 bar initial condition and $\approx 10^5\,\mathrm{kg\,m^{-2}}$ for the 10 bar case (we will quantify this in Section 5.3.3). Extending the at-

mosphere on the pure steam adiabat does not add any dry mass to the atmosphere (and instead assumes that the extra mass comes from evaporation from the surface ocean). We will refer to these two cases as the “1 bar" and “10 bar" cases interchangeably with “10^4 kg m^{-2}" and “10^5 kg m^{-2}" cases.

For both the 1 bar and 10 bar atmospheres, we perform separate runs with the G-star and M-star spectra described in Appendix B. SOCRATES spectral files for hydrogen-helium-water atmospheres were created for use over the range of temperatures and pressures pertinent in this study. Details of the spectral data used can be found in Appendix B and the spectral files can be found in an online repository (Innes, 2023). For each set of runs, we begin with a low instellation that gives surface temperatures between 270 K – 300 K and run the model to radiative-convective equilibrium. After the equilibrium state is found, we reinitialise the model with an incrementally higher instellation, chosen as a balance between numerical stability and computational efficiency. Increments of 5 W m^{-2} and 1 W m^{-2} were used for the 1 bar and 10 bar runs respectively. The initial temperature profile of the first run is a dry adiabat with an isothermal stratosphere – runs at higher instellations are then initialised on the final temperature profile of the previous run. When $q(T_s, p_s) = 1$ is reached at the bottom of the atmosphere (i.e. $p_{\mathrm{sat}}(T_s) = p_s$), we switch to the procedure described above where the surface temperature is held fixed and the instellation is iterated until both local and global radiative equilibrium are attained. We run the model until the surface temperature reaches 600 K, giving us a range of surface temperatures between 270 K and 600 K.

5.2.3 Results

Temperature and Humidity Profiles

Figures 5.2 and 5.3 show sample temperature-pressure profiles and specific humidity profiles for the M star and G star experiments. At pressure levels where $q > q_c$, there is

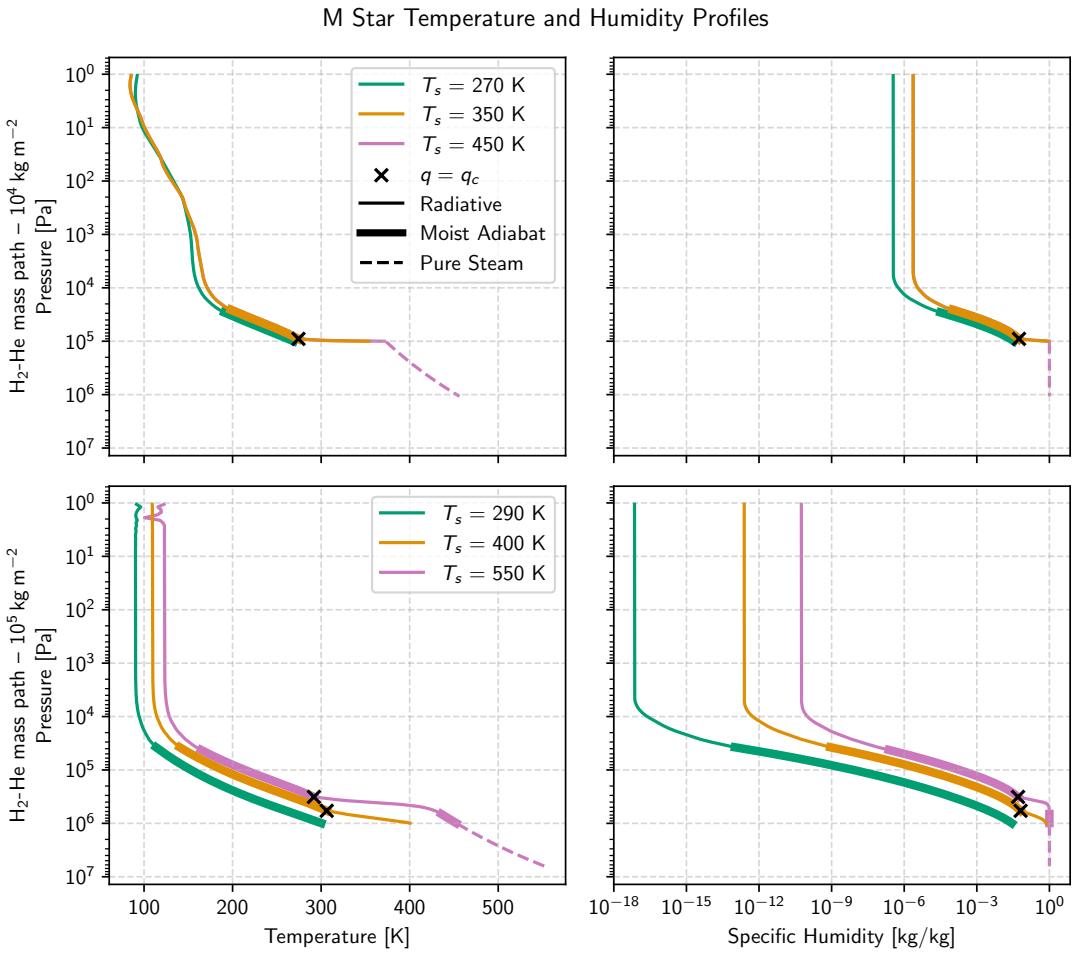

Figure 5.2: Sample of temperature-pressure profiles (left column) and specific humidity profiles (right column) for the M star experiments with dry mass paths of 10^4 kg m^{-2} (top row) and 10^5 kg m^{-2} (bottom row). The introduction of radiative layers in the lower atmosphere causes a sharp increase in the surface temperature before the lower atmosphere becomes pure steam. The radiative layers have lower lapse rates in the 10^5 kg m^{-2} case because less SW radiation penetrates to the lower atmosphere.

a sharp increase in lapse rate which corresponds to increased surface temperatures with respect to convecting lower atmospheres. Once the atmosphere reaches the pure steam limit in the lower atmosphere (q = 1) the temperature profile follows a pure steam adiabat. In the M star 1 bar experiment and both G star experiments, enough SW radiation penetrates the lower atmosphere to make the radiative layers have an extremely steep lapse rate compared to both the moist adiabat and the pure steam adiabat. However, in the M star 10 bar experiment (bottom row of Figure 5.2) attenuation of SW radiation

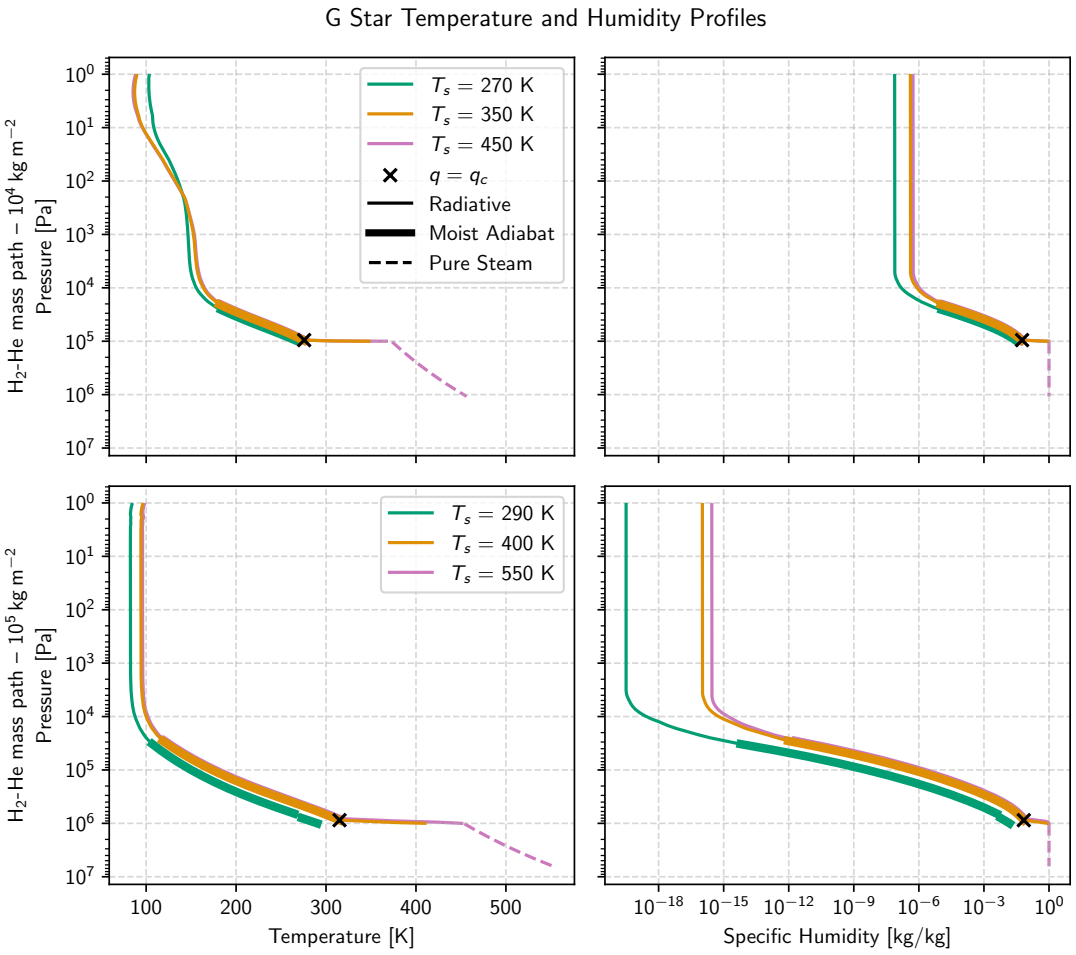

Figure 5.3: Same as Figure 5.2 but for the G star experiments.

results in a smoother transition between adiabatic and radiative regions.

Surface Temperature vs. Instellation

Figure 5.4 shows the surface temperature, T_s, as a function of the incoming instellation. We divide our graphs into three regions. In the region where $q(T_s, p_s) < q_c$ (green in Figure 5.4), the atmospheric T-p structure is a moist adiabat in the lower atmosphere with a radiative stratosphere at low pressures. Once $q(T_s, p_s) > q_c$ (orange in Figure 5.4), there is a radiative layer in the lower atmosphere. The steep lapse rates in this region tend to increase the surface temperature sharply with instellation than in the lower temperature cases. Lastly, when $q(T_s, p_s) = 1$ (pink in Figure 5.4), the bottom of the atmosphere

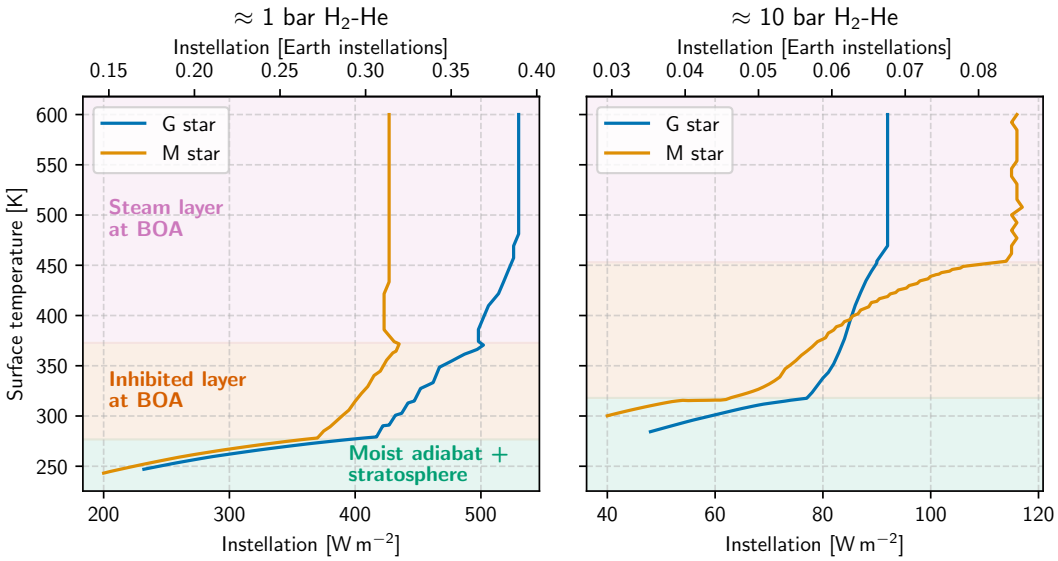

Figure 5.4: Surface temperature as a function of incoming instellation for different hydrogen-helium inventories. The introduction of layers with convective inhibition when the moisture content at the bottom of the atmosphere (BOA) is high enough (orange region) causes a rapid increase in surface temperature (and moisture content). Once the bottom of the atmosphere is pure steam (pink region), the atmosphere becomes optically thick and increasing surface temperature is no longer linked with an increase in cooling, causing a runaway state. Note the different x-axis scales on each subplot.

is pure steam and lies on a pure steam adiabat. At this point the atmosphere becomes optically thick at all wavelengths and the surface temperature decouples from the OLR. Further increases in the instellation cannot be compensated by additional cooling and the surface temperature increases until the ocean reservoir is depleted or the critical point of water is reached. In the latter case (applicable to sub-Neptunes with a significant water inventory), the hydrogen atmosphere is miscible with the supercritical water envelope. The possible equilibrated states of a super-runaway pure steam atmosphere are discussed in Pierrehumbert (2023). The addition of hydrogen in this scenario is beyond the scope of this work.

When our initial condition is a 1 bar hydrogen-helium atmosphere, the M-star runaway limit instellation is 435 W m^{-2}, and our G-star runaway limit is 530 W m^{-2}. The higher runaway limit for G-stars is due to the Rayleigh scattering cross-section being larger at shorter wavelengths, which leads to an increased SW albedo for the G-star

experiment where more of the instellation is at low wavelengths.

Interesting behaviour is caused by the sudden drop in maximum possible instellation received in both cases when the atmosphere becomes pure steam (at the boundary between the pink and orange regions in Figure 5.4). For global equilibrium, we require:

$$S = \frac{4\mathrm{OLR}}{1-\alpha}, \tag{5.4}$$

where α is the albedo. Inspecting the relevant terms, the drop in absorbed instellation at this boundary is caused by a sudden decrease in the albedo with the introduction of the steam layer. This initial drop is caused by a sudden increase in SW absorption from the sharp increase in water vapour at the bottom of the atmosphere. Less radiation reflects from the surface, decreasing α and therefore S in Equation 5.4 (assuming OLR remains approximately constant). Adding more steam at the bottom of the atmosphere (increasing surface temperature) eventually causes the albedo to increase again, since the albedo of a thick pure steam layer is greater than the surface albedo, 0.12. In the G-star case, more SW radiation penetrates into the lower atmosphere than the M-star case, leading to a larger increase in albedo and hence a larger increase in instellation.

The drop in absorbed SW radiation leads to a narrow range of instellations with multiple equilibrium surface temperatures, some of which are unstable (depending on the sign of $\mathrm{d}S/\mathrm{d}T_s$, (Koll and Cronin, 2019)). In the M-star case with 1 bar H_2-He, the drop in absorbed radiation leads to the atmosphere abruptly entering a runaway state at any instellation above 0.32 S_0.

With 10 bars of H_2-He as the initial condition, we see similar overall behaviour as the 1 bar case. The boundaries between the three regimes identified above have shifted to higher surface temperatures due to the higher surface pressure. Due to the much higher CIA optical depth of the dry gas inventory compared to the 1 bar case, there is more SW absorption in these atmospheres. This mutes the varying albedo effect at the pure steam boundary described above, and leads to the surface temperature increasing monotonically with instellation towards the runaway limit. This limit is 92 W m^{-2}

for the G-star and 116 W m^{-2} for the M-star case. We note that the M-star limit is now higher than the G-star, despite the higher albedos of the G-star irradiated atmospheres. In the M-star radiative regions at $p \approx 10$ bar, there is very little SW radiation penetrating the radiative layer. In the optically thick limit, radiative flux can be approximated as radiative diffusion (Pierrehumbert, 2010; Heng et al., 2014), with corresponding radiative equilibrium lapse rate:

$$\frac{\partial T}{\partial p} = \frac{3}{16} \frac{\kappa}{g \sigma T^3} S_{\rm net}, \tag{5.5}$$

where κ is the Rosseland mean opacity and $S_{\rm net}$ is the net SW flux penetrating the region, which is also the flux that must be carried upward through the region by radiative transfer. If $S_{\rm net}$ is small in the radiative region (as is the case with the M star 10 bar atmospheres), then the lapse rate is also relatively small, meaning increasing S has less of an effect on the surface temperature than in cases where more radiation penetrates into the deeper layers.

The curves in Figure 5.4 exhibit discrete stepping in regions where there are superadiabatic radiative layers in the atmosphere. This numerical artefact arises from the sensitivity of the surface temperature to the structure of the radiative layer. Discrete stepping is worse if the vertical resolution is low and there are few model levels in the radiative region. In this case, there is a large jump in surface temperature when a new model level becomes inhibited to convection. This behaviour motivated the use of higher vertical resolution in the lower atmosphere (discussed in Section 5.2.1) which reduces the size of the jumps in T_s but does not completely remove them. The structure of the stepping also changes as the instellation increment is increased or decreased, suggesting the surface temperature may be somewhat dependent on the initial state of the model (which is initialised from the final temperature profile of the previous run). We do not believe the numerical artefacts affect the conclusions of our work.

5.3 Discussion

5.3.1 Comparison of Runaway Limits to Canonical Values

Table 5.1 summarizes the runaway greenhouse instellations found in Sections 5.1 and 5.2. We can compare these to the classical runaway greenhouse limit calculated for hydrogen atmospheres assumed to be on a moist adiabat (e.g. Koll and Cronin, 2019). Since at high T_s the moist adiabat approaches the pure steam limit smoothly (Koll and Cronin, 2019), this is the same as asking the maximum instellation a pure steam atmosphere can receive and remain in global radiative equilibrium. The maximal OLR (sometimes called the Simpson-Nakajima limit), is approximately 280 W m^{-2} for Earth's surface gravity. In global equilibrium, this must be equal to $(1 - \alpha)S/4$ by Equation 5.4. Our estimation of the maximum instellation therefore depends on the calculated albedo, α, which varies by spectral type. We calculate the runaway limit for a pure steam atmosphere to be 1410 W m^{-2} (1.04 S_0) and 1150 W m^{-2} (0.847 S_0) for our G-star and M-star cases respectively.

Comparing these numbers to our model results, for our dry atmospheres the maximum instellation is around 20 S_0 for 1 bar of H_2-He mixture, 2 S_0 for 10 bars and less than 0.1 S_0 for 100 bars. Adding water vapour to the atmosphere, for 1 bar of solar H_2-He mixture the maximum instellation is less than half of the Simpson-Nakajima limit and is less than 10% of the classical limit with 10 bars of H_2-He mixture. This affects the placement of the inner-edge of the habitable zone, which is given by:

$$d = \left(\frac{L/L_\odot}{S/S_0}\right)^{1/2} \text{AU}, \tag{5.6}$$

where $L/L_\odot$ is the luminosity of the star normalized by the solar value. We take $L/L_\odot = 1$ for the G-star and $L/L_\odot = 0.0251$ for the M-star, the same as K2-18's luminosity (Benneke et al., 2019b).

Table 5.1: Summary of runaway instellations

H_2-He Pressure [bar]	Moisture	Stellar Type	Runaway Limit [W m^{-2}]	Runaway Limit [S_0]	HZ inner edge [AU]
1	✗	G	2.93×10^4	2.15×10^1	2.16×10^{-1}
1	✗	M	2.58×10^4	1.90×10^1	3.64×10^{-2}
1	✓	G	5.30×10^2	3.89×10^{-1}	1.60×10^0
1	✓	M	4.35×10^2	3.20×10^{-1}	2.80×10^{-1}
10	✗	G	4.05×10^3	2.97×10^0	5.80×10^{-1}
10	✗	M	2.80×10^3	2.06×10^0	1.10×10^{-1}
10	✓	G	9.20×10^1	6.76×10^{-2}	3.85×10^0
10	✓	M	1.17×10^2	8.60×10^{-2}	5.41×10^{-1}
100	✗	G	9.89×10^1	7.27×10^{-2}	3.71×10^0
100	✗	M	5.71×10^1	4.19×10^{-2}	7.74×10^{-1}
Classical Limit	✓	G	1.43×10^3	1.05×10^0	9.75×10^{-1}
Classical Limit	✓	M	1.18×10^3	8.70×10^{-1}	1.70×10^{-1}

Our new inner-edge estimates are presented in Table 5.1. For dry atmospheres, the estimates are closer to the host star than the classical limit for surface pressures of 1 and 10 bars and further from the host star for 100 bars of H_2-He mixture. This is consistent with the findings of Pierrehumbert and Gaidos (2011), where the greenhouse effect of H_2 becomes significant at surface pressures between 10 and 100 bars.

Adding the effect of moisture and convective inhibition, all inner-edge estimates are further from the host star than previous calculations (e.g., Koll and Cronin, 2019; Madhusudhan et al., 2021). For a 10 bar dry mass inventory, our values lie outside the traditional outer edge of the habitable zone (instellations between 0.2 and 0.4 S_0 Kopparapu et al., 2013).

5.3.2 Why Convective Inhibition Lowers the Runaway Limit

In this section we explore why, for a given instellation, the surface temperature is much hotter in our experiments than in traditional calculations of the inner edge of the habitable zone. Consider a planet with a given instellation, S. The instellation roughly sets

the stratospheric temperature as $T_{\text{strat}} \sim (S(1-\alpha)/4\sigma)^{1/4}$ and the temperature of the radiating layer where the characteristic LW optical depth, τ, is unity. With increasing pressure, the T-p profile will follow a radiative layer, followed by a moist adiabatic layer until it reaches the level where $q = q_c$. In our simulations, the atmosphere then follows a radiative lapse rate, which in general is much steeper than the equivalent moist adiabatic lapse rate so long as the atmosphere is opaque enough and has enough SW radiation penetrating to that level. This increased lapse rate leads to much higher surface temperatures for equivalent levels of instellation. This effect is illustrated in Figure 5.5(a). Once the bottom of the atmosphere becomes pure steam, the surface temperature increases steeply with small increases in instellation, since the bottom of the atmosphere becomes optically thick and decoupled from the OLR.

Equivalently, we can imagine the temperature-pressure profile in both the classical and inhibited scenarios starting from the same surface temperature, T_s. If $q(T_s, p_s) > q_c$ then our modelled atmospheres will follow a steep radiative lapse rate, compared to the shallower moist adiabat. Once $q < q_c$, the inhibited atmosphere will again follow a moist adiabat (albeit one with a much steeper lapse rate than the one departing from (T_s, p_s) owing to q now being more dilute). The resulting upper atmospheric temperature of the inhibited atmosphere will be much lower, leading to a much lower OLR. In global equilibrium, OLR $= S(1-\alpha)/4$, and so the maximum allowed instellation for a given surface temperature will be much lower. This is illustrated in Figure 5.5(b).

5.3.3 Why Increased Dry Mass Lowers the Runaway Limit

It is clear from Figure 5.4 that the increased dry mass path in the 10 bar H_2-He experiments lowers the maximum instellation limit. Figure 5.5(c) shows two atmospheres with the same surface temperature and different dry mass paths. The pressure level at which $\tau = 1$ is relatively constant between the two cases, because in the upper atmosphere $q << 1$ so $\tau = 1$ when $p(\tau = 1) \approx g/\kappa_d$ where κ_d is some characteristic grey

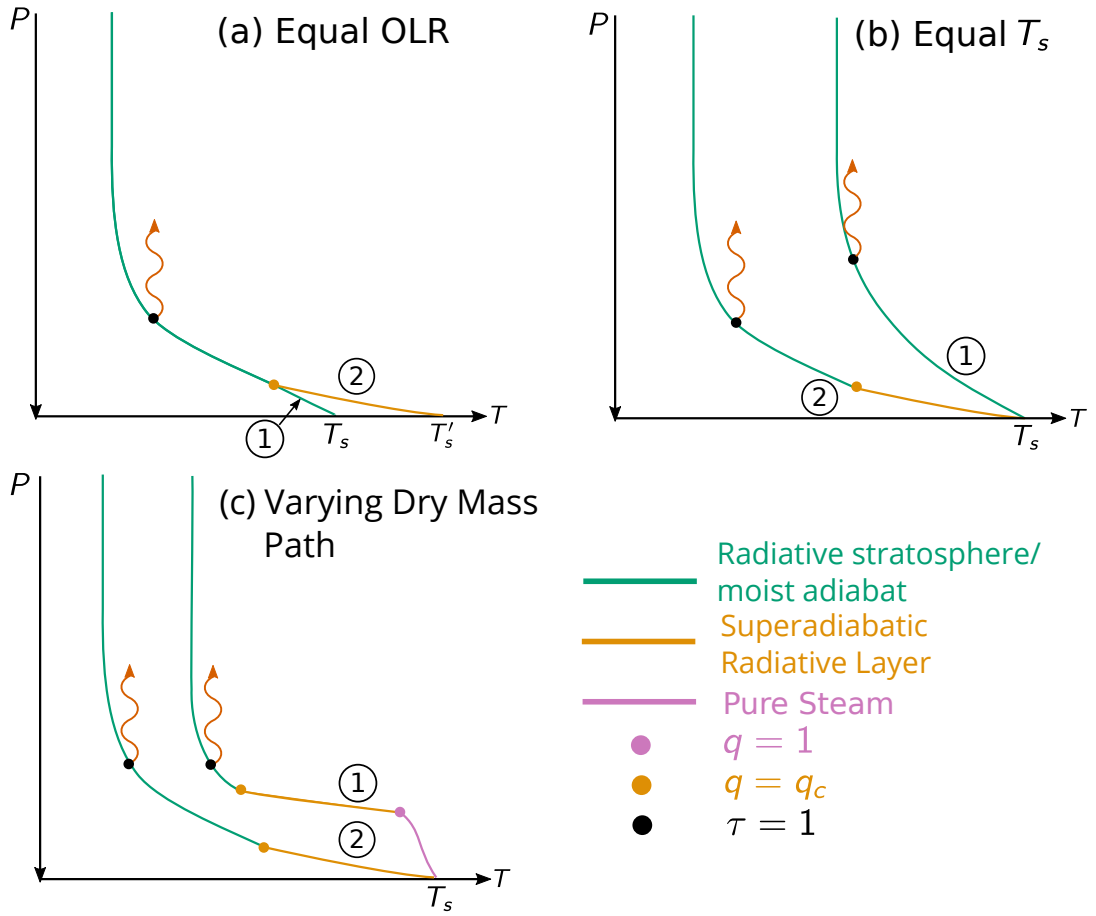

Figure 5.5: Three T-p profiles demonstrating the effect of superadiabatic layers on the radiative balance of the atmosphere. (a) We compare an atmosphere with convective inhibition (2) to one without (1), assuming an identical instellation. Although the radiating temperature (and OLR) is the same between the two cases, the atmosphere with the superadiabatic layer has a higher surface temperature. (b) We again consider an atmosphere with (2) and without (1) a superadiabatic layer, starting from a fixed surface temperature. In this case, the superadiabatic layer causes the radiation temperature (and therefore OLR) of the atmosphere to decrease, which in turn reduces the maximum instellation it can receive. (c) We consider two atmospheres with inhibited layers with different dry mass paths. The pressure at $\tau = 1$ is approximately constant between the two cases. The atmosphere with the greater dry mass path, (2), has a greater average lapse rate between the surface and the radiating level than (1), where the lower atmosphere is pure steam. The radiating level is therefore colder, reducing the maximum OLR of the atmosphere.

opacity of the dry gas inventory. The pressure at which $q = q_c$ is approximately constant with temperature (see Section 5.3.4). Increasing the dry mass path of the atmosphere also increases the pressure level at which q becomes unity and the atmosphere transitions to a steam layer. As seen in Figure 5.5(c), since the pure steam layer (pink) has a

much lower lapse rate than the radiative layer (orange), the average lapse rate between the surface and the $\tau = 1$ level increases with increasing mass path. A higher average lapse rate decreases the radiating temperature with increasing dry mass path, leading to a drop in the OLR (and hence maximum instellation) in the runaway limit.

5.3.4 Discussion of Analytic OLR

In Appendix C, we calculate the OLR from an inhibited atmosphere to be:

$$\mathrm{OLR} = \Gamma(1+4\alpha)\left(\frac{\kappa_d m_d}{\bar{\theta}}\right)^{-4\alpha}\left(q_0\frac{\kappa_v m_d}{\varepsilon\bar{\theta}}\right)^{4/(\beta_0-1)}\sigma T_0^4, \tag{5.7}$$

where $T_0 \approx 273$ K, $\beta_0 \equiv L/(R_v T_0)$, $q_0 \equiv 1/(\beta_0\varpi)$, $\alpha \equiv R_d/c_p$, $\bar{\theta} = 3/5$, $\varepsilon \equiv \mu_v/\mu_d$, Γ is the standard gamma function and κ_v and κ_d are the characteristic grey opacities of the moist and dry components of the atmosphere respectively. Choosing $\kappa_v = 0.01$ m^2 kg^{-1} to match the Simpson-Nakajima limit for a pure steam atmosphere, this leaves the OLR as a function of the dry opacity, κ_d and the dry mass path, m_d. Table 5.2 shows estimates of the analytic OLR when $\kappa_d = 1.6 \times 10^{-4}$ m^2 kg^{-1}, a sensible value for the dry opacity which corresponds to an H_2-He atmosphere that becomes optically thick at approximately 0.6 bars

The term in $m_d^{-4\alpha}$ represents the total optical depth of the dry component of the atmosphere – as this term increases, the radiating temperature drops and the OLR decreases. The second term in $m_d^{4/(\beta_0-1)}$ represents how increasing the dry mass of the atmosphere increases the temperature at which the atmosphere becomes radiative, which increases the OLR. In general, $\alpha \gg (\beta_0-1)^{-1}$, and we estimate $4(\beta_0-1)^{-1}-4\alpha \approx -8/7$, so the OLR decreases with dry mass, explaining the trend in Table 5.1. Moreover, Table 5.2 shows that the 10 bar M-star case is has a reduced dry mass compared to the equivalent G-star case, explaining its higher instellation limit since from Equation 5.7 this atmosphere will cool more efficiently. More care could be taken to ensure that the dry mass path of the atmosphere is conserved across our different simulations. With the current

Table 5.2: Comparison of model OLR with analytical calculations with a dry gas opacity of 1.6×10^{-4} kg m^{-2}

Expermiment	OLR [W m^{-2}]	Dry mass [kg m^{-2}]	Analytic OLR [W m^{-2}]
G-star, 1 bar H_2-He	101	9.92×10^3	111
M-star, 1 bar H_2-He	103	9.74×10^3	113
G-star, 10 bar H_2-He	14.0	8.91×10^4	12.3
M-star, 10 bar H_2-He	26.7	5.35×10^4	20.5

model setup, this would involve iterating the surface pressure so that the integral:

$$\int_0^{p_s} (1-q)\frac{\mathrm{d}p}{g}, \tag{5.8}$$

is conserved. This was deemed too computationally expensive for the current study. Alternatively, one could implement a self-consistent moisture scheme that keeps track of the mass of the vapour phase, which would naturally conserve dry mass.

Moreover, in Appendix C we show that the ratio of this OLR to the Simpson-Nakajima limit can be written as:

$$\frac{\mathrm{OLR}}{\mathrm{OLR_{SN}}} = \frac{\Gamma(1+4\alpha)}{\Gamma(1+4/\beta_0)}\left(q_0\frac{\kappa_v m_d}{\varepsilon\bar{\theta}}\right)^{4/(\beta_0-1)}\left(\frac{\kappa_d m_d}{\bar{\theta}}\right)^{-4\alpha}. \tag{5.9}$$

Since the ratio of gamma functions is of order unity, and $4(\beta_0 - 1)^{-1} \ll 1$, so long as $\kappa_d m_d/\bar{\theta} > 1$, i.e. the dry inventory of the atmosphere is optically thick, we should expect the OLR to be lower than the classical Simpson-Nakajima limit.

The analytic expression provides a relatively good estimate of the OLR but decreases slightly too steeply with increasing m_d – more experiments at different dry paths would need to be run to establish the limitations of the power-law formulation.

5.3.5 What Does a Super-Runaway State Look Like?

Having discussed how the runaway greenhouse threshold changes for inhibited atmospheres, it is natural to wonder what a super-runaway atmosphere would look like. For Earth-like planets with a finite water reservoir, eventually the water inventory will be

entirely in the atmosphere, and the lower atmosphere will not be in liquid-vapour phase equilibrium, allowing it to lie on a dry adiabat and increase its OLR (Boukrouche et al., 2021). However, for a Hycean world with an almost limitless supply of water this is not possible. As discussed in Pierrehumbert (2023), a super-runaway state is likely to consist of supercritical water vapour in the lower atmosphere. Since the supercritical phase is not constrained to lie on the phase equilibrium boundary between liquid and vapour (in contrast to the condensing layers above), a deep layer of the interior heats up until the supercritical water layer penetrates to high enough altitudes that radiation to space can increase beyond the runaway limit. In the pure water case discussed in Pierrehumbert (2023), this generally leaves a thin condensing region near the top of the atmosphere, but in the case with a substantial H_2 layer at the top, the radiating level is in the H_2 layer, so the condensing layer is eliminated entirely. The warming proceeds until the H_2 layer becomes hot enough to increase the OLR, but once supercritical water is in contact with the H_2, that layer would mix into the supercritical water and largely disappear, because H_2 (and presumably also He) is completely miscible in supercritical water (Soubiran and Militzer, 2015). A full thermal evolution model would be needed to determine how long this process would take. A curious possibility emerges because the runaway instellation threshold with an H_2 layer is considerably below the pure-steam limit. If the instellation lies between the two thresholds, once the H_2 layer is diluted into the supercritical water interior, a liquid ocean could form again, forcing some H_2 back into the atmosphere. One possibility is that the mixing between the layers results in just enough H_2 remaining in the outer layer for radiative balance to be achieved, predicting a self-regulation in the thickness of the H_2 layer.

The scenario we have modelled in this paper corresponds to a cold-start, in which the planet begins in a sub-runaway state and then undergoes a runaway as the stellar luminosity increases. This is a possible scenario for an F or G star, but an alternate scenario for the evolution is a hot-start, in which the planet begins in a super-runaway

state, either because of the heat of formation of the planet or because of intense illumination in the extended pre main-sequence stage of low mass stars. In a hot-start, the initial H_2-H_2O inventory would most likely begin in a supercritical mixed state. While the instellation remains above the runaway threshold, a significant separated H_2 layer would never form (unless H_2 is a major proportion of the initial composition). Once the planet cools down enough to be sub-runaway, though, a liquid ocean will form, leading an H_2 layer to effervesce out of the subcritical liquid ocean.

5.3.6 Mixing of H_2-He into the Pure Steam Layer

The layered structure that occurs in our model at high surface temperatures, with a pure steam layer at the bottom, is a self-consistent solution of the radiative-convective equations. It is a peculiarity of the compositional stability criterion (Equation 5.2a) that when $q > q_c$, $q \to 1$ appears to be a singular limit. When $q = 1$ exactly, the moist stability criterion is the usual criterion that the lapse rate be steeper than the adiabat. However, if even an infinitesimal amount of hydrogen or helium mixes into the pure steam layer, so $q = 1 - \delta$, with $\delta \ll 1$, the compositional stability criterion then nominally applies according to which lapse rate steeper than the moist adiabat are stable. Radiative cooling would then be expected to generate a steep radiative layer within the nearly pure steam layer, no matter how small δ may be. However, since the stabilizing compositional buoyancy becomes exceedingly week for small δ, many other mixing processes could intervene, so we find the generation of a radiative layer under these circumstances to be implausible. We cannot rule out the possibility, though; it is a matter that will need to be resolved by future resolved-convection modelling.

5.3.7 Escape of Hydrogen

For low mass planets with hydrogen-dominated atmospheres, we also need to consider the rate of atmospheric escape, which could significantly deplete the content of the at-

mosphere. We consider only Hydrogen escape, and neglect the depletion of water by photodissociation and escape since in our models with convective inhibition, water is effectively cold-trapped (See Figures 5.2 and 5.3). We will estimate the hydrogen loss rate in two limiting cases: diffusion-limited and energy-limited.

When the diffusion upward to the exosphere is the limiting factor, we can estimate the H escape rate via diffusion-limited escape to be (neglecting the thermal diffusion term):

$$\Phi_D = Dn\left(\frac{1}{H_a} - \frac{1}{H}\right), \tag{5.10}$$

where D is the molecular diffusion coefficient, n the total number density, H_a the scale height of the atmosphere and H the scale height of atomic hydrogen (Catling and Kasting, 2017; Tsai et al., 2021). Taking the value of D of H_2-H binary mix to be 1.1×10^8 cm^2 s^{-1} and a scale height of 200 km (calculated for the sub-Neptune K2-18 b), the H escape rate is approximately 2×10^{11} cm^{-2} s^{-1} at 10^{-8} bar.

When considering the absorption of EUV (Extreme Ultraviolet with wavelength shorter than 100 nm) photons in the exosphere to be the limiting factor, the energy-limited escape is given by:

$$\Phi_E = S_{\mathrm{EUV}}\eta\left(\frac{GMm}{r}\right)^{-1}, \tag{5.11}$$

where η is the heating efficiency, S_{EUV} is the EUV flux, and GMm/r is the gravitational binding energy of an H atom of mass m around a planet of mass M and radius r, with G being the universal gravitational constant. We assume a planetary radius of 2 $R_\oplus$ and a mass of 8 $M_\oplus$ such that the gravity is Earth-like, and assume that the EUV is absorbed at around the planetary radius. We use $\eta = 0.15$ as in Catling and Kasting (2017). For a 1 bar atmosphere, the energy-limited escape for a modern Sun-like star is about 2.5×10^{10} cm^{-2} s^{-1}, which is one order of magnitude lower than the diffusion-limited escape due to the lower instellation from our revised habitable orbits. Consequently, the energy-limited escape for a 1 bar atmosphere around a modern Sun-like star yields a lifetime of the hydrogen atmosphere of about 40 billion years, which would

impact the atmospheric composition but would not deplete the bulk hydrogen reservoir. If the Hycean planet is around an active M-star with at least ten times the EUV radiation of the Sun, the atmosphere would enter the diffusion-limited regime. In this case, the lifetime of a 1 bar hydrogen atmosphere is about 10 billion years, which could potentially deplete hydrogen and resulted in a helium-rich (Hu et al., 2015) or steam atmosphere (Schaefer et al., 2016). However, this scenario becomes increasingly unlikely as the thickness of the atmosphere increases. For a 10-bar atmosphere, an EUV stellar flux 100 times higher than the solar value is required to push the H escape rate to the diffusion-limited value. Even in this diffusion-limited regime, the lifetime of an H_2-atmosphere is still about 100 billion years owing to the combined effects of further orbital distance and thicker hydrogen envelope. Overall, unless the primordial hydrogen atmosphere is thin (i.e. around 1 bar) and the host star is active, our estimate suggests that the background hydrogen would not be significantly altered by the escaping processes. Although the analysis above provides an approximate estimate of escape rates, the result that low-equilibrium temperature, sub-Neptune-sized exoplanets can retain some of their primordial hydrogen envelopes is shared with more sophisticated models (Owen and Mohanty, 2016; Misener and Schlichting, 2021)

5.3.8 Implications for Observations

Our main result is that the runaway limit for sub-Neptune water worlds is greatly reduced with even 1 bar of hydrogen. Due to observational biases favouring the detection of low semi-major axis planets, most of the current observational candidates for Hycean worlds have relatively high equilibrium temperatures. From Table 5.1, the inner edge of the habitable zone is around 0.28 AU for our formulation. Table 1 of Madhusudhan et al. (2021) lists potential Hycean world candidates, all of which lie within our inner edge estimate and therefore would only be able to sustain a liquid water ocean if hydrogen were not detected in large abundances in the atmosphere. The well-studied sub-Neptune K2-

18 b, originally thought to lie right on the inner edge of the classical habitable zone, is well beyond the inner edge by this measure.

In this case, the planets most likely to host liquid water oceans on close-in orbits are either terrestrial planets with a higher mean-molecular weight background gas, or pure “water-worlds" with little to no H_2 envelope and an atmosphere predominantly composed of steam. The latter type of planets and their evolution have been studied previously in the highly-irradiated regime (Mousis et al., 2020; Aguichine et al., 2021), finding that water worlds may fit the observed mass-radius distribution of small radius planets. The super-Earth sized planet Kepler-138 d (Piaulet et al., 2023) is a candidate volatile-rich planet. It has a 1.5 $R_\oplus$ radius and low density making it not dense enough to be predominantly rocky, but also too dense to sustain a significant hydrogen envelope that would not be lost through atmospheric escape. Although this particular planet is above the runaway greenhouse instellation threshold, similar cool planets may be able to host liquid water oceans at near-Earth instellations.

The ability to observationally distinguish liquid water surfaces and super-runaway mixtures of H_2-H_2O would allow us to verify some of the predictions of this work. Mapping the transition from sub-runaway planets to super-runaway planets as a function of instellation would give us the runaway instellation limit, which could be compared to the predictions in Table 5.1 to provide evidence for or against robust super-adiabatic layers. The combined non-detection of ammonia and detection of methanol in a sub-Neptune atmosphere has been proposed as a method of distinguishing a shallow water surface (Tsai et al., 2021). However, this method requires around 20 transits with the James Webb Space Telescope which may prove unfeasible given time allocation restrictions. Our results also predict a sharp transition between sub-runaway atmospheres where the upper atmosphere is very dry (see Figures 5.2 and 5.3) to super-runaway atmospheres that are moist due to the mixing of H_2 and supercritical H_2O (Pierrehumbert, 2023). In contrast, the moistening of the upper atmosphere in the classical run-

away greenhouse limit without convective inhibition is more smooth as instellation is increased and would occur at higher instellations. Further complications arise from the presence of non-Hycean sub-Neptunes, where the presence of water in the atmosphere is not necessarily correlated with its interior structure or the presence of a surface. More work is needed to understand how we can observationally disentangle the various possible atmospheric structures of habitable zone sub-Neptunes.

5.3.9 Robustness of Calculations and Caveats

Day-Night Averaging

Our model is one-dimensional, and makes the assumption that the stellar radiation is redistributed evenly over the dayside and nightside of the planet. The superadiabatic layers in our model are sustained by the need to remove the stellar flux deposited at the surface of our model. If day-night heat redistribution is not efficient, then the nightside of these planets may be able to sustain shallower lapse rates which would aid with radiative cooling. However, for thick hydrogen atmospheres on temperate sub-Neptunes, general circulation models (Charnay et al., 2021; Innes and Pierrehumbert, 2022) have shown that the combination of slow rotation rate and low mean molecular weight atmospheres produces globally weak temperature gradients thanks to dynamical redistribution of heat. This suggests heat deposited near the surface would be transported horizontally to the nightside, maintaining the steep lapse rates globally. Scaling relations for shallow atmospheres also suggest low MMW atmospheres should have efficient heat redistribution (Koll, 2022).

Assumption of Saturation

Our model also assumes 100% relative humidity in the column (except above the stratospheric cold trap). One major effect of 3D dynamics is to cause subsiding regions (e.g.

due to the descending branch of a Hadley-like circulation, or night side subsidence on a tidally locked exoplanet). Descending dry air causes compressional heating and undersaturation, and can be responsible for regions where the OLR is locally greater the result of a globally-averaged calculation (Pierrehumbert and Swanson, 1995; Leconte et al., 2013). If an atmosphere is undersaturated to the point it lies below the critical water vapour mixing ratio q_c, then superadiabatic layers responsible for surface heating may not form. Moreover, on Earth moist convection is the main mechanism by which water vapour is transported vertically in the atmosphere. Within the inhibited superadiabatic layer, mixing by convection is suppressed and our assumption of 100% relative humidity may break down aloft. However, we note that if the near-surface layers are saturated (due to being close to the ocean surface) and the layers aloft are undersaturated, this induces an even greater mean-molecular weight gradient to stabilise the atmosphere to convection than before. Moreover, since undersaturated lofted parcels would travel on the dry adiabat, which has a steeper lapse rate than the moist adiabat, this would again help stabilise the atmosphere to convection. One could argue that decreasing relative humidity with height would affect the radiative calculations. However, from Section 5.3.3 and Appendix C we can see that the main driver of lower cooling is the radiative effect of the dry mass of the atmosphere. A decrease in relative humidity with height would likely decrease the thickness of the superadiabatic layer, in which case the reduction in OLR may not be as severe as in the fully saturated scenario. Lastly, large-scale 3D circulations such as overturning day-night cells on tidally-locked planets or Hadley cells on non-synchronously rotating planets may provide a mechanism to transport moisture through the atmosphere and maintain saturation. The role of global circulations in setting the moisture structure of Hycean worlds is an interesting avenue for further work.

Clouds and Hazes

Cloud and haze opacities were not included in our model. We expect their introduction to affect our results in three main ways. Firstly, the increase in LW opacity due to cloud water or hazes would exacerbate the greenhouse effect and, if taken independently from other cloud and haze radiative feedbacks, decreases the runaway instellation. Secondly, the SW scattering properties of clouds and hazes increase the effective planetary albedo. This opposes the greenhouse effect and increases the value of the runaway instellation. Thirdly, clouds and hazes may reduce the magnitude of shortwave radiation penetrating the lower atmosphere. This would reduce the radiative lapse rates in the inhibited layers by reducing S_{net} in Equation 5.5. The reduction of radiative lapse rates will decrease the surface temperature for any given instellation, raising the runaway instellation. A similar effect was modelled in Piette and Madhusudhan (2020), who demonstrated that surface water oceans were possible on K2-18 b if the haze scattering opacity was high enough. In this case, the lower atmosphere becomes isothermal, allowing for temperate oceans at high pressures. However, their model neglected the effect of convective inhibition. Moreover, as discussed in Section 5.2.1, saturated subadiabatic radiative layers are unstable to convection when $q > q_c$, implying that above the critical moisture threshold, the moist adiabat is the minimum possible lapse rate.

If the cooling effects of clouds and hazes dominate their potential warming effect, then our runaway instellations in Table 5.1 are likely too pessimistic and the inner edge of the habitable zone could be at lower orbital distances. The magnitude of the cloud and haze radiative effects is likely to be strongly dependent on the particles' microphysical properties and 3D spatial distribution (e.g., Yang et al., 2013; Turbet et al., 2021). These effects are beyond the scope of our simplified 1D model, though we encourage future efforts to quantify the impact of clouds and hazes on our results.

Other Heat Transport Mechanisms

We also need to consider other mechanisms which may be able to transport heat through the stabilised layers. For example, how efficient is thermal conduction at transporting flux deposited in the lower atmosphere? We can compare the efficiency of thermal conduction to radiation by comparing the thermal diffusion coefficient for conduction and radiation, as in Markham et al. (2022). For an ideal gas, the thermal diffusivity of conduction is:

$$k_{\text{cond}} = \rho \lambda c_v \sqrt{\frac{2k_B T}{\pi m}} \approx 1\,\text{W m K}^{-1}, \tag{5.12}$$

where λ is the mean free path, m is the weight of an average gas molecule, k_B is the Boltzmann constant and c_v its specific heat capacity at constant volume. We choose characteristic values to give an upper limit on k_{cond}. We use $T = 300$ K, $\lambda = k_B T/(\sqrt{2}\pi d^2 p)$ with $d = 290$ pm (the kinetic diameter of a hydrogen molecule, Mehio et al., 2014) and $m = 2$ amu. Density is calculated using the ideal gas law and we note the final result is independent of pressure.

The radiative diffusivity of an optically thick gas is approximately

$$k_{\text{rad}} = \frac{16}{3}\frac{\sigma T^3}{\kappa \rho} \approx 10^4\,\text{W m K}^{-1}, \tag{5.13}$$

where we have used $\kappa = 0.01$ kg m^{-2} and used the same T and ρ in our calculation of k_{cond}. We conclude that energy transport via radiation is much more efficient than thermal conduction. Other sources of heat transport that could be considered are advective heat transports. Although the superadiabatic regions are statically stable, eddy heat transport could play a role in transporting heat vertically, especially if the vertical wind shear is high. Moreover, we have also neglected latent heat fluxes, which could play a significant role if there is significant condensation or re-evaporation of condensates around the region of interest. Within the framework of a 1D model with no dynamics, it is very difficult to get an accurate estimate of the magnitude of these fluxes. Studying this system with a cloud-resolving model (e.g. Lefèvre et al., 2021; Tan et al., 2021) is key

to understanding the robustness of the superadiabatic layer against other mechanisms of heat transport. These models would also indicate the radiative effect of water clouds on the system and derived runaway greenhouse limits.

Possibility of Multiple Equilibria

Lastly, apart from in the region near the runaway limit (see Section 5.2.3), our model doesn't consider the possibility of multiple equilibrium states and hysteresis. Given that the phase structure of a water-world can change drastically on either side of the runaway limit from steam above a surface ocean to a supercritical envelope (Pierrehumbert, 2023), there is a possibility that much warmer surface temperatures could be achieved with a similar instellation if we modelled the atmosphere with a supercritical water layer mixed with hydrogen gas. Our models represent a "cold start", i.e. warming a planet up that initially starts with a surface water ocean. However, realistically a sub-Neptune will form hot and cool down from a state where the water is supercritical (Misener and Schlichting, 2022; Markham et al., 2022). Most rocky planets greater than Martian-to-Earth size will host a magma ocean in their early history (Lichtenberg et al., 2022). Interactions between a rocky planet's interior, magma ocean and atmosphere may be the limiting factor determining the plausibility of a liquid water ocean, in which case our estimates of runaway limits may be conservative. If there are multiple equilibrium solutions, it is possible that even when the instellation lies below the runaway threshold, the water will still be in a supercritical state. Moreover, in our model we have neglected the effect of internal heating from the residual heat of formation or tidal heating. Given that our model only requires $\approx 1\,\mathrm{W\,m^{-2}}$ of stellar flux penetrating the lower layers to drive steep superadiabatic lapse rates, a similar level of internal flux could equally sustain very high surface temperatures in the absence of a significant instellation. Estimates from Blain et al. (2021) place K2-18 b's internal temperature at somewhere between 1 and $4\,\mathrm{W\,m^{-2}}$.

Limitations of Convective Adjustment

Throughout this study we assume that any statically unstable parts of the atmosphere are instantaneously adjusted to an adiabatic temperature profile (e.g. Manabe and Strickler, 1964). There are several limitations of such schemes (see Arakawa (2004) for a detailed discussion of different cumulus parameterisations). Firstly, in 3D models, the fact that moist convection is only triggered when the large-scale relative humidity reaches 100% (or some specified fraction) often leads to infrequent, high-precipitation storms (Frierson et al., 2007). In our 1D model, however, we specify the large-scale relative humidity at 100%, in which case moist convection always occurs when the temperature profile is statically unstable. As such, this problem is mainly linked to our prescription of the moisture distribution in the atmosphere, as discussed in Section 5.3.9. Secondly, moist convective adjustment schemes prescribe the final state of an atmosphere that has undergone convection. In our case, this is the saturated moist pseudo-adiabat (Pierrehumbert, 2010). However, for atmospheres in convective quasi-equilibrium (Arakawa and Schubert, 1974), the final profile would be found through computing the balance between destabilising large-scale forcings and stabilising convective motions. More complex mass-flux parametrizations have been used to study convection in hydrogen-dominated atmospheres such as Jupiter's (Del Genio and McGrattan, 1990; Sankar and Palotai, 2022), which account for warming effect of dry, subsiding regions on the temperature profile. These schemes derive from mass-flux schemes used for Earth's atmosphere (e.g. Arakawa and Schubert, 1974) and as such are not explicitly designed to handle non-dilute atmospheres where water vapour makes up a significant fraction of the atmosphere. As such, we opt for a simple adjustment scheme that reflects our lack of knowledge about the details of moist convection in a non-dilute, hydrogen-dominated atmosphere. We encourage the use of convection-resolving models to act as the foundation for more complex convection parametrizations to be built on.

5.4 Conclusions

The aim of this chapter was to determine the sustainabilty of a liquid water ocean on a Hycean world with a significant H_2-He inventory. My major findings are:

1. Neglecting water vapour feedbacks, 10-20 bars of solar H_2-He mixture will drive a surface ocean supercritical when forced with solar instellation. A planet receiveing 10 times solar instellation would have to have less than 1 bar of hydrogen to sustain a liquid water ocean.

2. Including water vapour feedbacks, the presence of superadiabatic layers where convection is inhibited in the lower atmosphere reduces the runaway greenhouse instellation limit from the Simpson-Nakajima limit significantly. For a solar H_2-He inventory of around 10^4 kg m^{-2}, the runaway greenhouse limit to an instellation of approximately 530 W m^{-2} for a G-star and 435 W m^{-2} for an M-star. This reduces further to around 100 W m^{-2} for an H_2-He inventory of around 10^5 kg m^{-2}.

3. The reduced instellation limits correspond to moving the inner edge of the habitable zone to around 1.6 AU (3.85 AU) for a planet orbiting a G-star with 1 bar (10 bar) of H_2-He and equivalently 0.280 AU (0.543 AU) for a planet orbiting an M-star (c.f. 0.982 AU and 0.172 AU for a G-star and M-star respectively from previous models).

4. Analytical models of the OLR show the key parameter responsible for the reduction in the OLR is the total optical depth of the dry inventory, given that steep superadiabatic lapse rates in the inhibited layers dry the atmosphere aloft. A higher dry optical depth reduces the radiating temperature of the atmosphere and caps the maximum cooling from a H_2-H_2O atmosphere. If we model the atmosphere as having a constant, grey opacity for the dry gases, then the limiting OLR scales roughly as the inverse of the dry mass path.

5. The results suggest that most of the current Hycean world targets are within the inner limit of the habitable zone and unlikely to host liquid water oceans. The most promising targets for observing a liquid water ocean on a close-in orbit are therefore traditional terrestrial-like planets with a high-mean molecular weight background atmosphere or “water worlds" with negligible H_2-He envelopes.

We conclude by encouraging the use of 3D cloud resolving models to study the robustness of the inhibited, superadiabatic radiative layers to 3D dynamics and other sources of heat flux.

Chapter 6

Developing a GCM to Simulate Non-Dilute Water Vapour in Sub-Neptune Atmospheres

In the previous chapters I have described the circulation of dry sub-Neptunes, and shown how the combination of hydrogen and water vapour above a water ocean can push the inner edge of the habitable zone for Hycean worlds outwards. In this chapter, I will describe preliminary efforts to simulate sub-Neptunes with non-dilute water-hydrogen atmospheres in an attempt to unify the themes of my thesis thus far.

Why are we interested in modelling water vapour in the atmosphere of sub-Neptunes? Firstly, a wide range of atmospheric metallicities is expected for the sub-Neptune population of exoplanets (Fortney et al., 2013; Kreidberg et al., 2014; Madhusudhan et al., 2020). In hydrogen-dominated atmospheres with enhanced metallicities, water vapour is one of the most abundant species in the output of chemical equilbrium models (e.g., Blain et al., 2021; Tsai et al., 2021). Water vapour concentrations of around 35% can be reached for atmospheric metallicities of 100x solar (Tsai et al., 2021; Charnay et al.,

2021). If a planet is cool enough for water vapour to condense, we enter the regime where a condensible species makes up a large component of the atmosphere. On Earth-like planets, this has profound consequences on the dynamics as shown in Pierrehumbert and Ding (2016). As the atmosphere tends towards a saturated pure steam composition, the dynamics become barotropic and regions of undersaturation become difficult to sustain (assuming there is a condensate reservoir at the surface). However, as discussed in Chapter 2, Section 2.8, we expect non-dilute moisture to behave differently in the atmosphere of hydrogen-dominated exoplanets. For example, the inhibition of convection will affect the thermal structure and distribution of moisture in the atmosphere (c.f. Chapter 5).

Moreover, the moisture distribution and clouds formed in the atmospheres of sub-Neptunes affect transit spectroscopy measurements obtained by space telescopes. For example, the best-fit model for *Hubble* data of the temperate sub-Neptune (and Hycean world candidate) K2-18 b suggested the presence of water vapour with no clouds (Benneke et al., 2019a). On the other hand, subsequent measurements with the *James Webb Space Telescope* show that the 1.4 μm absorption feature was due to methane absorption and not water vapour (Madhusudhan et al., 2023). However, water clouds or water vapour could not be ruled out at pressure levels greater than 100 mbar. In addition, transit spectroscopy only probes a small section of an exoplanet's atmosphere near the terminators, so spatially inhomogeneous clouds (e.g., near the substellar point) would not be detectable. The cloud models typically used in retrievals are one-dimensional, heavily parameterised and incapable of capturing the 3D inhomogeneity of real clouds. GCM simulations can provide a physical understanding of where clouds form in the atmosphere of sub-Neptune, and whether we should expect to detect clouds and water vapour in the observable upper atmosphere.

Lastly, modelling condensible water vapour on temperate sub-Neptunes is of particular interest due to their proposed habitability (Madhusudhan et al., 2021; Seager et al.,

2021). The presence of liquid water is often viewed as a crucial precursor to the formation of life (Lammer et al., 2009). On sub-Neptunes, liquid water could be found either at the surface (on Hycean worlds) or in clouds. Whereas surface liquid water is widely accepted to be favourable for the development of life, the possibility of aerial biospheres is more speculative and is based on measurements of microorganisms in Earth's clouds (Vaïtilingom et al., 2012) and theories on the suitability of clouds on Venus to host life (e.g., Limaye et al., 2018). Using GCMs to model sub-Neptunes with condensing water vapour is way a to understand how atmospheric circulation, radiative transfer and water condensation interact to produce either habitable conditions at a surface, or long-lived clouds aloft.

Currently, there are few general circulation models that have been explicitly developed to handle non-dilute condensible substances. Leconte et al. (2013) used the LMD Generic GCM with non-dilute water vapour to calculate the inner edge of the habitable zone for an Earth-like climates with increased instellations. Pierrehumbert and Ding (2016) used the latitude-longitude version of the ExoFMS GCM with a non-dilute convective adjustment scheme and instantaneous rainout of precipitates to simulate extremely non-dilute Earth-like exoplanets.

In this chapter, I will outline the development of a new version of ExoFMS that uses the updated cubed-sphere, finite volume version of the GFDL FV3 dynamical core (Lin, 2004) to model non-dilute water vapour in the atmosphere of sub-Neptunes. In the interests of simplicity and clarity, I opt to implement basic microphysics and convection schemes with few free parameters, as opposed to more complex schemes used in other GCMs. The advantage of this approach is that it reflects our lack of knowledge of cloud microphysics and convection in non-dilute, hydrogen-dominated environments and instead relies on basic physical principles that should be valid over a wide range of planetary parameters. However, the absence of more complicated cloud-radiative coupling schemes and cloud microphysics may make the model too simple to produce

accurate predictions of observable quantities.

As shown in Chapter 5, for sub-Neptunes with a surface ocean below a hydrogen-dominated atmosphere a high opacity gradient in the vertical direction combined with the inhibition of convection can lead to extremely large temperature gradients forming in the lower atmosphere, next to the surface. In a GCM, this layer would form in the planetary boundary layer where the presence of a frictional surface induces turbulent motions. In Earth GCMs, turbulent fluxes of moisture and heat are parameterised, often with parameters tuned to fit observations of Earth's boundary layer (e.g., Mellor and Yamada, 1982). To avoid resolving steep temperature gradients in the boundary layer and constructing a boundary layer scheme for novel conditions, I will restrict the application of the GCM to gas giant sub-Neptunes without surfaces that are heated primarily by stellar radiation absorbed in the atmosphere.

The chapter is structured as followed. In Section 6.1 I describe the model I developed for studying moist sub-Neptunes, including a modified version of the convection scheme found in Ding and Pierrehumbert (2016) and a simple rainout scheme with re-evaporation that conserves enthalpy and mass. In Section 3.2 I demonstrate that the model can plausibly simulate non-dilute sub-Neptunes. I will qualitatively describe some of the salient features of the circulation in comparison to the dry dynamics seen in Chapter 3. This chapter focuses on the technical aspect of this novel model development, and the aim is to demonstrate its abiity to tackle the questions listed above, without a full description of the impact of moisture on every aspect of the circulation. In Section 6.3 I discuss some of the improvements that could be made to the model and potential applications of the model. I will summarise my findings in Section 6.4.

6.1 Methods

We use an updated version of the ExoFMS GCM (e.g., Lee et al., 2022; Innes and Pierrehumbert, 2022; Hammond and Pierrehumbert, 2017) to perform our simulations. ExoFMS uses the FV3 finite volume dynamical core (Lin, 2004) and cubed-sphere grid (Putman and Lin, 2007) which reduces errors around polar regions. In comparison to the core used in Innes and Pierrehumbert (2022), the new version includes the up-to-date FV3 dynamical core[1]. Updates to the cubed-sphere edge handling result in less grid-imprinting than the previous version (Chen, 2021), where errors could accumulate at the interfaces between the six cubed-sphere faces.

6.1.1 Non-Dilute Dynamics

We allow for the condensible component of the atmosphere to be a large proportion of the atmosphere (e.g., $q \gtrsim 0.1$) where q is the mass mixing ratio of the condensible. To do this, several adjustments need to be made for the dynamical core, most of which are identical to those described in the supplementary materials of Pierrehumbert and Ding (2016).

To summarize, the thermodynamic conserved variable in the dynamical core is the virtual potential temperature:

$$\theta_v = T(1 + (R_v/R_d - 1)q)\left(\frac{p_0}{p}\right)^{\kappa}, \tag{6.1}$$

where R_v and R_d are the gas constants of the vapour and dry gases respectively, T is the temperature, p the pressure, and p_0 is a reference pressure (chosen to be 1 Pa). The value of the adiabatic index, κ, is given by $\overline{R}/\overline{c}_p$ where $\overline{R}$ and $\overline{c}_p$ are the local gas constants and

[1] https://github.com/NOAA-GFDL/GFDL_atmos_cubed_sphere/

specific heat capacities, given by

$$\overline{R} = (1 - q)R_d + qR_v \tag{6.2}$$

$$\overline{c}_p = (1 - q)c_{p,d} + qc_{p,v} \tag{6.3}$$

where $c_{p,d}$ and $c_{p,v}$ are the specific heat capacities of the dry and vapour components respectively at constant pressure. In calculations of the geopotential, Φ, we use the equation:

$$\delta\Phi = -R_d T_v \delta \ln p, \tag{6.4}$$

as opposed to the computationally more efficient version used in (Pierrehumbert and Ding, 2016)

$$\delta\Phi = -c_{pd}\theta_v \delta(p^\kappa), \tag{6.5}$$

which avoids the recalculation of T_v in the dynamical core. However, we note that Equation 6.5 is only strictly correct in the case where κ is constant with height. For example, if κ decreases sharply enough with increasing pressure, then Equation 6.5 does not guarantee that height decreases with increasing pressure, a clear violation of the hydrostatic equation. For example, in an extreme case consider an atmosphere that transitions from pure water in a layer at 2000 Pa ($\kappa_v = R_v/c_{p,v} \approx 0.29$) to pure hydrogen at 1000 Pa ($\kappa_d = R_d/c_{p,d} \approx 0.25$). Here $\delta(p^\kappa) = -0.83 < 0$, and the geopotential Φ would be non-monotonic with pressure.

In grid cells where precipitation or re-evaporation of water vapour occurs, the pressure thickness of the layer, δp, needs to be altered to reflect its change in mass. For a change in concentration of a tracer species δq_i, the updated pressure thickness, $\delta p'$, is given by:

$$\delta p' = \delta p\left(1 + \sum_i \delta q_i\right). \tag{6.6}$$

Each tracer index q_i must also be updated to reflect the change in mass of the layer, such that $\delta p(q_i + \delta q_i) = \delta p' q_i'$, i.e.:

$$q_i' = \frac{q_i + \delta q_i}{1 + \sum_i \delta q_i}. \tag{6.7}$$

Similar adjustments have been made to account for the condensation of CO_2 in the Martian atmosphere (Forget et al., 1998). We note that changes in water vapour and water condensates due to the convective adjustment scheme should *not* be considered in the sum over i in Equations 6.6 and 6.7, since the scheme is constructed such that the pressure thickness of each layer is unchanged despite mixing of water substances between the two (see Ding and Pierrehumbert, 2016).

6.1.2 Convective Adjustment

We use a convection scheme largely based on Ding and Pierrehumbert (2016) to remove convective instability. Consider a parcel of air at pressure level p_2 below layer p_1 where $p_1 < p_2$. Our method for triggering convection is as follows:

1. Test whether the parcel p_2 is above 100% relative humidity. If so, skip to step 5

2. Calculate the virtual temperature of a parcel of air lifted from p_2 to p_1 on the local dry adiabat (with adiabatic index $\overline{R}/\overline{c}_p$ where $\overline{R}$ and $\overline{c}_p$ are the local mass-weighted gas constant and specific heat capacities calculated at level 2, as in Equations 6.2 and 6.3). In our numerical framework, this is given by:

$$T_v' = T_2\left(\frac{p_1}{p_2}\right)^{\kappa}(1 + (R_v/R_d - 1)q_2). \tag{6.8}$$

3. Calculate the relative humidity in the parcel. If the parcel's relative humidity is above 100%, skip to step 5.

4. If the virtual temperature of the lifted parcel is greater than the local virtual temperature, $T_v' > T_{v1}$, then adjust the temperature of layers 1 and 2 to the dry adiabat in such a way that conserves the total enthalpy of the two layers and fully mixes the vapour and condensate components of the gases before and after convection (i.e., $q_1 = q_2$ post-convection).

5. If during steps 1 or 3 we encounter saturation, test for moist convection by first calculating the pseudo-moist adiabatic temperature gradient at layer 2, given by (Pierrehumbert, 2010):

$$\frac{\mathrm{d}\ln T}{\mathrm{d}\ln p} = \frac{\overline{R}}{\overline{c}_p}\frac{1 - q + L/(\overline{R}T)q(1 - \varpi q)}{1 - q + L/(\overline{c}_p T)\beta q(1 - \varpi q)} \equiv \kappa_m, \tag{6.9}$$

where L is the latent heat of the phase change involved (either sublimation or vaporization depending on the temperature), $\beta \equiv \mathrm{d}\ln p_{\mathrm{sat}}/\mathrm{d}\ln T$ is the gradient of the phase boundary for water and $\varpi \equiv 1 - R_d/R_v$, such that $\varpi > 0 (< 0)$ for condensibles with mean molecular weights greater than (less than) the background mean weight.

6. Calculate the virtual temperature of a parcel of air lifted from p_2 to p_1 with gradient κ_m. If this virtual temperature, T_v', is greater than the surrounding air, then the enthalpy-conserving moist adjustment process described in Ding and Pierrehumbert (2016) is carried out. This retains the hydrostatic pressure of each layer and creates condensate ready to be rained out in the precipitation scheme.

This process is iterated pairwise over layers upwards from the bottom of the atmosphere and downwards from the top of the atmosphere multiple times until the temperature converges. Using the virtual temperature to test for stability inherently accounts for gradients in mean molecular weight which can inhibit convection in hydrogen-dominated atmospheres (e.g., Guillot, 1995; Leconte et al., 2017; Li and Ingersoll, 2015; Innes et al., 2023).

The logic and structure of the scheme is illustrated in Figure 6.1.

6.1.3 Large-Scale Condensation

In convectively stable regions of the atmosphere, large scale motions and radiative cooling can create super-saturated regions.

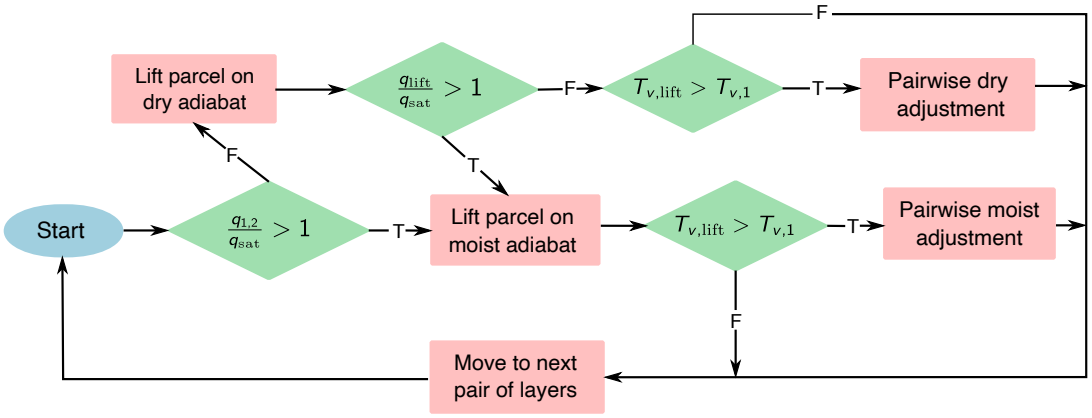

Figure 6.1: Flowchart illustrating the logical structure of the moist convection scheme.

When a super-saturated cell in the model is encountered, the specific humidity is relaxed to the saturation value such that the enthalpy of the cell is conserved:

$$h_d(T)m_d + h_v(T)m_v + h_c(T)m_c = h_d(T')m_d + h_v(T')m'_v + h_c(T')(m_v - m'_v + m_c) \tag{6.10}$$

$$m'_c = m_c + m_v - m'_v, \tag{6.11}$$

where the h_i and m_i refer to the respective enthalpy and masses of species i (where v, c and d refer to vapour, condensate and dry components) and primed variables represent quantities after condensation. Since the end mass of vapour, m'_v, is a non-linear quantity in final temperature T', we solve Equation 6.10 with a Newton iteration.

6.1.4 Precipitation

We use a very simple precipitation scheme where all of the condensate is rained out immediately after it has formed, either via moist convection or large scale condensation (as described above). To do this in a mass and enthalpy-conserving way, we iterate from the top of the atmosphere downwards. If there is condensate in a layer, it is removed and transported to the first layer below it with under 90% relative humidity. We then attempt to re-evaporate it in this layer in an enthalpy-conserving way by solving an equation

similar to 6.10. If during this process we create super-saturation in the layer, we avoid a computationally expensive iteration to find the correct amount of re-evaporation by simply moving the condensate to the next layer down and attempting re-evaporation there. This scheme requires that we have at least one under-saturated layer near the bottom of the atmosphere that can sustain the re-evaporation of precipitation without becoming supersaturated. In practice, for sub-Neptunes with no distinct surface, we can set the bottom boundary pressure of the model high enough that this is always the case, since the high pressures and temperatures at the bottom of the atmosphere create undersaturated regions.

6.1.5 Radiative Transfer

We use a simple semi-grey scheme based on the method of short characteristics (Olson and Kunasz, 1987), with one band in the longwave and one band in the shortwave part of the spectrum. We calculate the optical depth of the atmosphere, τ, as:

$$\mathrm{d}\tau_i = (\kappa_{v,i} q + \kappa_{d,i}(1-q))\left(f_i + (1-f_i)\frac{p}{p_0}\right)\frac{\mathrm{d}p}{g}, \tag{6.12}$$

where $\kappa_{v,i}$ and $\kappa_{d,i}$ represent the opacities of the moist and dry components of the atmosphere respectively in band i. The parameter f_i defines a fraction of the opacity in band i that is proportional to pressure, accounting for the presence of collision-induced absorption molecules in the atmosphere (notably hydrogen and water). Although this f_i parameter could be different for the vapour and dry species, we opt to keep it fixed between the components of the atmosphere for simplicity's sake. We define the reference pressure p_0 as the pressure at the bottom of the atmosphere, 30 bar, and g is the gravitational acceleration.

The benefit of using a semi-grey scheme over a more complex correlated-k treatment of the radiative transfer is its computational simplicity, which allows us to run a much larger suite of simulations. Moreover, we wish to focus mostly on the effect

of latent heat release and water vapour on the atmosphere, and a simplified radiation scheme makes it easier to disentangle the effects of latent heating on the atmosphere. A more realistic radiative transfer scheme would allow for cooling in the window regions of molecular spectra and more accurately reflect the pressure and temperature dependence of the opacities.

We choose values for the water vapour opacities from Menou (2012) and a value of f_{LW} that results in a pure-steam atmosphere reproducing the OLR of a pure steam atmosphere calculated with a real gas model (i.e., the runaway greenhouse limit of $\approx$ 280 W m^{-2}). For our choice of dry opacities and f_{SW}, we tune our grey gas model to reproduce a more sophisticated correlated-k calculation performed using the HELIOS radiative transfer code (Malik et al., 2017, 2019). The HELIOS calculation was performed for the exoplanet K2-18 b with 100x solar metallicity in Tsai et al. (2021).

Similar to the model used to simulate temperature-pressure profiles in Chapter 5, HELIOS finds temperature-pressure profiles in radiative-convective equilibrium using the correlated-k technique and finding two-stream fluxes based on the method of Toon et al. (1989). Radiative-convective equilibrium is found through an accelerated-timestepping method. There were 130 vertical levels between 10^{-3} and 10^{8} Pa. The fixed chemical composition used in the calculation was found using the VULCAN photochemical model (Tsai et al., 2017). The computation of this temperature-pressure profile was not performed by the author of this thesis, but the data was used with the permission of S.M. Tsai.

In Tsai et al. (2021), the water mass mixing ratio was approximately 0.35 for 100x solar metallicity. Since we wish to model the effects of non-dilute water vapour in the atmosphere, we use a value for the dry opacity that reflects the increased abundance of other absorbers (e.g., CH_4, CO, CO_2 etc.) in the high-metallicity atmospheres in which high-water vapour concentrations would be found (in contrast to Chapter 3 where a 1x solar metallicity value was used). The values chosen for our opacities can be found in

Parameter	Value	Unit
$\kappa_{v,LW}$	2.0×10^{-2}	$m^2\,kg^{-1}$
$\kappa_{v,SW}$	4.0×10^{-4}	$m^2\,kg^{-1}$
$\kappa_{d,LW}$	2.0×10^{-3}	$m^2\,kg^{-1}$
$\kappa_{d,SW}$	2.0×10^{-5}	$m^2\,kg^{-1}$
f_{LW}	0.8	—
f_{SW}	0.2	—

Table 6.1: Parameters for the radiative transfer in our model

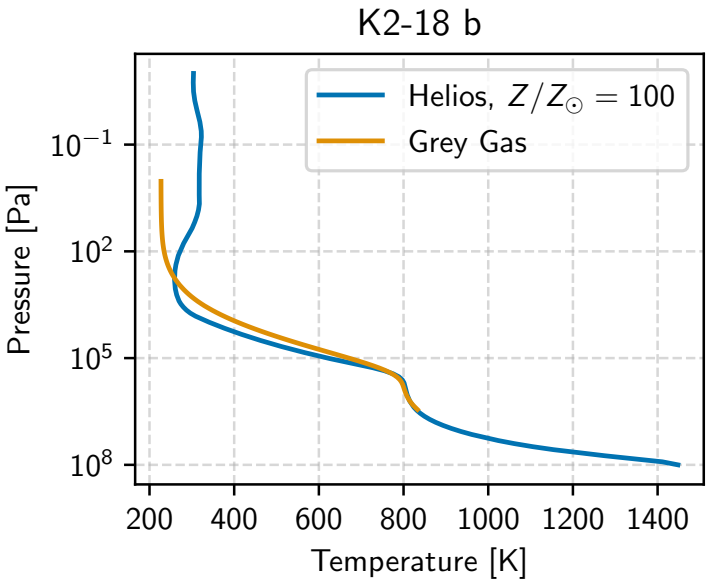

Figure 6.2: Comparison of a real gas model for K2-18 b with 100x solar metallicity (blue) to our grey gas model (orange).

Table 6.1 and a comparison with the real-gas model can be found in Figure 6.2.

6.1.6 Model Parameters

In this section we describe our set of test experiments with the new dynamical core. We have chosen to model one planet with a fixed radius and rotation rate, and vary only the deep water vapour content of the atmosphere. We set up the GCM to model a K2-18 b-like sub-Neptune with similar parameters to the CAMEMBERT sub-Neptune GCM intercomparison project (see Table 2 of Christie et al., 2022). The planetary parame-

ters are derived from Cloutier et al. (2019) and Benneke et al. (2019b). We use a physical timestep of 1800 s split further into 16 dynamical timesteps for computational efficiency (following Komacek and Abbot (2019)). We use the C32 cubed-sphere grid which corresponds to an approximate horizontal resolution of 2.85° in both latitude and longitude. We assume that the background dry gas is a solar metallicity H_2-He mix, giving a He mass fraction of 0.25188 and a H_2 fraction of 0.74812 (Asplund et al., 2009). To induce condensation, we model a planet with half the instellation of K2-18 b, i.e. $S = 685$ W m^{-2}. Note since we do not include short wave scattering in our model, this is analogous (but not identical) to studying K2-18 b with a Bond albedo of 0.5.

To demonstrate the effect of latent heating and moisture on the dynamics, we vary the water vapour concentration of the deep atmosphere from 0.0 (dry) to 0.7 (extremely non-dilute). To isolate the effect of mean-molecular weight gradients and latent heating on the dynamics, we also include a case where we switch off the effect of moisture on the opacity of the gases (we label these cases "H_2O radiatively inactive" and "H_2O radiatively active" respectively). We fix the value of q in the opacity equation (Equation 6.12) to 0.35 everywhere (representing 100x solar metallicity). Table 6.2 summarises the model parameters used. The C32 cubed-sphere grid was used, giving an approximate horizontal resolution of 3°. The vertical levels were equally spaced logarithmically between 1 and 3×10^6 Pa In the following results section, we will refer to our runs using the labels *qx_{rad,norad}* where *x* refers to the deep water vapour content of the atmosphere and the label "rad" or "norad" refers to whether the water vapour is radiatively active ("rad") or not ("norad"). For example, *q0.1_norad* refers to the experiment with deep water vapour content $q_{\mathrm{deep}} = 0.1$ and no radiatively active water vapour.

6.2 Preliminary Results

Parameter	Value	Unit
Planetary Parameters		
Gravitational field strength	12.4	$m\,s^{-2}$
Planetary radius	1.5×10^8	m
Rotation period	32.94	Earth days
Instellation	685	$W\,m^{-2}$
Atmospheric Parameters		
Dry mean molecular weight	2.288166	$g\,mol^{-1}$
Deep water concentration	**0.0, 0.1, 0.3, 0.5, 0.7**	$kg\,kg^{-1}$
Top Boundary Pressure	1	Pa
Bottom Boundary Pressure	3.0×10^6	Pa
Moist opacity	**On, Off**	—
Numerical Parameters		
Physical timestep	1800	s
Dynamical timestep	112.5	s
Cubed sphere resolution	C32	—
Vertical Resolution	50	Number of levels
Total run time	10000	Earth days

Table 6.2: Model parameters for our suite of GCM runs. Bold quantities highlight parameters that are varied between our model runs

6.2.1 Temperature and Moisture Profiles

First we examine the vertical temperature and moisture profiles at

different locations in the atmosphere. We choose to show only the profiles for the *q0.5_norad* and *q0.5_rad* experiments since these are qualitatively similar to the other simulations. Figure 6.3 shows the temperature, specific humidity and relative humidity at longitudes $\lambda = \{0°, -180°\}$ and latitudes $\phi = \{0°, 80°\}$, where the substellar point is located at $(\lambda, \phi) = (0°, 0°)$. Temperatures are very uniform horizontally, showing a maximum deviation of around 10 K from the global average in both experiments. The *q0.5_norad* experiment was initialised with a radiative equilibrium profile assuming global heat redistribution, and the final temperature profile is very close to the initial condition. The *q0.5_rad* experiment is cooled slightly compared to the initial condition, likely due to the loss of moisture from the upper atmosphere which reduces the

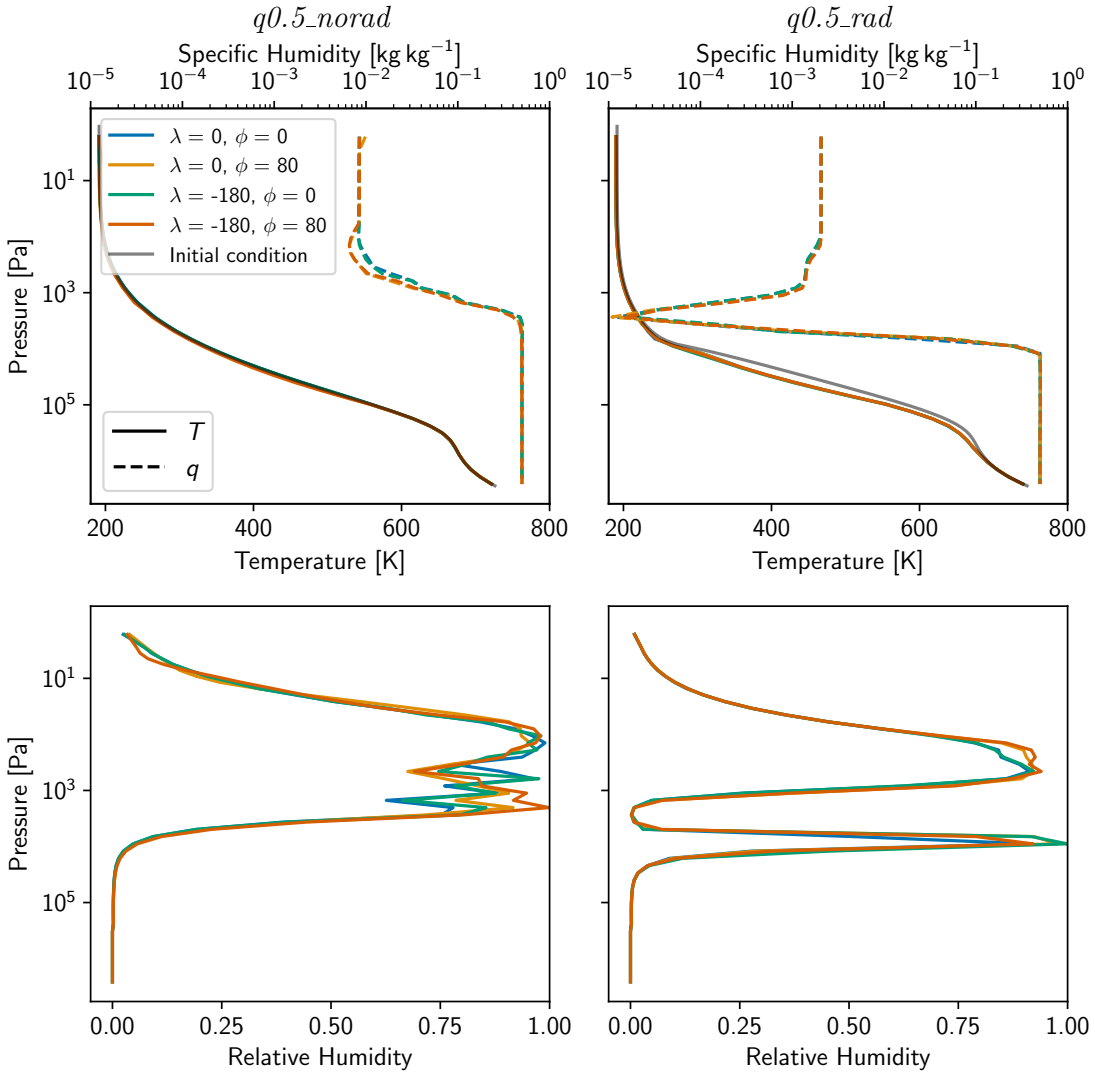

Figure 6.3: Temperature, specific humidity and relative humidity profiles for the *q0.5_norad* and *q0.5_rad* experiments at different longitudes (λ) and latitudes (ϕ). The temperature profiles (top row, solid lines) are horizontally uniform and vary ≈ 10 K at maximum from the global average. Likewise, the specific humidity (top row, dashed line) is also very horizontally uniform, but varies from equator to pole at around the 100 - 1000 Pa level in the *q0.5_norad* experiment. In the *q0.5_rad* experiment, the specific and relative humidities (bottom row) drop significantly above the condensation layer at around 10^4 Pa.

longwave optical depth. The temperature profile is also affected by the presence of dry convection (see Section 6.2.3). The presence of weak horizontal temperature gradients is consistent with the analysis provided in Section 3.2.2, in which we demonstrated that temperate, tidally-locked sub-Neptunes are likely to exhibit weak temperature gradients owing to their slow rotation rate and long radiative timescales.

Both runs also show horizontally uniform specific humidities, with horizontal variations only seen in the *q0.5_norad* experiment at high latitudes. Profiles of specific humidity in both cases drop from the deep value of 0.5 between 10^3 and 10^4 Pa, where the maximum value of the water vapour concentration is controlled by its saturation value at that temperature and pressure. Whereas in the *q0.5_norad* experiment the moisture drops its deep value to its upper atmospheric value of around 0.01 (unchanged from the initial condition) relatively smoothly, there is a strong depletion of water vapour at the 3000 Pa level in the *q0.5_rad* experiment. This is also reflected in the relative humidities. The *q0.5_norad* experiment shows a high relative humidity of > 70% at levels above the base of the cloud deck (peaking again at around 100 Pa), but the *q0.5_rad* run shows a steep drop off in the humidity above the cloud base to a minimum of 0.001 at 3000 Pa. Relative humidity then increases again to reach a maximum of around 90% at 100 Pa. We are currently unsure of the mechanism responsible for generating this depletion in water vapour, since its partial pressure is well below the value of the saturation vapour pressure, $p_{\mathrm{sat}}(T_{\mathrm{min}})$, where T_{min} is the minimum instantaneous temperature during the run. To understand why this undersaturated layer forms, one would have to study the moisture fluxes in the model, which we leave to future work.

6.2.2 Zonal Winds

Figure 6.4 shows the zonal mean zonal winds for the ten experiments. The dry *q0.0* experiments (top row) exhibit similar high-latitude jets to those seen in Chapter 3. In the absence of moisture we should expect the simulations to be in a similar regime to the PKh experiment in Chapter 3. The jet structures are qualitatively similar except from the absence of the equatorial superrotating jet in the upper atmosphere in the *q0.0_norad* in comparison to the PKh experiments. The maximum mean jet speed is also lower ($\approx$ 100 m s^{-1} compared to $\approx$ 300 m s^{-1}). We note that we have run this set of experiments for only half the length of time as the results in Chapter 3 (which were run

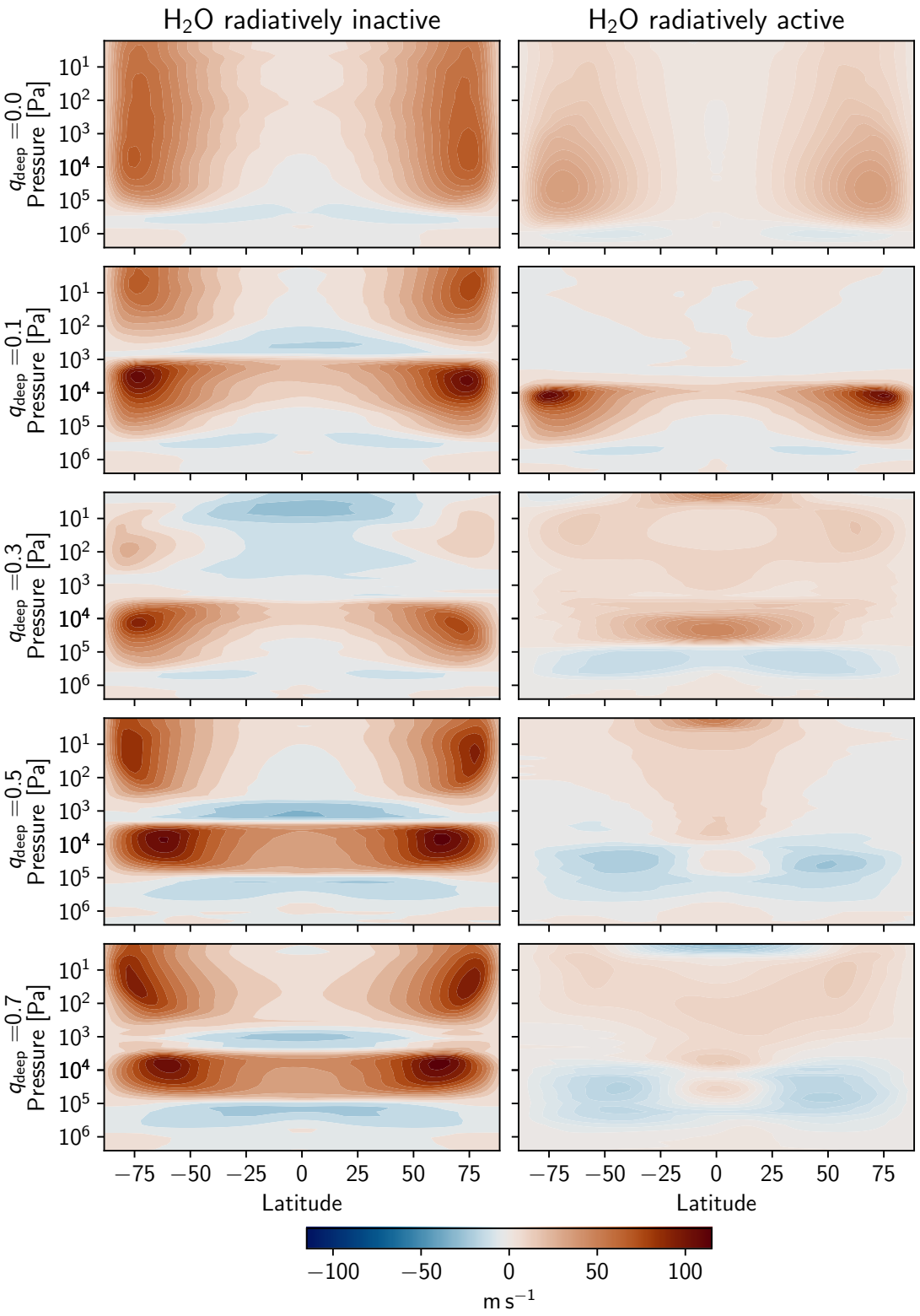

Figure 6.4: The zonal mean zonal wind. Left: Radiative effect of H_2O not included. Right: Radiative effect of H_2O included.

for 20000 Earth days) in order to facilitate simulating a wider range of deep moisture contents. Therefore, it is possibles the models models may not have fully equilibrated to their final states.

The run *qo.o_rad* has lower wind speeds, mainly because stellar radiation is absorbed lower in the atmosphere in this case (owing to the low opacity of the dry gas). The greater density of the lower layers requires more energy to accelerate winds of similar magnitude to the winds at lower pressures in *qo.o_rad*. Considering the radiatively inactive cases first, the predominant trend in the zonal winds on increasing the deep water vapour content is the disruption of the high-latitude jets centred polewards of ±60° latitude. This is the result of the "humidity wind" effect discussed in Chapter 2, where the reversal of the virtual temperature gradient between equator and pole reverses the vertical wind shear. This can be summarised in the equation:

$$\frac{\partial \ln T_v}{\partial \phi} = (1 - \varpi \beta q) \frac{\partial \ln T}{\partial \phi}. \tag{6.13}$$

where $\beta \equiv L/R_v T$ and $\varpi \equiv 1 - \mu_d/\mu_v$ as defined previously. When the value of the specific humidity is greater than $1/(\varpi\beta)$, virtual temperature gradients are opposite in sign to gradients in thermodynamic temperature. Figure 6.5 illustrates how the wind speed in the high-latitude jets in the *qo.7_norad* experiment drops when entering the region where the water vapour concentration is falling with increasing height due to condensation (left panel). The zonally averaged heating contrast between equator and pole causes a decrease in thermodynamic temperature moving polewards away from the equator (right panel). However, the corresponding drop in specific humidity causes the virtual temperature to *increase* between the equator and pole. The vertical wind shear implied by Equation 2.34 is therefore negative, as seen in Figure 6.4. For the *norad* simulations, as the deep water vapour content of the atmosphere is increased, the jets below the negative shear layer become more constricted in height and move towards lower latitudes. In all cases there is superrotation at the equator at the level of the

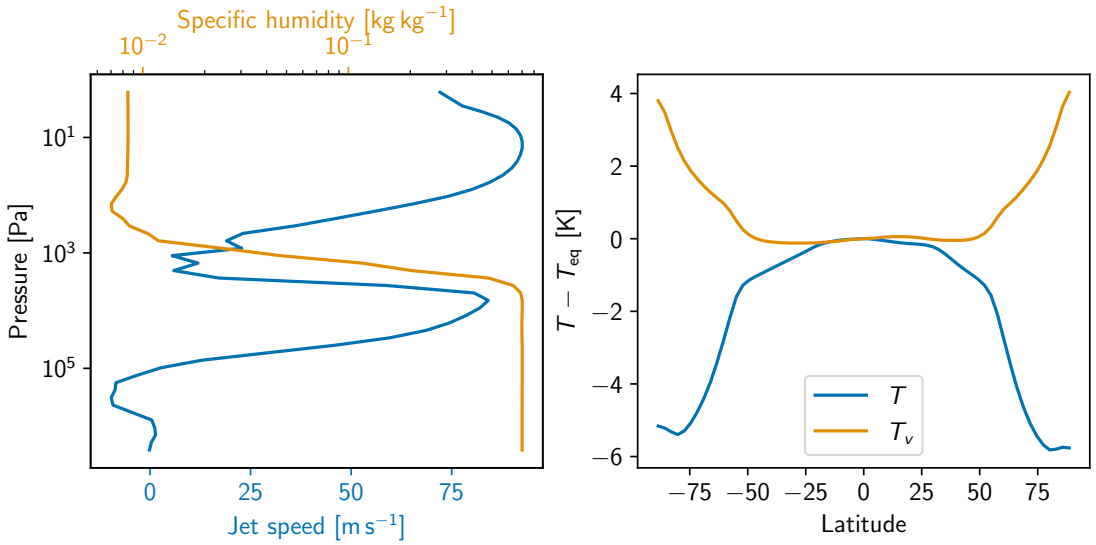

Figure 6.5: Left: The zonal wind speed of the high latitude zonal jet (blue) and the specific humidity (orange) for the *q0.7_norad* experiment. The pressure level of the reversal in the vertical shear of the jet corresponds to the weather layer in the model where condensation occurs. Right: The zonally averaged temperature (T) and virtual temperature (T_v) at the 5000 Pa. Values are displayed relative to their value at the equator. Although the thermodynamic temperature drops between the equator and the poles, the virtual temperature increases.

high-latitude jets that strengthens with the addition of more water vapour to the deep atmosphere.

In the *rad* experiments, we find similar high-latitude jets only for the *q0.0_rad* and *q0.1_rad* experiments, which qualitatively look similar to the *norad* set of experiments. In both cases the maximum jet speed is at higher pressures because the shortwave absorption in the atmosphere occurs at higher pressures. In the *rad* experiments, the opacity is linked to the water vapour content, and the dry component has low opacity (see Table 6.1), which explains this change. The relative dryness of the upper atmosphere (and subsequent lack of shortwave absorption there) also explains the reduced wind speeds in this region.

As the deep water vapour content of the atmosphere increases from 0.1 to 0.3, there is a change in the circulation structure, with high-latitude jets replaced with a single, weak superrotating jet at the equator. Increasing the deep water vapour concentration further to 0.5 and 0.7 replaces the single jet with two weaker jets above and below ≈ 200

mbar of the same strength as the weak prograde motion in the upper atmosphere.

To understand the nature of the circulation better, we plot the temperature anomaly (deviation from the horizontal mean temperature) at 100 mbar for all the experiments (Figure 6.6). The *norad* experiments exhibit structure similar to the dry experiments presented in Chapter 3, with weak temperature gradients everywhere apart from at vortices near or at the poles. The temperature contrast reaches a maximum magnitude of $\approx$ 15 K between the equator and the polar vortices in the *q0.7_norad* experiment. A similar structure is seen for the *q0.0_rad* and *q0.1_rad* experiments. A significant change is seen on moving to the *q0.3_rad* experiment, where the high latitude jet structure is replaced by a Matsuno-Gill like pattern (Matsuno, 1966; Gill, 1980), reminiscent of the wave structure seen in shallow water models of exoplanet atmospheres (e.g., Showman and Polvani, 2011; Hammond and Pierrehumbert, 2018). At higher deep water contents, the flow is organised into a strong day-night circulation with the main temperature contrast being between the substellar and antistellar point. The transition from high latitude zonally symmetric flow to day-night flow in the *rad* experiments can be understood by inspecting the diabatic heating rates due to radiative transfer (Figure 6.7). For all experiments other than the *q0.3_rad*, *q0.5_rad* and *q0.7_rad* experiments, there is radiative heating on the dayside and cooling on the nightside, with the structure around 1000 to 10000 Pa altered by the dynamics somewhat. However, a qualitative shift is seen in the atmosphere of the *q0.{0.3,0.5,0.7}_rad* experiments, where there is strong radiative cooling at levels directly above the condensation layer, and strong radiative cooling below. In the cooling layers, the cooling extends onto the dayside. Likewise, in the heating layers, the heating extends onto the nightside. Inspection of the vertical profiles of the radiative fluxes show that the contrast in heating and cooling is due to the variation in longwave fluxes. The strong heating contrast is caused by the sudden increase in longwave opacity on moving from a dry layer (with $\kappa \approx \kappa_d$) to one where the opacity is order of magnitudes greater ($\kappa \sim \kappa_v \gg \kappa_d$). The strength of this radiative forcing is an order

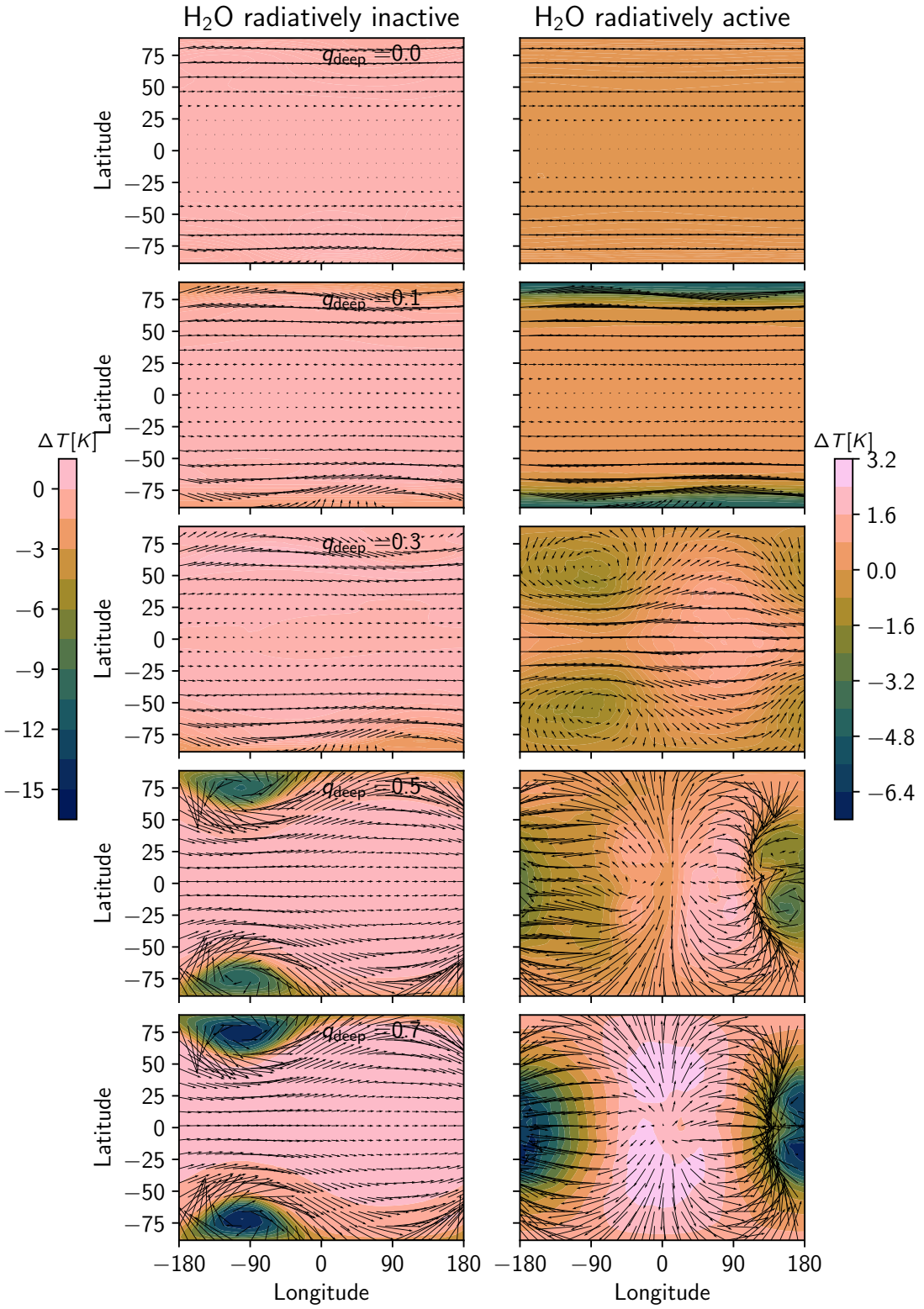

Figure 6.6: Temperature anomaly at the 10^4 Pa level. The *norad* experiments exhibit a drop in temperature near high-latitude vortices. The *rad* experiments transition from zonal flow to day-night flow as the water vapour concentration increases, with the *q0.3_rad* case showing a stationary wave pattern.

of magnitude higher than in the other experiments with lower water vapour content or with no radiatively active H_2O. The strength of the vertical motions in an atmosphere that has weak temperature gradients is given by:

$$\omega \frac{\partial \theta}{\partial p} = \dot{Q} \frac{\theta}{c_p T}, \tag{6.14}$$

which can be derived from Equation 2.4d in the steady state by neglecting horizontal variations in potential temperature. In particular, for a constant stratification, $\partial\theta/\partial p$, the quantity $\partial\omega/\partial p = -\nabla \cdot_p \boldsymbol{u}$ i.e. the strength of the divergence, approximately scales with the vertical gradient of the heating rate, $\partial\dot{Q}/\partial p$. This suggests we may expect stronger divergent (i.e., day-to-night) circulation in the presence of a strongly vertically varying heating rate.

6.2.3 Validation of Hydrological Cycle

Convection

We now inspect the validity of the convection scheme described in 6.1.2. In the *norad* experiments, the convective adjustment scheme is never triggered. The radiative equilibrium temperature profiles are stable to dry convection but have lapse rates greater than the moist adiabat. However, moist convection is never triggered for two reasons. Firstly, in oversaturated regions with lapse rates greater than that of the moist adiabat, the water vapour content is greater than the critical value required to shut off convection, i.e. $q > 1/(\beta\bar{\omega})$ (see Equation (2.32)). In these regions, compositional gradients stabilise the atmosphere. Secondly, the atmosphere directly above the region where condensation first occurs is undersaturated, and therefore cannot be unstable to the adjustment scheme described in 6.1.2. Supersaturation in this region requires either radiative cooling or strong upwelling motions from the large scale circulation. Neither of these mechanisms are present in the *norad* experiments.

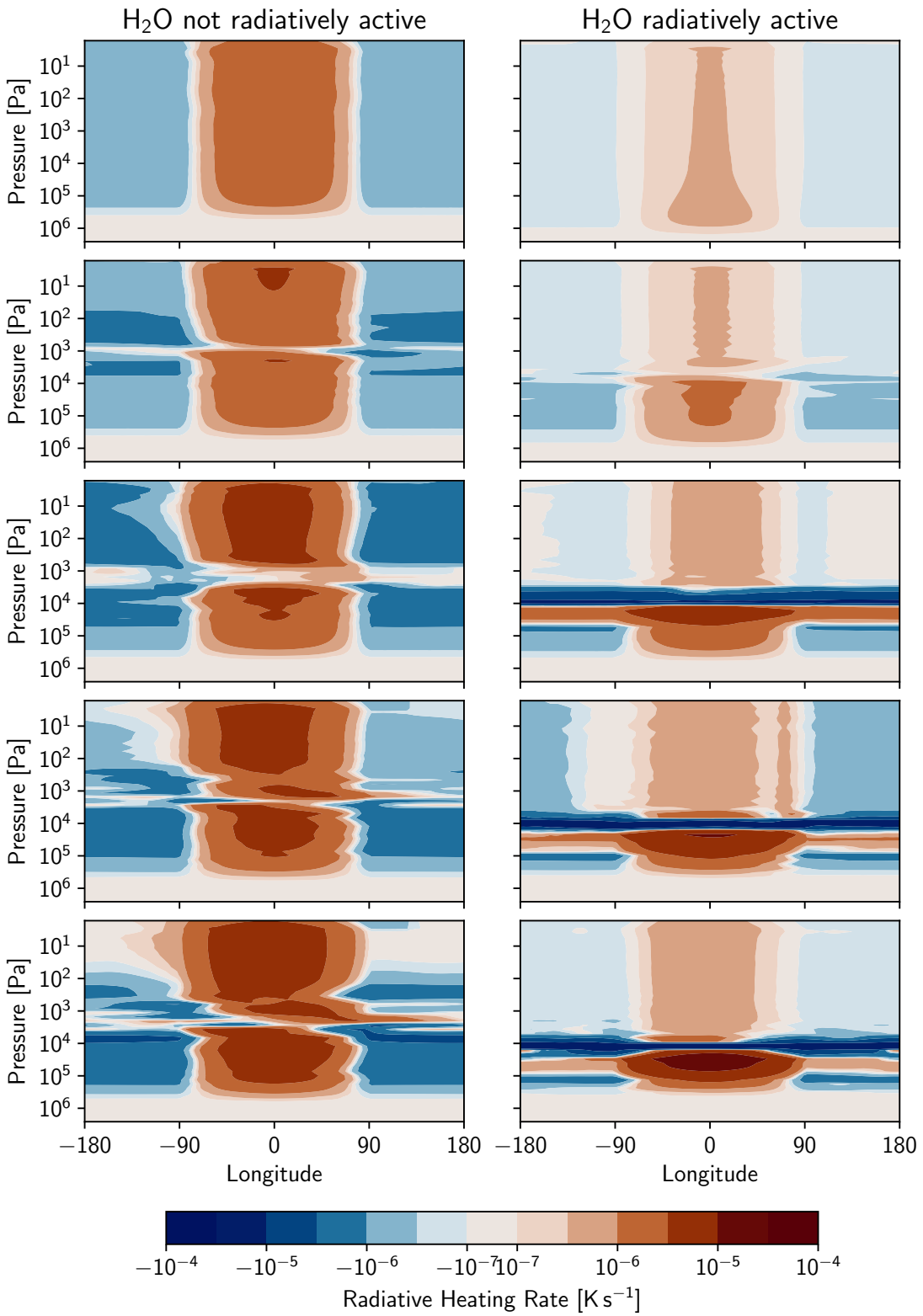

Figure 6.7: Radiative heating rates. In *rad* experiments where there is a strong opacity contrast between the dry upper layers and the moist lower layers, there is strong heating and cooling around the level of condensation.

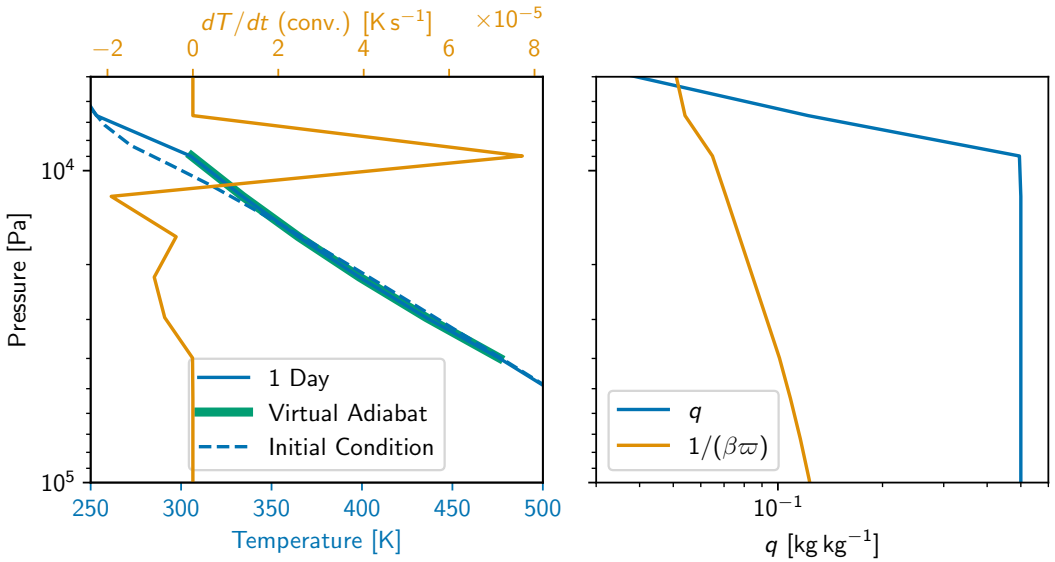

Figure 6.8: Left: The substellar temperature profile at t = 0 days (dashed blue) and t = 1 days (solid blue) for the *q0.5_rad* experiment. The initial profile is in radiative equilibrium and is unstable to dry convection. The convective heating rates (orange) show that the adjustment scheme removes this instability by heating the upper layers and cooling the lower layers, transporting heat upwards in an enthalpy-conserving manner. The end profile is a dry virtual adiabat (thick green line). Right: The specific humidity profile in the layer (blue) and the critical water vapour content above which convection is inhibited (orange). Convection is inhibited in regions where $q > 1/(\beta\varpi)$, and cannot occur in the regions where $q < 1/(\beta\varpi)$ because the atmosphere is undersaturated.

In the *rad* experiments, dry convection is present in experiments *q0.3_rad*, *q0.5_rad* and *q0.7_rad*. The superadiabatic lapse rates are induced by the the sharp increase in opacity on moving downwards from the dry upper atmosphere to the moist lower atmopshere. Figure 6.8 shows the temperature and moisture profiles in the convective region of the *q0.5_rad* experiment at the substellar point at times t = 0 (left panel, dashed blue) and t = 1 day (solid blue). The initial profile is in pure radiative equilibrium, and the dry adjustment scheme acts to remove the superadiabatic regions. The adjusted profile after 1 day lies on the "virtual adiabat", given by:

$$T(p) = T(p_0) \exp\left[\int_{p_0}^{p} \frac{\overline{R}(p)}{\overline{c}_p(p)} \, \mathrm{d}p\right], \tag{6.15}$$

where p_0 is the pressure at the base of the adiabat. This temperature profile is stable to infinitesimal displacements but only stable to finite displacements when $\overline{R}/\overline{c}_p$ is con-

stant within the layer (see Habib and Pierrehumbert (2023) for a more detailed discussion). The convective heating rate (left panel, orange line), shows that the net effect of the adjustment is to heat the upper layer and cool the lower layer, corresponding to an upwards heat flux. Immediately above the dry convection layer, there is a discontinuity in the lapse rate, which is much higher than the dry adiabatic lapse rate. This layer is stabilised by compositional gradients. To understand this effect, we can inspect the specific humidity profile (right panel of Figure 6.8). Water vapour concentration is approximately constant in the dry convecting layer (recall the dry adjustment scheme explicitly mixes the water vapour profile towards a fully mixed state) but drops in the layer immediately above. In this layer, $q > 1/(\beta\varpi)$ and the atmosphere is stable by the criterion in Equation 2.32. Above the stabilised layer, the atmosphere is undersaturated and has a lapse rate stable to the dry adiabat, so no convection occurs there.

Large-Scale Condensation

The time-averaged mean state of the all the simulations has regions of large scale condensation in all moist experiments apart from the *q0.3_norad* experiment, where no large-scale condensation occurred in the 100 days over which the output was averaged. Figure 6.9 shows the temperature tendency due to large-scale condensation at the level of maximum tendency for each experiment. For the *norad* experiments, large scale condensation becomes significant only in the *q0.5* and *q0.7* experiments, where the condensation is concentrated in the cold cores of the high-latitude vortices. By inspecting the vertical velocities in the cores of the vorticies, we can see that the condensation is induced by upwards vertical velocities in the centre of the vorticies. In the *rad* experiments, for $q_{\text{deep}} \geq 0.3$ large scale condensation occurs globally (note there is no retained condensate in the model, so condensation rates reflect local condensation). In the *q0.3_rad* experiment, there is an area of greater condensation at 90° E at the equator, corresponding to an area of convergence and upwelling. For the *q0.5* and *q0.7* exper-

iments, the large scale condensation is strongest on the nightside, where the radiative cooling is strongest (see Figure 6.7) and in regions of strong upwelling on the dayside. The time-averaging of the results in Figure 6.9 obscures the time variability of large-scale condensation, particularly in the *rad* experiments with $q_{\text{deep}} > 0.1$. Whereas the time-averaged condensation pattern suggests a global uniform background level of condensation, in reality condensation is spatially heterogeneous and appears in storm-like outbursts which vary in space and time. This variation would be important in determining the impact of cloud cover on observations of temperate sub-Neptunes. For example, spatial patchiness and time variability may mean that several transit observations are required to capture cloud properties.

6.3 Discussion

6.3.1 Dynamics

In Section 6.2 we gave a brief overview of the range of dynamics seen across a range of deep water contents in the atmosphere of a temperate sub-Neptune. The dry experiments, *q0.0_norad* and *q0.0_rad* exhibit similar dynamics to the results presented in Chapter 3, and give us confidence that there has been minimal impact in updating the dynamical core of the GCM. In the *norad* experiments, we demonstrated that compositional gradients can cause the sign of horizontal virtual temperature gradients to be opposite to the thermodynamic temperature gradients. The resulting reversal in zonal wind shear causes a separation between high latitude jets in the lower atmosphere and zonal jets aloft. The virtual effect is also seen in the circulation of the *rad* experiments with day-to-night flow, however it is less clear how this affects the circulation, since most of the return flow occurs below the level of condensation. In all the experiments with water vapour present, there is a separation between the dynamics above and below the weather layer. We posit that this is due to a compositionally-induced inversion in

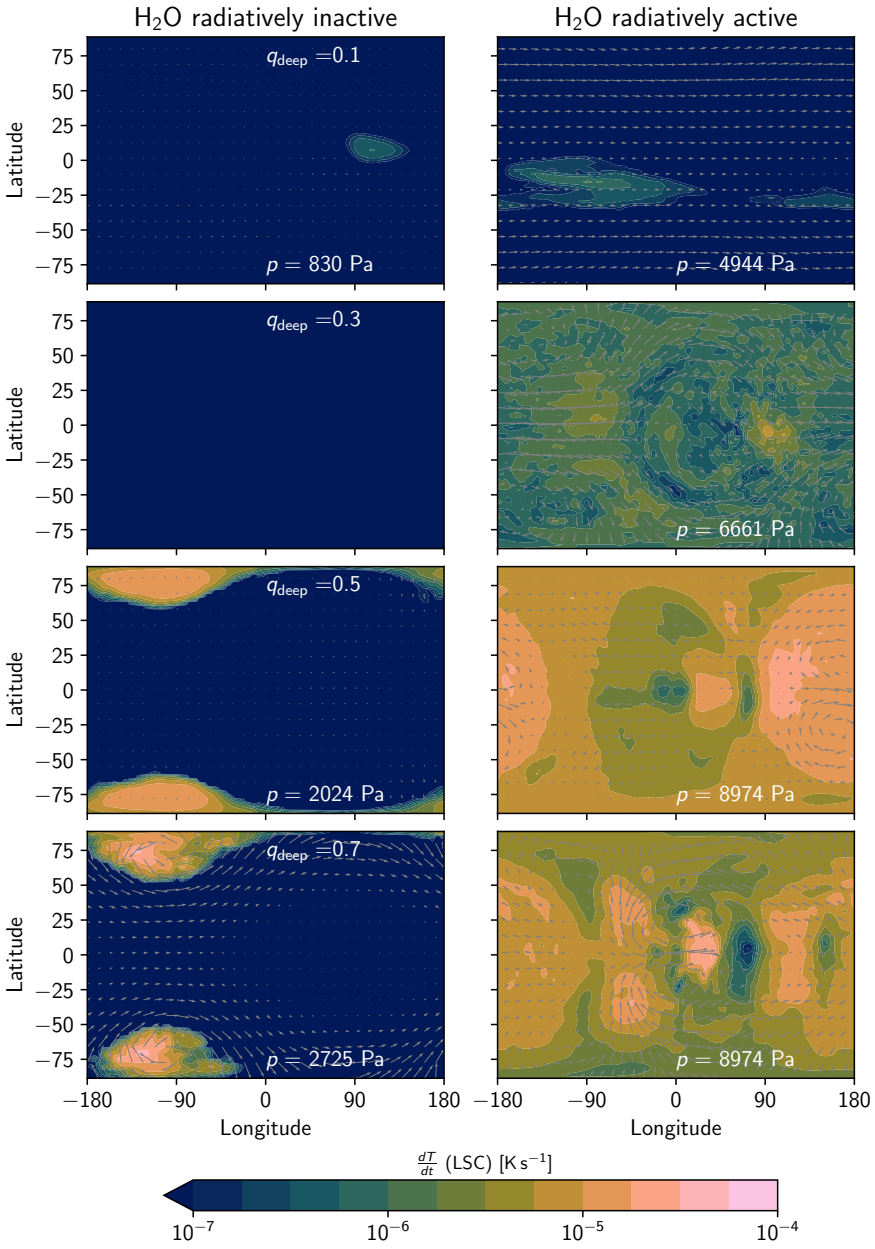

Figure 6.9: Large scale condensation temperature tendency at the pressure level of the maximum tendency for each experiment. The *q0.3_norad* experiment saw no condensation over the 100 day averaging period. In the *norad* experiments, condensation occurs due to upwelling in the high-latitude vortices. In the *rad* experiments, large scale condensation is induced globally for $q_{\text{deep}} > 0.1$. The largest tendencies occur where the radiative cooling is strongest or upwards vertical velocities are greatest.

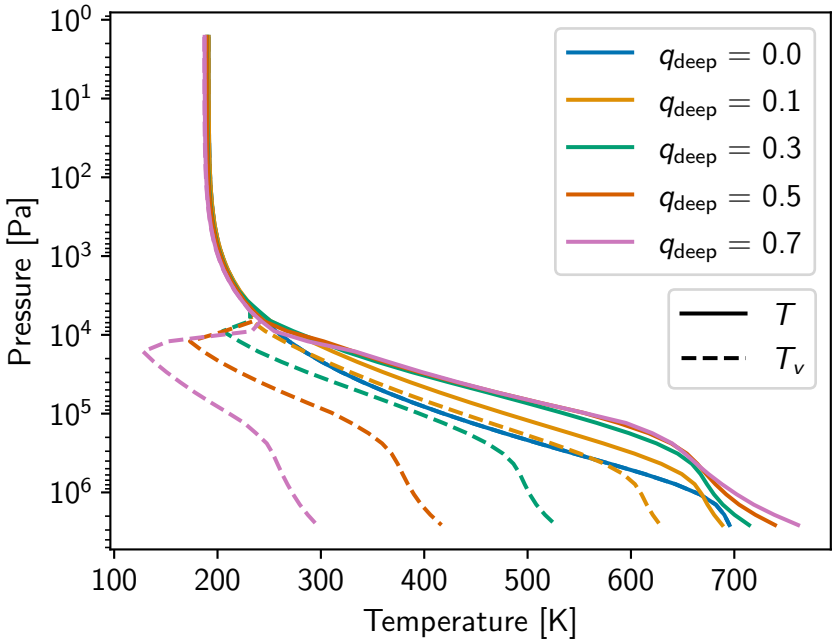

Figure 6.10: Globally-averaged temperature profiles (solid lines) and virtual temperature profiles (dashed lines) for the *rad* experiments. Condensation induces an inversion in the virtual temperature profiles at around 10000 Pa due to compositional stratification.

virtual temperature that occurs in the weather layer, where a sudden drop in vapour composition from $\mathcal{O}(1)$ to $<< 1$ results in a corresponding increase of the virtual temperature on the order of:

$$\Delta T_v \approx T \varpi q_{\text{deep}}, \tag{6.16}$$

which evaluates as a jump of order 10 K for $q_{\text{deep}} = 0.1$, $T = 250$ K and a jump of order 100 K at $q_{\text{deep}} = 0.7$. Figure 6.10 shows this inversion for all of the *rad* experiments with $q_{\text{deep}} > 0$. This inversion acts like a "lid" to the dynamics (c.f. capping inversions in the Earth's boundary layer), reflecting waves and preventing mixing between the regions above and below the inversion.

A surprising finding of the experiments was the dominant effect of including the radiative effect of water vapour on the dynamics. The circulations of the *q0.5_rad* and *q0.7_rad* runs exhibit much stronger divergent day-to-night flow than the rest of the experiments. These experiments also show much more time variability in the flow, a result of the complex interaction between the temperature field, the water vapour tracer

and the radiative forcing that is absent in the *norad* experiment, where the vapour field only interacts with the temperature field and is independent of the radiation scheme. More work is needed to fully understand what causes this regime change in the flow. In particular, to bridge the gap between the *rad* and the *norad* experiments, we could run a simulation where the optical depth is horizontally uniform and has a step in the vertical direction corresponding to a sharp increase in water vapour content in the weather layer. This would allow us to understand if the change in dynamics is linked to the vertical profile of heating and cooling, or related to the coupling of the opacity to the non-dilute water component of the atmosphere.

In Chapter 3 we highlighted the discrepancy between the circulation structures of our idealised, dry simulations in comparison to those in Charnay et al. (2021), who use the LMD Generic GCM to simulate K2-18 b over a range of metallicities and rotation rates. In their simulations, which include clouds and non-grey radiative transfer, the large scale circulation is largely day-to-night, even at low water vapour contents. Their simulations, run at twice the incoming stellar irradiation as our experiments, have limited condensation in the upper atmosphere. They are therefore difficult to compare directly to our simulations, where the transition to day-to-night flow occurs in simulations the vapour content of the atmosphere changes by orders of magnitude over a small pressure range. However, our results suggest that the flow is sensitive to the radiative transfer. In future, test experiments with non-grey SOCRATES radiative transfer (see Chapter 5) could be run to see if the flow is robust to changes in the radiative transfer scheme. However, simulations of Hot Jupiter and terrestrial exoplanets tend to show qualitative agreement between simulations run with simplified radiative transfer schemes (e.g., Pierrehumbert and Hammond, 2019; Heng et al., 2011a) and more sophisticated correlated-k schemes (e.g., Lee et al., 2021; Turbet et al., 2022).

The aim of this chapter was to demonstrate the ability of the GCM to simulate non-dilute, hydrogen-dominated atmospheres. As such, most of the analysis provided

above is descriptive and does not attempt to provide a fundamental understanding of how non-dilute water vapour affects the circulation. In future, a detailed study of the momentum budget of the atmosphere (e.g., Mayne et al., 2017; Hammond et al., 2020) could be undertaken to understand why some simulations show high latitude jets whereas others exhibit day-to-night flow. In Chapter 3, a Helmholtz decomposition of the atmospheric circulation (Hammond and Lewis, 2021) was particularly useful for understanding the strength of the thermodynamically direct day-to-night circulation – similar analysis could be useful in diagnosing the change in the strength of divergent circulation in the *rad* experiments with high water vapour content. Lastly, future work could look at the effect of water vapour on the energy budget of the atmosphere. In particular, looking at the flux of the latent heat, Lq, in comparison to dry static energy flux should give a picture of how influential moisture is in comparison to sensible heat transport.

6.3.2 Possibility of Shear Instabilities

In many of our experiments, there is high vertical shearing of horizontal winds (especially in the *norad* experiments with high water vapour content). If the shear is large enough, dynamical instabilities can form, generating turbulence and mixing across the sheared layer. A useful dimensionless parameter in determining whether an atmosphere is unstable to vertical shear instabilities is the *Richardson number*. This is the ratio between buoyancy and mechanical source terms in the turbulent kinetic energy (TKE) budget (Lee, 2018). Linear stability analysis shows that a necessary condition for the generation of shearing instabilities in a Boussinesq fluid is for the *gradient* Richardson number (a type of Richardson number where the turbulent fluxes are related to vertical gradients in the mean field) to be < 0.25 (Howard, 1961). The exact critical value can exceed 0.25 when the disturbances are non-linear (Lee, 2018). Earth climate models often account for turbulent mixing due to shearing instabilities in their boundary

layer parameterisations, since strong wind shears are expected near the Earth's surface. In contrast, our sub-Neptune simulations has no boundary layer scheme, and shear instabilities may not be correctly resolved. As a simple estimate of whether shearing instabilities are important, we calculate the maximum bulk Richardson number:

$$Ri_b = \frac{g\Delta\theta_v\Delta z}{\overline{\theta_v}((\Delta u)^2 + (\Delta v)^2)} \tag{6.17}$$

between neighbouring model layers at the latitude of the strongest zonal jet. In this equation, Δ represents a vertical difference, barred quantities are vertical means, u and v are the horizontal wind speeds, z is the height, g the gravitational acceleration and θ_v the virtual potential temperature. The minimum value in all experiments was in ≈ 12 in the *q0.5_norad* experiment, which suggests that shear instabilities will not play a major role in any of these simulations. Part of the reason behind the large value of Ri_b here is the increased static stability due to the compositional gradients. As discussed in Section 6.3.1, the strong horizontal wind shear in the *q0.5_norad* experiment is a result of the vertical composition gradient. However, this same vertical gradient in water vapour greatly increases the static stability of the layer (increasing $\Delta\theta_v$) and stabilises the shearing layers from shear instabilities. As a test, if θ is substituted for θ_v in the equation for Ri_b (i.e. neglecting compositional variations), the minimum Ri_b value is much lower, at ≈ 3. Analysis of the dry simulations detailed in Chapter 3 showed that the minimum Ri_b was ≈ 4 in the P6d experiment (which had the maximum mean zonal wind speed of any GCM run for this thesis, at 800 m s^{-1}). Therefore shear instabilities are not expected to be important in these experiments either.

6.3.3 Inhibition of Convection

In all of our experiments with radiatively active water vapour, convection is inhibited, as expected from a simple comparison of the water vapour content at each level with the amount required to inhibit convection, $q_c = 1/(\beta\varpi)$ (Guillot, 1995). Another way of

viewing the strong compositional stabilisation is the inversion of the virtual temperature profiles in Figure 6.10. In addition, the strong drop in relative humidity above the level of condensation (see Figure 6.3) further enhances the stabilisation beyond what would be predicted for a fully saturated atmosphere. One might ask why the superadiabatic temperature layer does not exhibit a strong temperature jump, in comparison to those seen in Chapter 5. The lapse rate of a grey gas atmosphere can be given by Pierrehumbert (2010):

$$\frac{\mathrm{d}\ln T}{\mathrm{d}\ln p} = \frac{1}{4}\frac{\tau}{\tau+1}\frac{\mathrm{d}\ln \tau}{\mathrm{d}\ln p}, \tag{6.18}$$

where we have neglected absorption of shortwave radiation. To have strongly superadiabatic temperature gradients, we must have $\tau \gtrsim 1$ and $\mathrm{d}\ln\tau/\mathrm{d}\ln p \gg 1$, i.e., τ strongly increasing with pressure. The latter condition is satisfied in the weather layer where water vapour is increasing by orders of magnitude over a small pressure range. However, in our simulation setups, the atmosphere is not optically thick in the longwave part of the spectrum at the weather layer (i.e. $\tau < 1$). The longwave optical depth at the 10^4 Pa layer where condensation occurs is dominated by the dry component, which yields $\tau \approx 0.1$ at this level. For strongly superadiabatic temperature gradients we require condensation to occur at a deeper level, which would increase the radiative lapse rate ≈ 10 times. To achieve this, one would have to reduce the instellation (or equivalently increase the longwave opacity).

An interesting result of our simulations is that moist convection does not occur in the upper atmosphere of our simulations, above the inhibited layer. There are two main reasons for this behaviour. Firstly, the atmosphere above the inhibited layer, being optically thin in the longwave region of the spectrum, quickly becomes isothermal, with stable lapse rates. Secondly, the atmosphere above the inhibited layer is undersaturated, (see Figure 6.3), which prevents the triggering of moist convection by our adjustment scheme. We note that the original convection scheme of Ding and Pierrehumbert (2016) allows for the triggering of convection in superadiabatic regions where there

is not enough water vapour to saturate both layers. In this scheme, adjustment would take place and leave both layers undersaturated. This is supposed to represent "shallow", non-precipitating convection in Earth-like atmospheres. Our scheme imposes a more stringent requirement that layers must be saturated. This is one of the flaws of a hard convective adjustment scheme, since sub-grid variance of the water vapour may allow some regions of a grid cell to be saturated and convect even when the grid-averaged water vapour content is sub-saturated. This could be improved by adding a parametrisation of sub-grid variability that allows for convection to be triggered at relative humidities of less than 100%. Nonetheless, our results suggest that large scale motions alone cannot transport water vapour from the deep atmosphere upwards in order to sustain convection aloft.

6.3.4 Location of Condensation and Cloud Cover

Although the current setup of the GCM does not include cloud tracer species, the distribution of the large-scale condensation will correlate strongly to where clouds are found, especially in the case where cloud sedimentation timescales are fast in comparison to advective timescales (Charnay et al., 2021). Condensation in the absence of radiative feedbacks is largely limited to the polar vortices in the *q0.5_norad* and *q0.7_norad* experiments. In contrast, condensation is seen at almost all latitudes and longitudes in the *rad* experiments. As discussed in the previous section, the condensation in the *rad* experiments occurs predominantly in regions of strong radiative cooling and upwelling, both of which are an order of magnitude stronger in the *rad* compared to the *norad* experiments. The heating via large scale condensation in the *q0.{3,5,7}_rad* simulations is located in spatially inhomogeneous storms which suggests cloud cover may be patchy and varying in time. Similar temporal variability in cloud cover at the terminator was also predicted to produce variability in the transit depth measurements of K2-18b's atmosphere (Charnay et al., 2021).

In all experiments, cold trapping limits condensation to pressures greater than 1000 Pa (10 mbar), within the range of pressures provided for the photosphere of K2-18b in Madhusudhan et al. (2023) who retrieve photospheric pressures between 1 and 100 mbar. The exact pressure level of condensation is very sensitive to the temperature structure of the atmosphere and therefore to the assumed instellation, composition and radiative transfer scheme used. Further work could be done to study the sensitivity of the location of condensation to these parameters.

6.3.5 Future Work

There are several avenues for future work that could be pursued with the GCM described in this chapter.

Firstly, understanding the impact of moisture on the circulation from a theoretical perspective is important. As discussed in Section 6.3.1, there are several aspects of the dynamics that we have described, such as the transition to day-to-night flow at high water vapour contents, that we do not currently fully understand. Efforts to understand the nature of this circulation could include running more diagnostic tests (e.g., performing a Helmholtz decomposition of the circulation or diagnosing the momentum budget), to running a larger suite of model runs over more instellations and planetary rotation rates.

Once the nature of the circulation is better understood, more complicated cloud microphysics and radiative transfer schemes could be added to the model to bridge the gap between the theoretical understanding of the circulation and observations of temperate sub-Neptunes. In order to avoid the complexity of cloud microphysics schemes used in Earth GCM models, a simplified cloud model such as the one used in Seeley and Wordsworth (2021) could be used, where clouds formed from large scale condensation autoconvert to rain with a timescale τ_a, fall with a fixed velocity V and evaporate into undersaturated air with timescale τ_e. The timescales can be estimated using scal-

ing arguments, as in Rossow (1978). Adding a cloud species would allow us to directly simulate the radiative feedback of cloud properties on the circulation. This could have a significant impact given we posited that the change in circulation regime seen in our results is driven by the radiative effect of a sharp increase in water vapour concentration in the layers where cloud condensate concentration would likely be high. The addition of more realistic radiation and cloud microphysics schemes would also enable us to more accurately simulate transit spectra of sub-Neptune atmospheres for comparison with observations taken by telescopes such as *JWST*.

Lastly, with the addition of a surface ocean the model could be used to simulate Hycean worlds. This would be particularly interesting as a way of extending the work in Chapter 5 and understanding how 3D circulation impacts the habitability of these planets. The non-detection of ammonia in the atmosphere of K2-18 b's atmosphere (Madhusudhan et al., 2023) has been cited as evidence of liquid water oceans. Previous GCM studies of Earth-like exoplanets have highlighted the importance of the spatial distribution of clouds in setting the inner edge of the habitable zone (Yang et al., 2013). In addition, 3D dynamics will be important in setting the vertical water vapour profile in the atmosphere and therefore the location of convective inhibition. To adapt the GCM to include a surface ocean, particular care would have to be taken with the model layers close to the surface, where large gradients in moisture and temperature are predicted (e.g., Figures 5.2 and 5.3). In Chapter 5, a 1D model was used with 100 layers dedicated to resolving the steep radiative layers at the bottom of the model. This high vertical resolution would be computationally intractable in a 3D GCM. In addition, a boundary layer scheme to represent the turbulent heat and moisture fluxes near the surface would need to be added to the model. It is not clear what scheme should be used, since many parameterisations are tuned to the Earth's boundary layer. However, a simple one with few free parameters such as the one in Thatcher and Jablonowski (2016), which specifies a single turbulent diffusivity that decreases with height within the boundary, could be

used and tested across its limited parameter space.

6.4 Conclusions

In this chapter I have described the development of a GCM with a simple hydrological cycle with the aim of modelling temperate sub-Neptunes with a non-dilute water component. The convection scheme, large scale condensation and evaporation parameterisations conserve enthalpy and are simple enough not to rely on many free parameters given the unconstrained nature of the hydrological cycle on sub-Neptunes. The GCM was then run over a range of temperate sub-Neptunes with different deep water vapour contents to test its capabilities. Omitting the radiative effect of water vapour, I find that the circulation resembles that of the results in Chapter 3, with weak horizontal temperature gradients and high latitude jets. Large scale condensation is induced in limited regions inside the high latitude jets in cases with enhanced deep water vapour content. Compositional gradients act to separate the jets vertically below and above the altitude where the water vapour content is set by the Clausius Clapeyron relation. Including the radiative effects of water vapour, the wind structures transition from high latitude jets to day-to-night flow is observed as the water vapour content is increased. The vertical gradient in water content induces superadiabatic temperature gradients. Below the level of condensation, this induces dry convection. At the level of condensation, convection is inhibited by compositional gradients and no moist convection is observed, only large scale condensation. The large scale condensation is strongest on the nightside (where radiative cooling is strongest) and in areas of strong upwelling on the dayside. No moist convection is seen above the inhibited layers as the relative humidity is greatly reduced above the layers of condensation. Further work is needed to investigate the impact of moisture on the dynamics. Lastly, I outline several avenues for further work, including using the model to simulate observations of sub-Neptunes and developing the model

further to model the habitability of Hycean worlds.

Chapter 7

Conclusions

The aim of this thesis was to advance the understanding of the circulation and habitability of temperate sub-Neptune exoplanets. Whereas Chapter 3 focuses solely on attempting to understand the dry dynamics of sub-Neptunes, Chapter 5 forgoes any treatment of circulation and attempts to characterise the habitability of Hycean world sub-Neptunes purely through the use of radiative-convective equilibrium models. Chapter 6 attempts to bridge the gap between these chapters, by showing how non-dilute condensing water vapour can profoundly impact the circulation of sub-Neptunes. In future, models built along the same principles as the one in Chapter 6 will be important in determining the habitability and observable properties of water-rich sub-Neptunes.

In Chapter 1 I introduced sub-Neptunes and explained why they are interesting targets to model. Sub-Neptunes are one of the most common types of planet in our galaxy, and their increased radius compared to rocky planets makes them attractive targets for observation with transmission spectroscopy. Several sub-Neptunes in the traditional habitable zone have been discovered (Madhusudhan et al., 2021), which has led to a drive to model their habitability. There has been a particular focus on the exoplanet K2-

18 b, claimed to be a Hycean world, with surface oceans beneath a hydrogen-dominated atmosphere.

In Chapter 2 I provided an overview of the atmospheric dynamics of exoplanets, focusing particularly on the effects of planetary waves and condensation. I highlighted why we might expect sub-Neptunes to have different circulation patterns to Hot Jupiters and terrestrial exoplanets.

In Chapter 3 I ran a suite of GCM simulations for dry, temperate sub-Neptunes, demonstrating that their circulation would be characterised by weak horizontal temperature gradients over a broad range of parameter space. I showed that the zonal circulation was dominated by high latitude jets in comparison to the circulation of Hot Jupiter and terrestrial exoplanets, whose circulations generally exhibit a single equatorial jet. I was also able to provide a scaling relation that linked the strength of the day-to-night overturning circulation to the planetary instellation.

In Chapter 4 I provided an overview of how traditional models of planetary habitability calculate the inner edge of the habitable zone. Chapter 5 challenges the assumption that the temperature structure of Hycean worlds will be governed by the moist adiabat. I show that compositional gradients induced by the condensation of water vapour can inhibit convection and lead to superadiabatic temperature gradients in the lower atmosphere, which would move the inner edge of the habitable zone outwards for Hycean worlds.

Lastly, in Chapter 6 I present preliminary work to develop a GCM capable of handling the condensation of non-dilute water vapour in a hydrogen-dominated atmosphere. I describe the model, and demonstrate that it is able to reproduce results predicted from theory, such as the inhibition of convection in condensing layers and the disruption of zonal jets due to compositional effects. Preliminary results suggest that there is a change from predominantly zonal to predominantly day-to-night flow as the deep water vapour content of sub-Neptune atmospheres is increased. I posit that this

change is caused by the strong radiative heating and cooling present in the weather layer. Future work is needed to fully disentangle the effects of radiative and latent heating on the circulation structure.

The work presented in this thesis provides several avenues for future exploration. The 1D model used in Chapter 5 could be extended to include the effects of clouds and hazes on the radiative transfer. Since these have been proposed as a way of maintaining much cooler surface temperatures than expected from clear-sky calculations (Piette and Madhusudhan, 2020), including them in the model could provide a more accurate estimate of the inner edge of the habitable zone. On top of developing a deeper understanding of the results presented in Chapter 6, the GCM could be extended to include a simplified cloud scheme and correlated-k radiative transfer. This model would provide a more powerful tool for simulating specific sub-Neptune targets and understanding how cloud formation would impact observations of them. Regarding the runaway greenhouse limit for Hycean worlds, convection-resolved modelling of the hydrogen-water system is required to determine if the superadiabatic layers found in a 1D model are robust. Such simulations would be useful in informing the development of more accurate boundary layer and convective parameterisations to be used in 3D GCMs. A long term goal would be the simulation of Hycean worlds with a GCM, which would permit a more physically realistic calculation of their habitability.

The study of sub-Neptune exoplanets is a fast-moving field. The claimed discovery of water vapour on K2-18 b in 2019 was the catalyst for much of this thesis. Since then there has been intense interest in describing the planet's interior structure, atmosphere and habitability. Although the *James Webb Space Telescope* has put doubt on the presence of water vapour in the atmosphere, there is still debate surrounding its potential habitability. Hopefully new observations, in tandem with modelling efforts, will shed light on the prevalence of water on these planets. As we enter a new era of sub-Neptune characterisation I expect the pace of discovery to increase further still, and I look for-

ward to sharing in the insights gained by the community.

Bibliography

Achterberg, R. K., B. J. Conrath, P. J. Gierasch, F. M. Flasar, and C. A. Nixon (2008). Titan's Middle-Atmospheric Temperatures and Dynamics Observed by the Cassini Composite Infrared Spectrometer. In: *Icarus*, 194 (1), pp. 263–277. DOI: 10.1016/j.icarus.2007.09.029 (cit. on p. 30).

Adams, E. R., S Seager, and L. Elkins-Tanton (2008). Ocean Planet or Thick Atmosphere: On the Mass-Radius Relationship for Solid Exoplanets with Massive Atmospheres. In: *The Astrophysical Journal*, 673 (2), pp. 1160–1164. DOI: 10.1086/524925 (cit. on p. 4).

Aguichine, A., O. Mousis, M. Deleuil, and E. Marcq (2021). Mass–Radius Relationships for Irradiated Ocean Planets. In: *The Astrophysical Journal*, 914 (2), p. 84. DOI: 10.3847/1538-4357/abfa99 (cit. on p. 127).

Amundsen, D. S., N. J. Mayne, I. Baraffe, J. Manners, P. Tremblin, B. Drummond, C. Smith, D. M. Acreman, and D. Homeier (2016). The UK Met Office Global Circulation Model with a Sophisticated Radiation Scheme Applied to the Hot Jupiter HD 209458b. In: *Astronomy & Astrophysics*, 595, A36. DOI: 10.1051/0004-6361/201629183 (cit. on p. 18).

Andrews, D. G. and M. E. McIntyre (1976). Planetary Waves in Horizontal and Vertical Shear: The Generalized Eliassen-Palm Relation and the Mean Zonal Acceleration. In: *Journal of the Atmospheric Sciences*, 33 (11), pp. 2031–2048. DOI: 10.1175/1520-0469(1976)033<2031:PWIHAV>2.0.CO;2 (cit. on p. 76).

Arakawa, A. (2004). The Cumulus Parameterization Problem: Past, Present, and Future. In: *Journal of Climate*, 17 (13), pp. 2493–2525. DOI: 10.1175/1520-0442(2004)017<2493:RATCPP>2.0.CO;2 (cit. on p. 133).

Arakawa, A. and W. H. Schubert (1974). Interaction of a Cumulus Cloud Ensemble with the Large-Scale Environment, Part I. In: *Journal of the Atmospheric Sciences*, 31 (3), pp. 674–701. DOI: 10.1175/1520-0469(1974)031<0674:IOACCE>2.0.CO;2 (cit. on p. 133).

Asplund, M., N. Grevesse, A. J. Sauval, and P. Scott (2009). The Chemical Composition of the Sun. In: *Annual Review of Astronomy and Astrophysics*, 47, pp. 481–522. DOI: 10.1146/annurev.astro.46.060407.145222 (cit. on pp. 102, 149).

Barnes, R. (2017). Tidal Locking of Habitable Exoplanets. In: *Celestial Mechanics and Dynamical Astronomy*, 129 (4), pp. 509–536. DOI: 10.1007/s10569-017-9783-7 (cit. on p. 84).

Batalha, N. M. (2014). Exploring Exoplanet Populations with NASA's Kepler Mission. In: *Proceedings of the National Academy of Sciences of the United States of America*, 111 (35), pp. 12647–12654. DOI: 10.1073/pnas.1304196111 (cit. on p. 3).

Batalha, N. M. et al. (2013). Planetary Candidates Observed by Kepler. III. Analysis of the First 16 Months of Data. In: *Astrophysical Journal, Supplement Series*, 204 (2), p. 2013. DOI: 10.1088/0067-0049/204/2/24 (cit. on p. 3).

Bean, J. L., J. M. Désert, P. Kabath, B. Stalder, S. Seager, E. Miller-Ricci Kempton, Z. K. Berta, D. Homeier, S. Walsh, and A. Seifahrt (2011). The Optical and Near-Infrared Transmission Spectrum of the Super-Earth GJ1214b: Further Evidence for a Metal-Rich Atmosphere. In: *Astrophysical Journal*, 743 (1), p. 92. DOI: 10.1088/0004-637X/743/1/92 (cit. on p. 5).

Beichman, C. et al. (2014). Observations of Transiting Exoplanets with the James Webb Space Telescope (JWST). In: *Publications of the Astronomical Society of the Pacific*, 126 (946), pp. 1134–1173. DOI: 10.1086/679566 (cit. on p. 8).

Benneke, B., H. A. Knutson, J. Lothringer, I. J. Crossfield, J. I. Moses, C. Morley, L. Kreidberg, B. J. Fulton, D. Dragomir, A. W. Howard, I. Wong, J. M. Désert, P. R. McCullough, E. M. Kempton, J. Fortney, R. Gilliland, D. Deming, and J. Kammer (2019a). A Sub-Neptune Exoplanet with a Low-Metallicity Methane-Depleted Atmosphere and Mie-scattering Clouds. In: *Nature Astronomy*, 3 (9), pp. 813–821. DOI: 10.1038/s41550-019-0800-5 (cit. on pp. 50, 51, 86, 138).

Benneke, B., M. Werner, E. Petigura, H. Knutson, C. Dressing, I. J. M. Crossfield, J. E. Schlieder, J. Livingston, C. Beichman, J. Christiansen, J. Krick, V. Gorjian, A. W. Howard, E. Sinukoff, D. R. Ciardi, and R. L. Akeson (2017). Spitzer Observations Confirm and Rescue the Habitable-Zone Super-Earth K2-18 b for Future Characterization. In: *The Astrophysical Journal*, 834 (2), p. 187. DOI: 10.3847/1538-4357/834/2/187 (cit. on p. 5).

Benneke, B., I. Wong, C. Piaulet, H. A. Knutson, J. Lothringer, C. V. Morley, I. J. M. Crossfield, P. Gao, T. P. Greene, C. Dressing, D. Dragomir, A. W. Howard, P. R. McCullough, E. M.-R. Kempton, J. J. Fortney, and J. Fraine (2019b). Water Vapor and Clouds on the Habitable-zone Sub-Neptune Exoplanet K2-18b. In: *The Astrophysi-*

cal Journal, 887 (1), p. L14. DOI: 10.3847/2041-8213/ab59dc (cit. on pp. 5–7, 117, 149).

Berta, Z. K., D. Charbonneau, J. Bean, J. Irwin, C. J. Burke, J. M. Désert, P. Nutzman, and E. E. Falco (2011). The GJ1214 Super-Earth System: Stellar Variability, New Transits, and a Search for Additional Planets. In: *Astrophysical Journal*, 736 (1), p. 12. DOI: 10.1088/0004-637X/736/1/12 (cit. on p. 82).

Blain, D, B Charnay, and B Bézard (2021). 1D Atmospheric Study of the Temperate Sub-Neptune K2-18b. In: *Astronomy and Astrophysics*, 646. DOI: 10.1051/0004-6361/202039072 (cit. on pp. 50, 51, 85, 86, 132, 137).

Borysow, A (2002). Collision-Induced Absorption Coefficients of H2 Pairs at Temperatures from 60 K to 1000 K. In: *Astronomy and Astrophysics*, 390 (2), pp. 779–782. DOI: 10.1051/0004-6361:20020555 (cit. on p. 210).

Boukrouche, R., T. Lichtenberg, and R. T. Pierrehumbert (2021). Beyond Runaway: Initiation of the Post-runaway Greenhouse State on Rocky Exoplanets. In: *The Astrophysical Journal*, 919 (2), p. 130. DOI: 10.3847/1538-4357/ac1345 (cit. on pp. 91, 110, 123).

Bowen, I. S. (1926). The Ratio of Heat Losses by Conduction and by Evaporation from Any Water Surface. In: *Physical Review*, 27 (6), pp. 779–787. DOI: 10.1103/PhysRev.27.779 (cit. on p. 37).

Carone, L., R. Keppens, and L. Decin (2015). Connecting the Dots – II. Phase Changes in the Climate Dynamics of Tidally Locked Terrestrial Exoplanets. In: *Monthly Notices of the Royal Astronomical Society*, 453 (3), pp. 2413–2438. DOI: 10.1093/mnras/stv1752 (cit. on pp. 16, 35).

Casagrande, L., C. Flynn, and M. Bessell (2008). M Dwarfs: Effective Temperatures, Radii and Metallicities. In: *Monthly Notices of the Royal Astronomical Society*, 389 (2), pp. 585–607. DOI: 10.1111/j.1365-2966.2008.13573.x (cit. on p. 52).

Cassan, A. et al. (2012). One or More Bound Planets per Milky Way Star from Microlensing Observations. In: *Nature*, 481 (7380), pp. 167–169. DOI: 10.1038/nature10684 (cit. on p. 1).

Catling, D. C. and J. F. Kasting (2017). *Atmospheric Evolution on Inhabited and Lifeless Worlds*. Cambridge: Cambridge University Press. DOI: 10.1017/9781139020558 (cit. on p. 125).

Charnay, B, D Blain, B Bézard, J Leconte, M Turbet, and A. Falco (2021). Formation and Dynamics of Water Clouds on Temperate Sub-Neptunes: The Example of K2-18b. In: *Astronomy and Astrophysics*, 646, A171. DOI: 10.1051/0004-6361/202039525 (cit. on pp. 34, 43, 44, 80, 85–87, 128, 137, 165, 169).

Charnay, B., V. Meadows, and J. Leconte (2015a). 3D Modeling of GJ1214 b's Atmosphere: Vertical Mixing Driven by an Anti-Hadley Circulation. In: *Astrophysical Journal*, 813 (1), p. 15. DOI: 10.1088/0004-637X/813/1/15 (cit. on pp. 32, 34).

Charnay, B., V. Meadows, A. Misra, J. Leconte, and G. Arney (2015b). 3D Modeling of GJ1214b's Atmosphere: Formation of Inhomogeneous High Clouds and Observational Implications. In: *Astrophysical Journal Letters*, 813 (1), p. L1. DOI: 10.1088/2041-8205/813/1/L1 (cit. on pp. 34, 63).

Charney, J. G. (1948). On the Scale of Atmospheric Motions. In: *The Atmosphere—A Challenge: The Science of Jule Gregory Charney*. Springer, pp. 251–265 (cit. on p. 11).

Chen, X. (2021). The LMARS Based Shallow-Water Dynamical Core on Generic Gnomonic Cubed-Sphere Geometry. In: *Journal of Advances in Modeling Earth Systems*, 13 (1), e2020MS002280. DOI: 10.1029/2020MS002280 (cit. on p. 141).

Christie, D. A. et al. (2022). CAMEMBERT: A Mini-Neptunes General Circulation Model Intercomparison, Protocol Version 1.0.A CUISINES Model Intercomparison Project. In: *The Planetary Science Journal*, 3 (11), p. 261. DOI: 10.3847/PSJ/ac9dfe (cit. on pp. 34, 86, 148).

Ciddor, P. E. (1996). Refractive Index of Air: New Equations for the Visible and near Infrared. In: *Applied Optics*, 35 (9), pp. 1566–1573. DOI: 10.1364/AO.35.001566 (cit. on p. 210).

Cloutier, R., N. Astudillo-Defru, R. Doyon, X. Bonfils, J. M. Almenara, B. Benneke, F. Bouchy, X. Delfosse, D. Ehrenreich, T. Forveille, C. Lovis, M. Mayor, K. Menou, F. Murgas, F. Pepe, J. Rowe, N. C. Santos, S. Udry, and A. Wünsche (2017). Characterization of the K2-18 Multi-Planetary System with HARPS : A Habitable Zone Super-Earth and Discovery of a Second, Warm Super-Earth on a Non-Coplanar Orbit. In: *Astronomy and Astrophysics*, 608, A35. DOI: 10.1051/0004-6361/201731558 (cit. on p. 51).

Cloutier, R, N Astudillo-Defru, R Doyon, X Bonfils, J. M. Almenara, F Bouchy, X Delfosse, T Forveille, C Lovis, M Mayor, K Menou, F Murgas, F Pepe, N. C. Santos, S Udry, and A Wünsche (2019). Confirmation of the Radial Velocity Super-Earth K2-18c with HARPS and CARMENES. In: *Astronomy and Astrophysics*, 621. DOI: 10.1051/0004-6361/201833995 (cit. on pp. 5, 50, 149).

Cuthbertson, C. and M. Cuthbertson (1932). The Refraction and Dispersion of Neon and Helium. In: *Proceedings of the Royal Society of London. Series A, Containing Papers of a Mathematical and Physical Character*, 135 (826), pp. 40–47. DOI: 10.1098/rspa.1932.0019 (cit. on p. 210).

Del Genio, A. D. and K. B. McGrattan (1990). Moist Convection and the Vertical Structure and Water Abundance of Jupiter's Atmosphere. In: *Icarus*, 84 (1), pp. 29–53. DOI: 10.1016/0019-1035(90)90156-4 (cit. on p. 133).

Ding, F. and R. T. Pierrehumbert (2016). Convection in Condensible-Rich Atmospheres. In: *The Astrophysical Journal*, 822 (1), p. 24. DOI: 10.3847/0004-637X/822/1/24 (cit. on pp. 40, 106, 107, 140, 143, 144, 168).

Dobbs-Dixon, I. and E. Agol (2013). Three-Dimensional Radiative-Hydrodynamical Simulations of the Highly Irradiated Short-Period Exoplanet HD 189733b. In: *Monthly Notices of the Royal Astronomical Society*, 435 (4), pp. 3159–3168. DOI: 10.1093/mnras/stt1509 (cit. on p. 20).

Donahue, T. M., J. H. Hoffman, R. R. Hodges, and A. J. Watson (1982). Venus Was Wet: A Measurement of the Ratio of Deuterium to Hydrogen. In: *Science (New York, N.Y.)*, 216 (4546), pp. 630–633. DOI: 10.1126/science.216.4546.630 (cit. on p. 90).

Dressing, C. D. and D. Charbonneau (2013). The Occurrence Rate of Small Planets around Small Stars. In: *Astrophysical Journal*, 767 (1), p. 95. DOI: 10.1088/0004-637X/767/1/95 (cit. on p. 8).

Drummond, B, N. J. Mayne, I Baraffe, P Tremblin, J Manners, D. S. Amundsen, J Goyal, and D Acreman (2018). The Effect of Metallicity on the Atmospheres of Exoplanets with Fully Coupled 3D Hydrodynamics, Equilibrium Chemistry, and Radiative Transfer. In: *Astronomy and Astrophysics*, 612, p. 105. DOI: 10.1051/0004-6361/201732010 (cit. on pp. 34, 81).

Edson, A., S. Lee, P. Bannon, J. F. Kasting, and D. Pollard (2011a). Atmospheric Circulations of Terrestrial Planets Orbiting Low-Mass Stars. In: *Icarus*, 212 (1), pp. 1–13. DOI: 10.1016/j.icarus.2010.11.023 (cit. on p. 24).

Edson, A., S. Lee, P. Bannon, J. F. Kasting, and D. Pollard (2011b). Atmospheric Circulations of Terrestrial Planets Orbiting Low-Mass Stars. In: *Icarus*, 212 (1), pp. 1–13. DOI: 10.1016/j.icarus.2010.11.023 (cit. on p. 37).

Edwards, J. M. and A. Slingo (1996). Studies with a Flexible New Radiation Code. I: Choosing a Configuration for a Large-Scale Model. In: *Quarterly Journal of the Royal Meteorological Society*, 122 (531), pp. 689–719. DOI: 10.1002/qj.49712253107 (cit. on pp. 102, 209).

Emanuel, K. A. and R. Hide (1995). Atmospheric Convection. In: *Physics Today*, 48 (4), pp. 88–89. DOI: 10.1063/1.2807986 (cit. on p. 39).

Fauchez, T. J. et al. (2021). TRAPPIST Habitable Atmosphere Intercomparison (THAI) Workshop Report. In: *The Planetary Science Journal*, 2 (3), p. 106. DOI: 10.3847/psj/abf4df (cit. on p. 86).

Fearn, D. R. and D. E. Loper (1981). Compositional Convection and Stratification of Earth's Core. In: *Nature*, 289 (5796), pp. 393–394. DOI: 10.1038/289393a0 (cit. on p. 40).

Forget, F., F. Hourdin, and O. Talagrand (1998). CO2Snowfall on Mars: Simulation with a General Circulation Model. In: *Icarus*, 131 (2), pp. 302–316. DOI: 10.1006/icar.1997.5874 (cit. on p. 143).

Fortney, J. J., C. Mordasini, N. Nettelmann, E. M. Kempton, T. P. Greene, and K. Zahnle (2013). A Framework for Characterizing the Atmospheres of Low-Mass Low-Density Transiting Planets. In: *Astrophysical Journal*, 775 (1), p. 80. DOI: 10.1088/0004-637X/775/1/80 (cit. on pp. 4, 137).

Frank, F., P. Jöckel, S. Gromov, and M. Dameris (2018). Investigating the Yield of H_2O and H_2 from Methane Oxidation in the Stratosphere. In: *Atmospheric Chemistry and Physics*, 18 (13), pp. 9955–9973. DOI: 10.5194/acp-18-9955-2018 (cit. on p. 107).

Fressin, F., G. Torres, D. Charbonneau, S. T. Bryson, J. Christiansen, C. D. Dressing, J. M. Jenkins, L. M. Walkowicz, and N. M. Batalha (2013). The False Positive Rates of Kepler and the Occurence of Planets. In: *The Astrophysical Journal*, 766, p. 81. DOI: 10.1088/0004-637X/766/2/81 (cit. on pp. 3, 47).

Frierson, D. M., I. M. Held, and P. Zurita-Gotor (2006). A Gray-Radiation Aquaplanet Moist GCM. Part I: Static Stability and Eddy Scale. In: *Journal of the Atmospheric Sciences*, 63 (10), pp. 2548–2566. DOI: 10.1175/JAS3753.1 (cit. on p. 37).

Frierson, D. M., J. Lu, and G. Chen (2007). Width of the Hadley Cell in Simple and Comprehensive General Circulation Models. In: *Geophysical Research Letters*, 34 (18). DOI: 10.1029/2007GL031115 (cit. on pp. 37, 133).

Fulton, B. J., E. A. Petigura, A. W. Howard, H. Isaacson, G. W. Marcy, P. A. Cargile, L. Hebb, L. M. Weiss, J. A. Johnson, T. D. Morton, E. Sinukoff, I. J. M. Crossfield, and L. A. Hirsch (2017). The California- Kepler Survey. III. A Gap in the Radius Distribution of Small Planets. In: *The Astronomical Journal*, 154 (3), p. 109. DOI: 10.3847/1538-3881/aa80eb (cit. on pp. 3, 4).

Gaudi, B. S. et al. (2018). *The Habitable Exoplanet Observatory (HabEx) Mission Concept Study Interim Report*. DOI: 10.48550/arXiv.1809.09674. arXiv: 1809.09674 [astro-ph] (cit. on p. 91).

Gettelman, A and S. C. Sherwood (2016). Processes Responsible for Cloud Feedback. In: *Current Climate Change Reports*, 2 (4), pp. 179–189. DOI: 10.1007/s40641-016-0052-8 (cit. on p. 38).

Gierasch, P. J. (1975). Meridional Circulation and the Maintenance of the Venus Atmospheric Rotation. In: *Journal of the Atmospheric Sciences*, 32 (6), pp. 1038–1044. DOI: 10.1175/1520-0469(1975)032<1038:MCATMO>2.0.CO;2 (cit. on p. 21).

Gill, A. E. (1980). Some Simple Solutions for Heat-Induced Tropical Circulation. In: *Quarterly Journal of the Royal Meteorological Society*, 106 (449), pp. 447–462. DOI: 10.1002/qj.49710644905 (cit. on pp. 26, 28, 156).

Gillon, M., E. Jehin, S. M. Lederer, L. Delrez, J. De Wit, A. Burdanov, V. Van Grootel, A. J. Burgasser, A. H. Triaud, C. Opitom, B. O. Demory, D. K. Sahu, D. Bardalez Gagliuffi, P. Magain, and D. Queloz (2016). Temperate Earth-sized Planets Transiting a Nearby Ultracool Dwarf Star. In: *Nature*, 533 (7602), pp. 221–224. DOI: 10.1038/nature17448 (cit. on p. 52).

Goldblatt, C., T. D. Robinson, K. J. Zahnle, and D. Crisp (2013). Low Simulated Radiation Limit for Runaway Greenhouse Climates. In: *Nature Geoscience*, 6, pp. 661–667. DOI: 10.1038/NGEO1892 (cit. on pp. 102, 107, 210).

Guillot, T., A. Burrows, W. B. Hubbard, J. I. Lunine, and D. Saumon (1996). Giant Planets at Small Orbital Distances. In: *The Astrophysical Journal*, 459 (1). DOI: 10.1086/309935 (cit. on p. 17).

Guillot, T. (1995). Condensation of Methane, Ammonia, and Water and the Inhibition of Convection in Giant Planets. In: *Science*, 269 (5231), pp. 1697–1699. DOI: 10.1126/science.7569896 (cit. on pp. 41, 98, 144, 167).

Gupta, A. and H. E. Schlichting (2019). Sculpting the Valley in the Radius Distribution of Small Exoplanets as a By-Product of Planet Formation: The Core-Powered Mass-Loss Mechanism. In: *Monthly Notices of the Royal Astronomical Society*, 487 (1), pp. 24–33. DOI: 10.1093/mnras/stz1230 (cit. on p. 3).

Habib, N. and R. T. Pierrehumbert (2023). *Modelling Non-Condensing Compositional Convection for Applications to Super-Earth and Sub-Neptune Atmospheres*. arXiv: 2310.08202 [astro-ph] (cit. on p. 161).

Hammond, M. and N. T. Lewis (2021). The Rotational and Divergent Components of Atmospheric Circulation on Tidally Locked Planets. In: *Proceedings of the National Academy of Sciences of the United States of America*, 118 (13). DOI: 10.1073/pnas.2022705118 (cit. on pp. 32, 33, 63, 66, 87, 166).

Hammond, M. and R. T. Pierrehumbert (2017). Linking the Climate and Thermal Phase Curve of 55 Cancri e. In: *The Astrophysical Journal*, 849 (2), p. 152. DOI: 10.3847/1538-4357/aa9328 (cit. on pp. 19, 20, 48, 141).

Hammond, M. and R. T. Pierrehumbert (2018). Wave-Mean Flow Interactions in the Atmospheric Circulation of Tidally Locked Planets. In: *The Astrophysical Journal*, 869 (1), p. 65. DOI: 10.3847/1538-4357/aaec03 (cit. on pp. 30, 48, 69, 156).

Hammond, M., S.-M. Tsai, and R. T. Pierrehumbert (2020). The Equatorial Jet Speed on Tidally Locked Planets. I. Terrestrial Planets. In: *The Astrophysical Journal*, 901 (1), p. 78. DOI: 10.3847/1538-4357/abb08b (cit. on p. 166).

Haqq-Misra, J., E. T. Wolf, M. Joshi, X. Zhang, and R. K. Kopparapu (2018). Demarcating Circulation Regimes of Synchronously Rotating Terrestrial Planets within the Habitable Zone. In: *The Astrophysical Journal*, 852 (2), p. 67. DOI: 10.3847/1538-4357/aa9f1f (cit. on pp. 16, 17, 20, 24, 32, 39).

Harpsøe, K. B. et al. (2012). The Transiting System GJ1214: High-precision Defocused Transit Observations and a Search for Evidence of Transit Timing Variation. In: *Astronomy and Astrophysics*, 549, p. 10. DOI: 10.1051/0004-6361/201219996 (cit. on p. 5).

Held, I. M. and A. Y. Hou (1980). Nonlinear Axially Symmetric Circulations in a Nearly Inviscid Atmosphere. In: *Journal of the Atmospheric Sciences*, 37 (3), pp. 515–533. DOI: 10.1175/1520-0469(1980)037<0515:NASCIA>2.0.CO;2 (cit. on pp. 22, 62).

Held, I. M. (2019). 100 Years of Progress in Understanding the General Circulation of the Atmosphere. In: *Meteorological Monographs*, 59 (1), pp. 6.1–6.23. DOI: 10.1175/AMSMONOGRAPHS-D-18-0017.1 (cit. on p. 12).

Heng, K., D. M. Frierson, and P. J. Phillipps (2011a). Atmospheric Circulation of Tidally Locked Exoplanets: II. Dual-band Radiative Transfer and Convective Adjustment. In: *Monthly Notices of the Royal Astronomical Society*, 418 (4), pp. 2669–2696. DOI: 10.1111/j.1365-2966.2011.19658.x (cit. on pp. 17, 165).

Heng, K., J. M. Mendonça, and J. M. Lee (2014). Analytical Models of Exoplanetary Atmospheres. II. Radiative Transfer via the Two-Stream Approximation. In: *Astrophysical Journal, Supplement Series*, 215 (1). DOI: 10.1088/0067-0049/215/1/4 (cit. on p. 116).

Heng, K., K. Menou, and P. J. Phillipps (2011b). Atmospheric Circulation of Tidally Locked Exoplanets: A Suite of Benchmark Tests for Dynamical Solvers. In: *Monthly Notices of the Royal Astronomical Society*, 413 (4), pp. 2380–2402. DOI: 10.1111/j.1365-2966.2011.18315.x (cit. on pp. 17, 18, 32).

Hide, R. (1969). Dynamics of the Atmospheres of the Major Planets with an Appendix on the Viscous Boundary Layer at the Rigid Bounding Surface of an Electrically-Conducting Rotating Fluid in the Presence of a Magnetic Field. In: *Journal of the At-*

mospheric Sciences, 26 (5), pp. 841–853. DOI: 10.1175/1520-0469(1969)026<0841:DOTAOT>2.0.CO;2 (cit. on p. 25).

Horinouchi, T., Y. Y. Hayashi, S. Watanabe, M. Yamada, A. Yamazaki, T. Kouyama, M. Taguchi, T. Fukuhara, M. Takagi, K. Ogohara, S.-Y. Murakami, J. Peralta, S. S. Limaye, T. Imamura, M. Nakamura, T. M. Sato, and T. Satoh (2020). How Waves and Turbulence Maintain the Super-Rotation of Venus' Atmosphere. In: *Science*, 368 (6489), pp. 405–409. DOI: 10.1126/science.aaz4439 (cit. on pp. 31, 70).

Howard, L. N. (1961). Note on a Paper of John W. Miles. In: *Journal of Fluid Mechanics*, 10 (4), pp. 509–512. DOI: 10.1017/S0022112061000317 (cit. on p. 166).

Hu, R., S. Seager, and Y. L. Yung (2015). Helium Atmospheres on Warm Neptune-and-Sub-Neptune-Sized Exoplanets and Applications to GJ436 b. In: *The Astrophysical Journal*, 807 (1), p. 8. DOI: 10.1088/0004-637X/807/1/8 (cit. on p. 126).

Husser, T. O., S Wende-Von Berg, S Dreizler, D Homeier, A Reiners, T Barman, and P. H. Hauschildt (2013). A New Extensive Library of PHOENIX Stellar Atmospheres and Synthetic Spectra. In: *Astronomy and Astrophysics*, 553, p. 6. DOI: 10.1051/0004-6361/201219058 (cit. on p. 209).

Iga, S. I. and Y. Matsuda (2005). Shear Instability in a Shallow Water Model with Implications for the Venus Atmosphere. In: *Journal of the Atmospheric Sciences*, 62 (7 II), pp. 2514–2527. DOI: 10.1175/JAS3484.1 (cit. on pp. 31, 70).

Ingersoll, A. (1969). The Runaway Greenhouse: A History of Water on Venus. In: *Journal of the Atmospheric Sciences*, 26 (6), pp. 1191–1198. DOI: 10.1175/1520-0469(1969)026<1191:trgaho>2.0.co;2 (cit. on pp. 38, 92, 107).

Innes, H. (2023). *The Runaway Greenhouse Effect on Hycean Worlds: Data*. DOI: 10.5281/ZENODO.8071023 (cit. on p. 111).

Innes, H. and R. T. Pierrehumbert (2022). Atmospheric Dynamics of Temperate Sub-Neptunes. I. Dry Dynamics. In: *The Astrophysical Journal*, 927 (1), p. 38. DOI: 10.3847/1538-4357/ac4887 (cit. on pp. 47, 128, 141).

Innes, H., S.-M. Tsai, and R. T. Pierrehumbert (2023). The Runaway Greenhouse Effect on Hycean Worlds. In: *The Astrophysical Journal*, 953 (2), p. 168. DOI: 10.3847/1538-4357/ace346 (cit. on pp. 101, 144).

Jablonowski, C. and D. L. Williamson (2011). The Pros and Cons of Diffusion, Filters and Fixers in Atmospheric General Circulation Models. In: *Lecture Notes in Computational Science and Engineering*. Vol. 80, pp. 381–493. DOI: 10.1007/978-3-642-11640-7_13 (cit. on pp. 71, 73).

Jucker, M. (2021). Scaling of Eliassen-Palm Flux Vectors. In: *Atmospheric Science Letters*, 22 (4), e1020. DOI: 10.1002/asl.1020 (cit. on p. 80).

Karman, T., I. E. Gordon, A. van der Avoird, Y. I. Baranov, C. Boulet, B. J. Drouin, G. C. Groenenboom, M. Gustafsson, J. M. Hartmann, R. L. Kurucz, L. S. Rothman, K. Sun, K. Sung, R. Thalman, H. Tran, E. H. Wishnow, R. Wordsworth, A. A. Vigasin, R. Volkamer, and W. J. van der Zande (2019). Update of the HITRAN Collision-Induced Absorption Section. In: *Icarus*, 328, pp. 160–175. DOI: 10.1016/j.icarus.2019.02.034 (cit. on p. 210).

Kaspi, Y. and A. P. Showman (2015). Atmospheric Dynamics of Terrestrial Exoplanets over a Wide Range of Orbital and Atmospheric Parameters. In: *Astrophysical Journal*, 804 (1). DOI: 10.1088/0004-637X/804/1/60 (cit. on pp. 20, 22, 23, 37, 62, 81).

Kasting, J. F. (1988). Runaway and Moist Greenhouse Atmospheres and the Evolution of Earth and Venus. In: *Icarus*, 74 (3), pp. 472–494. DOI: 10.1016/0019-1035(88)90116-9 (cit. on p. 90).

Kasting, J. F., D. P. Whitmire, and R. T. Reynolds (1993). Habitable Zones around Main Sequence Stars. In: *Icarus*, 101 (1), pp. 108–128. DOI: 10.1006/icar.1993.1010 (cit. on pp. 91, 108).

Kataria, T, A. P. Showman, J. J. Fortney, M. S. Marley, and R. S. Freedman (2014). The Atmospheric Circulation of the Super Earth GJ 1214b: Dependence on Composition and Metallicity. In: *Astrophysical Journal*, 785 (2). DOI: 10.1088/0004-637X/785/2/92 (cit. on p. 81).

Kempton, E. M.-R. et al. (2023). A Reflective, Metal-Rich Atmosphere for GJ 1214b from Its JWST Phase Curve. In: *Nature*, 620 (7972), pp. 67–71. DOI: 10.1038/s41586-023-06159-5 (cit. on p. 5).

Kite, E. S. and M. N. Barnett (2020). Exoplanet Secondary Atmosphere Loss and Revival. In: *Proceedings of the National Academy of Sciences of the United States of America*, 117 (31), pp. 18264–18271. DOI: 10.1073/pnas.2006177117 (cit. on p. 44).

Kite, E. S., B. Fegley Jr., L. Schaefer, and E. B. Ford (2020). Atmosphere Origins for Exoplanet Sub-Neptunes. In: *The Astrophysical Journal*, 891 (2), p. 111. DOI: 10.3847/1538-4357/ab6ffb (cit. on pp. 35, 44).

Knutson, H. A., D. Charbonneau, L. E. Allen, J. J. Fortney, E. Agol, N. B. Cowan, A. P. Showman, C. S. Cooper, and S. T. Megeath (2007). A Map of the Day–Night Contrast of the Extrasolar Planet HD 189733b. In: *Nature*, 447 (7141), pp. 183–186. DOI: 10.1038/nature05782 (cit. on pp. 17, 18).

Knutson, H. A., D. Dragomir, L. Kreidberg, E. M. Kempton, P. R. McCullough, J. J. Fortney, J. L. Bean, M. Gillon, D. Homeier, and A. W. Howard (2014). Hubble Space Telescope Near-IR Transmission Spectroscopy of the Super-Earth HD 97658B. In:

Astrophysical Journal, 794 (2), p. 55. DOI: 10.1088/0004-637X/794/2/155 (cit. on p. 5).

Koll, D. D. B. (2022). A Scaling for Atmospheric Heat Redistribution on Tidally Locked Rocky Planets. In: *The Astrophysical Journal*, 924 (2), p. 134. DOI: 10.3847/1538-4357/ac3b48 (cit. on p. 128).

Koll, D. D. B. and D. S. Abbot (2016). Temperature Structure and Atmospheric Circulation of Dry Tidally Locked Rocky Exoplanets. In: *The Astrophysical Journal*, 825 (2), p. 99. DOI: 10.3847/0004-637x/825/2/99 (cit. on p. 24).

Koll, D. D. B. and T. W. Cronin (2019). Hot Hydrogen Climates Near the Inner Edge of the Habitable Zone. In: *The Astrophysical Journal*, 881 (2), p. 120. DOI: 10.3847/1538-4357/ab30c4 (cit. on pp. 95–97, 102, 115, 117, 118, 214, 216, 217).

Koll, D. D. and D. S. Abbot (2015). Deciphering Thermal Phase Curves of Dry, Tidally Locked Terrestrial Planets. In: *Astrophysical Journal*, 802 (1), p. 21. DOI: 10.1088/0004-637X/802/1/21 (cit. on pp. 19, 32, 64).

Komabayasi, M. (1967). Discrete Equilibrium Temperatures of a Hypothetical Planet with the Atmosphere and the Hydrosphere of One Component-Two Phase System under Constant Solar Radiation. In: *Journal of the Meteorological Society of Japan. Ser. II*, 45 (1), pp. 137–139. DOI: 10.2151/jmsj1965.45.1_137 (cit. on pp. 38, 92).

Komacek, T. D. and D. S. Abbot (2019). The Atmospheric Circulation and Climate of Terrestrial Planets Orbiting Sun-like and M Dwarf Stars over a Broad Range of Planetary Parameters. In: *The Astrophysical Journal*, 871 (2), p. 245. DOI: 10.3847/1538-4357/aafb33 (cit. on pp. 22, 39, 81, 149).

Komacek, T. D., M. F. Jansen, E. T. Wolf, and D. S. Abbot (2019). Scaling Relations for Terrestrial Exoplanet Atmospheres from Baroclinic Criticality. In: *The Astrophysical Journal*, 883 (1), p. 46. DOI: 10.3847/1538-4357/ab3980 (cit. on p. 20).

Komacek, T. D. and A. P. Showman (2016). Atmospheric Circulation of Hot Jupiters: Dayside-Nightside Temperature Differences. In: *The Astrophysical Journal*, 821 (1), p. 16. DOI: 10.3847/0004-637x/821/1/16 (cit. on pp. 12, 17–19, 60, 83).

Kopparapu, R. K. (2013). A Revised Estimate of the Occurrence Rate of Terrestrial Planets in the Habitable Zones around Kepler M-dwarfs. In: *Astrophysical Journal Letters*, 767 (1), p. 8. DOI: 10.1088/2041-8205/767/1/L8 (cit. on pp. 6, 38, 91).

Kopparapu, R. K., R. Ramirez, J. F. Kasting, V. Eymet, T. D. Robinson, S. Mahadevan, R. C. Terrien, S. Domagal-Goldman, V. Meadows, and R. Deshpande (2013). Habitable Zones around Main-Sequence Stars: New Estimates. In: *Astrophysical Journal*, 765 (2), p. 131. DOI: 10.1088/0004-637X/765/2/131 (cit. on p. 118).

Kopparapu, R. K., E. T. Wolf, G. Arney, N. E. Batalha, J. Haqq-Misra, S. L. Grimm, and K. Heng (2017). Habitable Moist Atmospheres on Terrestrial Planets near the Inner Edge of the Habitable Zone around M Dwarfs. In: *The Astrophysical Journal*, 845 (1), p. 5. DOI: 10.3847/1538-4357/aa7cf9 (cit. on pp. 16, 20).

Kostiuk, T., K. E. Fast, T. A. Livengood, T. Hewagama, J. J. Goldstein, F. Espenak, and D. Buhl (2001). Direct Measurement of Winds on Titan. In: *Geophysical Research Letters*, 28 (12), pp. 2361–2364. DOI: 10.1029/2000GL012617 (cit. on p. 30).

Kreidberg, L., J. L. Bean, J. M. Désert, B. Benneke, D. Deming, K. B. Stevenson, S. Seager, Z. Berta-Thompson, A. Seifahrt, and D. Homeier (2014). Clouds in the Atmosphere of the Super-Earth Exoplanet GJ 1214b. In: *Nature*, 505 (7481), pp. 69–72. DOI: 10.1038/nature12888 (cit. on pp. 5, 137).

Lacis, A. A. and V. Oinas (1991). A Description of the Correlated k Distribution Method for Modeling Nongray Gaseous Absorption, Thermal Emission, and Multiple Scattering in Vertically Inhomogeneous Atmospheres. In: *Journal of Geophysical Research*, 96 (D5), pp. 9027–9063. DOI: 10.1029/90JD01945 (cit. on p. 209).

Lammer, H., J. H. Bredehöft, A. Coustenis, M. L. Khodachenko, L. Kaltenegger, O. Grasset, D. Prieur, F. Raulin, P. Ehrenfreund, M. Yamauchi, J. E. Wahlund, J. M. Grießmeier, G. Stangl, C. S. Cockell, Yu. N. Kulikov, J. L. Grenfell, and H. Rauer (2009). What Makes a Planet Habitable? In: *Astronomy and Astrophysics Review*, 17, pp. 181–249. DOI: 10.1007/s00159-009-0019-z (cit. on p. 139).

Laraia, A. L. and T. Schneider (2015). Superrotation in Terrestrial Atmospheres. In: *Journal of the Atmospheric Sciences*, 72 (11), pp. 4281–4296. DOI: 10.1175/JAS-D-15-0030.1 (cit. on p. 22).

Lean, J. L. and M. T. DeLand (2012). How Does the Sun's Spectrum Vary? In: *Journal of Climate*, 25 (7), pp. 2555–2560. DOI: 10.1175/JCLI-D-11-00571.1 (cit. on p. 209).

Lebonnois, S., F. Hourdin, V. Eymet, A. Crespin, R. Fournier, and F. Forget (2010). Superrotation of Venus' Atmosphere Analyzed with a Full General Circulation Model. In: *Journal of Geophysical Research: Planets*, 115 (E6). DOI: 10.1029/2009JE003458 (cit. on pp. 12, 31, 70).

Leconte, J., F. Forget, B. Charnay, R. Wordsworth, and A. Pottier (2013). Increased Insolation Threshold for Runaway Greenhouse Processes on Earth-like Planets. In: *Nature*, 504 (7479), pp. 268–271. DOI: 10.1038/nature12827 (cit. on pp. 16, 91, 129, 139).

Leconte, J., F. Selsis, F. Hersant, and T. Guillot (2017). Condensation-Inhibited Convection in Hydrogen-Rich Atmospheres: Stability against Double-Diffusive Processes and Thermal Profiles for Jupiter, Saturn, Uranus, and Neptune. In: *Astronomy and*

Astrophysics, 598, p. 98. DOI: 10.1051/0004-6361/201629140 (cit. on pp. 41, 98, 106, 144).

Leconte, J., H. Wu, K. Menou, and N. Murray (2015). Asynchronous Rotation of Earth-mass Planets in the Habitable Zone of Lower-Mass Stars. In: *Science*, 347 (6222), pp. 632–635. DOI: 10.1126/science.1258686 (cit. on p. 21).

Lee, E. K. H., V. Parmentier, M. Hammond, S. L. Grimm, D. Kitzmann, X. Tan, S.-M. Tsai, and R. T. Pierrehumbert (2021). Simulating Gas Giant Exoplanet Atmospheres with Exo-FMS: Comparing Semi-Grey, Picket Fence and Correlated-k Radiative-Transfer Schemes. In: *MNRAS*, 000, pp. 1–17 (cit. on pp. 72, 81, 165).

Lee, E. K. H., J. P. Wardenier, B. Prinoth, V. Parmentier, S. L. Grimm, R. Baeyens, L. Carone, D. Christie, R. Deitrick, D. Kitzmann, N. Mayne, M. Roman, and B. Thorsbro (2022). 3D Radiative Transfer for Exoplanet Atmospheres. gCMCRT: A GPU-accelerated MCRT Code. In: *The Astrophysical Journal*, 929 (2), p. 180. DOI: 10.3847/1538-4357/ac61d6 (cit. on p. 141).

Lee, G. K., S. L. Casewell, K. L. Chubb, M. Hammond, X. Tan, S. M. Tsai, and R. T. Pierrehumbert (2020). Simplified 3D GCM Modelling of the Irradiated Brown Dwarf WD 0137—349B. In: *Monthly Notices of the Royal Astronomical Society*, 496 (4), pp. 4674–4687. DOI: 10.1093/mnras/staa1882 (cit. on p. 48).

Lee, X. (2018). Generation and Maintenance of Atmospheric Turbulence. In: *Fundamentals of Boundary-Layer Meteorology*. Ed. by X. Lee. Springer Atmospheric Sciences. Cham: Springer International Publishing, pp. 57–79. ISBN: 978-3-319-60853-2. DOI: 10.1007/978-3-319-60853-2_4 (cit. on p. 166).

Lefèvre, M., M. Turbet, and R. Pierrehumbert (2021). 3D Convection-resolving Model of Temperate, Tidally Locked Exoplanets. In: *The Astrophysical Journal*, 913 (2), p. 101. DOI: 10.3847/1538-4357/abf2c1 (cit. on p. 131).

Lewis, N. T., N. A. Lombardo, P. L. Read, and J. M. Lora (2023). Equatorial Waves and Superrotation in the Stratosphere of a Titan General Circulation Model. In: *The Planetary Science Journal*, 4 (8), p. 149. DOI: 10.3847/PSJ/ace76f (cit. on p. 31).

Li, C. and A. P. Ingersoll (2015). Moist Convection in Hydrogen Atmospheres and the Frequency of Saturn's Giant Storms. In: *Nature Geoscience*, 8 (5), pp. 398–403. DOI: 10.1038/ngeo2405 (cit. on pp. 41, 98, 144).

Lian, Y. and A. P. Showman (2010). Generation of Equatorial Jets by Large-Scale Latent Heating on the Giant Planets. In: *Icarus*, 207 (1), pp. 373–393. DOI: 10.1016/j.icarus.2009.10.006 (cit. on p. 70).

Lichtenberg, T., D. J. Bower, M. Hammond, R. Boukrouche, P. Sanan, S.-M. Tsai, and R. T. Pierrehumbert (2021). Vertically Resolved Magma Ocean–Protoatmosphere

Evolution: H2, H2O, CO2, CH4, CO, O2, and N2 as Primary Absorbers. In: *Journal of Geophysical Research. Planets*, 126 (2), e2020JE006711. DOI: 10.1029/2020JE006711 (cit. on p. 91).

Lichtenberg, T., L. K. Schaefer, M. Nakajima, and R. A. Fischer (2022). *Geophysical Evolution During Rocky Planet Formation*. arXiv: 2203.10023 [astro-ph, physics:physics] (cit. on p. 132).

Limaye, S. S., R. Mogul, D. J. Smith, A. H. Ansari, G. P. Słowik, and P. Vaishampayan (2018). Venus' Spectral Signatures and the Potential for Life in the Clouds. In: *Astrobiology*, 18 (9), pp. 1181–1198. DOI: 10.1089/ast.2017.1783 (cit. on p. 139).

Lin, S. J. (2004). A "Vertically Lagrangian" Finite-Volume Dynamical Core for Global Models. In: *Monthly Weather Review*, 132 (10), pp. 2293–2307. DOI: 10.1175/1520-0493(2004)132<2293:AVLFDC>2.0.CO;2 (cit. on pp. 48, 139, 141).

Lin, S. J. and R. B. Rood (1997). An Explicit Flux-Form Semi-Lagrangian Shallow-Water Model on the Sphere. In: *Quarterly Journal of the Royal Meteorological Society*, 123 (544), pp. 2477–2498. DOI: 10.1002/qj.49712354416 (cit. on p. 48).

Liu, J. and T. Schneider (2011). Convective Generation of Equatorial Superrotation in Planetary Atmospheres. In: *Journal of the Atmospheric Sciences*, 68 (11), pp. 2742–2756. DOI: 10.1175/JAS-D-10-05013.1 (cit. on p. 70).

Lopez, E. D. and J. J. Fortney (2013). The Role of Core Mass in Controlling Evaporation: The Kepler Radius Distribution and the Kepler-36 Density Dichotomy. In: *The Astrophysical Journal*, 776 (2). DOI: 10.1088/0004-637X/776/1/2 (cit. on p. 4).

Lopez, E. D., J. J. Fortney, and N. Miller (2012). How Thermal Evolution and Mass-Loss Sculpt Populations of Super-Earths and Sub-Neptunes: Application to the Kepler-11 System and Beyond. In: *Astrophysical Journal*, 761 (1), p. 59. DOI: 10.1088/0004-637X/761/1/59 (cit. on p. 4).

Lora, J. M., J. I. Lunine, and J. L. Russell (2015). GCM Simulations of Titan's Middle and Lower Atmosphere and Comparison to Observations. In: *Icarus*, 250, pp. 516–528. DOI: 10.1016/j.icarus.2014.12.030 (cit. on p. 12).

Madhusudhan, N., M. C. Nixon, L. Welbanks, A. A. A. Piette, and R. A. Booth (2020). The Interior and Atmosphere of the Habitable-zone Exoplanet K2-18b. In: *The Astrophysical Journal Letters*, 891 (1), p. L7. DOI: 10.3847/2041-8213/ab7229 (cit. on pp. 6, 44, 47, 85, 137).

Madhusudhan, N., A. A. A. Piette, and S. Constantinou (2021). Habitability and Biosignatures of Hycean Worlds. In: *The Astrophysical Journal*, 918, p. 1. DOI: 10.3847/1538-4357/abfd9c (cit. on pp. 6, 91, 118, 126, 138, 175).

Madhusudhan, N., S. Sarkar, S. Constantinou, M. Holmberg, A. Piette, and J. I. Moses (2023). *Carbon-Bearing Molecules in a Possible Hycean Atmosphere*. arXiv: 2309.05566 [astro-ph] (cit. on pp. 7, 138, 170, 171).

Malik, M., L. Grosheintz, J. M. Mendonça, S. L. Grimm, B. Lavie, D. Kitzmann, S.-M. Tsai, A. Burrows, L. Kreidberg, M. Bedell, J. L. Bean, K. B. Stevenson, and K. Heng (2017). HELIOS: An Open-source, GPU-accelerated Radiative Transfer Code for Self-consistent Exoplanetary Atmospheres. In: *The Astronomical Journal*, 153 (2), p. 56. DOI: 10.3847/1538-3881/153/2/56 (cit. on pp. 105, 147).

Malik, M., D. Kitzmann, J. M. Mendonça, S. L. Grimm, G.-D. Marleau, E. F. Linder, S.-M. Tsai, and K. Heng (2019). Self-Luminous and Irradiated Exoplanetary Atmospheres Explored with HELIOS. In: *The Astronomical Journal*, 157 (5), p. 170. DOI: 10.3847/1538-3881/ab1084 (cit. on p. 147).

Manabe, S. and R. F. Strickler (1964). Thermal Equilibrium of the Atmosphere with a Convective Adjustment. In: *Journal of the Atmospheric Sciences*, 21 (4), pp. 361–385. DOI: 10.1175/1520-0469(1964)021<0361:teotaw>2.0.co;2 (cit. on p. 133).

Marcy, G. W., L. M. Weiss, E. A. Petigura, H. Isaacson, A. W. Howard, and L. A. Buchhave (2014a). Occurrence and Core-Envelope Structure of 1-4x Earth-size Planets around Sun-like Stars. In: *Proceedings of the National Academy of Sciences of the United States of America*, 111 (35), pp. 12655–12660. DOI: 10.1073/pnas.1304197111 (cit. on p. 3).

Marcy, G. W. et al. (2014b). Masses, Radii, and Orbits of Small Kepler Planets: The Transition from Gaseous to Rocky Planets. In: *Astrophysical Journal, Supplement Series*, 210 (2), p. 2014. DOI: 10.1088/0067-0049/210/2/20 (cit. on pp. 3, 4).

Markham, S., T. Guillot, and D. Stevenson (2022). Convective Inhibition with an Ocean: I. Supercritical Cores on Sub-Neptunes/Super-Earths. In: *Astronomy & Astrophysics*, 665, A12. DOI: 10.1051/0004-6361/202243359 (cit. on pp. 131, 132).

Matsuno, T. (1966). Quasi-Geostrophic Motions in the Equatorial Area. In: *Journal of the Meteorological Society of Japan. Ser. II*, 44 (1), pp. 25–43. DOI: 10.2151/jmsj1965.44.1_25 (cit. on pp. 26, 28, 156).

Mayne, N. J., B Drummond, F Debras, E Jaupart, J Manners, I. A. Boutle, I Baraffe, and K Kohary (2019). The Limits of the Primitive Equations of Dynamics for Warm, Slowly Rotating Small Neptunes and Super Earths. In: *The Astrophysical Journal*, 871 (1), p. 56. DOI: 10.3847/1538-4357/aaf6e9 (cit. on p. 34).

Mayne, N. J., F. Debras, I. Baraffe, J. Thuburn, D. S. Amundsen, D. M. Acreman, C. Smith, M. K. Browning, J. Manners, and N. Wood (2017). Results from a Set of Three-Dimensional Numerical Experiments of a Hot Jupiter Atmosphere. In: *As-*

tronomy and Astrophysics, 604, p. 79. DOI: 10.1051/0004-6361/201730465 (cit. on pp. 17, 166).

Mayor, M, M Marmier, C Lovis, S Udry, D Ségransan, F Pepe, W Benz, J. L. Bertaux, F Bouchy, X Dumusque, G. L. Curto, C Mordasini, D Queloz, and N. C. Santos (2011). The HARPS Search for Southern Extra-Solar Planets XXXIV. Occurrence, Mass Distribution and Orbital Properties of Super-Earths and Neptune-mass Planets. In: *Astronomy & Astrophysics* (cit. on p. 3).

McElroy, M. B., M. J. Prather, and Jose M. Rodriguez (1982). Escape of Hydrogen from Venus. In: *Science (New York, N.Y.)*, 215 (4540), pp. 1614–1615. DOI: 10.1126/science.215.4540.1614 (cit. on p. 90).

Mehio, N., S. Dai, and D.-e. Jiang (2014). Quantum Mechanical Basis for Kinetic Diameters of Small Gaseous Molecules. In: *The Journal of Physical Chemistry A*, 118 (6), pp. 1150–1154. DOI: 10.1021/jp412588f (cit. on p. 131).

Mellor, G. L. and T. Yamada (1982). Development of a Turbulence Closure Model for Geophysical Fluid Problems. In: *Reviews of Geophysics*, 20 (4), pp. 851–875. DOI: 10.1029/RG020i004p00851 (cit. on p. 140).

Mendonça, J. and P. Read (2016). Exploring the Venus Global Super-Rotation Using a Comprehensive General Circulation Model. In: *Planetary and Space Science*, 134, pp. 1–18. DOI: 10.1016/j.pss.2016.09.001 (cit. on p. 31).

Menou, K. (2012). Atmospheric Circulation and Composition of GJ1214b. In: *Astrophysical Journal Letters*, 744 (1), p. 16. DOI: 10.1088/2041-8205/744/1/L16 (cit. on pp. 34, 50, 51, 147).

Merlis, T. M. and T. Schneider (2010). Atmospheric Dynamics of Earth-Like Tidally Locked Aquaplanets. In: *Journal of Advances in Modeling Earth Systems*, 2 (4). DOI: 10.3894/JAMES.2010.2.13 (cit. on pp. 16, 37).

Miguel, Y and L Kaltenegger (2014). Exploring Atmospheres of Hot Mini-Neptunes and Extrasolar Giant Planets Orbiting Different Stars with Application to HD 97658b, WASP-12b, CoRoT-2b, XO-1b, and HD 189733b. In: *Astrophysical Journal*, 780 (2), p. 166. DOI: 10.1088/0004-637X/780/2/166 (cit. on p. 4).

Misener, W. and H. E. Schlichting (2021). To Cool Is to Keep: Residual H/He Atmospheres of Super-Earths and Sub-Neptunes. In: *Monthly Notices of the Royal Astronomical Society*, 503 (4), pp. 5658–5674. DOI: 10.1093/mnras/stab895 (cit. on p. 126).

Misener, W. and H. E. Schlichting (2022). The Importance of Silicate Vapour in Determining the Structure, Radii, and Envelope Mass Fractions of Sub-Neptunes. In:

Monthly Notices of the Royal Astronomical Society, 514 (4), pp. 6025–6037. DOI: 10.1093/mnras/stac1732 (cit. on p. 132).

Mitchell, J. L. and G. K. Vallis (2010). The Transition to Superrotation in Terrestrial Atmospheres. In: *Journal of Geophysical Research E: Planets*, 115 (12). DOI: 10.1029/2010JE003587 (cit. on pp. 22, 31, 70, 73).

Mlawer, E. J., V. H. Payne, J. L. Moncet, J. S. Delamere, M. J. Alvarado, and D. C. Tobin (2012). Development and Recent Evaluation of the MT-CKD Model of Continuum Absorption. In: *Philosophical Transactions of the Royal Society A: Mathematical, Physical and Engineering Sciences*, 370 (1968), pp. 2520–2556. DOI: 10.1098/rsta.2011.0295 (cit. on p. 210).

Montet, B. T., T. D. Morton, D. Foreman-Mackey, J. A. Johnson, D. W. Hogg, B. P. Bowler, D. W. Latham, A. Bieryla, and A. W. Mann (2015). Stellar and Planetary Properties of K2 Campaign 1 Candidates and Validation of 17 Planets, Including a Planet Receiving Earth-like Insolation. In: *Astrophysical Journal*, 809 (1), p. 25. DOI: 10.1088/0004-637X/809/1/25 (cit. on p. 5).

Mousis, O., M. Deleuil, A. Aguichine, E. Marcq, J. Naar, L. A. Aguirre, B. Brugger, and T. Gonçalves (2020). Irradiated Ocean Planets Bridge Super-Earth and Sub-Neptune Populations. In: *The Astrophysical Journal*, 896 (2), p. L22. DOI: 10.3847/2041-8213/ab9530 (cit. on p. 127).

Nakajima, S., Y.-Y. Hayashi, and Y. Abe (1992). A Study on the "Runaway Greenhouse Effect" with a One-Dimensional Radiative–Convective Equilibrium Model. In: *Journal of the Atmospheric Sciences*, 49 (23), pp. 2256–2266. DOI: 10.1175/1520-0469(1992)049<2256:ASOTGE>2.0.CO;2 (cit. on p. 94).

Newman, M. and C. Leovy (1992). Maintenance of Strong Rotational Winds in Venus' Middle Atmosphere by Thermal Tides. In: *Science (New York, N.Y.)*, 257 (5070), pp. 647–650. DOI: 10.1126/science.257.5070.647 (cit. on p. 30).

Noda, S., M. Ishiwatari, K. Nakajima, Y. O. Takahashi, S. Takehiro, M. Onishi, G. L. Hashimoto, K. Kuramoto, and Y. Y. Hayashi (2017). The Circulation Pattern and Day-Night Heat Transport in the Atmosphere of a Synchronously Rotating Aquaplanet: Dependence on Planetary Rotation Rate. In: *Icarus*, 282, pp. 1–18. DOI: 10.1016/j.icarus.2016.09.004 (cit. on pp. 16, 24).

Olson, G. L. and P. Kunasz (1987). Short Characteristic Solution of the Non-LTE Line Transfer Problem by Operator Perturbation—I. The One-Dimensional Planar Slab. In: *Journal of Quantitative Spectroscopy and Radiative Transfer*, 38 (5), pp. 325–336. DOI: 10.1016/0022-4073(87)90027-6 (cit. on p. 146).

Owen, J. E. and S. Mohanty (2016). Habitability of Terrestrial-Mass Planets in the HZ of M Dwarfs – I. H/He-dominated Atmospheres. In: *Monthly Notices of the Royal Astronomical Society*, 459 (4), pp. 4088–4108. DOI: 10.1093/mnras/stw959 (cit. on p. 126).

Owen, J. E. and Y. Wu (2013). Kepler Planets: A Tale of Evaporation. In: *Astrophysical Journal*, 775 (2), p. 105. DOI: 10.1088/0004-637X/775/2/105 (cit. on p. 3).

Owen, J. E. and Y. Wu (2017). The Evaporation Valley in the Kepler Planets. In: *The Astrophysical Journal*. DOI: 10.3847/1538-4357/aa890a (cit. on p. 50).

Palotai, C., S. Brueshaber, R. Sankar, and K. Sayanagi (2023). Moist Convection in the Giant Planet Atmospheres. In: *Remote Sensing*, 15 (1), p. 219. DOI: 10.3390/rs15010219 (cit. on p. 39).

Parmentier, V. and I. J. M. Crossfield (2018). Exoplanet Phase Curves: Observations and Theory. In: *Handbook of Exoplanets*. Ed. by H. J. Deeg and J. A. Belmonte. Cham: Springer International Publishing, pp. 1419–1440. ISBN: 978-3-319-55333-7. DOI: 10.1007/978-3-319-55333-7_116 (cit. on p. 12).

Pecaut, M. J. and E. E. Mamajek (2013). Intrinsic Colors, Temperatures, and Bolometric Corrections of Pre-Main-Sequence Stars. In: *Astrophysical Journal, Supplement Series*, 208 (1). DOI: 10.1088/0067-0049/208/1/9 (cit. on p. 83).

Peck, E. R. and S. Huang (1977). Refractivity and Dispersion of Hydrogen in the Visible and near Infrared. In: *Journal of the Optical Society of America*, 67 (11), p. 1550. DOI: 10.1364/josa.67.001550 (cit. on p. 210).

Petigura, E. A., A. W. Howard, and G. W. Marcy (2013). Prevalence of Earth-size Planets Orbiting Sun-like Stars. In: *Proceedings of the National Academy of Sciences of the United States of America*, 110 (48), pp. 19273–19278. DOI: 10.1073/pnas.1319909110 (cit. on p. 3).

Piaulet, C. et al. (2023). Evidence for the Volatile-Rich Composition of a 1.5-Earth-radius Planet. In: *Nature Astronomy*, 7 (2), pp. 206–222. DOI: 10.1038/s41550-022-01835-4 (cit. on p. 127).

Pierrehumbert, R. T. and K. L. Swanson (1995). Baroclinic Instability. In: *Annu. Rev. Fluid Mech*, 27, pp. 419–67. DOI: 10.1146/annurev.fluid.27.1.419 (cit. on p. 129).

Pierrehumbert, R. T. (2002). The Hydrologic Cycle in Deep-Time Climate Problems. In: *Nature*, 419 (6903), pp. 191–198. DOI: 10.1038/nature01088 (cit. on p. 39).

Pierrehumbert, R. T. (2010). *Principles of Planetary Climate*. Cambridge: Cambridge University Press. ISBN: 978-0-521-86556-2. DOI: 10.1017/cbo9780511780783 (cit. on pp. 37, 40, 49, 92, 108, 116, 133, 144, 168).

Pierrehumbert, R. T. (2023). The Runaway Greenhouse on Sub-Neptune Waterworlds. In: *The Astrophysical Journal*, 944 (1), p. 20. DOI: 10.3847/1538-4357/acafdf (cit. on pp. 110, 114, 123, 127, 132).

Pierrehumbert, R. T. and F. Ding (2016). Dynamics of Atmospheres with a Non-Dilute Condensible Component. In: *Proceedings of the Royal Society A: Mathematical, Physical and Engineering Sciences*, 472 (2190), p. 2190. DOI: 10.1098/rspa.2016.0107 (cit. on pp. 15, 44, 48, 56, 57, 109, 138, 139, 141, 142).

Pierrehumbert, R. T. and M. Hammond (2019). Atmospheric Circulation of Tide-Locked Exoplanets. In: *Annual Review of Fluid Mechanics*, 51 (1), pp. 275–303. DOI: 10.1146/annurev-fluid-010518-040516 (cit. on pp. 12, 15, 48, 52, 57, 71, 165).

Pierrehumbert, R. and E. Gaidos (2011). Hydrogen Greenhouse Planets Beyond the Habitable Zone. In: *The Astrophysical Journal Letters*, 734 (1), p. L13. DOI: 10.1088/2041-8205/734/1/L13 (cit. on pp. 97, 102, 103, 118).

Piette, A. A. and N. Madhusudhan (2020). On the Temperature Profiles and Emission Spectra of Mini-Neptune Atmospheres. In: *The Astrophysical Journal*, 904 (2), p. 154. DOI: 10.3847/1538-4357/abbfb1 (cit. on pp. 6, 51, 91, 109, 130, 177).

Putman, W. M. and S. J. Lin (2007). Finite-Volume Transport on Various Cubed-Sphere Grids. In: *Journal of Computational Physics*, 227 (1), pp. 55–78. DOI: 10.1016/j.jcp.2007.07.022 (cit. on pp. 51, 141).

Rajpurohit, A. S., C Reylé, F Allard, D Homeier, M Schultheis, M. S. Bessell, and A. C. Robin (2013). The Effective Temperature Scale of M Dwarfs. In: *Astronomy and Astrophysics*, 556, p. 15. DOI: 10.1051/0004-6361/201321346 (cit. on p. 52).

Rauer, H. et al. (2014). The PLATO 2.0 Mission. In: *Experimental Astronomy*, 38 (1), pp. 249–330. DOI: 10.1007/s10686-014-9383-4 (cit. on p. 91).

Rauscher, E. and K. Menou (2010). Three-Dimensional Modeling of Hot Jupiter Atmospheric Flows. In: *Astrophysical Journal*, 714 (2), pp. 1334–1342. DOI: 10.1088/0004-637X/714/2/1334 (cit. on p. 17).

Rauscher, E. and K. Menou (2012). A General Circulation Model for Gaseous Exoplanets with "Double-Gray" Radiative Transfer. In: *Astrophysical Journal*, 750 (2), p. 96. DOI: 10.1088/0004-637X/750/2/96 (cit. on p. 18).

Read, P. L. (1986). Super-Rotation and Diffusion of Axial Angular Momentum: I. 'Speed Limits' for Axisymmetric Flow in a Rotating Cylindrical Fluid Annulus. In: *Quarterly Journal of the Royal Meteorological Society*, 112 (471), pp. 231–251. DOI: 10.1002/qj.49711247113 (cit. on pp. 25, 69).

Rhines, P. B. (1975). Waves and Turbulence on a Beta-Plane. In: *Journal of Fluid Mechanics*, 69 (3), pp. 417–443. DOI: 10.1017/S0022112075001504 (cit. on p. 16).

Rogers, L. A. and S Seager (2010). Three Possible Origins for the Gas Layer on GJ 1214B. In: *Astrophysical Journal*, 716 (2), pp. 1208–1216. DOI: 10.1088/0004-637X/716/2/1208 (cit. on pp. 4, 6).

Rossow, W. B. (1978). Cloud Microphysics: Analysis of the Clouds of Earth, Venus, Mars and Jupiter. In: *Icarus*, 36 (1), pp. 1–50. DOI: 10.1016/0019-1035(78)90072-6 (cit. on p. 171).

Rossow, W. B. and G. P. Williams (1979). Large-Scale Motion in the Venus Stratosphere. In: *Journal of the Atmospheric Sciences*, 36 (3), pp. 377–389. DOI: 10.1175/1520-0469(1979)036<0377:LSMITV>2.0.CO;2 (cit. on p. 21).

Sanchez-Lavega, A. (1994). Saturn's Great White Spots. In: *Chaos: An Interdisciplinary Journal of Nonlinear Science*, 4 (2), pp. 341–353. DOI: 10.1063/1.166012 (cit. on p. 41).

Sankar, R. and C. Palotai (2022). A New Convective Parameterization Applied to Jupiter: Implications for Water Abundance near the 24°N Region. In: *Icarus*, 380, p. 114973. DOI: 10.1016/j.icarus.2022.114973 (cit. on p. 133).

Schaefer, L., R. D. Wordsworth, Z. Berta-Thompson, and D. Sasselov (2016). Predictions of the Atmospheric Composition of GJ 1132b. In: *The Astrophysical Journal*, 829 (2), p. 63. DOI: 10.3847/0004-637X/829/2/63 (cit. on p. 126).

Scheucher, M., F Wunderlich, J. L. Grenfell, M Godolt, F Schreier, D Kappel, R Haus, K Herbst, and H Rauer (2020). Consistently Simulating a Wide Range of Atmospheric Scenarios for K2-18b with a Flexible Radiative Transfer Module. In: *The Astrophysical Journal*, 898 (1), p. 44. DOI: 10.3847/1538-4357/ab9084 (cit. on pp. 50, 52, 53).

Schwarzschild, K. (1906). On the Equilibrium of the Sun's Atmosphere. In: *Nachrichten von der Königlichen Gesellschaft der Wissenschaften zu Göttingen. Math.-phys. Klasse*, 195, pp. 41–53 (cit. on p. 106).

Seager, S., J. J. Petkowski, M. N. Günther, W. Bains, T. Mikal-Evans, and D. Deming (2021). Possibilities for an Aerial Biosphere in Temperate Sub Neptune-Sized Exoplanet Atmospheres. In: *Universe*, 7 (6), p. 172. DOI: 10.3390/universe7060172 (cit. on pp. 35, 47, 138).

Seeley, J. T. and R. D. Wordsworth (2021). Episodic Deluges in Simulated Hothouse Climates. In: *Nature*, 599 (7883), pp. 74–79. DOI: 10.1038/s41586-021-03919-z (cit. on p. 170).

Sergeev, D. E., F. H. Lambert, N. J. Mayne, I. A. Boutle, J. Manners, and K. Kohary (2020). Atmospheric Convection Plays a Key Role in the Climate of Tidally Locked Terres-

trial Exoplanets: Insights from High-resolution Simulations. In: *The Astrophysical Journal*, 894 (2), p. 84. DOI: 10.3847/1538-4357/ab8882 (cit. on pp. 20, 37).

Shaw, T. A. and T. G. Shepherd (2007). Angular Momentum Conversation and Gravity Wave Drag Parameterization: Implications for Climate Models. In: *Journal of the Atmospheric Sciences*, 64 (1), pp. 190–203. DOI: 10.1175/JAS3823.1 (cit. on p. 73).

Showman, A. P. and T Guillot (2002). Atmospheric Circulation and Tides of "51 Pegasus b-like" Planets. In: *Astronomy and Astrophysics*, 385 (1), pp. 166–180. DOI: 10.1051/0004-6361:20020101 (cit. on pp. 17, 18, 20).

Showman, A. P., R. D. Wordsworth, T. M. Merlis, and Y. Kaspi (2013). Atmospheric Circulation of Terrestrial Exoplanets. In: *Comparative Climatology of Terrestrial Planets*. DOI: 10.2458/azu_uapress_9780816530595-ch12 (cit. on p. 25).

Showman, A. P., J. Y.-K. Cho, and K. Menou (2009). Atmospheric Circulation of Exoplanets. In: (cit. on p. 18).

Showman, A. P., N. K. Lewis, and J. J. Fortney (2015). Three-Dimensional Atmospheric Circulation of Warm and Hot Jupiters: Effects of Orbital Distance, Rotation Period, and Non-Synchronous Rotation. In: *The Astrophysical Journal*, 801, p. 95. DOI: 10.1088/0004-637X/801/2/95 (cit. on pp. 12, 17, 20, 21).

Showman, A. P. and L. M. Polvani (2010). The Matsuno-Gill Model and Equatorial Superrotation. In: *Geophysical Research Letters*, 37 (18), n/a–n/a. DOI: 10.1029/2010GL044343 (cit. on p. 30).

Showman, A. P. and L. M. Polvani (2011). Equatorial Superrotation on Tidally Locked Exoplanets. In: *Astrophysical Journal*, 738 (1), p. 71. DOI: 10.1088/0004-637X/738/1/71 (cit. on pp. 11, 29, 69, 156).

Showman, A. P., X. Tan, and V. Parmentier (2020). Atmospheric Dynamics of Hot Giant Planets and Brown Dwarfs. In: *Space Science Reviews*, 216 (8), p. 139. DOI: 10.1007/s11214-020-00758-8 (cit. on pp. 17, 18).

Simpson, G. (1929). On Some Studies in Terrestrial Radiation. In: *Quarterly Journal of the Royal Meteorological Society*, 55 (229), pp. 73–73. DOI: 10.1002/qj.49705522908 (cit. on p. 94).

Soubiran, F. and B. Militzer (2015). Miscibility Calculations for Water and Hydrogen in Giant Planets. In: *The Astrophysical Journal*, 806 (2), p. 228. DOI: 10.1088/0004-637X/806/2/228 (cit. on pp. 98, 123).

Spiga, A., S. Guerlet, E. Millour, M. Indurain, Y. Meurdesoif, S. Cabanes, T. Dubos, J. Leconte, A. Boissinot, S. Lebonnois, M. Sylvestre, and T. Fouchet (2020). Global Climate Modeling of Saturn's Atmosphere. Part II: Multi-annual High-Resolution

Dynamical Simulations. In: *Icarus*, 335, p. 113377. DOI: 10.1016/j.icarus.2019.07.011 (cit. on p. 12).

Takagi, M. and Y. Matsuda (2007). Effects of Thermal Tides on the Venus Atmospheric Superrotation. In: *Journal of Geophysical Research (Atmospheres)*, 112 (D09112), p. D09112. DOI: 10.1029/2006JD007901 (cit. on p. 30).

Tan, X., M. Lefèvre, and R. T. Pierrehumbert (2021). Convection Modeling of Pure-steam Atmospheres. In: *The Astrophysical Journal Letters*, 923 (1), p. L15. DOI: 10.3847/2041-8213/ac3e69 (cit. on p. 131).

Thatcher, D. R. and C. Jablonowski (2016). A Moist Aquaplanet Variant of the Held–Suarez Test for Atmospheric Model Dynamical Cores. In: *Geoscientific Model Development*, 9 (4), pp. 1263–1292. DOI: 10.5194/gmd-9-1263-2016 (cit. on p. 171).

Tollefson, J., I. D. Pater, P. S. Marcus, S. Luszcz-Cook, L. A. Sromovsky, P. M. Fry, L. N. Fletcher, and M. H. Wong (2018). Vertical Wind Shear in Neptune's Upper Atmosphere Explained with a Modified Thermal Wind Equation. In: *Icarus*, 311, pp. 317–339. DOI: 10.1016/j.icarus.2018.04.009 (cit. on p. 43).

Toon, O. B., C. P. McKay, T. P. Ackerman, and K. Santhanam (1989). Rapid Calculation of Radiative Heating Rates and Photodissociation Rates in Inhomogeneous Multiple Scattering Atmospheres. In: *Journal of Geophysical Research*, 94 (D13). DOI: 10.1029/jd094id13p16287 (cit. on p. 147).

Tsai, S. M., I. Dobbs-Dixon, and P. G. Gu (2014). Three-Dimensional Structures of Equatorial Waves and the Resulting Super-Rotation in the Atmosphere of a Tidally Locked Hot Jupiter. In: *Astrophysical Journal*, 793 (2). DOI: 10.1088/0004-637X/793/2/141 (cit. on pp. 30, 69).

Tsai, S.-M., H. Innes, T. Lichtenberg, J. Taylor, M. Malik, K. Chubb, and R. Pierrehumbert (2021). Inferring Shallow Surfaces on Sub-Neptune Exoplanets with JWST. In: *The Astrophysical Journal Letters*, 922 (2), p. L27. DOI: 10.3847/2041-8213/ac399a (cit. on pp. 6, 44, 125, 127, 137, 147).

Tsai, S.-M., J. R. Lyons, L. Grosheintz, P. B. Rimmer, D. Kitzmann, and K. Heng (2017). VULCAN: An Open-source, Validated Chemical Kinetics Python Code for Exoplanetary Atmospheres. In: *The Astrophysical Journal Supplement Series*, 228, p. 20. DOI: 10.3847/1538-4365/228/2/20 (cit. on p. 147).

Turbet, M., E. Bolmont, G. Chaverot, D. Ehrenreich, J. Leconte, and E. Marcq (2021). Day-Night Cloud Asymmetry Prevents Early Oceans on Venus but Not on Earth. In: *Nature*, 598, pp. 276–280. DOI: 10.1038/s41586-021-03873-w (cit. on pp. 91, 130).

Turbet, M., T. J. Fauchez, J. Leconte, E. Bolmont, G. Chaverot, F. Forget, E. Millour, F. Selsis, B. Charnay, E. Ducrot, M. Gillon, A. Maurel, and G. L. Villanueva (2023). *Water Condensation Zones around Main Sequence Stars*. arXiv: 2308.15110 [astro-ph, physics:physics] (cit. on p. 91).

Turbet, M., T. J. Fauchez, D. E. Sergeev, I. A. Boutle, K. Tsigaridis, M. J. Way, E. T. Wolf, S. D. Domagal-Goldman, F. Forget, J. Haqq-Misra, R. K. Kopparapu, F. H. Lambert, J. Manners, N. J. Mayne, and L. Sohl (2022). The TRAPPIST-1 Habitable Atmosphere Intercomparison (THAI). I. Dry Cases—The Fellowship of the GCMs. In: *The Planetary Science Journal*, 3 (9), p. 211. DOI: 10.3847/PSJ/ac6cf0 (cit. on p. 165).

Vaïtilingom, M., E. Attard, N. Gaiani, M. Sancelme, L. Deguillaume, A. I. Flossmann, P. Amato, and A.-M. Delort (2012). Long-Term Features of Cloud Microbiology at the Puy de Dôme (France). In: *Atmospheric Environment*, 56, pp. 88–100. DOI: 10.1016/j.atmosenv.2012.03.072 (cit. on p. 139).

Vallis, G. K. (2017). *Atmospheric and Oceanic Fluid Dynamics: Fundamentals and Large-Scale Circulation, Second Edition*. Cambridge University Press. ISBN: 978-1-107-58841-7. DOI: 10.1017/9781107588417 (cit. on pp. 14, 15, 25–27, 37, 62, 78).

Wagner, W. and A. Pruß (2002). The IAPWS Formulation 1995 for the Thermodynamic Properties of Ordinary Water Substance for General and Scientific Use. In: *Journal of Physical and Chemical Reference Data*, 31 (2), pp. 387–535. DOI: 10.1063/1.1461829 (cit. on pp. 104, 107).

Wang, H. and R. Wordsworth (2020). Extremely Long Convergence Times in a 3D GCM Simulation of the Sub-Neptune Gliese 1214b. In: *The Astrophysical Journal*, 891 (1), p. 7. DOI: 10.3847/1538-4357/ab6dcc (cit. on pp. 34, 54, 82, 87).

Wang, P. and J. L. Mitchell (2014). Planetary Ageostrophic Instability Leads to Superrotation. In: *Geophysical Research Letters*, 41 (12), pp. 4118–4126. DOI: 10.1002/2014GL060345 (cit. on pp. 31, 69, 70, 73, 74, 87).

Way, M. J., A. D. Del Genio, I. Aleinov, T. L. Clune, M. Kelley, and N. Y. Kiang (2018). Climates of Warm Earth-like Planets. I. 3D Model Simulations. In: *The Astrophysical Journal Supplement Series*, 239 (2), p. 24. DOI: 10.3847/1538-4365/aae9e1 (cit. on p. 20).

Weiss, L. M. and G. W. Marcy (2014). The Mass-Radius Relation for 65 Exoplanets Smaller than 4 Earth Radii. In: *Astrophysical Journal Letters*, 783 (1), p. 6. DOI: 10.1088/2041-8205/783/1/L6 (cit. on pp. 3, 4).

Widemann, T., E. Lellouch, and J.-F. Donati (2008). Venus Doppler Winds at Cloud Tops Observed with ESPaDOnS at CFHT. In: *Planetary and Space Science*. Ground-

Based and Venus Express Coordinated Campaign, 56 (10), pp. 1320–1334. DOI: 10.1016/j.pss.2008.07.005 (cit. on p. 30).

Winn, J. N. and D. C. Fabrycky (2015). The Occurrence and Architecture of Exoplanetary Systems. In: *Annu. Rev. Astron. Astrophys*, 53, pp. 409–447. DOI: 10.1146/annurev-astro-082214-122246 (cit. on p. 3).

Wolf, E. T. and O. B. Toon (2014). Delayed Onset of Runaway and Moist Greenhouse Climates for Earth. In: *Geophysical Research Letters*, 41 (1), pp. 167–172. DOI: 10.1002/2013GL058376 (cit. on p. 91).

Wolfgang, A., L. A. Rogers, and E. B. Ford (2016). Probabilistic Mass-Radius Relationship for Sub-Neptune-Sized Planets. In: *The Astrophysical Journal*, 825 (1), p. 19. DOI: 10.3847/0004-637x/825/1/19 (cit. on p. 3).

Yang, J., G. Boué, D. C. Fabrycky, and D. S. Abbot (2014). Strong Dependence of the Inner Edge of the Habitable Zone on Planetary Rotation Rate. In: *Astrophysical Journal Letters*, 787 (1). DOI: 10.1088/2041-8205/787/1/L2 (cit. on pp. 16, 20, 38, 91).

Yang, J., N. B. Cowan, and D. S. Abbot (2013). Stabilizing Cloud Feedback Dramatically Expands the Habitable Zone of Tidally Locked Planets. In: *Astrophysical Journal Letters*, 771 (2), p. L45. DOI: 10.1088/2041-8205/771/2/L45 (cit. on pp. 38, 39, 91, 130, 171).

Young, R. M. B., P. L. Read, and Y. Wang (2019). Simulating Jupiter's Weather Layer. Part I: Jet Spin-up in a Dry Atmosphere. In: *Icarus*, 326, pp. 225–252. DOI: 10.1016/j.icarus.2018.12.005 (cit. on p. 12).

Yu, X., J. I. Moses, J. J. Fortney, and X. Zhang (2021). How to Identify Exoplanet Surfaces Using Atmospheric Trace Species in Hydrogen-dominated Atmospheres. In: *The Astrophysical Journal*, 914 (1), p. 38. DOI: 10.3847/1538-4357/abfdc7 (cit. on p. 6).

Zhang, X. and A. P. Showman (2017). Effects of Bulk Composition on the Atmospheric Dynamics on Close-in Exoplanets. In: *The Astrophysical Journal*, 836 (1), p. 73. DOI: 10.3847/1538-4357/836/1/73 (cit. on pp. 18, 19, 34, 58, 60, 82, 83).

Zhang, X. and A. P. Showman (2018). Global-Mean Vertical Tracer Mixing in Planetary Atmospheres. II. Tidally Locked Planets. In: *The Astrophysical Journal*. DOI: 10.3847/1538-4357/aada7c (cit. on p. 85).

Zi-Ping Sun, C. R. Stoker, and G. Schubert (1991). Thermal and Humidity Winds in Outer Planet Atmospheres. In: *Icarus*, 91 (1), pp. 154–160. DOI: 10.1016/0019-1035(91)90134-F (cit. on p. 43).

Zurita-Gotor, P., Á. Anaya-Benlliure, and I. M. Held (2022). The Sensitivity of Superrotation to the Latitude of Baroclinic Forcing in a Terrestrial Dry Dynamical Core.

In: *Journal of the Atmospheric Sciences*, 79 (5), pp. 1311–1323. DOI: 10.1175/JAS-D-21-0269.1 (cit. on p. 31).

Appendix A

Effect of Pressure-Dependent Opacities

We present here a comparison of the P6c experiment (see Table 3.2) to an identical one run with the SW opacity proportional to p (hereafter referred to as the pressure-dependent opacity (PDO) experiment). We changed the opacity such that the total SW optical depth of the atmosphere remained the same.

A.1 Temperature Profiles

As shown in Figure 3.1, including pressure-dependent SW opacities increases the temperature at the bottom of the atmosphere. It also increases the pressure of the characteristic SW heating level where $\tau_{SW} = 1$ by a factor of $\sqrt{\tau_{SW_0}}$, where τ_{SW_0} is the total SW optical depth of the atmosphere. In the context of our experiments, this moves the $\tau = 1$ level from 0.8 bar to 2.8 bar.

In Figure A.1 we look at the latitudinal variation in temperature in both experiments. We note that the longitudinal variation at all latitudes is extremely small in both cases (on the order of 10^{-2} K). We see that the drop in temperature between equator and pole is smaller in the PDO experiment, which confirms that we are still well within the weak temperature gradient regime discussed in the main text.

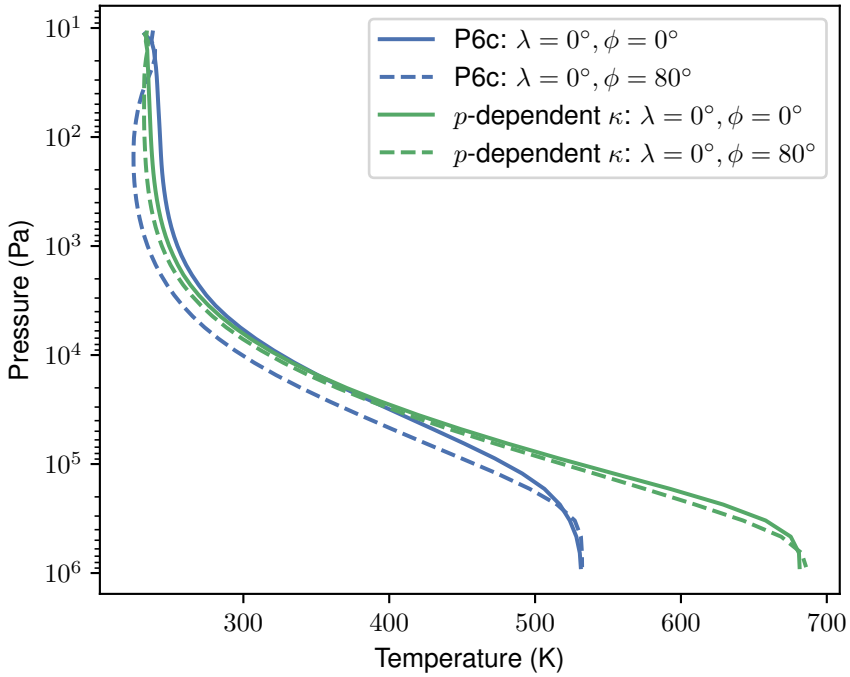

Figure A.1: Latitudinal temperature variation of the two experiments. The case with pressure-dependent opacity shows a much smaller equator to pole temperature contrast.

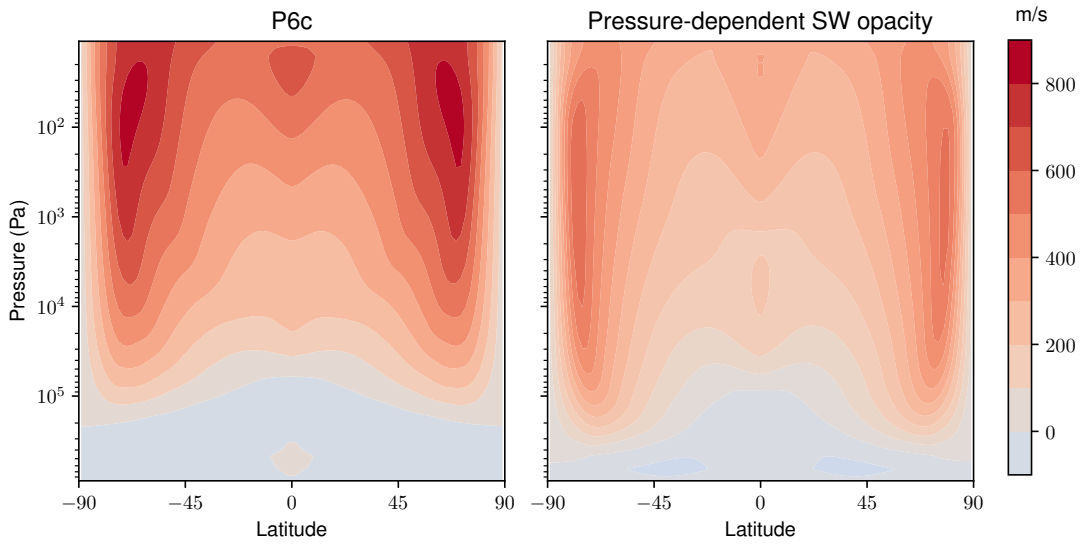

Figure A.2: The zonal-mean zonal wind profiles.

A.2 Zonal Wind

n Figure A.2 we compare the zonal-mean zonal wind profiles between the two experiments. The PDO experiment shows qualitatively similar zonal wind structure, with two

high latitude, cyclostrophically balanced zonal jets and equatorial superrotation with a maximum in the upper atmosphere. We note that the magnitude of the zonal wind in the PDO experiment is significantly lower than in the P6c experiment, which is consistent with the lower equator-to-pole temperature difference seen in section A.1, since this is proportional to the vertical wind shear in cyclostrophic balance. However, since we currently have no theory predicting the strength of this wind and temperature gradient a priori, we cannot explain why the magnitude of this wind differs on changing the SW heating profile.

We also note that the jets extend to higher pressures in the PDO experiment. This makes sense since the characteristic level of SW heating (discussed in section A.1) is at a higher pressure in this experiment, which drives the dynamics at this level.

The instability discussed in section 3.2.5 was also present in the PDO experiment.

A.3 Mass Streamfunctions

Lastly, we compare the mass streamfunctions of the two experiments. Qualitatively, the structure of the streamfunctions is similar between the two experiments. In the PDO runs, the level of the maximum streamfunction increases in pressure, which is linked once again to the characteristic level of SW heating moving to higher pressures. The magnitude of the tidally-locked streamfunction (which we related to the strength of the instellation in section 3.2.4) is of the same order of magnitude but not identical between the two experiments. Our scaling in section 3.2.4 linked the streamfunction to the magnitude of the solar heating. Since the maximum magnitude of the streamfunction is roughly at the level of characteristic SW heating in both cases (0.8 bar for P6c, 2.2 bar for PDO), we would expect the integrated heating at this level not to vary between cases. However, changes in the mean dry static energy, and physics not accounted for by the crude approximations made in deriving the scaling law may cause the two values

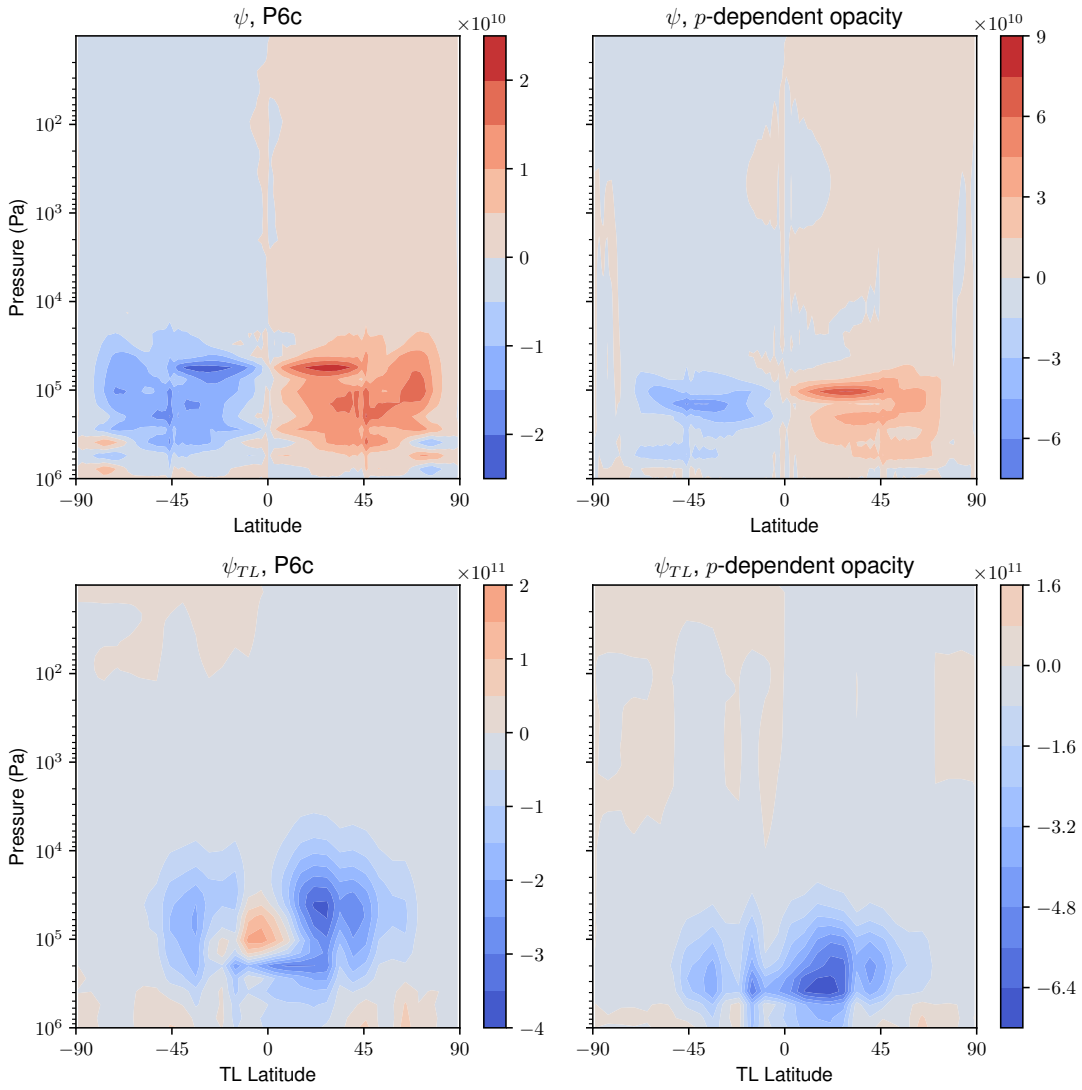

Figure A.3: The mass streamfunction (in units of kg/s) in conventional latitude-longitude coordinates (top row) and tidally-locked coordinates (bottom row) for the P6c (left) and PDO (right). experiments.

to be different.

Appendix B

Calculation of Radiative Fluxes

This appendix describes the methods used to calculate radiative fluxes in Chapter 5.

We calculate the radiative fluxes using the SOCRATES code, based on Edwards and Slingo (1996). SOCRATES uses the correlated-k method to efficiently calculate two-stream fluxes in both the longwave (LW) and shortwave (SW) regions of the spectrum. Gaseous overlap is treated with the equivalent extinction method with resorting and rebinning (Lacis and Oinas, 1991). In Section 5.1, we calculate LW fluxes in 300 bands equally spaced in wavenumber between 1 cm^{-1} and 5000 cm^{-1}. In the SW region, we perform two separate calculations for a G-type star (using the Lean and DeLand (2012) solar spectrum) and an M-type star (calculated using PHOENIX (Husser et al., 2013) for a 3500 K star with $\log(g) = 5.0$ and solar metallicities and alpha element abundances), each with 300 bands equally spaced in wavenumber. Since the calculations in Section 5.1 specify a temperature-pressure profile, the computational expense of calculating the fluxes in 300 bands in both the LW and SW calculation is minimal. We calculate k-coefficients on a 20-by-20 grid in temperature-pressure space over our range of interest. Since we only used this file to calculate fluxes for pure H_2-He atmospheres or pure steam atmospheres, it assumes self-broadening of water lines at 100% water vapour

concentration.

For the M-star we use the range 250 cm^{-1} to 40 000 cm^{-1} and for the G-star we use 250 cm^{-1} to 50 000 cm^{-1}. We consider the collision-induced absorption (CIA) due to H_2-H_2 and H_2-He interactions as the main sources of absorption. We calculate H_2-He opacities using the HITRAN database (Karman et al., 2019) and use the HITRAN database with additional data from Borysow (2002) for the calculation of H_2-H_2 opacities. In the SW calculation we include the effects of Rayleigh scattering by both hydrogen and helium, calcualting the cross sections using fits of refractive indices taken from Peck and Huang (1977) and Cuthbertson and Cuthbertson (1932) respectively. A SW surface albedo of 0.12 was specified (Goldblatt et al., 2013) and the surface temperature was assumed to be identical to the temperature of the lowest layer of the atmosphere.

Water vapour absorption k-coefficients are calculated using HITRAN data (Karman et al., 2019) and continuum absorption is calculated with the MT_CKD model version 3.0 (Mlawer et al., 2012). The refractive index of water used to calculate the Rayleigh scattering coefficients was taken from Ciddor (1996).

For the calculations in Section 5.2 we use 30 bands in each of the LW and SW regions and a 10-by-10 temperature-pressure grid to speed up the convergence of the numerical iteration required to find the correct temperature-pressure profile. We also calculate the effect of self broadening at 5 different water vapour concentrations linearly spaced between 0.2 and 1.0. We benchmarked the 30 band spectral files against the 300 band spectral files in the following ways. Firstly, we checked that the 30 band LW spectral file reproduced the OLR of the 300 band file for a pure steam atmosphere. The OLRs computed agreed to within 1%. Similarly, for a pure H_2 atmosphere on the dry adiabat the OLRs calculated with 30 bands and 300 bands were the same to within 1%. A qualitative inspection of the spectral output also showed that the OLR binned from 300 bands to 30 bands matched the 30 band output very well. In the SW region, we compared the net flux at a pressure level in the middle of the atmosphere for both a pure steam and pure

hydrogen atmosphere. For the M-star, the difference between the net fluxes is always less than 1%. For the G-star files, the reduced resolution impacts the Rayleigh scattering, with the 300 band case showing more Rayleigh scattered flux than the 30 band case. This caused variations in the net flux on the order of 10%.

To test the effect of decreasing the number of bands on the iterated temperature-pressure profiles, we re-ran two simulations (M-star and G-star cases) with surface temperatures around 300 K with 10^4 kg m^{-2} dry mass content and using modified 300 band spectral files. These files included the effect of self-broadening but reduced the temperature-pressure grid resolution to 10-by-10 in order to allow the model to run in a reasonable length of time. The resulting temperature-pressure profiles are very similar to those obtained with the 30 band files, with the surface temperatures obtained in both M-star and G-star experiments being within 1.2 K of the 30 band experiments.

Appendix C

Analytic OLR Calculations

In this appendix an analytic expression for the outgoing longwave radiation (OLR) from a hydrogen-dominated atmosphere with convective inhibition is derived. Interpretation of these results is provided in Section 5.3.4.

In the optically thick limit ($\tau \gg 1$), the OLR of a grey atmosphere is given by:

$$\mathrm{OLR} \approx \int_0^\infty \sigma T(\tau)^4 e^{-\tau}\, \mathrm{d}\tau\,. \tag{C.1}$$

To calculate this integral, we require the temperature profile $T(\tau)$ and the optical depth:

$$\tau(p) = \int_0^p \frac{\mathrm{d}p'}{\bar{\theta} g}(\kappa_d(1-q) + q\kappa_v), \tag{C.2}$$

where κ_d and κ_v are characteristic grey opacities for the dry and condensible phases of the atmosphere respectively and $\bar{\theta}$ is the average zenith angle, accounting for the angular distribution of the LW radiation. To simplify the problem, we split our atmospheres into two regions separated at $q = q_c = 1/(\beta\varpi)$, since we expect the lapse rates in these two regions to be very different. We assume that the moisture at this level is dilute such that we can make the approximation:

$$q \approx \varepsilon \frac{p_{\mathrm{sat}}}{p}. \tag{C.3}$$

This approximation is approximately valid if $q_c < 0.1$, i.e. $T < 0.1L\varpi/R_v = 480$ K assuming $\beta = L/R_vT$. We can verify that this is the case in all of our simulations. We then approximate $p_{\text{sat}}(T)$ in the same way as Koll and Cronin (2019), writing:

$$p_{\text{sat}}(T) = p_0\left(\frac{T}{T_0}\right)^{\beta_0}, \tag{C.4}$$

where $\beta_0 \equiv L/(R_vT_0)$ and (p_0, T_0) is some reference point on the vapour-liquid phase curve of water chosen to be close to our region of interest. Like in Koll and Cronin (2019), we will choose p_0 as the pressure where a pure steam atmosphere has unity optical thickness:

$$p_0 = \frac{g\bar{\theta}}{\kappa_v}. \tag{C.5}$$

This gives $(p_0, T_0) = (588.6\text{ Pa}, 272.6\text{ K})$ for $g = 9.81\text{ m s}^{-2}$, $\kappa_v = 0.01\text{ m}^2\text{ kg}^{-1}$, $\bar{\theta} = 3/5$ - remarkably close to the triple point of water vapour. If Equation C.3 holds, then the temperature and pressure (T_*, p_*) at which $q = q_c$ satisfies:

$$\varepsilon\frac{p_0}{p_*}\left(\frac{T_*}{T_0}\right)^{\beta_0} = \frac{R_vT_0}{p}, \tag{C.6}$$

$$T_* = T_0\left(\frac{1}{\beta_0\varpi}\frac{p_*}{\varepsilon p_0}\right)^{1/(\beta_0-1)}. \tag{C.7}$$

By noting that $\beta_0 \gg 1$ in our range of T_0 (Koll and Cronin, 2019), we can readily verify our dilute approxmation:

$$\frac{T_*}{L\varpi/R_v} \approx \frac{1}{\beta_0\varpi} = 0.06 \tag{C.8}$$

for $T_0 = 272.6$ K. We will also define $q_0 = 1/(\beta_0\varpi)$ as the moisture inhibition threshhold at $T = T_0$.

We then want to relate our pressure p_* to the dry mass path. We note that since q_c is relatively dilute, the atmosphere will quickly dry on the moist adiabat extending upwards from this point, leaving most of the upper atmosphere dry. For a dry mass path m_d, we can then write $p_* \approx m_dg$.

We assume that the temperature structure of the upper atmosphere ($p < p_*$) is approximately a dry adiabat emanating from (p_*, T_*). This neglects the effect of moisture on the lapse rate, which can be significant but quickly leads to intractable solutions since lapse rate $\mathrm{d}T/\mathrm{d}p$ depends on $q(p, T)$. This dry adiabat has the form:

$$T = T_* \left(\frac{p}{p_*} \right)^{\alpha}, \quad \alpha \equiv \frac{R_d}{c_p}. \tag{C.9}$$

This allows us to write an equation for how τ varies with $\ln T$:

$$\frac{\mathrm{d}\tau}{\mathrm{d}\ln T} = \left(\frac{\mathrm{d}\ln T}{\mathrm{d}\ln p} \right)^{-1} p \frac{\mathrm{d}\tau}{\mathrm{d}p} \tag{C.10}$$

$$= \alpha^{-1} \left[\frac{\kappa_d p}{\bar{\theta} g} + (\kappa_v - \kappa_d) \frac{\varepsilon p_{\mathrm{sat}}}{\bar{\theta} g} \right] \tag{C.11}$$

$$= \alpha^{-1} \left[\frac{\kappa_d p_*}{\bar{\theta} g} \left(\frac{T}{T_*} \right)^{1/\alpha} + (\kappa_v - \kappa_d) \frac{\varepsilon p_0}{\bar{\theta} g} \left(\frac{T}{T_0} \right)^{\beta_0} \right]. \tag{C.12}$$

Integrating this relation and letting $\tau = 0$ when $(T, p) = (0, 0)$ yields:

$$\tau = \alpha^{-1} \left[\frac{\alpha \kappa_d p}{\bar{\theta} g} + (\kappa_v - \kappa_d) \frac{p}{\beta_0 \bar{\theta} g} q \right]. \tag{C.13}$$

To calculate the OLR, ideally we would invert Equation C.13 to find $T(\tau)$ in Equation C.1. However, due to the mixed powers of T in Equation C.13 (one term in $T^{1/\alpha}$ and one in T^{β_0}), this cannot be done analytically. To proceed, we compare the magnitude of the two terms and argue that the second term can be neglected so long as:

$$q \ll \frac{\beta_0 \alpha}{\kappa_v / \kappa_d - 1}. \tag{C.14}$$

Let us take characteristic values of β_0 at $T_0 = 273$ K, $\alpha \approx 2/7$, and $\kappa_v = 0.01$ m^2 kg^{-1} and $\kappa_d = 1.6 \times 10^{-4}$ m^2 kg^{-1} (this value of κ_d yields good agreement between our final analytical OLR and simulations and is consistent with H_2 becoming optically thick in the infra-red between 0.1 and 1 bar). In this case, Equation C.14 gives:

$$q \ll 0.1. \tag{C.15}$$

We assert this to be true around the $\tau \sim 1$ region of the atmosphere, even if it doesn't strictly hold at $p = p_*$.

We then have:

$$T = T_*\left(\frac{\tau}{\tau_*}\right)^{\alpha}, \quad \tau_* \equiv \frac{\kappa_d p_*}{\bar{\theta} g} = \frac{\kappa_d m_d}{\bar{\theta}}, \tag{C.16}$$

which when inserted into C.1 yields

$$\mathrm{OLR} = \Gamma(1 + 4\alpha)\tau_*^{-4\alpha}\sigma T_*^4, \tag{C.17}$$

where Γ is the standard gamma function. Expanding T_* from Equation C.7 and τ_* from Equation C.16 yields:

$$\mathrm{OLR} = \Gamma(1 + 4\alpha)\left(\frac{\kappa_d m_d}{\bar{\theta}}\right)^{-4\alpha}\left(q_0 \frac{\kappa_v m_d}{\varepsilon \bar{\theta}}\right)^{4/(\beta_0 - 1)} \sigma T_0^4. \tag{C.18}$$

We immediately see that this OLR limit does not depend on the surface temperature, which is characteristic of a runaway greenhouse atmosphere. The first bracket corresponding to τ_* represents the effect of increasing the dry opacity of the atmosphere. This shifts the radiating temperature up the adiabat with exponent α, and therefore reduces the OLR of the atmosphere. The second bracket traces back to Equation C.7 and represents how increasing the dry mass of the atmosphere increases the temperature at which the atmosphere becomes inhibited, T_*. Increasing the base temperature of the adiabat is associated with an increase in the OLR, albeit with a weak dependence of $m_d^{4/(\beta_0 - 1)}$. We can see that the OLR depends on the dry mass path m_d with an exponent of:

$$4(\beta_0 - 1)^{-1} - 4\alpha \approx -4\alpha, \tag{C.19}$$

since $\beta_0 \gg 1$. For a diatomic ideal gas $-4\alpha \approx -8/7$, so we would expect the OLR to drop of sharply with dry mass path.

We can compare Equation C.18 with Equation 24 in (Koll and Cronin, 2019), for a pure steam atmosphere, which was an estimate of the classical Simpson-Nakajima limit:

$$\mathrm{OLR}_{\mathrm{SN}} = \Gamma(1 + 4/\beta_o)\left(\frac{\kappa_v p_o}{\bar{\theta} g}\right)^{-4/\beta_o} \sigma T_o^4 = \Gamma(1 + 4/\beta_o)\sigma T_o^4. \tag{C.20}$$

Taking the ratio of this equation and Equation C.18 gives:

$$\frac{\mathrm{OLR}}{\mathrm{OLR}_{\mathrm{SN}}} = \frac{\Gamma(1 + 4\alpha)}{\Gamma(1 + 4/\beta_o)}\left(q_o \frac{\kappa_v m_d}{\varepsilon \bar{\theta}}\right)^{4/(\beta_o - 1)} \left(\frac{\kappa_d m_d}{\bar{\theta}}\right)^{-4\alpha}. \tag{C.21}$$

In general, since $4/(\beta_o - 1) \ll 1$ and the gamma function ratio is of order unity, so long as $\kappa_d m_d/\bar{\theta} > 1$ (i.e. the dry mass of the atmosphere is optically thick), the OLR limit will be lower than the classical Simpson-Nakajima limit.

Lastly, if we note that if one were to take the opposite limit of Equation C.14 (i.e. the moist optical depth at $\tau \sim 1$ dominates the OLR, we would find:

$$\mathrm{OLR} = \Gamma(1 + 4/\beta_o)\left(\frac{c_p}{L T_o}\right)^{-4/\beta_o} \sigma T_o^4, \tag{C.22}$$

which is identical to the “dilute limit" found in Koll and Cronin (2019). This limit does not depend on the dry mass path and is only moderately lower than the Simpson-Nakajima limit. Since our results vary greatly with dry mass path and are much lower than this limit, this should reassure us that Equation C.14 is a good assumption.